Time efficient radiation model for plasma spectroscopy and model based control of transient thermal arcs

Michael Mallon

Danksagung

"We are each our own devil and we make this world our hell."
(Zitat: Oscar Wilde)

Diese Arbeit passt zu dem Zitate, sie ist für mich Fluch und Segen zugleich, aber auf jeden Fall eine Reise die ich nicht in meinem Leben missen möchte. Ich möchte diese Gelegenheit nutzen um allen zu Danken, die mich über die Jahre auf dieser Reise begleitet haben.

Zunächst gilt mein Dank gilt meinem Doktorvater, Professor Jochen Schein. Ich danke dir Jochen für deine Unterstützung und die Möglichkeiten, die ich durch dich über die Jahre erfahren durfte. Seit ich mit meiner ersten verrückten Idee vor deiner Tür gelandet bin ist es schon viele Jahre her, mein Leben war damals noch stark vom militärischen Alltag geprägt doch dank dir konnte meine Affinität zur Wissenschaft weiter wachsen und gedeihen lassen.

Ich danke auch all den hervorragenden Kollegen des LPT. Trotz das ich viele Jahre lang allein in meinem Kämmerlein geforscht habe, wurde ich von euch in den letzten beiden Jahren herzlich aufgenommen, dafür vielen Dank. Ich möchte nun einigen lieben Kollegen im speziellen danken. Euch Marvin, Ruslan, Pavel und Jörn vielen dank für die interessanten Diskussion und das freundschaftliche Arbeitsumfeld.

Im speziellen gilt nun mein Dank drei besonderen Personen die mich über die vielen Jahre hinweg immer begleitet haben. Ich danke dir Karsten für die unzähligen tollen Diskussion, die Ratschläge und vor allem die vielen Guten Ideen. Sollte ich doch mal ein Buch schreiben wird es mit Sicherheit "Quanten Kung Fu" im Titel tragen.

Ich danke dir Marina für die wundervolle Zusammenarbeit. Da ich oft nicht gut mit Worten bin sage ich hier einfach nur Danke und ich freue mich das wir in den nächsten Jahren sicherlich noch oft zusammenarbeiten werden.

Zu guter Letzt gilt mein größter Dank einem brillanten Physiker, Freund und Kollegen José-Luis Marqués. Als ich noch Student war hast du José meine Neugierde zur Plasmaphysik geweckt und so habe ich meine gesamte Studienzeit und alle Arbeiten derselbigen gewidmet. Als ich danach meine Zeit bei der Bundeswehr abgeleistet habe, hast du mich über 6 Jahre hinweg weiter betreut. Danke dass du dir in all den Jahren stets die Zeit genommen hast, mich mit exzellenten Erklärungen für kompliziertesten Sachverhalte zu begeistern. Danke für den steten Austausch, für Ideen und Kommentare und auch Danke das ich gerade in schwierigen Zeiten, ob persönlicher oder fachlicher Probleme, immer zählen konnte.

Danke dir meine geliebte Frau Janine und dir mein kleiner Sonnenschein Thalia. Ohne euch wäre das Leben nicht lebenswert.

Was bleibt noch zum Schluss!

Einer meiner Lehrmeister (Zitat unbekannt) hat einmal gesagt: "Ein Meister ist wie eine Schale heißes Wasser, wenn er aufhört an sich zu arbeiten ist er nur noch Wasser."

Abstract

Many applications of plasma technology at atmospheric pressure use the plasma as a high temperature source. For these thermal plasma jet processes, control and process observation are crucial methods needed to ensure the process stability, reliability and enable new capabilities within the process likewise.

Maintaining such a plasma in a steady state of operation and compensate deviations coming from internal disturbances (turbulent flow, inhomogenous axial heat flux, etc.) or due to externally changed conditions (ripple in the current/voltage power supply, erosion of the electrodes) is not an easy task and requires deep insight into the basic physics of the underlying process. Hence, if maintaining a plasma in a stationary state is already a difficult task, to imprint a pulsed pattern, becomes a very demanding job. Designing a efficient feedback control for such a plasma discharge seems to be challenging task, where a solution still has to be found. A lot of the present systems rely on empirical models in order to predict the process behaviour. Yet even works, which are based on physical models, do not consider plasma dynamics. Consequently, there is a need of a thermal arc plasma model, which on one hand considers all the relevant physical phenomena and on the other hand is simple enough to allow an efficient calculation with lower need of computational effort.

Also there is a high demand for techniques that analyse the data from measurements of transient phenomena and extract plasma parameters, which are of interest for the regarded process (like particle densities and temperatures). This is most notably relevant for plasma discharges where metal vapour is present. This work pursues a dual approach.

At first this work aims to design a flatness based control, able to track a desired plasma temperature trajectory at a relatively high frequency rate. The tracking of this behaviour will be achieved by one physical quantity alone, the cathode temperature.

The second idea of this work is to develop a simplified radiation model, which links the emitted radiation of the plasma to the radial plasma temperature and electron density distribution within the thermal arc.

Combining both contributions, the model based control and the radiation model, will help to constitute a new tool set to gain and maintain stability of the plasma discharge and observe the process parameter evolution.

This novel approach bridges the gap between different scientific disciplines like plasma physics, quantum mechanics, radiation dynamics and control theory by developing a method that enables the control of the plasma discharge through one physical quantity alone, the cathode spot temperature.

Zusammenfassung

Viele Anwendungen in der Plasmatechnik, bei atmosphärischen Druck, nutzen das erzeugte Plasma als Quelle für hohe Temperaturen. Für diese thermischen Plasma Prozesse ist es wichtige Methoden der Regelung und Prozessbeobachtung anzuwenden, um die geforderte Prozessstabilität, Verlässlichkeit zu gewährleisten und neue Einsatzmöglichkeiten für den Prozess zu erschließen.

Ein Plasma in einem stationären Zustand zu halten und Abweichungen auszugleichen, welche aus internen Störungen (Turbulenzen, asymmetrischer axialer Wärmefluss usw.) oder externen Quellen (Welligkeit der Stromquelle oder Erosion der Elektroden) resultieren können, ist keine leichte Aufgabe. Hierbei ist ein großes Verständnis für die grundlegenden physikalischen Effekte notwendig, welche dem Prozess zugrunde liegen. Da das beibehalten eines stationären Zustandes schon keine leichte Aufgabe ist, ist leicht ersichtlich, dass das Einprägen eines komplexen Musters in ein solches Plasma system eine herausfordernde Aufgabe ist. Eine Regelung hierfür zu entwerfen ist eine ebenfalls fordernde Aufgabe, für die er noch gilt eine Lösung zu finden. Viele der bestehenden Systeme nutzen empirische Modelle, um das Prozessverhalten vorherzusagen. Obgleich es auch arbeiten gibt die sich auf physikalische Modellierungen stützen, wird die Plasma Dynamik bei keinem der aktuellen Modelle einbezogen. Demzufolge gibt es einen Bedarf für ein Modell eines thermischen Plasmas, das auf der einen Seite genug der grundlegenden physikalischen Phänomene berücksichtigt, aber zugleich auch einfach genug ist, damit schnell Berechnungen durch geführt werden können.

Zudem gibt es einen großen Bedarf an Techniken mit denen Daten aus spektroskopischen Messungen, solcher transienter Phänomene untersucht und die relevanten Plasmaparameter, welche für den Prozess interessant sind (wie zum Beispiel die Partikeldichten und die Plasmatemperatur), abgeleitet werden können. Das is besonders von Interesse, wenn man Prozesse betrachtet in denen Metall Dämpfe im Plasma vorkommen. Diese Arbeit verfolgt daher einen dualen Ansatz.

Zunächst soll ein Flachheit basiertes Regelmodell entworfen werden, das in der Lage ist ein Muster in die Plasmatemperatur der betrachteten Prozesses einzubringen und dies mit hohen Frequenzen zu wiederholen.

Die zweite Idee ist die Entwicklung eines vereinfachten Strahlungsmodells, welches in der Lage die Eigenschaften der zugrunde liegenden Plasmatemperatur (und Elektronendichte-) Verteilungen einzubeziehen und daraus die emittierte Strahlung des Plasmas zu berechnen.

Diese beiden Entwicklungen (die Flachheits basierte Regelung und das Strahlungsmodell) zusammengenommen, stellen ein einheitlichen neuen Ansatz dar um einen thermischen Plasmaprozess zu stabilisieren und zu die Entwicklung seiner Plasmaparameter zu überwachen.

Dieser neuartige kombinierte Ansatz stellt eine Brücke zwischen verschiedenen Disziplinen der Wissenschaft dar, der Plasmaphysik, der Quantenmechnaik, der Strahlungsdynamik und der Regelungstechnik. Die Plasmadynamik wird dabei durch eine einzige physikalische Größe beobachtet, die Kathoden Temperatur.

Contents

List of Abbreviations

Notation	Description	Unit
τ	collision time	s
ω	angular frequency	$\mathrm{rad\,s^{-1}}$
λ_D	Debye length	m
λ_L	Landau length	m
ℓ_{arc}	axial length of cylindrical plasma core	m
$r_0 = r_{cool}$	radius of the cylindrically symmetric cool surrounding atmosphere	m
r_c	cathode radius	m
r_p	radius of efective plasma core if considered as homogeneous cylinder	m
z_c	cathode's longitudinal width	m
ℓ_s	length of the cathode sheath	m
$\mathcal{Z}$	partition function	$-$
p	gas pressure	$\mathrm{Pa} = \mathrm{kg\,m^{-1}\,s^{-2}}$
T	temperatur	K
$T_0 = T_{cool}$	temperature of cool surrounding atmosphere	K
T_p	homogeneous temperature of (cylindrical) plasma core	K
T_c	cathode surface temperature	K
$T_{e,s-ps}$	electron temperature presheath-sheath boundary	K
$T_{h,s-ps}$	heavy particle temperature presheath-sheat boundary	K
$T_{e,\infty}$	electron temperature bulk boundary	K
$T_{h,\infty}$	heavy particle temperature bulk boundary	K
$\Psi_{therm,p}$	thermal potential of the plasma	$\mathrm{W\,m^{-1}}$
v	velocity	$\mathrm{m\,s^{-1}}$
v_{Bohm}	Bohm velocity scale at sheath-core edge	$\mathrm{m\,s^{-1}}$
m_i	ion mass	kg
$n_{e,s-ps}$	electron density presheath-sheath boundary	$\mathrm{m^{-3}}$
$n_{i,s-ps}$	ion density presheath-sheath boundary	$\mathrm{m^{-3}}$
$n_{e,\infty}$	electron density within homogeneous plasma core	$\mathrm{m^{-3}}$
$n_{i,\infty}$	ion density within homogeneous plasma core	$\mathrm{m^{-3}}$
$\lambda_{th,an}$	anode thermal conductivity	$\mathrm{Wm^{-1}K^{-1}}$
$\lambda_{th,c}$	cathode thermal conductivity	$\mathrm{Wm^{-1}K^{-1}}$
$c_{p,c}$	cathode's heat capacity	
$c_{p,p}(T_p)$	heat capacity (at constant pressure) of plasma core	

ρ_c	cathode's mass density	kg m^{-3}
$\rho_p(T_p)$	mass density of plasma	kg m^{-3}
$\sigma_{el}(T_p)$	electric conductivity of plasma	
E_{ion}	first ionization energy	eV
E_{arc}	electric field along homogeneous plasma core	Vm^{-1}
E_{cath}	electric field cathode surface	Vm^{-1}
Φ_{an}	anode work function	eV
Φ_c	cathode work function	eV
A_R	Richardson constant	$\text{A m}^{-2}\,\text{K}^{-2}$
$j_{e,th}$	thermionic electron density	Am^{-2}
$j_{i,s-ps}$	ion current density sheath-presheath boundary	Am^{-2}
$j_{e,back,s-ps}$	back diffusing electron current density sheath-presheath boundary	Am^{-2}
U_{ps}	sheath voltage drop	V
U_s	voltage across cathode sheath	V
I_{arc}	electric current along plasma arc	A
I_λ	spectrally resolved radiative intensity by an extrenal observer	$\text{W m}^{-1}\,\text{sr}^{-1}$
I_{rad}	total radiative intensity	W
ϵ_λ	spectral emission coefficient	$\text{W m}^{-3}\,\text{sr}^{-1}\,\text{m}^{-1}$
κ_λ	spectral absorption coefficient	m^{-1}
f_{pulse}	process pulse repetition rate	s^{-1}
$f_{control}$	controller sampling frequency	s^{-1}
f_{obs}	observer sampling frequency	s^{-1}
$\tau_{control}$	controller gain parameter	$-$
τ_{obs}	observer gain parameter	$-$

Universal constants	Description	Unit
e, q_e	electron elemental charge	1.6022×10^{-19} A s
h	Plank constant	6.6261×10^{-34} $J\,s$
k_B	Boltzmann constant	1.3807×10^{-23} J K^{-1}
m_e	electron mass	9.1094×10^{-31} kg
N_A	Avogadro number	6.022×10^{23} (particle) $\equiv 1$ mol
ε_0	dielectric permittivity $\frac{1}{4\pi\varepsilon_0} \approx 9 \times 10^9$ $\text{kg m}^3\,\text{A}^{-2}\,\text{s}^{-4}$	$8,8542 \times 10^{-12}$ $\text{kg}^{-1}\,\text{m}^{-3}\,\text{A}^2\,\text{s}^4$
μ_0	magnetic permeability des Vakuums	$4\pi \times 10^{-7}$ $\text{kg m A}^{-2}\,\text{s}^{-2}$
$c = \frac{1}{\sqrt{\mu_0\varepsilon_0}}$	light speed in vaccum	$2,9979 \times 10^8$ m s^{-1}

Chapter 1

Introduction

1.1 Review of literature

Many applications of plasma technology at atmospheric pressure use the plasma as a high temperature source, to either melt powder injected into a plasma flow and deposite it on a substrate (Plasma Spraying) [1, 2], for the destruction of hazardous materials (Plasma waste destruction) [3] or for welding metal substrates placed just below the plasma arc [4–6].

All these processes belong to the category of so called thermal plasma discharges (thermal arcs), which are defined by the following characteristics:

- All species are assumed to have Maxwellian velocity distribution. Therefore Local Thermodynamic Equilibrium (LTE) or at least partial Local Thermodynamic Equilibrium (pLTE) is applicable.

- The plasma temperature is in the range of a few eV

- Excited states within heavy particles are assumed to be populated, according to the Boltzmann term

- The strength of external magnetic fields is assumed to be less than the own magnetic field of the arc and is therefore be neglected.

- The boundary conditions of the arc are determined by the surrounding gas flow, a solid or liquid wall.

Typical discharge parameters for this category of processes are listed in Table 1.1. This work will limit all following discussions to the case of atmospheric pressure discharges, although the ideas can generally be extended into other pressure ranges aswell.

Quantity	Range
power density	10^7 - $10^9\,\mathrm{J\,m^{-3}}$
current density	10^7 - $10^9\,\mathrm{A\,m^{-2}}$
electrical field strength	10^2 - $10^8\,\mathrm{V\,m^{-1}}$
discharge power	10^2 - $10^5\,\mathrm{J\,m^3}$

Table 1.1: Characteristic physical quantities for thermal plasmas in industrial applications

Maintaining such a plasma in a steady state of operation and compensate deviations coming from internal disturbances (turbulent flow, inhomogenous axial heat flux, etc.) or due to externally changed conditions (ripple in the current/voltage power supply, erosion of the electrodes) is not an easy task and requires deep insight into the basic physics of the underlying processes. Designing an efficient feedback control for such a plasma discharge seems to be an obvious solution for such a problem. However due to the low mass density of the plasma gas and its relatively high thermal conductivity the plasma dynamics (temporal and spatial evolution of the plasma parameters) act on a very short time scale and dynamic control would need to fit into such a time frame to influence the plasma effectively. Hence, if maintaining a plasma in a stationary state for such a process is already a difficult task, to imprint a pulsed pattern, which can be kept in a stable way for a long time, becomes a very demanding job where a solution still has to be found.

To make the solution strategy for this problem more evident it is convenient to choose one of the mentioned processes and outline the solution therefore in detail. For the category of atmospheric plasma arcs a paragon is the Gas Tungsten Arc Welding process (GTAW), since from the perspective of arc welding this process is rather stable and well understood [7, 8]. Yet improving the reliability and efficiency of such a common welding technique always plays an important role for industrial applications.
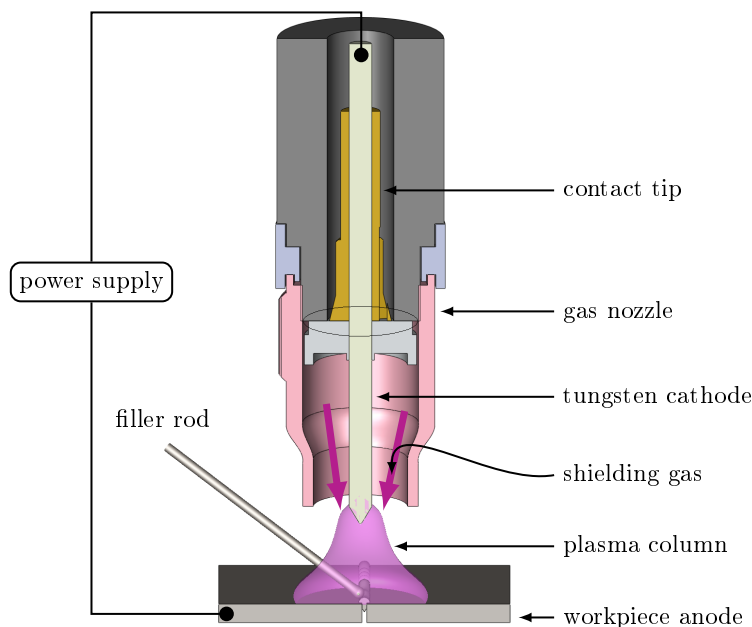
Figure 1.1: Schematic of the GTAW torch [9]

Gas Tungsten Arc Welding Gas tungsten arc welding (GTAW) [4], also known as tungsten inert gas (TIG) welding in case inert gases are used, is characterized by a refractory electrode typically made of tungsten. Figure 1.1 shows a schematical drawing of the eletrode arrangement and the arc between the cathode at the top and the anode at the bottom. A constant current (DC) is typically fed to the electrodes by a power supply, to induce the breakdown of the gas and maintain the resulting plasma. Sometimes pulsed DC currents are used to achieve a ceratin behaviour of the arc or maintain its stability. The plasma in turn is used as a high temperature source to melt the underlying workpiece. The upper electrode (cathode) is surrounded by a shielding gas supplied by a gas nozzle around the electrode. The plasma composition mainly results from the choice of the working gas or gas mixture. GTAW is used to produce high quality welds, but it is more complex than comparable processes, such as shielded metal arc welding and slower than other comparable welding processes. Mostly noble gases

like Argon or Argon-Helium are use as shielding gases to reduce the effect of oxidation at the hot cathode tip, during operation [7]. A related process, Plasma Arc Welding (PAW), has a comparable welding torch to focus this surrounding gas stream even stronger.

The GTAW process will be analysed in detail in this work, due to the similarities in geometry and polarity of the electrodes compared to the other thermal arc processes. The results and developed techniques however can be applied to the other mentioned thermal plasma processes as well. For GTAW typically parameters such as process current, arc voltage, arc length or weld pool temperature are used as a feedback variable [10]. These approaches, although posing as a practical solution, are limited in their precision to follow a desired behaviour of the plasma evolution and are not able to follow the desired behaviour, when instabilities emerge within the process. A lot of those systems rely on empirical models in order to predict the process behaviour [11, 12]. Yet even works, which are based on physical models, do not consider plasma dynamics at all [13–16]. The control approaches for these systems utilize either linear transfer functions [13, 15, 17, 18] or neural network based controlling schemes [19] to handle the system dynamics. Common models of welding plasmas are computed using finite volume methods [20], which require high computation times and thus are not suitable for feedback control applications.

The control aspect will be extensively discussed later on in this work, but beforehand it shall be regarded that modern industrial applications involving thermal arcs have to fulfill other important requirements as well. For example the automation of a process, as well as the steady increase in operational safety and reliability have become essential qualities. Still few works exist to deliver solutions for the observation of dynamical plasma process parameters in real time. To gather the data from the physical system (a experimental setup or a industrial plasma application) some of the best techniques to analyze such plasma processes are optical measurement techniques, since these don't disturb the plasma further by introducing new boundary layers (like it would be the case of Langmuir probes [21, 22]). To analyze the measured spectral intensities and extract the desired information on the plasma parameters, substantial knowledge of physical principles of the applied measuring technique is required, as well as its coupling to the desired physical quantity. Subsequently there is a high demand for techniques that correlate the data from measurements of transient phenomena to the plasma parameters, which are of interest for the regarded process (like particle densities and temperatures). This is most notably relevant for plasma discharges where metal vapour is present [23–25].

From the perspective of optical spectroscopy there are again various techniques to analyze the plasma behaviour, especially if the local temperature and electron density of the plasma is required. One such technique is Stark line broadening measurement, which is often applied when it comes to measurement of the electron density. However especially for the Quadratic Stark effect, the line width also depends on temperature [26]. Hence Stark line broadening needs to be combined with other diagnostic methods in order to obtain both plasma temperature and electron density. Simultaneous evaluation of several Stark broadened lines can be used to deduce both electron temperature and density [27, 28]. However such a method requires a reliable model of the Stark effect for several well-detectable optically thin lines in prevailing plasma conditions. There are few works describing the Stark effect depending on electron temperature and density [29, 30]. Yet even if those models take into account various effects such as ion collisions or presence of electric fields, the evaluation of sufficiently strong spectral lines (e.g. Ar I lines) does not always provide an accurate result for simultaneous determination of electron density and temperature [9]. This is in particular the case, when it comes to evaluation of spectra containing metal vapour.

One of the more (if not the most) elaborate techniques is the Thomson scattering measurement of laser radiation by the free electrons in a plasma, it is considered as the most reliable method for electron temperature and density diagnostics in fusion related plasmas [31]. Although this technique was developed to analyse fusion processes, it was also utilized to measure plasma parameters in low temperature plasmas, such as atmospheric gas discharges [32–38]. Yet the most severe drawback of this technique, it is quite complicated to setup and to smooth away faults that would lead to ambiguous results, which makes it hard to apply to dynamical processes.

Optical emission spectroscopy (OES) [39] is another technique, which offers a simple experimental

set-up and thus is potentially more suitable for real time diagnostics for process observation applications. A lot of techniques of this type need the information on the chemical composition of the plasma and whether a optically thin line can be found to apply such a method [40]. Also most techniques of this type rely on evaluation of a specific feature of the radiation spectra, which allows to extract either electron temperature or density. For example line intensity ratios of two or more optically thin lines can be used in order to determine the electron temperature [41–43]. The current state-of-the-art approach of this category is the Fowler-Milne method and its derivative techniques [44–47].

Fowler-Milne method This method takes a optically thin line of the radiation spectrum emitted from the plasma and compares the relative radial distribution of this line with theoretical values the the corresponding emission coefficient, to determine the spatial temperature distribution [48]. Originally developed for applications involving pure Argon plasmas, their have been various modifications throughout the year to make the method applicable to gas mixture and even plasmas with impurites (e.g. metal vapour [49]).

However such a technique is difficult to apply to plasmas, where absorption plays an important role, which is the case for processes where metal vapour is present. In order to evaluate the radiation intensities and spectra gathered with this OES technique where absorption plays an important role,the current state-of-the-art technique is the Net Emission Coefficient (NEC) approach [50, 51].

Net Emission Coefficient approach This method is based on the difference between the emitted and absorbed power within a volume unit of the plasma. This volume unit is defined by the radius of an emitting sphere of plasma and is commonly used in thermal plasma modelling. This plasma radius is fixed for the entire plasma geometry and must be predefined. Therefore only global radiative heat transfer to the surrounding (e.g. a solid wall) can be described [51].

Both approaches however are not sufficient in cases of strong absorption. One drawback of the Fowler-Milne method, it still needs optically thin lines to evaluate the plasma temperature, which in complex gas compositions is not guaranteed. The NEC approach incorporates the spectral absorption on lines, but introduces a arbitrary effective radius of an emitting sphere as free parameter to account for this absorption. The dimension of that radius is not easy to determine and local emission characteristics below this radius are unaccounted for. Although in recent years there was a parallel development, trying to extend the NEC approach with a similar technique to this work [52]. No further progress could be found in the literature and a functional scheme is still missing, while this thesis provides a working technique extending current NEC approaches [53].

1.2 Originality of this work

For applications involving thermal arcs, process control and monitoring are crucial methods needed to ensure the process stability, reliability and extend the applicability of the process likewise. Understanding and including the impact of the plasma dynamics into physical models for the control and the spectroscopical monitoring of the plasmas within the process are a profound way to improve the process itself.

Consequently, there is a demand for a thermal arc model, which on one hand considers all the relevant physical phenomena and on the other hand is simple enough to allow an efficient calculation with lower need of computational effort. This work pursues a dual approach to achieve this goal, see Figure 1.2.

At first this work aims to design a model based control, able to track a desired plasma temperature trajectory in a stable way and at the highest possible pulse repetition rate. This novel approach bridges the gap between plasma physics and control theory by developing a method that enables the control of motion of the plasma discharge through one physical quantity alone, the cathode spot temperature.

The second idea of this work is to develop a physical model which links the emitted radiation of the plasma to the radial plasma temperature and electron density profile within the thermal arc. For this purpose the spectrum of the radiation coming from the plasma is calculated with a new approach.
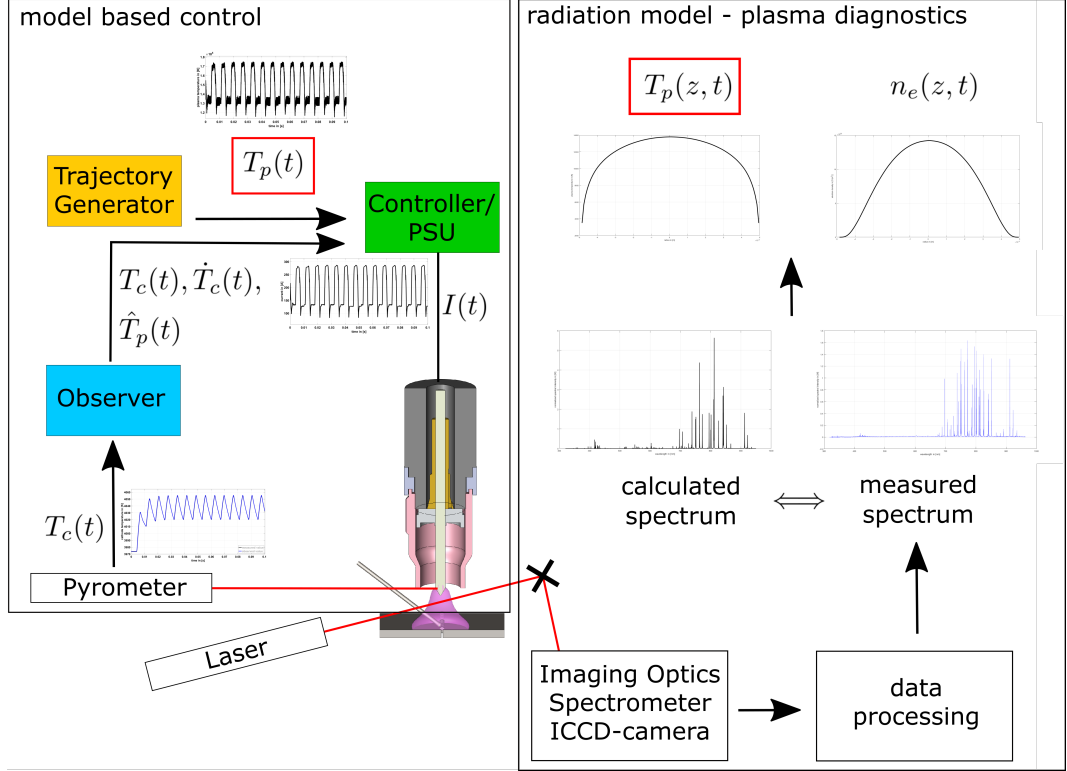
Figure 1.2: Schematic representation of this thesis dual modeling approach. The model based control for process tracking and the radiation model for the data processing part of plasma diagnostics.

Instead of concentrating on either the line intensity or on the line broadening of few spectral lines, the spectrum is considered in a wide range of wavelengths at once. The results are compared to spectrally resolved OES measurements of a thermal arc under the same conditions of operation, as well as Thomson scattering an Stark broadening measurement as references sources of experimental data. Thus particular details of each single line are expected to be balanced when a large spectral window is taken into account, effectively putting their combined influence on one free parameter of the radiation model, the radial distance to a cold surrounding.

Both models use the arc current, electrode distance and the gas composition as boundary conditions to calculate the plasma parameters. For the radiation model the geometry of the thermal arc is approximated as a cylinder with radial degree of freedom and constant axial and azimuthal distribution. The model based control further simplifies this assumption to a single value across the radial coordinate. Although the spatial coordinates are limited to accelerate the computations, all values retain the full temporal dependence. The radial plasma temperature and electron density distribution is determined by the equations of the models and the radial distance to a cold surrounding. This radial distance is obtained from a best fit of the calculated spectrally resolved radiation profiles compared to measured normalized spectra of an OES measurement.

Combining both contributions, the model based control and the radiation model, will help to constitute a new tool set to gain and maintain stability of the plasma discharge and observe the plasma parameter evolution. The model based control will regulate the input current to influence the plasma dynamics evolution. The tracking of this behaviour will be achieved by one physical quantity alone, the cathode spot temperature. The radiation model will work as a more elaborate tool for real time spectral analysis of the plasma radiation, to estimate local plasma temperature and electron density of the plasma. By introducing a cost function minimalization technique, the spectral analysis can be

5

performed on complex gas compositions as well, utilizing the thermal boundary condition (the radial distance to a cold surrounding) as single optimization parameter for this technique.

These techniques will be demonstrated for a GTAW process with pure Ar and Ar-He gas mixtures (the model based control will be demonstrated with Argon alone). Possible extensions towards other applications will be briefly outlined in the conclusion.

1.3   Outline of this work

The work is organized in three main parts.

- The first part will establish the set of physical equations needed to develop the diagnostic technique and the model based control separately. A description for the temperature evolution of a plasma close to a cathode will be formulated. Next the plasma composition and particle densities will be derived using a formulation of the Saha-Eggert equation. Both inputs are then combined to formulate the equations and fundamental principles for the interface between the cathode region and the plasma. The specific impact on the evolution of the physical properties within the sheath, like the electric field and more importantly the heat transfer between the solid metal cathode and the plasma, are derived.

- The second part of the work is a chapter on the fundamental quantum physics behind the interaction of electromagnetic radiation with the particles of a plasma. The intention is to briefly recapitulate the concepts behind these photon particle interactions, discuss the most relevant questions and derive a mathematical scheme to describe these questions. This scheme will be used to describe the connection to quantities that are of direct importance to plasma spectroscopy experiments. These quantities are the line profile, the broadening width and the correlated emission and absorption coefficients of the radiation coming from the plasma.
  A simplified description of the Stark broadening width will be formulated and all quantities will be combined to derive the total radiated power, emitted from the plasma. The radiation model will be analysed for the working gases Argon and Argon-Helium (in varying gas compositions) and compared to experimental data for these working gases in a GTAW process.

- The last part of the work intends to bridge the gap between plasma physics and control theory by formulating a scheme that enables the control of the plasma discharge dynamics through one physical quantity, the cathode spot temperature. The following part will outline the idea behind flatness based control and gather the mathematical techniques, required to solve the given equations of state. The purpose is then to imprint a trajectory of the plasma temperature into the model based control and derive the resulting control output. This is directly applied to the plasma system, which in this case will be a numerical model of a thermal plasma jet. Therefore a state controlling law is derived and the required control components are developed. The model based control will be demonstrated for an Argon plasma within a GTAW process.

- Concluding this work are the chapters dealing with the results from the above mentioned calculations and the discussion of their reasonability and physical background. The outlook will examine further extensions and applications of these developed techniques.

Chapter 2

Plasma Physics Theory

> *"The technologies which have had the most profound effects on human life are usually simple."*
>
> Freeman Dyson

At atmospheric pressure a plasma arc is a very hot gas, composed of free charges (negative electrons as well as positive ions) and neutral particles, where particularly the free electrons are moving chaotically due to their high temperature T_p and low mass (compared to the ion mass, $m_e \ll m_i$). At macroscopic length scales a plasma is neutrally charged, i.e., the total amount of negative charged electrons equals the amount of positive ions. This charge neutrality is still satisfied when zooming into finer length scales, until reaching a limit, the so-called Debye length λ_D. Below this length a partial separation between electrons and their respective ions can be observed, produced by the thermal motion of the free electrons. The Debye length has nevertheless a tiny value, since the charge separation itself induces a large electric field (large because of the plasma's high charge density) stopping any further separation, it is given by $\lambda_D = \sqrt{\dfrac{\varepsilon_0 k_B T_p}{e^2 n_e}}$ ([54],§ 1), with n_e the density of free electrons within the plasma, e the electron charge, ε_0 the vacuum dielectric constant and $k_B = 1.38 \times 10^{-23}$ J/K the Boltzmann constant. For atmospheric pressure $P = 10^5$ Pa and a gas temperature of $T_p = 12\,000$ K the typical ionization degree is about $10\,\%$ and thus $n_e \sim 0.1 \dfrac{P}{k_B T_p} = 6 \times 10^{22}$ m^{-3}, resulting in a Debye length of $\lambda_D \approx 30$ nm (the Debye length will appear again later on in this work). The plasma property of showing charge neutrality above the Debye length, but not below it, is denoted quasineutrality.

The following chapter establishes the set of physical equations for the discoveries later on in this work. At first a description for the temperature evolution of a plasma in proximity to the cathode is formulated. It is a description that is based on other approaches, such as the Mayr model [55]. Secondly the equations for the plasma composition are derived in case of an atmospheric plasma discharge. Both of these descriptions are then connected to formulate equations for the interface region between the solid metal electrode (the cathode) and the thermal arc to describe the evolution of the electric field and more importantly the heat transfer within this region.

The purpose for this chapter is to derive descriptions that contain enough of the true physical behaviour of the regarded plasma system, but are also efficient enough to perform fast computations, in regard to the time scale of the process of interest. These would be of use for a radiation model for faster spectral plasma diagnostics, to derive the electron density and temperature in the plasma. As well as a model based control for the tracking of plasma parameters such as the plasma temperature along a desired trajectory.

2.1 Dynamics for a cylindrically symmetrical plasma arc

The full dynamic system considered in this work consists of the plasma arc itself, burning between two metallic electrodes, and on the physical effects occuring at (and close to) those electrodes. For the plasma arc the investigated configuration is displayed in Figure 4.1, where an axially symmetric plasma gas is confined in radial direction by a cylindrical cold boundary of radius r_0 kept at a constant temperature T_0 (chosen equal to the room temperature and reference temperature for the enthalpy). In
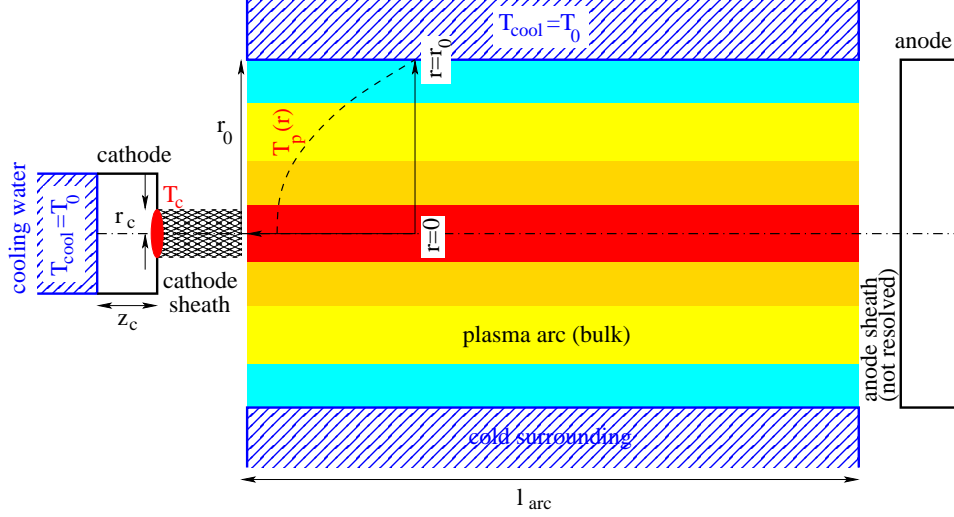
Figure 2.1: Schematic representation of the considered cylindrical plasma arc configuration

axial direction the plasma arc is limited by two planar electrodes (a negative electrode or cathode and a positive electrode or anode); the transition from the bulk plasma to each of the electrodes is managed by the so-called sheaths (cathode and anode sheath). The anode is distinctively less important for the very existence of the plasma arc than the cathode, and at atmospheric pressure the voltage at the anode sheath is nearly an order of magnitude lower than that corresponding for the cathode sheath [56]. Therefore the anode sheath and the anode itself will no longer be taken into account for the modeling of the plasma dynamics system; the cathode sheath, on the contrary and despite its very reduced length dimension at atmospheric pressure (the schematic Figure 2.1 does not represent the real cathode sheath size), will be considered in detail in the next section. Additionally, it is assumed in a first approximation that there is no appreciable pressure gradient along the axial direction such that the gas flow between the electrodes is low and laminar. Also the thermal diffusion along the arc is considered negligible when compared to the the radial diffusion towards the cold surrounding.

The energy content of a plasma gas at a local temperature T_p is described by its enthalpy density, defined as

$$h_p(T_p) = \int_{T_0}^{T_p} \rho_p(T)\, c_{p,\,p}(T)\, dT$$

where ρ_p and $c_{p,\,p}$ denote, respectively, the mass density and the specific heat (at constant pressure) of the plasma gas, both nonlinear functions of the gas temperature. According to approximations discussed above, the dynamic equation for the local change of enthalpy within a concentric layer of radius r, infinitesimal width Δr and arc length ℓ_{arc} is mainly given by two effects:

- the radial heat diffusion due to a radial temperature gradient down to T_0

- and the local power generation within the arc

8

This can be mathematically formulated [57, 58]:

$$\frac{\partial}{\partial t}\left(2\pi r\Delta r\ell_{arc}\int_{T_0}^{T_p}\rho_p(T)\,c_{p,p}(T)\,dT\right) \approx -\left[\overbrace{-2\pi\left(r+\frac{\Delta r}{2}\right)\ell_{arc}\left(\lambda_{th,p}\frac{\partial T_p}{\partial r}\right)\Big|_{r+\Delta r/2}}^{\text{heat leaving layer at } r+\Delta r/2}\right.$$

$$\left.\underbrace{\overbrace{+2\pi\left(r-\frac{\Delta r}{2}\right)\ell_{arc}\left(\lambda_{th,p}\frac{\partial T_p}{\partial r}\right)\Big|_{r-\Delta r/2}}^{\text{heat entering layer at } r-\Delta r/2}}_{\text{energy balance due to heat diffusion in radial direction}}\right]$$

$$+\underbrace{2\pi r\Delta r\ell_{arc}\,S_p(T_p)}_{\text{local power source}} \tag{2.1}$$

with $\lambda_{th,p}$ the thermal conductivity of the plasma gas, again a nonlinear function of the local plasma temperature T_p, which determines the radial heat flow density $\lambda_{th,p}\frac{\partial T_p}{\partial r}$ (=power per unit area).

The stationary temperature distribution of this system is determined by the thermal heat conductivity λ_{th} and the electrical conductivity σ_{el} of the plasma. Albeit there are different approaches to calculate these properties, like the Chapman-Enskog method, this will not be a main focus of this work and the parameters will derived from the literture. The thermophysical properties for Argon as working gas are taken from the appendix tables [59, 60]. For mixtures of Argon and Helium as working gas with different concentrations, the transport parameters can be derived from the data of [61, 62]. The local source term $S_p(T_p)$ (power locally generated/lost per unit volume) corresponds to the Joule heating produced by the electric current density j_{el} flowing along the (non-perfect conducting) plasma arc

$$\text{Joule heating:} \quad S_p(T_p) = j_{el}E_{arc} = \sigma_{el}(T_p)\,E_{arc}^2 \tag{2.2}$$

with σ_{el} the electrical conductivity of the plasma gas, again a strongly nonlinear function of the plasma temperature T_p, which relates the electric current density to the electric field E_{arc} along the plasma arc: $j_{el} = \sigma_{el}(T_p)\,E_{arc}$. The energy loss to the cathode, concentrated at the inner most core, is also neglected compared to the radial heat diffusion and the Joule heating. For an infinitesimal $\Delta r \to 0$ the eq. (2.1) can be written as the following differential equation

$$\rho_p(T_p)\,c_{p,p}(T_p)\,\frac{\partial T_p}{\partial t} \approx \frac{1}{r}\frac{\partial}{\partial r}\left(\lambda_{th,p}(T_p)\,r\frac{\partial T_p}{\partial r}\right) + S_p(T_p) \tag{2.3}$$

whose solution is thus a cylindrically symmetrical plasma temperature profile $T_p(r,t)$ with no dependence on the azimuthal angle or on the axial coordinate.

The electric field E_{arc} is practically independent of the radial coordinate — each radial location within the plasma arc "sees" the same electric field — and thus the electric current along the arc I_{arc}, given by the current density j_{el} integrated over the circular arc cross section from $r = 0$ till $r = r_0$, is related to such electric field according to

$$I_{arc} = \int_0^{r_0} 2\pi r\,j_{el}\,dr = E_{arc}\int_0^{r_0}\sigma_{el}(T_p(r))\,2\pi r\,dr$$

$$\sigma_{el}E_{arc}^2 = \frac{\sigma_{el}}{\left(\displaystyle\int_0^{r_0}\sigma_{el}(T_p(r))\,2\pi r\,dr\right)^2}I_{arc}^2 \tag{2.4}$$

The shape and size of the plasma discharge alongside its thermal properties is crucial information to understand the motion of the regarded plasma system. Here the effects of the flow stream on the energy distribution are much less then the effects of the charge carrier transport. Close to the cathode the entrainment of cold gas from the surrounding atmosphere can be neglected in a first approximation and therefore no turbulence correction to the thermal conductivity is required. With the assumption

of cylindrical symmetry the radial temperature distribution of the plasma $T_p(r)$ only depends on the radial energy dissipation due to heat diffusion and radiation emission, which balance the electrical Joule heating. The radiative heat flux is one order of magnitude smaller than the diffusion heat flux and therefore neglected in a first approximation for the shaping of the temperature profile. Hence the dynamic equation for the plasma temperature distribution is described by

$$\rho_p c_{p,\,p} \frac{\partial T_p}{\partial t} = \overbrace{\frac{1}{r}\frac{\partial}{\partial r}\left(\lambda_{th,\,p}(T_p)\, r \frac{\partial T_p}{\partial r}\right)}^{\substack{\text{loss due to diffusion in radial} \\ \text{direction, with } \frac{\partial T_p}{\partial r} \text{ \& } \frac{\partial^2 T_p}{\partial r^2}<0}} + \overbrace{\frac{\sigma_{el}}{\left(\int_0^{r_0}\sigma_{el}(T_p(r))\,2\pi r\,dr\right)^2} I_{arc}^2}^{\text{Joule heating}} + \overbrace{\ldots\ldots\ldots}^{\substack{\text{other non-modelled} \\ \text{effects}}} \tag{2.5}$$

where the ... is a reminder of those effects whose details are not being resolved in detail since less relevant than the two explicitly considered contributions: radial heat diffusion and Joule heating. The boundary conditions for such equation are $\left.\frac{\partial T}{\partial r}\right|_{\mathrm{r}=0} = 0$ (axial symmetry) and $T\,(r = r_{cool}) = T_{cool}$ (outer boundary). The above stated differential equation need to be solved numerically, due to the strong non-linear dependence of the electrical conductivity from the temperature. Nevertheless the non-modelled effects will be taken into account in a collective, effective way as a stochastic noise term when integrating the plasma dynamics. It is worth noting that the electric current I_{arc}, assuming it is generated by an external current source, serves as input variable for the arc dynamics (Equation (2.5)); more properly the input is given by the squared electric current. If, on the other hand, the system is driven by a voltage source instead, it will assumed that an underlying fast control is able for the voltage source to imprint the required electric current which derives from some later developed control design.

Remark 1: although meant to be applied to a plasma arc enclosed by a cylindrically cooled wall, previous eq. (2.5) is still applicable in a first approximation to an axially symmetric free burning arc at atmospheric pressure, at least close to the cathode [63]. At such location the mixing of the cold surrounding atmosphere with the outer plasma fringes is just starting to develop, without producing any appreciable radial widening of the plasma arc. The only unknown parameter when applying the model to the free burning arc is the radius r_0, which has to be experimentally determined, for instance by some imaging method at the edge where mixing with the atmosphere is clearly localized.

Remark 2: if desired, and after having determined the radial plasma temperature profile, the voltage along the plasma arc can be estimated from electric field (Equation (2.4)) as

$$U_{arc} = E_{arc}\,\ell_{arc} \tag{2.6}$$

2.2 Saha-Eggert Equation

The foundation for every plasma calculation is the knowledge of the plasma composition or more precisely the underlying plasma kinetics. However under certain assumption this aspect can be carried out without evaluating all underlying chemical kinetic equations. Since the central region of the plasma arc being considered operates at atmospheric pressure, as initially stated in the introduction for the regarded plasma processes, there is nearly no deviation (see [59], § 1) between the temperature for the thermal motion of free electrons and that for the heavier ions, so that local thermal equilibrium (LTE) or at least partial local thermal equilibrium (pLTE) can be assumed. In this case reaction kinetics take place on a much shorter time scale, therefore local chemical equilibrium (LCE) follows as well. Under these constraints one can solve the plasma composition with the Saha-Eggert equation.

The general theory for the case of pLTE is presented first, with the two temperature Saha-Eggert equation being derived. Where one assumes the electrons and heavy particles have seperate equilized temperature distributions, so that the coefficient $\theta = \frac{T_{e,\infty}}{T_{h,\infty}}$ can be introduced. This fundamental formulation will primarily be essential for the conclusion of this work. Throughout the main part of this work the simplified case with equal electron and heavy particle temperatures $\theta = 1$ will be pursued, since for the regarded plasma process and working gases the LTE condition is sufficient.

The consecutive derivations will in general follow the formulations of [64–66].

2.2.1 Saha-Eggert equation for monatomic gases

A monoatomic gas shall be regarded (e.g. argon or helium), where the electrons have a temperature T_e greater than the temperature T_h of all the heavy particles (atoms and ions). It will further on be assumed that ionization up to the second level will take place, which is sufficient for the temperatures relevant in the regarded plasma process [67]. Now the concentrations of all particles n_e (free electrons), n_A (neutral atoms), n_{A^+} (single charged ions), $n_{A^{++}}$ (double charges ions) in equlibrium must be determined. For the four unknowns, their are four equations to be deduced from:

- Dalton's ideal gas law (1 equation) [59]

- Saha equation for each ionization level (1+1 equations)

- quasi neutrality condition (1 equation)

The first equation expresses the relation between gas pressure p, the temperatures T_e and T_h and the particle densities:

$$P = n_e k_B T_e + (n_A + n_{A^+} + n_{A^{++}})\, k_B T_h \;\Rightarrow\; \frac{P}{k_B T_e} = n_e + \frac{1}{\theta}\left(n_A + n_{A^+} + n_{A^{++}}\right) \qquad (2.7)$$

with θ being the quotient between electron temperature and temperature of the heavy particles, $\theta = \dfrac{T_e}{T_h}$.

For the Saha equations the partition functions for the neutral atoms, the single charged ions and double charged ions are formulated:

$$\mathcal{Z}_A = \sum_k g_{A,k} \exp\left(-\frac{E_{A,k}}{k_B T_e}\right)$$

$$\mathcal{Z}_{A^+} = \sum_k g_{A^+,k} \exp\left(-\frac{E_{A^+,k}}{k_B T_e}\right)$$

$$\mathcal{Z}_{A^{++}} = \sum_k g_{A^{++},k} \exp\left(-\frac{E_{A^{++},k}}{k_B T_e}\right)$$

where E_k denotes the k-th bound energy for each plasma species and g_k is its corresponding degeneracy factor (i.e., "how many electrons can be stored in energy level E_k of each species"). Those values can be derived from the data in the NIST-database [68]. Now the Saha factors can be formulated:

$$K_I = \frac{2\,\mathcal{Z}_{A^+}}{\mathcal{Z}_A}\left(\frac{2\pi m_e k_B T_e}{h^2}\right)^{3/2}\exp\left(-\frac{E_{A,ion}}{k_B T_e}\right)$$
$$K_{II} = \frac{2\,\mathcal{Z}_{A^{++}}}{\mathcal{Z}_A^+}\left(\frac{2\pi m_e k_B T_e}{h^2}\right)^{3/2}\exp\left(-\frac{E_{A^+,ion}}{k_B T_e}\right) \tag{2.8}$$

and the corresponding Saha equations are:

$$\frac{n_e\,n_{A^+}}{n_A} = K_I\,, \qquad \frac{n_e\,n_{A^{++}}}{n_{A^+}} = K_{II} \tag{2.9}$$

with $E_{A,ion}$ being the ionization energy of the neutral atom and $E_{A^+,ion}$ being the one for the single ionized atom. Important to notice is the fact that the temperature in the partition functions (Equation (2.8)) and the Saha factors (Equation (2.8)) is the electron temperature T_e. This is the case since the collisions with the free electrons are the main source for the excitation of the atoms/ions and responsible for ionization.

It is worth noting that the density n_e of free electrons, is given by the inverse of the volume occupied by one single free electron with thermal velocity $\sqrt{\frac{k_B T}{m_e}}$ (and momentum $\sqrt{m_e k_B T}$), where the length scale of such volume is given by the position uncertainty derived from the Heisenberg relation: $\ell_e \sim \frac{h}{\sqrt{m_e k_B T}}$ and $n_e \sim \frac{1}{\ell_e^3} \sim \left(\frac{\sqrt{m_e k_B T}}{h}\right)^3$. The last equation is the quasi neutrality condition:

$$n_e = n_{A^+} + 2n_{A^{++}} \tag{2.10}$$

Combining all equation leads to the following:

$$\frac{P}{k_B T_e} = n_e\left[1 + \frac{1}{\theta}\frac{1 + \dfrac{K_I}{n_e} + \dfrac{K_I K_{II}}{n_e^2}}{\dfrac{K_I}{n_e} + 2\dfrac{K_I K_{II}}{n_e^2}}\right] = n_e\left[1 + \frac{1}{\theta}\frac{n_e^2 + n_e\,K_I + K_I K_{II}}{n_e\,K_I + 2K_I K_{II}}\right]$$

or in polynomial form:

$$n_e^3 + n_e^2\,(1+\theta)\,K_I + n_e\,K_I\left((1+2\theta)\,K_{II} - \theta\frac{P}{k_B T_e}\right) - 2\theta K_I K_{II}\frac{P}{k_B T_e} = 0 \tag{2.11}$$

It is a cubic equation for the electron density n_e

$$n_e^3 + c_2\,n_e^2 + c_1\,n_e + c_0 = 0 \tag{2.12}$$

with

$$c_2 = (1+\theta)\,K_I > 0$$
$$c_1 = K_I\left((1+2\theta)\,K_{II} - \theta\frac{P}{k_B T_e}\right) < 0$$
$$c_0 = -2\theta K_I K_{II}\frac{P}{k_B T_e} < 0$$

with c_1 being of negative value, since at atmospheric pressures the term $\frac{P}{k_B T_e}$ is much larger than the Saha factor of the second ionization. Equation (2.12) can be solved iteratively with an initial solution $n_e^{(prev)}$ that is continuously evolved to a better solution due to linearization of the equation, leading

to $n_e^{(next)}$. Care must be taken with such iterative scheme to ensure convergence of the solution, all coefficient multipling $n_e^{(next)}$ must be of the same sign. The following linear approximation

$$\left(n_e^{(next)}\right)^3 \approx \left(n_e^{(prev)}\right)^3 + 3\left(n_e^{(next)}\right)^2\left(n_e^{(next)} - n_e^{(prev)}\right)$$

$$\left(n_e^{(next)}\right)^2 \approx \left(n_e^{(prev)}\right)^2 + 2\left(n_e^{(next)}\right)\left(n_e^{(next)} - n_e^{(prev)}\right)$$

can be used to transform Equation (2.12) into a linear equation for $n_e^{(next)}$

$$0 \approx n_e^{(next)}\left[3\left(n_e^{(prev)}\right)^2 + 2c_2\, n_e^{(prev)}\right] - \left[2\left(n_e^{(prev)}\right)^3 + c_2\left(n_e^{(prev)}\right)^2 + |c_1|\, n_e^{(prev)} + |c_0|\right]$$

with the solution

$$n_e^{(next)} \approx \frac{1}{3\left(n_e^{(prev)}\right)^2 + 2n_e^{(prev)}(1+\theta)\,K_I} \times \left[2\left(n_e^{(prev)}\right)^3 + \left(n_e^{(prev)}\right)^2(1+\theta)\,K_I\right.$$

$$\left. + K_I\left(-(1+2\theta)\,K_{II} + \theta\frac{P}{k_B T_e}\right)n_e^{(prev)} + 2\theta K_I K_{II}\frac{P}{k_B T_e}\right]$$

The electron density $n_e^{(next)}$ will now be taken as initial solution $n_e^{(prev)}$ for the next iteration to achieve an even better solution $n_e^{(next)}$ with Equation (2.13). The process is executed until the difference between two consecutive calculations falls below some defined boundary value. The first electron density value can be derived with Equation (2.12), by neglecting the second ionisation ($K_{II} \to 0$):

$$n_e^2 + n_e(1+\theta)\,K_I - \theta K_I\frac{P}{k_B T_e} \approx 0$$

$$n_e^{(prev)} = -\frac{1+\theta}{2}K_I + \sqrt{\left(\frac{1+\theta}{2}K_I\right)^2 + \theta K_I\frac{P}{k_B T_e}} \qquad (2.13)$$

After finding the solution for the electron density the other particle densities can be easily calculated:

$$n_A = \frac{n_e}{\dfrac{K_I}{n_e} + 2\dfrac{K_I K_{II}}{n_e^2}} \qquad n_{A^+} = n_A\frac{K_I}{n_e} \qquad n_{A^{++}} = n_{A^+}\frac{K_{II}}{n_e} \qquad (2.14)$$

The procedure must now be corrected if the number of ionized atoms exceeds a certain number density and lots of positively charged particles are now present. The electrons are now affected not only by the positive charge of their respective core, but also by the other positive charges around effectively reducing the required ionization energy needed to free more electrons. The length scale for such an attraction force is of the order of the Debye-length λ_D:

$$\lambda_D = \sqrt{\frac{\varepsilon_0 k_B}{e^2\left(\dfrac{n_e}{T_e} + \dfrac{n_{A^+}}{T_e/\theta} + \dfrac{4n_{A^{++}}}{T_e/\theta}\right)}} \qquad (2.15)$$

This mechnism is called the Schottky correction for the ionisation energies, which take the following form:

$$E_{A,ion} = E_{A,ion}^{(0)} - \frac{e^2}{4\pi\varepsilon_0}\frac{1}{\lambda_D}$$

$$(2.16)$$

$$E_{A^+,ion} = E_{A^+,ion}^{(0)} - \frac{2e^2}{4\pi\varepsilon_0}\frac{1}{\lambda_D}$$

13

with $E_{A,ion}^{(0)}$ and $E_{A^+,ion}^{(0)}$ being the uncorrected values for the ionization energies of the respective gas atom from NIST database.[1]

2.2.2 Saha-Eggert equation extension for arbitrary gas mixtures

Now one considers a gas in thermodynamic equilibrium with an arbitrary composition defined by $k = A, B, C, \ldots$, in all possible ionization levels. The ideal gas law takes the following form:

$$\frac{P}{k_B T_e} = n_e + \frac{1}{\theta} \left[(n_A + n_{A^+} + n_{A^{++}} + \ldots) + (n_B + n_{B^+} + n_{B^{++}} + \ldots) \right.$$
$$\left. + (n_C + n_{C^+} + n_{C^{++}} + \ldots) + \ldots \right] \tag{2.17}$$

The Saha equation for all ionized species for one gas component e.g. A takes the form:

$$K_{A,1} = \frac{n_{A^+} n_e}{n_A} \quad K_{A,2} = \frac{n_{A^{++}} n_e}{n_A^+} \quad \ldots$$
$$(n_A + n_{A^+} + n_{A^{++}} + \ldots) = n_A \left(1 + \frac{K_{A,1}}{n_e} + \frac{K_{A,1} K_{A,2}}{n_e^2} + \ldots \right) \equiv n_A \, g_A \tag{2.18}$$

with $K_{A,j}$ being the Saha factor for the jth ionization. All quantities g_k, for the gases $k = A, B, C, \ldots$, are always positive. With the following partial derivative

$$\frac{\partial g_A}{\partial n_e} = -\frac{1}{n_e} \left(\frac{K_{A,1}}{n_e} + 2\frac{K_{A,1} K_{A,2}}{n_e^2} + \ldots \right) \leq 0$$

and analogously for all gas species $k = A, B, C, \ldots$, the quasi neutrality condition can be reformulated:

$$n_e = (n_{A^+} + 2\,n_{A^{++}} + \ldots) + (n_{B^+} + 2\,n_{B^{++}} + \ldots) + (n_{C^+} + 2\,n_{C^{++}} + \ldots) + \ldots$$
$$= n_A \left(\frac{K_{A,1}}{n_e} + \frac{2\,K_{A,1} K_{A,2}}{n_e^2} + \ldots \right) + n_B \left(\frac{K_{B,1}}{n_e} + \frac{2\,K_{B,1} K_{B,2}}{n_e^2} + \ldots \right)$$
$$+ n_C \left(\frac{K_{C,1}}{n_e} + \frac{2\,K_{C,1} K_{C,2}}{n_e^2} + \ldots \right) + \ldots$$
$$= -n_e \sum_{k=A,B,C,\ldots} n_k \frac{\partial g_k}{\partial n_e} \tag{2.19}$$

or simply

$$\sum_{k=A,B,C,\ldots} n_k \frac{\partial g_k}{\partial n_e} = -1 \tag{2.20}$$

---

[1]This correction accounts for the negative biasing of the work function, due to the electric field of the space charge, when a plasma is present. It effectively reduces the required ionisation energy to produce further electrons. It is valid as long as thermionic emission is the dominant process ($E \sim 10^8 \frac{V}{m}$), which is the case for the regarded setup. However since this configuration already displays high value of the electric field strength further improvements to the model can easily be made by including the effect of field emission on the electron number density, via the Fowler-Nordheim [69] or the Murphy Good equation [70]

with f_k being the mol fraction of each respective gas $k = A, B, C, \ldots$, which will further on be assumed to be constant

$$f_A = \frac{(n_A + n_{A^+} + n_{A^{++}})}{(n_A + n_{A^+} + \ldots) + (n_B + n_{B^+} + \ldots) + (n_C + n_{C^+} + \ldots) + \ldots}$$

$$= \frac{n_A\, g_A}{\sum\limits_{k=A,B,C,\ldots} n_k\, g_k}$$

$$f_{k'} = \frac{n_{k'}\, g_{k'}}{\sum\limits_{k=A,B,C,\ldots} n_k\, g_k}, \quad \text{mit } k' = A, B, C, \ldots \tag{2.21}$$

$$n_{k'} = \frac{f_{k'}}{g_{k'}} \left[\sum\limits_{k=A,B,C,\ldots} n_k\, g_k \right], \quad \text{mit } k' = A, B, C, \ldots$$

From the quasi neutrality it follows:

$$\frac{1}{\sum\limits_{k=A,B,C,\ldots} n_k\, g_k} = - \sum\limits_{k=A,B,C,\ldots} \frac{f_k}{g_k} \frac{\partial g_k}{\partial n_e} \tag{2.22}$$

Which modifies the ideal gas law Equation (2.17) to

$$\frac{P}{k_B T_e} = n_e - \frac{1}{\theta} \frac{1}{\sum\limits_{k=A,B,C,\ldots} \frac{f_k}{g_k} \frac{\partial g_k}{\partial n_e}} \tag{2.23}$$

This nonlinear equation will now again be solved iteratively according to the scheme introduced in the last section. With $n_e^{(prov)}$ being the provisional solution for n_e, which is replaced by a better solution $n_e^{(next)}$ in the next iteration. For a given T_e, θ and f_k, g_k and $\frac{\partial g_k}{\partial n_e}$ are calculated according to:

$$g_k = 1 + \frac{K_{k,1}}{n_e^{(prov)}} + \frac{K_{k,1}\, K_{k,2}}{\left(n_e^{(prov)}\right)^2} + \ldots$$

$$\frac{\partial g_k}{\partial n_e} = -\frac{K_{k,1}}{\left(n_e^{(prov)}\right)^2} - \frac{2\, K_{k,1}\, K_{k,2}}{\left(n_e^{(prov)}\right)^3} + \ldots \tag{2.24}$$

and Equation (2.23) is approximated in the following form:

$$\frac{P}{k_B T_e} \approx n_e^{(next)} - \frac{1}{\theta} \frac{1}{\sum\limits_{k=A,B,C,\ldots} \frac{f_k}{g_k} \frac{\partial g_k}{\partial n_e}\Big|_{n_e^{(prov)}}} \underbrace{\frac{n_e^{(next)}}{n_e^{(prov)}}}_{\approx 1}$$

$$n_e^{(next)} \approx \frac{\dfrac{P}{k_B T_e}}{1 - \dfrac{1}{\theta} \dfrac{1}{n_e^{(prov)}} \sum\limits_{k=A,B,C,\ldots} \dfrac{f_k}{g_k} \dfrac{\partial g_k}{\partial n_e}\Big|_{n_e^{(prov)}}} \tag{2.25}$$

This scheme always delivers a positive solution, since all terms $\frac{\partial g_k}{\partial n_e}$ stay negative. This procedure converges faster compared to the simpler algorithm in Section 2.2.1 and will reach a solution after around 5 - 10 iterations. Now again the ionization energies $E_{k,j}^{(ion,0)}$ need to be corrected for the influence of the electrostatic force of the surrounding ions (for gas species k and ionization level j).

$$E_{k,j}^{(ion)} = E_{k,j}^{(ion,0)} - \frac{j\, e^2}{4\pi\varepsilon_0} \frac{1}{\lambda_D}$$

with the new formulation

$$\lambda_D = \sqrt{\frac{\varepsilon_0 k_B}{e^2 \frac{n_e}{T_e} + \theta \left(e^2 \frac{n_{A+} + n_{B+} + n_{C+} + \cdots}{T_e} + 4e^2 \frac{n_{A++} + n_{B++} + n_{C++} + \cdots}{T_e} + \cdots \right)}}$$

for the Debye length. In all these relations above the interactions between electrons and heavy particles have been neglected. As stated initially the deviations resulting from this simplification to the real solution will remain small, since for all the formulations LTE and LCE could be assumed.

Some additional remarks:

The formulation for the gas density ρ_p of the plasma (for both cases regarded in this work; Argon and Argon-Helium mixtures) shall be given.

$$\rho_p = \sum_i m_i n_i = m_e n_e + m_{Ar} \left(n_{Ar} + n_{Ar+} + n_{Ar++} \right)$$
$$m_{He} \left(n_{He} + n_{He+} \right) \tag{2.26}$$

Although this has been stated indirectly with Equation (2.25), the formulation Equation (2.26) will be important for the calculations carried out in this work, where ρ_p is often needed.

Later on in this work the derivative of the electron density over the electron temperature (and therefore the plasma temperature) will be needed. It will be formulated in a simple forward difference, see Equation (2.27)

$$\frac{d n_e}{d T_p} = \frac{n_e(i+1) - n_e(i)}{T_p(i+1) - T_p(i)} \tag{2.27}$$

with i being the running index of the electron temperature vector $T_e = T_p = 5000$ - $30\,000\,\mathrm{K}$ with a resolution of $\Delta T_e = 100\,\mathrm{K}$. Thereby the calculation of this chapter are decoupled from the realtime calculations of the radiation and control model (later on described in this work). They will be referenced through lookup tables. This procedure accelerates the calculations and is therefore applied wherever possible.

2.3 Cathode Sheath Model

> *"A great deal of my work is just playing with equations and seeing what they give."*
>
> Paul Dirac

At atmospheric pressure a thermal arc consists of a plasma in thermal equilibrium, where free electrons and ions have equivalent kinetic energies and therefore temperature. As a consequence ionization equilibrium exists as well and the particle densites can be derived from Saha-Eggert equation [67, 71]. This assumption holds for the central region of the thermal arc, whereas at the plasma edges (towards the electrodes) there must be deviations from equilibrium in order to sustain the plasma arc. This central region of the arc will be called plasma bulk. The injected electric current I_{arc} provides the power input into the plasma for maintaining its ionization high enough for the plasma arc to remain conducting. Such a current, as a flow of freely moving charged particles, must at first leave the metallic electrodes and "jump" into free space.

The negative electrode plays the leading role here, conclusively the transition of the plasma bulk to the negative electrode or cathode, see Figure 2.2, shall be regarded in more detail, since this region is essential to the existence of the arc (far more than the positiv electrode; the anode) [57]. Due to
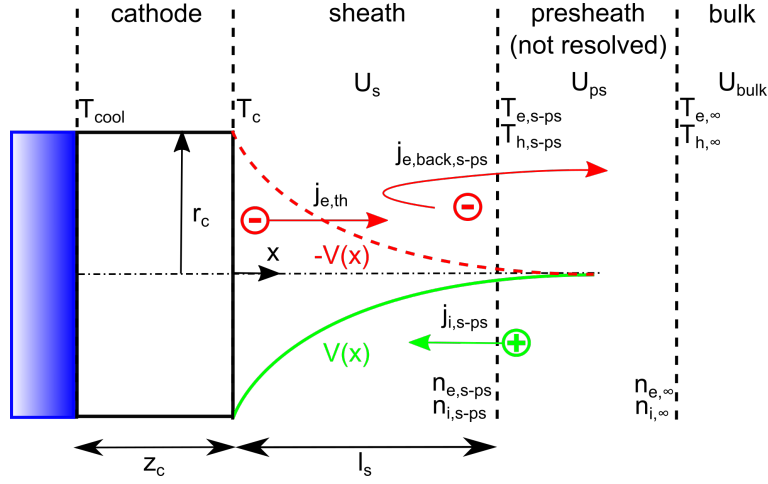
Figure 2.2: Schematic representation of a planar, 1-dimensional sheath between cathode and plasma core

concentrating the electric current into one or several spots of strongly reduced area at the cathode surface and due to the influence of ions impinging on the cathode surface, the local heating becomes strong enough for the electrons to break free from their metallic bonding to the cathode. This effect is called thermoemission (or thermionic emission) and its corresponding current density for emitted electrons is given by the Richardson equation [72]

$$j_{e,\,th} = A_R\, T_c^2 \exp\left(-\frac{e\Phi_c}{k_B T_c}\right)\,, \tag{2.28}$$

where T_c denotes the temperature of the hot cathode area (cathode spot); at atmospheric pressure only one single stable spot occurs for electric currents below 400 A [73, 74]. From now on it will be considered that the whole electric current is concentrated into one active spot of radius r_c. In the previous equation $A_R = \dfrac{4\pi e m_e k_B^2}{h^3} = 1.20 \times 10^6\ \dfrac{\mathrm{A}}{\mathrm{m^2\,K^2}}$ is the Richardson constant and $e\Phi_c$ represents the cathode's work function, i.e., the energy to be gained by each electron in order to be "liberated" from the cathode. This work function is dependent of multiple physical and geometrical parameters itself. The majority of these effects will be disregarded for this work, only the impact of the space charge

formation will be implemented and discussed in detail later on. This is applicable since this effect is the most important contribution to the modification of the work function [69]. The thermoemission can be enhanced by tunneling effect (or quantum tunneling), driven by a strong electric field close to the cathode spot (the so-called field emission, combined with the thermoemission as the thermofield emission) [72, 75], but its effect for a plasma arc at atmospheric pressure operating at a current in the order of 100 - 200 A is negligible, since the occuring electric field in the neighborhood of the cathode is at least one order of magnitude smaller to that necessary for field emission being of any relevance [75].

Once set free, the thermal emitted electrons must be accelerated by a strong voltage in order to gain a kinetic energy high enough for producing ionization when colliding with neutral atoms inside the plasma core. The responsible electric potential is created inside a space layer close to the cathode where nearly every free electron has been removed and thus electric charge neutrality no longer holds, this layer is called cathode sheath and the voltage developed across it U_s. The basic structure of the cathode sheath is schematically represented in Figure 2.2. Since the ionization energy of most gases is about 10 eV, the scale for the sheath voltage U_s developed in the sheath is also $5-10$ V. The electric potential inside the sheath must be negative in order to produce an electric field oriented towards the cathode.

From the very definition of Debye length as the largest length scale where electric charge separation (and thus a strong electric field) can still exist within a plasma, the longitudinal extension of the cathode sheath is in the order of magnitude of the Debye length. As already discussed, for a plasma at atmospheric pressure the Debye length is ~ 30 nm and therefore the sheath length is much smaller than the longitudinal extension of the plasma arc. With the sheath length in the order of $\ell_s \sim 30$ nmm at atmospheric pressure, the developed electric field inside the sheath has an order of magnitude of $\frac{U_s}{\ell_s} = E_s \sim 10^8$ V/m [2]. Such a strong electric field pushes electrons towards the plasma and attracts ions from the plasma towards the cathode, but without leaving nearly any time for collisions between both kind of particles or between ions (electrons, being much lighter than ions, have still the possibility of colliding among themselves). Hence the sheath is considered as collisionless for ions, meaning that the ion current density (as well as the electron current density because there is no interaction to the ions) is conserved within the sheath region.

The cathode sheath voltage determines the energy flow to the cathode surface and contributes thus to the evolution of the temperature T_c of the cathode spot. The dynamics of T_c is obtained in a similar way to the equation of motion for the local enthalpy distribution in a plasma arc Equation (2.5). Here z_c denotes the cathode's axial width from its surface, facing from the plasma arc to the cold surrounding at temperature T_0 (in the back of the cathode). With r_c being the radius of the cathode "hot" spot, the change in enthalpy of the cathode's volume behind the spot is mainly determined by three effects:

- the axial heat diffusion due to the temperature difference between spot and cooling water;

- the energy loss due to radiation from the cathode surface, with emissivity ε_c;

- and the power gain from the plasma arc (this term contains the three major effects on the charge distribution, see Figure 2.2

Thus leading to the mathematical formulation

$$\pi r_c^2 z_c \rho_c \, c_{p,\,c} \frac{\partial T_c}{\partial t} = \underbrace{-\pi r_c^2 \left(\lambda_{th,\,c} \frac{T_c - T_0}{z_c} + \varepsilon_c \sigma_{SB} T_c^4 \right)}_{\text{heat loss due to diffusion and radiation}} + \underbrace{\dot{W}_{p \to c}}_{\substack{\text{power gain} \\ \text{from plasma}}} \tag{2.29}$$

where ρ_c, $c_{p,\,c}$ and $\lambda_{th,\,c}$ denote the mass density, the specific heat and the thermal conductivity of the metallic cathode material respectively. All of them considered as constant parameters and $\sigma_{SB} = \frac{2\pi^5 k_B^4}{15h^3c^2} = 5.67 \times 10^{-8} \, \frac{\text{W}}{\text{m}^2 \, \text{K}^4}$, being the Stefan-Boltzmann constant. The emissivity coefficient ε_{cath} of the cathode surface will be considered close to 1, since most operating cathodes display a rough

---

[2]This electric field strength, although large, is still not strong enough for making any field-effect correction to the thermoemission from the cathode, as already mentioned.

and partially oxidized surface. The relation between the cathode sheath voltage and the power $\dot{W}_{p \to c}$, flowing axially from the plasma (actually from the inner most plasma core) into the cathode spot, will be derived in the following Section 2.3.2.

Prior to that however it must be discussed that this essential sheath can only exist due to the presence of another layer between the plasma bulk and the sheath, where ionization is the dominant process. This transition region, the so-called cathode pre-seath, see (Figure 2.2), where collisions gradually reach the frequency needed at the plasma core to maintain its ionization level. For the sheath to exist Maxwell's equations (in this case the Poisson equation) must be fullfilled in the sheath region and the electrostatic potential must be real. For this to happen the ions must reach a minimum velocity at the interface of the sheath and presheath, the Bohm-velocity (see Section 2.3.1). To ensure that the ions achieve this velocity is the essential function of the presheath. Inside the pre-sheath the electron density is not equal to the electron density $n_{e,\infty}$ within the fully developed plasma core, although it has the same order of magnitude. Nevertheless, since the voltage across the pre-sheath is mostly below 1 V and thus nearly an order of magnitude smaller than the sheath voltage U_s, this connecting region will be no longer considered and a direct transition from cathode sheath to plasma core will be assumed for the following discussion. For a detailed discussion of the equations describing the pre-sheath see [56].

2.3.1   Stability of the cathode sheath and the Bohm velocity

The physical situation within the sheath can be regarded as a purely *electrostatic* problem, neglecting the time derivative in the first order, since the electric field is very strong ($E_s \sim 10^8$ V/m)) and the dimension of the sheath is small ($\ell_s \sim 30$ nm at atmospheric conditions. This can be described by the following Maxwell equations:

$$\mathrm{rot}\vec{E} = \vec{0}, \qquad \mathrm{div}\vec{E} = \frac{\rho_{el}}{\varepsilon}$$

with ρ_{el} being the volume density of the electrical charge. The first equation can be fullfilled with the following assumption

$$\vec{E} = -\vec{\nabla}V = - \begin{pmatrix} \dfrac{\partial V}{\partial x} \\[2mm] \dfrac{\partial V}{\partial y} \\[2mm] \dfrac{\partial V}{\partial z} \end{pmatrix}$$

with V being the electrostatic potential, which has only a dependence in the z-coordinate normal to the cathode surface since the problem is regarded one dimensional.

$$\vec{E} = \begin{pmatrix} 0 \\ 0 \\ -\dfrac{dV}{dz} \end{pmatrix}$$

Applying this approach to the second equation we derive Poissons equation for the potential $V(z)$

$$\mathrm{div}\vec{E} = \frac{\rho_{el}}{\varepsilon_0} \quad \Rightarrow \quad -\frac{d^2 V(z)}{dz^2} = \frac{-e\, n_e(z) + e\, n_i(z)}{\varepsilon_0} \tag{2.30}$$

If $n_{e,s-ps}$ is the density of free electrons on the boundary between sheath and presheath, then the electron density of an arbitrary position z from the cathode surface, with the potential $V(z)$, is described through the following relation

$$n_e(z) = n_{e,s-ps} \exp\left(-\frac{(-e)V(z)}{k_B T_e} \right) \tag{2.31}$$

with a jump of the potential at position $z = z_{s-ps}$

$$V(z = z_{s-ps}) = 0$$

In eq. (2.31) T_e is the temperature of the free eelctrons, which is assumed constant since the small dimension does not allow temperature gradients to arise within the sheath. At the interface to the presheath this temperature T_e equals that from the presheath $T_e = T_{e,s-ps}$

The ions do not have a defined temperature in comparison to the electrons, since the ions are more indolent due to their larger mass, collision between ions can be neglected in a first approximation. They follow the electric filed lines on straight paths. The electrons do indeed have the possibility to collide within the sheat, since they are more agile. The collisions with other electrons are the dominant mechanism of energy transfer whereby a electron temperature can be defined.

The motion of the ions in the sheath is collision free, therefore the total energy (kinetic +potential energy) is conserved and equals the ion energy at the sheath-presheath boundary ($z = z_{s-ps}$):

$$\frac{m_i}{2}\left(v_i(z)\right)^2 + (+e)V(z) = \frac{m_i}{2}v_{i,s-ps}^2 + 0 \quad \Rightarrow \quad v_i = v_{i,s-ps}\sqrt{1 - \frac{2eV}{m_i v_{i,s-ps}^2}} \qquad (2.32)$$

with the origin of the potential at this sheath-presheath boundary. The ion velocity can subsequently be derived at an arbitrary position within the sheath. One remark at this instance, if the ion velocity would vanish at the sheat-presheath boundary $v_{i,s-ps} = 0$, Equation (2.32) would not be fullfilled. From the assumption of collision free ion motion within the sheath it follows that the ion current density remains constant over the sheath dimension.

$$n_i(z)\,v_i(z) = n_{i,s-ps}\,v_{i,s-ps} \quad \Rightarrow \quad n_i = n_{i,s-ps}\frac{1}{\sqrt{1 - \frac{2eV}{m_i v_{i,s-ps}^2}}} \qquad (2.33)$$

with the equation above the ion particle density can be derived at an arbitrary position. With $n_{i,s-ps}$ being the ion particle density ar the sheath-presheath boundary: Now one can see that since no charge separation takes place in the presheath anymore (that was the defining function of the sheath), it follows $n_{i,s-ps} = n_{e,s-ps}$. With Equation (2.31), the assumption $T_e = T_{e,s-ps}$) and Equation (2.33) substituted into Equation (2.30), the following equation for the electrostatic potential in the sheath arises

$$\frac{d^2V}{dz^2} = \frac{e\,n_{e,s-ps}}{\varepsilon_0}\exp\left(\frac{eV}{k_B T_{e,s-ps}}\right) - \frac{e\,n_{e,s-ps}}{\varepsilon_0}\frac{1}{\sqrt{1 - \frac{2eV}{m_i v_{i,s-ps}^2}}} \qquad (2.34)$$

At the position $z = z_{s-ps}$ the electric potential $V(z)$ and the electrical field $-\dfrac{dV}{dz}$ turn to zero [3], as a consequence one can multiply Equation (2.34) with $\dfrac{dV}{dz}$ and integrate from $z = z_{s-ps}$ and an arbitrary position z within the sheath to gain the following relation:

$$\int_{z_{s-ps}}^{z}\frac{d^2V}{dz^2}\frac{dV}{dz}\,dz = \frac{1}{2}\left(\frac{dV}{dz}\right)^2$$

$$\frac{1}{2}\left(\frac{dV}{dz}\right)^2 = \frac{n_{e,s-ps}k_B T_{e,s-ps}}{\varepsilon_0}\times\left[\exp\left(\frac{eV}{k_B T_{e,s-ps}}\right) - 1 + \frac{m_i v_{i,s-ps}^2}{k_B T_{e,s-ps}}\left(\sqrt{1 - \frac{2eV}{m_i v_{i,s-ps}^2}} - 1\right)\right]$$
$$(2.35)$$

---

[3]The electrical field is only approximately zero, since the electric filed within the plasma bulk E_{arc} causes a additional drift motion of the electrons. This electrical field however is 5-6 orders of magnitude smaller than the electrical field close to the cathode surface E_{cath}, since the sheath is of miniscule extent.

Now lets focus on the position close to the sheath-presheath-boundary ($z \to z_{s-ps}$): The potential is small there (because the presheath potential is zero) and therefore all terms on the right side of Equation (2.35) are expanded in a Taylor series

$$
\overbrace{\exp\left(\frac{eV}{k_B T_{e,s-ps}}\right) - 1}^{\approx \frac{eV}{k_B T_{e,s-ps}} + \frac{1}{2}\left(\frac{eV}{k_B T_{e,s-ps}}\right)^2} + \frac{m_i v_{i,s-ps}^2}{k_B T_{e,s-ps}} \overbrace{\left(\sqrt{1 - \frac{2eV}{m_i v_{i,s-ps}^2}} - 1\right)}^{\approx -\frac{eV}{m_i v_{i,s-ps}^2} - \frac{1}{2}\left(\frac{eV}{m_i v_{i,s-ps}^2}\right)^2}
$$

$$
\approx \frac{1}{2}\left(\frac{eV}{k_B T_{e,s-ps}}\right)^2 \left[1 - \frac{k_B T_{e,s-ps}}{m_i v_{i,s-ps}^2}\right]
$$

$$
\frac{1}{2}\left(\frac{dV}{dz}\right)^2 \approx \frac{1}{2} \frac{e^2 n_{e,s-ps}}{\varepsilon_0 k_B T_{e,s-ps}} \left[1 - \frac{k_B T_{e,s-ps}}{m_i v_{i,s-ps}^2}\right] \tag{2.36}
$$

The left side of the equation is squared and hence always positive, conclusively the right side must also be positive. This is only fullfilled if the ion velocity on the sheath presheath boundary applies to the condition:

$$
v_{i,s-ps} \geq \sqrt{\frac{k_B T_{e,s-ps}}{m_i}} \tag{2.37}
$$

This minimal value for the ion velocity is called Bohm velocity:

$$
v_{Bohm} = \sqrt{\frac{k_B T_{e,s-ps}}{m_i}} \tag{2.38}
$$

it defines the essentiell condition for the existence of a sheath.

2.3.2 Solution to the cathode sheath model and the cathode spot temperature equation

To find a solution to the cathode sheath equation at first the necessary boundary conditions shall be summerized

- material parameters:
  - thermal conductivity of the cathode material $\lambda_{th,c}$;
  - work function of the cathode material Φ_c;
  - First ionization energy of the gas E_{ion};
  - The surface emissivity ϵ_c (which is assumed to be of constant value)

- dimensions and physical boundary conditions:
  - gas pressure P;
  - temperature of the ambient environment T_{cool};
  - thickness of the cathode material z_c;
  - temperature of the LTE plasma bulk $T_{e,\infty} = T_{h,\infty} \equiv T_\infty$, solution to Equations (2.59) and (2.60) for the central celle ($T_\infty \equiv T[i = 1]$), combined with the electron density $n_{e,\infty}$ in the plasma bulk

- parameters derived from Figure 2.2:
  - temperature of the cathode T_c;
  - electron temperature $T_{e,s-ps}$ at the sheath-presheath interface;
  - temperature of the heavy particles $T_{h,s-ps}$ at the sheath-presheath interface;

21

- ○ radius r_c of the emitting cathode surface area;
- ○ voltage drop U_s in the sheath;
- ○ voltage drop U_{ps} in the presheath;
- ○ electron density (also ion density) $n_{e,s-ps}$ at the sheath-presheath interface

- Important assumptions: The number of unknown variables is reduced to 5 with the following relations:

$$T_{e,s-ps} = T_\infty\,, \qquad \text{und} \qquad T_{h,s-ps} = T_c \tag{2.39}$$

The first assumptions results from the fact that the electrons emitted by the cathode surface are accelerated in the sheath. They enter the presheath, start ionizing the gas atoms within and by the time they enter the plasma bulk ionization equilibrium has already been established. During this process the radius of the contact ares expands from r_c at the sheath-presheath boundary to the radius of the plasma bulk r_{bulk}, which is much larger the r_c. Energy is dissipated during that process, which results in a radial distribution of the temperature in the arc, instead of a homogenous temperature throughout its extend. The shape is discussed in Section 2.1. Only the electrons entering the central diagonal matrix element of the arc at $i = 1$, are barely effected by the energy dissipation. Therefore their temperature $T_{e,s-ps}$ is approximately equal to the temperature in the centre of the arc $T[i = 1]$: $T_{e,s-ps} \approx T[i = 1]$.

The second assumption is based on the small dimension of the cathode sheath $\ell_s \sim 20$ nm at atmospheric pressure. This leads to the ions and atoms being "affected" by the temperature of the cathode.

In the following discussion two more effects on the current density will be left out in order to reduce the problem to the essential quantities. A more refined model could easily include both effects, since their processing is straight forward but their impact is minor. The first one being the current density due to back diffusing electrons ($j_{e,back,s-ps} = 0$). With the current density being calculated with the equation:

$$j_{e,back,s-ps} = -\frac{1}{4}en_{e,back,s-ps}v_{e,back,s-ps}e^{-\frac{eU_s}{k_B T_{e,s-ps}}}$$
$$v_{e,back,s-ps} = \sqrt{\frac{8k_B T_{e,SE}}{\pi m_e}} \tag{2.40}$$

The second effect is the radiation from the hot cathode surface. This additional heating of the near cathode region will be neglected at first. Coupled with that problem also the radiation of the plasma heating the cathode or being reflected from its surface and recoil into the plasma can be neglected, because its intensity is orders of magnitude lower than the radiation from the cathode surface itself [74].

For the 5 unknown variables, now 5 equations are needed to solve the stationary one dimensional cathode sheath (without radiation impact). The number of equations needed will be further reduced, since the impact of the presheath voltage drop U_{ps} can be disregarded, as stated initially. In principle one could formulate the following simplified relation for the presheath.

$$n_{e,s-ps} = n_{e,\infty}e^{-(-e)U_{ps}/k_B T_{e,s-ps}} \tag{2.41}$$

which in turn leads to $U_{ps} = \dfrac{k_B T_{e,s-ps}}{e} \ln\left(\dfrac{n_{e,s-ps}}{n_{e,\infty}}\right)$. The value of this contribution is of the order of less than 1 V and is further neglected, since it is much smaller than either the sheath or the bulk voltage drop.

The 4 remaining unknowns will be calculated from the following relations:

1. The current density from the electrons which results from thermionic emission from the cathode material, defined by the Richardson equation [76]:

$$j_{e,th} = \frac{4\pi e m_e k_B^2}{h^3}T_c^2 \exp\left(-\frac{e\Phi_c}{k_B T_c}\right) \equiv A_R\, T_c^2 \exp\left(-\frac{e\Phi_c}{k_B T_c}\right) \tag{2.42}$$

with T_c being the cathode surface temperature and Φ_c being the work function of the cathode material. As stated above the ion current density at the presheath-sheath boundary will be derived from the criterion of the Bohm velocity, which defines the existence of the sheath itself [77]:

$$v_{Bohm} = \sqrt{\frac{k_B T_{e,s-ps}}{m_i}} \;\; \Rightarrow \; j_{i,s-ps} = e n_{e,s-ps} \sqrt{\frac{k_B T_{e,s-ps}}{m_i}} \tag{2.43}$$

The first required equation is the simplified energy conservation at the presheath-sheath boundary. The electrons emitted from the cathode gain energy within the sheath of a value, charge times voltage drop U_s. The ion current density leaving the boundary towards the cathode carries an energy per charge equal to the ionization energy of the gas, which is gained through the constant ionisation within the presheath. Regarding the predefined environmantal conditions the plasma will be operated in, it is sufficient to take only the first ionisation for this equation into account, since the amount of higher ionized particles is order of magnitude lower.

Such an energy flow is compensated by the ions leaving the plasma and flying toward the cathode, where each ion carries at least an energy per unit charge in the order of E_{ion}/e, being E_{ion} the ionization energy of the neutral atoms within the plasma gas. Hence following energy flow balance applies [74]

$$j_{e,th}\, U_s \approx j_{i,s-ps} \frac{E_{ion}}{e} \tag{2.44}$$

with E_{ion} being the first ionization energy of the gas. Thus leading to the equation for the cathode sheath voltage drop U_s.

$$U_s \approx \frac{\overbrace{e\, n_{e,\infty}(\overline{T}_p) \sqrt{\dfrac{k_B \overline{T}_p}{m_i}}}^{\substack{\text{ion current } j_{i,\,s-ps} \text{ leaving} \\ \text{plasma core at Bohm velocity}}}}{\underbrace{A_R T_c^2 \exp\left(-\dfrac{e\Phi_c}{k_B T_c}\right)}_{\substack{\text{electron current } j_{e,\,th} \text{ thermally} \\ \text{emitted at hot cathode spot}}}} \frac{E_{ion}}{e} \tag{2.45}$$

2. The second required equation is the Saha-Eggert eq. (2.13) at the presheath-sheath boundary, which has been defined in Equation (2.25) and will be to be solved iterativley.

$$n_e \approx \frac{\dfrac{P}{k_B T_e}}{1 - \dfrac{1}{\theta} \dfrac{1}{n_e^{(prov)}} \displaystyle\sum_{k=A,B,C,\ldots} \dfrac{f_k}{g_k} \left.\dfrac{\partial g_k}{\partial n_e}\right|_{n_e^{(prov)}}} \tag{2.46}$$

The electron density at the boundary $n_{e,s-ps}$ is derived from that equation.

3. The third equation is a simplified energy conservation at the cathode-sheath boundary. The ions from the presheath carries an energy of E_{ion}/e per charge towards the surface of the cathode, plus the the energy the ions gain while traveling through the sheath U_s. A part of this energy is lost at the cathode surface due to recombination with the electrons. The energy required to release one electron from the cathode surface for the purpose of recombination is equal to the work function Φ_c. Each ions then carry the energy according to the following equation towards the cathode $\dfrac{E_{ion}}{e} + U_s - \Phi_c$. The emitted thermal electrons have an energy of $e\Phi_c$ when released from the surface of the cathode, the combined energy flux follows as

$$j_{i,s-ps}\left(U_s + \frac{E_{ion}}{e} - \Phi_c\right) - j_{e,th}\Phi_c\,.$$

Regarding the cathode surface there is an energy loss (per unit time and surface) equal to $-j_{e,\,th}\Phi_c$ due to the electrons "breaking free" from the cathode, and there is an energy gain (per unit time and surface) given by $+j_{i,\,s-ps}\left(\dfrac{E_{ion}}{e} + U_s - \Phi_c\right)$ of the impinging ions which left the plasma with voltage E_{ion}/e, gained energy due to the acceleration inside the sheath and partially lost again energy by entering the metal cathode [74, 78].

In steady state this energy flux is carried away by heat conduction within the cathode material. The cooling effect of the cathode is defined by the cathode width z_c

$$\lambda_{th,c}\frac{T_c - T_{cool}}{z_c} = j_{i,s-ps}\left(U_s + \frac{E_{ion}}{e} - \Phi_c\right) - j_{e,th}\Phi_c \tag{2.47}$$

with T_{cool} being the temperature of the cooling system, for example a water cooled heat sink and $\lambda_{th,c}$ being the thermal conductivity of the cathode material. This equation will further be the base for the calculation of the cathode temperature T_c.

4. The last equation needed is the current conservation at the cathode: The current I flows through the cross section defined by the cathode spot radius r_c and equals the sum of the ions and electron fluxes.

$$\frac{I}{\pi r_c^2} = j_{e,th} + j_{i,s-ps} \tag{2.48}$$

The cathode spot radius r_c is derived with this equation.

Given these 4 equations, the total amount of energy per unit time and surface flowing into the cathode spot surface is given by

$$\dot{w}_{p\to c} = \frac{\dot{W}_{p\to c}}{\pi r_c^2} = -j_{e,\,th}\Phi_c + j_{i,\,s-ps}\left(\frac{E_{ion}}{e} + U_s - \Phi_c\right)$$
$$\overset{\text{eq. (2.45)}}{=} (j_{e,\,th} + j_{i,\,s-ps})(U_s - \Phi_c) = (j_{e,\,th} + j_{i,\,s-ps})\left(\frac{E_{ion}}{e}\frac{j_{i,\,s-ps}}{j_{e,\,th}} - \Phi_c\right) \tag{2.49}$$

This is actually a formulation for the the power gain by the cathode divided by the cathode spot area (in this case simplified by a circle of radius r_c), which corresponds to a positive contribution increasing the cathode spot temperature T_c. Combining the Equations (2.29), (2.44) and (2.47) on gets a nonlinear equation for the cathode temperature (later on this will be called the equation of motion and is a refined form of Equation (2.29)) for T_c

$$\rho_c\, c_{p,\,c}\frac{\partial T_c}{\partial t} = -\overbrace{\left(\lambda_{th,\,c}\frac{T_c - T_0}{z_c^2} + \frac{\varepsilon_c}{z_c}\sigma_{SB}T_c^4\right)}^{\substack{\text{power loss per unit volume}\\\text{due to diffusion and radiation}}}$$

$$+ \frac{1}{z_c}\overbrace{\left(A_R T_c^2\exp\left(-\frac{e\Phi_c}{k_B T_c}\right) + e\,n_{e,\,\infty}(\overline{T}_p)\sqrt{\frac{k_B\overline{T}_p}{m_i}}\right)}^{\substack{\text{power gain per unit volume}\\\text{from plasma arc}}} \times$$

$$\times\left(\frac{E_{ion}}{e}\frac{e\,n_{e,\,\infty}(\overline{T}_p)\sqrt{\dfrac{k_B\overline{T}_p}{m_i}}}{A_R T_c^2\exp\left(-\dfrac{e\Phi_c}{k_B T_c}\right)} - \Phi_c\right) \tag{2.50}$$

The work function $e\Phi_c$ is always much smaller than the ionization energy E_{ion}. The solution scheme for this equation will be presented in the next section, but first some characteristics of that equation shall be clarified.

24

- Before one calculates T_c a significant effect has to be included: The "expulsion" of the electrons from the sheath and the remain of the more indolent ions near the cathode surface generates a tremendous electric field. This field further promotes the extraction of electrons from the cathode surface, which in turn leads to a effective reduction of the work function of the cathode material. This leads to the so called Schottky correction [69]:

$$\Phi_c \rightarrow \Phi_{c,eff} = \Phi_c - \sqrt{\frac{eE_c}{4\pi\varepsilon_0}} \tag{2.51}$$

The integral over all charges in the proximity above the cathode contribute to this correction term. In this one dimensional case no spatial contributions resulting from the shaping of the surface are incooporated. The electrostatic field near the cathode surface E_c can be derived from Equation (2.35), with $\dfrac{dV}{dz}$ evaluated at $z = 0$, furthermore $V(z = 0) = -|U_s|$ and the application of the Bohm velocity for the ions $v_{i,s-ps} = v_{Bohm}$

$$E_c = \sqrt{\frac{2n_{e,s-ps}k_B T_{e,s-ps}}{\varepsilon_0}\left[\exp\left(-\frac{e\,|U_s|}{k_B T_{e,s-ps}}\right) + \sqrt{1 + \frac{2e\,|U_s|}{k_B T_{e,s-ps}}} - 2\right]} \tag{2.52}$$

This adaption of the work function takes a few iterations at constant cathode temperature to find a converged solution. Only after this convergence the cathode temperature can again be calculated according to the procedure presented later on in this work.

- With reference to the remark Section 2.1 the total voltage spent between cathode and anode is mainly given by the sum of the cathode sheath voltage U_s Equation (2.45) and the arc voltage U_{arc} Equation (2.6)

$$U_{total} \approx \frac{E_{ion}}{e} \frac{e\,n_{e,\infty}(\overline{T}_p)\sqrt{\dfrac{k_B \overline{T}_p}{m_i}}}{A_R T_c^2\,\exp\left(-\dfrac{e\Phi_c}{k_B T_c}\right)} + + \frac{\ell_{arc}}{\displaystyle\int_0^{r_0} \sigma_{el}(T_p(r))\,2\pi r\,dr} I_{arc} \tag{2.53}$$

where the contributions of the anode sheath and the cathode pre-sheath have been neglected for being one order of magnitude smaller.

2.4 Developing a numerically stable integration of the equations of motion

> *"In nature nothing remains constant. Everything is in a perpetual state of transformation, motion and change."*
>
> David Bohm

Before beginning with the calculations for a radiation model or the design of an appropriate control for driving the system "plasma arc - cathode spot temperature'' along a desired trajectory, it needs to be discussed how the two different derived dynamic equations of the previous sections are to be integrated. Due to the nonlinear character of many of the terms in the equations of motion, a numerical solution is the only way to follow the dynamics evolution, with the time coordinate being discretized in time steps of duration Δt. Without taking very good care, such discretization can quickly lead to nonsensical numerical solutions as soon as Δt is not chosen small enough. Instead of reducing Δt down to tiny values, which may even require to work with time scales where the derived dynamics are no longer valid, the time step will be kept at a scale about $\Delta t \sim 1~\mu$s, but simultaneously the different nonlinear terms will be implemented according to their sign and strength in such a way that the integration over many time steps can be performed in a stable way.[4] This requires nevertheless the development of an own integration algorithm, instead of using already commercial codes which are not well suited for such nonlinear dynamics. The general derivation of this scheme is described in Appendix A.2.1. The adaption for the equations of motion for plasma temperature and cathode spot temperature will be carried out in the following.

2.4.1 Numerical integration of the detailed system dynamics

To solve the plasma temperature dynamics (see Equation (2.5)), the plasma arc radial extension, from the arc symmetry axis $r = 0$ to the radius r_0 of the cold surrouding, is discretized in N concentric layers, each denoted by index j and having variable width $\Delta r(j)$: radial coordinate $r(j)$ marks the middle of each layer and a radial coordinate with a half integer index like $r(j + 1/2)$ denotes the division line between the j-th and the $(j+1)$-th layer (see Figure 2.3). With the assumption of a constant cell width one can deduce the following description:

$$r(j) = r(j - 1) + \frac{\Delta r(j - 1)}{2} + \frac{\Delta r(j)}{2}$$

$$r(j - 1/2) = r(j) - \frac{\Delta r(j)}{2} \qquad r(j + 1/2) = r(j) + \frac{\Delta r(j)}{2}$$

with $r(1 - 1/2) = 0$ for the inner most layer. The temperature within the j-th layer is assumed to be homogeneously distributed in the layer, $T_p(j)$, but change between layers, using a similar notation for any thermodynamic parameter of the plasma gas: for instance $\lambda_{th,p}(T_p(r(j))) \equiv \lambda_{th,p}(j)$ and $\lambda_{th,p}(T_p(r(j + 1/2))) \equiv \lambda_{th,p}(j + 1/2)$. The values of temperature and of the thermal conductivity at the division line between two concentric layers are obtained from the following condition of a continuous heat flow across the division line (see [79], § 4) in 3 steps:

---

[4]The selection of a fitting time scale can be quite challenging, the following thoughts shall clarify the regarded selection. It should be emphasized that generally one is free to choose the time scale, but the regarded model should be detailed enough to cover the targeted dynamics of the system. If the time scale is chosen to small for the driving effects of the dynamics, their impact would effectively be canceled. The simulated dynamics would then be different from the intended ones. Therefore it is not adequate to just start with the smallest possible value for Δt, but rather derive an estimate of the temporal scaling order through the given effects and material properties present in the regarded problem. For the thermal model the dominant process is diffusive heat transport, now a time scale can be defined which estimates how information is transfered, based on this process, from one part of the plasma to another. It follows that $\tau \sim \frac{\rho\,c_p\,x}{\lambda_{th}}$, with x being a characteristic length scale. This length scale depends on the configuration chosen for the model, for control applications it is thereby enough to limit the spatial resolution to gain advance on temporal evolution of the underlying mathematics. Therefore the length scale is defined by the value of radial distance between two consecutive points of the discretization, which is $\Delta r = \frac{r_0}{50} = 8e - 5[m]$. With this quantity a proper order of magnitude can be derived, for the sake of numerical stability and convergence. The precise value can then be found by taking into account the convergence rate of the solution.
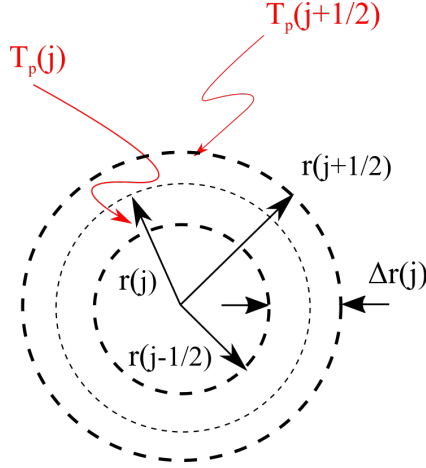
Figure 2.3: Scheme to discretize the radial plasma temperature distribution in N concentric layers of width $\Delta r(j)$ and center coordinate $r(j)$ with $j = 1, \ldots, N$; $r(j + 1/2)$ is the radial coordinate for the edge to the $(j + 1)$-th layer

1. Heat is flowing across the division line at $r(j + 1/2)$ due to the temperature gradient between $(j+1)$-th and j-th layer, $\lambda_{th,\,p}(j + 1/2)\dfrac{T_p(j + 1) - T_p(j)}{r(j + 1) - r(j)}$, and this heat flow must be also equal, on the one hand, to the heat flow within the j-th layer due to the temperature difference $(T_p(j + 1/2) - T_p(j))$, and on the other hand, to the heat flow within the $(j + 1)$-th layer due to the temperature difference $(T_p(j + 1) - T_p(j + 1/2))$

$$\lambda_{th,\,p}(j + 1/2)\frac{T_p(j + 1) - T_p(j)}{r(j + 1) - r(j)} = \lambda_{th,\,p}(j)\frac{T_p(j + 1/2) - T_p(j)}{r(j + 1/2) - r(j)} = \lambda_{th,\,p}(j + 1)\frac{T_p(j + 1) - T_p(j + 1/2)}{r(j + 1) - r(j + 1/2)}$$

2. $T_p(j + 1/2)$ denotes the temperature at the division line which follows from the last equality in the previous chain of 2 equalities: $T_p(j + 1/2) = \dfrac{\frac{\lambda_{th,\,p}(j)}{r(j+1/2)-r(j)}T_p(j) + \frac{\lambda_{th,\,p}(j+1)}{r(j+1)-r(j+1/2)}T_p(j + 1)}{\frac{\lambda_{th,\,p}(j)}{r(j+1/2)-r(j)} + \frac{\lambda_{th,\,p}(j+1)}{r(j+1)-r(j+1/2)}}$

3. And thus $\lambda_{th,\,p}(j + 1/2)$ results from the first equality

$$\frac{\lambda_{th,\,p}(j + 1/2)}{r(j + 1) - r(j)} = \frac{\dfrac{\lambda_{th,\,p}(j)}{r(j + 1/2) - r(j)}\dfrac{\lambda_{th,\,p}(j + 1)}{r(j + 1) - r(j + 1/2)}}{\dfrac{\lambda_{th,\,p}(j)}{r(j + 1/2) - r(j)} + \dfrac{\lambda_{th,\,p}(j + 1)}{r(j + 1) - r(j + 1/2)}}$$

$$\lambda_{th,\,p}(j + 1/2) = \frac{\lambda_{th,\,p}(j)\,\lambda_{th,\,p}(j + 1)}{\lambda_{th,\,p}(j)\Delta r(j + 1) + \lambda_{th,\,p}(j + 1)\Delta r(j)}\,(\Delta r(j) + \Delta r(j + 1))$$

(2.54)

The discrete formulation for $\dfrac{1}{r}\dfrac{\partial}{\partial r}\left(\lambda_{th}(T)\,r\,\dfrac{\partial T}{\partial r}\right)$ follows for the cell element $[i]$

$$\frac{1}{r[i]}\frac{1}{\Delta r}\left[r[i + 1/2]\lambda_{th}[i + 1/2]\frac{T[i + 1] - T[i]}{\Delta r} - r[i - 1/2]\lambda_{th}[i - 1/2]\frac{T[i] - T[i - 1]}{\Delta r}\right]$$

Regarding the electric field E_{arc} along the plasma arc, its relation to the arc current I_{arc} expressed in (Equation (2.4)) by means of an integral is now written in its discretized version as a sum over all concentric layers of the plasma arc

$$I_{arc} = E_{arc}\int_0^{r_0}\sigma_{el}(T_p(r))\,2\pi r\,dr \approx \sum_{j=1}^N \underbrace{\pi\left(r(j + 1/2)^2 - r(j - 1/2)^2\right)}_{= 2\pi r(j)\Delta r(j)}\sigma_{el}(T_p(j))$$

(2.55)

27

again with $r(j-1/2) = 0$ for layer index $j = 1$. Now the dynamic eq. (2.5) are integrated over each cylindrical concentric layer, and after applying the general procedure with the 2 methods explained in eq. (A.3), the following algebraic discretized equations result

$$j=1: \ 2\pi r(j)\Delta r(j)\,\rho_p(j)c_{p,\,p}(j)\frac{T_p(j,t+\Delta t) - T_p(j,t)}{\Delta t} = \frac{2\pi r(j+1/2)\,\lambda_{th,\,p}(j+1/2)\left(T_p(j+1) - T_p(j)\right)}{r(j+1) - r(j)}$$
$$-\,0 + 2\pi r(j)\Delta r(j)\,\sigma_{el}(j)\,E_{arc}^2\,,$$

$$1<j<N: \ 2\pi r(j)\Delta r(j)\,\rho_p(j)c_{p,\,p}(j)\frac{T_p(j,t+\Delta t) - T_p(j,t)}{\Delta t} = \frac{2\pi r(j+1/2)\,\lambda_{th,\,p}(j+1/2)\left(T_p(j+1) - T_p(j)\right)}{r(j+1) - r(j)}$$
$$-\,\frac{2\pi r(j-1/2)\,\lambda_{th,\,p}(j-1/2)\left(T_p(j) - T_p(j-1)\right)}{r(j) - r(j-1)}$$
$$+\,2\pi r(j)\Delta r(j)\,\sigma_{el}(j)\,E_{arc}^2\,,$$

$$j=N: \ 2\pi r(j)\Delta r(j)\,\rho_p(j)c_{p,\,p}(j)\frac{T_p(j,t+\Delta t) - T_p(j,t)}{\Delta t} = \frac{2\pi r(j+1/2)\,\lambda_{th,\,p}(T_0)\left(T_0 - T_p(j)\right)}{r_0 - r(j)}$$
$$-\,\frac{2\pi r(j-1/2)\,\lambda_{th,\,p}(j-1/2)\left(T_p(j) - T_p(j-1)\right)}{r(j) - r(j-1)}$$
$$+\,2\pi r(j)\Delta r(j)\,\sigma_{el}(j)\,E_{arc}^2$$

$$j=1: \ T_p(j+1,t+\Delta t)\overbrace{\left[-\frac{2\Delta t\,\lambda_{th,\,p}(j+1/2)}{\rho_p(j)c_{p,\,p}(j)}\left(1+\frac{\Delta r(j)}{2r(j)}\right)\frac{1}{\Delta r(j)\left(\Delta r(j)+\Delta r(j+1)\right)}\right]}^{a_{j,\,j+1}}$$
$$T_p(j,t+\Delta t)\underbrace{\left[1 - a_{j,\,j+1} + \xi\,\frac{\Delta t\,\sigma_{el}(j)}{\rho_p(j)c_{p,\,p}(j)}\left(\frac{I_{arc}}{\sum_{j=1}^N 2\pi r(j)\Delta r(j)\,\sigma_{el}(j)}\right)^2 \frac{1}{T_p^{(prov)}(j,t+\Delta t)}\right]}_{a_{j,\,j}}$$
$$= T_p(j,\overset{\Downarrow}{t}) + \underbrace{\left(1+\underline{\xi}\right)\frac{\Delta t\,\sigma_{el}(j)}{\rho_p(j)c_{p,\,p}(j)}\left(\frac{I_{arc}}{\sum_{j=1}^N 2\pi r(j)\Delta r(j)\,\sigma_{el}(j)}\right)^2}_{b_j} \qquad (2.56)$$

$$1<j<N: \ T_p(j-1,t+\Delta t)\overbrace{\left[-\frac{2\Delta t\,\lambda_{th,\,p}(j-1/2)}{\rho_p(j)c_{p,\,p}(j)}\left(1-\frac{\Delta r(j)}{2r(j)}\right)\frac{1}{\Delta r(j)\left(\Delta r(j)+\Delta r(j-1)\right)}\right]}^{a_{j,\,j-1}}$$
$$T_p(j+1,t+\Delta t)\overbrace{\left[-\frac{2\Delta t\,\lambda_{th,\,p}(j+1/2)}{\rho_p(j)c_{p,\,p}(j)}\left(1+\frac{\Delta r(j)}{2r(j)}\right)\frac{1}{\Delta r(j)\left(\Delta r(j)+\Delta r(j+1)\right)}\right]}^{a_{j,\,j+1}}$$
$$T_p(j,t+\Delta t)\underbrace{\left[1 - a_{j,\,j-1} - a_{j,\,j+1} + \xi\,\frac{\Delta t\,\sigma_{el}(j)}{\rho_p(j)c_{p,\,p}(j)}\left(\frac{I_{arc}}{\sum_{j=1}^N 2\pi r(j)\Delta r(j)\,\sigma_{el}(j)}\right)^2 \frac{1}{T_p^{(prov)}(j,t+\Delta t)}\right]}_{a_{j,\,j}}$$
$$= T_p(j,\overset{\Downarrow}{t}) + \underbrace{\left(1+\underline{\xi}\right)\frac{\Delta t\,\sigma_{el}(j)}{\rho_p(j)c_{p,\,p}(j)}\left(\frac{I_{arc}}{\sum_{j=1}^N 2\pi r(j)\Delta r(j)\,\sigma_{el}(j)}\right)^2}_{b_j} \qquad (2.57)$$

$$
j = N : \overbrace{T_p(j-1, t+\Delta t) \underbrace{\left[-\frac{2\Delta t\, \lambda_{th,\,p}(j-1/2)}{\rho_p(j)c_{p,\,p}(j)} \left(1 - \frac{\Delta r(j)}{2r(j)}\right) \frac{1}{\Delta r(j)\left(\Delta r(j) + \Delta r(j-1)\right)} \right]}_{a_{j,\,j-1}}}
$$

$$
T_p(j, t+\Delta t) \left[1 - a_{j,\,j-1} + \frac{2\Delta t\, \lambda_{th,\,p}(T_0)}{\rho_p(j)c_{p,\,p}(j)} \left(1 + \frac{\Delta r(j)}{2r(j)}\right) \frac{1}{(\Delta r(j))^2} \right.
$$

$$
\left. \underbrace{+\xi \frac{\Delta t\, \sigma_{el}(j)}{\rho_p(j)c_{p,\,p}(j)} \left(\frac{I_{arc}}{\sum_{j=1}^{N} 2\pi r(j)\Delta r(j)\, \sigma_{el}(j)}\right)^2 \frac{1}{T_p^{(prov)}(j, t+\Delta t)}}_{a_{j,\,j}} \right]
$$

$$
= T_p(j, \overset{\Downarrow}{t}) + \frac{2\Delta t\, \lambda_{th,\,p}(T_0)}{\rho_p(j)c_{p,\,p}(j)} \left(1 + \frac{\Delta r(j)}{2r(j)}\right) \frac{1}{(\Delta r(j))^2} T_0
$$

$$
\underbrace{+ \left(1 + \underline{\xi}\right) \frac{\Delta t\, \sigma_{el}(j)}{\rho_p(j)c_{p,\,p}(j)} \left(\frac{I_{arc}}{\sum_{j=1}^{N} 2\pi r(j)\Delta r(j)\, \sigma_{el}(j)}\right)^2}_{b_j} \tag{2.58}
$$

where all the thermodynamical parameters are evaluated at the corresponding position and for the provisional temperature at the next time step. Notice that for the central core ($j = 1$) there is no contribution $a_{j,\,j-1}$ since due to the cylindrical symmetry at $r = 0$ condition $\frac{\partial T_p}{\partial r} = 0$ is satisfied. Determining the radial plasma temperature distribution reduces thus to solving the following algebraic equation group

$$
\begin{pmatrix}
a_{1,1} & a_{1,2} & 0 & \dots & \dots & \dots & 0 \\
a_{2,1} & a_{2,2} & a_{2,3} & 0 & \dots & \dots & 0 \\
\vdots & \vdots & \ddots & \vdots & \vdots & \vdots & \vdots \\
\vdots & 0 & a_{j,\,j-1} & a_{j,\,j} & a_{j,\,j+1} & 0 & \dots \\
\vdots & \vdots & \vdots & \vdots & \ddots & \vdots & \vdots \\
0 & \dots & \dots & \dots & 0 & a_{N,\,N-1} & a_{N,\,N}
\end{pmatrix}
\begin{pmatrix}
\overline{T}_p(t+\Delta t) \\
T_p(2, t+\Delta t) \\
\vdots \\
T_p(j, t+\Delta t) \\
\vdots \\
T_p(N, t+\Delta t)
\end{pmatrix}
=
\begin{pmatrix}
b_1 \\
b_2 \\
\vdots \\
b_j \\
\vdots \\
b_N
\end{pmatrix}
\tag{2.59}
$$

with $\overline{T}_p \equiv T_p(j = 1)$ the plasma core temperature. Implementing the non-modelled effects, denoted by . . . in eq. (2.5), as a stochastic contribution is easily carried out by adding the double underline term into the the right hand side of eq. (2.59)

$$
\begin{pmatrix}
a_{1,1} & a_{1,2} & 0 & \dots & \dots & \dots & 0 \\
a_{2,1} & a_{2,2} & a_{2,3} & 0 & \dots & \dots & 0 \\
\vdots & \vdots & \ddots & \vdots & \vdots & \vdots & \vdots \\
\vdots & 0 & a_{j,\,j-1} & a_{j,\,j} & a_{j,\,j+1} & 0 & \dots \\
\vdots & \vdots & \vdots & \vdots & \ddots & \vdots & \vdots \\
0 & \dots & \dots & \dots & 0 & a_{N,\,N-1} & a_{N,\,N}
\end{pmatrix}
\begin{pmatrix}
\overline{T}_p(t+\Delta t) \\
T_p(2, t+\Delta t) \\
\vdots \\
T_p(j, t+\Delta t) \\
\vdots \\
T_p(N, t+\Delta t)
\end{pmatrix}
=
\begin{pmatrix}
b_1 \\
b_2 \\
\vdots \\
b_j \\
\vdots \\
b_N
\end{pmatrix}
+ \Delta t \sqrt{\tilde{\sigma}_0^2}
\underline{\underline{\begin{pmatrix}
\eta_1 \\
\eta_2 \\
\vdots \\
\eta_j \\
\vdots \\
\eta_N
\end{pmatrix}}}
\tag{2.60}
$$

where $\vec{\eta}$ is a vector of N white noise components standard normally distributed (i.e. Gaussian distributed with unit standard deviation) the strength $\tilde{\sigma}_0$ of this standard white noise has dimensions of K/s and should be chosen in such a way that $\Delta t \sqrt{\tilde{\sigma}_0^2}\, \vec{\eta}$ is yielding a contribution about 10 % as strong as vector $\vec{b}$.

For the single equation of motion for T_c eq. (2.50) a similar procedure yields

$$T_c(t + \Delta t) \left[1 + \frac{\Delta t\, \lambda_{th,\, c}}{z_c^2 \rho_c c_{p,\, c}} + \frac{\Delta t\, \varepsilon_c \sigma_{SB}}{\rho_c c_{p,\, c}\, z_c} \left(T_c^{(prov)} \right)^3 \right.$$

$$+ \frac{\Delta t}{z_c \rho_c c_{p,\, c}} \left(A_R \left(T_c^{(prov)} \right)^2 \exp\left(-\frac{e\Phi_c}{k_B T_c^{(prov)}} \right) + e n_{e,\,\infty}^{(prov)} \sqrt{\frac{k_B \overline{T}_p^{(prov)}}{m_i}} \right) \left. \frac{\Phi_c}{T_c^{(prov)}} \right]$$

$$= T_c(\overset{\Downarrow}{t}) + \frac{\Delta t\, \lambda_{th,\, c}}{z_c^2 \rho_c c_{p,\, c}} T_0 + \frac{\Delta t\, E_{ion} n_{e,\,\infty}^{(prov)} \sqrt{\frac{k_B \overline{T}_p^{(prov)}}{m_i}}}{z_c \rho_c c_{p,\, c}} \left(1 + \frac{e n_{e,\,\infty}^{(prov)} \sqrt{\frac{k_B \overline{T}_p^{(prov)}}{m_i}}}{A_R \left(T_c^{(prov)} \right)^2 \exp\left(-\frac{e\Phi_c}{k_B T_c^{(prov)}} \right)} \right) \quad (2.61)$$

In both eqs. (2.59) and (2.61) the abbreviations $T_{p/c}^{(prov)} \equiv T_{p/c}^{(prov)}(t + \Delta t)$ have been used for the provisional solution at the next time step. The improved solution just obtained is now used as the provisional value for obtaining an even better improved solution. This whole process is iterated until the change between two consecutive iterations for the same time step drops below some desired value.

Chapter 3

Radiation model and Quantum Mechanics

> *"Quantum mechanics, with its leap into statistics, has been a mere palliative for our ignorance."*
>
> Rene Thom

This chapter will formulate all essential physical effects to derive the radiated power coming from a plasma arc and puts them into a mathematical scheme. The state of the art procedures to deal with radiation intensity as stated in the introduction are either based on the emission coefficient measurement for weakly absorbed lines as in the Fowler-Milne method [44–48], or the net emission coefficient (NEC) approach [50, 51], which takes into account absorption of an emitting sphere with predefined radius. This work extends the latter approach by introducing a segregated radial temperature profile in order to obtain more insight on the local emission of radiation, to calculate the radiation intensity (emission of a spectral line corrected by the absorption of the incoming intensity) for each radial element. Additionally using Plank's law for radiative processes in quasi equilibrium, the absorption characteristics are deduced as well from the emission coefficients and the local information on the plasma temperature [80]. The integral over the radial dimension and the integral over all wavelength leads to the total radiation intensity emitted by the plasma. At last a cost function is introduced that evaluates the difference between the calculated spectrum for a specific radius r_{cool} and a measured spectrum of an OES measurement of a process with the same input parameters as the calculation. The minimization of that function yields the temperature profil associated to r_{cool} that fits the radiation profile the best. This technique poses a novel tool for experimental analysis, since no Abel inversion is needed to compare measurements and computed spectral information. The purpose of this chapter is to derive a simplified description that contains enough of the ''true'' physical behaviour of the radiation processes, but is accurate enough and fast computable to be of use for analysing spectral lines for real time measurements. The presented approach has been published by the author in [53].

The chapter covers the following steps to derive the required equations:

1. A brief introduction to the concepts of quantum mechanics shall be given. Essentially covering the formulation of the Hamiltonian operator for a quantum system and the introduction of the uncertainty principle, which leads to the linear Schrödinger equation and the state function.

2. The derivation of Fermi's Golden rule and the formulation for the state transition rate for the interaction of an electromagnetic wave with an electron within a bound state of an atom (the formulation for ions is derived likewise).

3. Deriving a description of the spectral intensity resulting from the transition of an electron between two bound states (this process is called bound-bound or discrete transition). This requires the knowledge of the line shape (or line profile) of the emitted electromagnetic wave and the underlying phyical mechnisms that lead to this shaping. With respect to the regarded plasma system the driving mechanism for this shaping (or rather broadening) of spectral lines is pressure broadening (also called the Stark effect) [81].

4. At last the simulation environment and the code structure of the Matlab model is presented.

3.1 A brief introduction to Quantum Mechanics

The intension of this section is to briefly recape the concepts behind photon particle interactions, especially electrons in a bound state of an atom (and ions likewise). The general discussion of the basic quantum mechnical mathematics will follow the explainations given in [82].

At first consider a particle of mass m whose one dimensional position is denoted by q and its velocity by $\dot{q}$ (from now on ˙ represents the time derivative). The motion is due to the action of a (conservative) force derived from a potential energy $E_{pot}(q)$ and the resulting equation of motion is thus

$$m\ddot{q} = -\frac{\partial E_{pot}}{\partial q} \tag{3.1}$$

By introducing the momentum $p = m\dot{q}$ as a coordinate independent of the position q the above equation of motion can be derived from the Hamiltonian $H(q, p)$, defined as the total energy i.e. the sum of kinetic and potential energy

$$H(q, p) = \frac{p^2}{2m} + E_{pot}(q) \tag{3.2}$$

through the Hamiltonian equations of motion

$$\dot{q} = \frac{\partial H}{\partial p} \qquad \text{and} \qquad \dot{p} = -\frac{\partial H}{\partial q} \tag{3.3}$$

The first Hamiltonian equation is nothing else but the relation between velocity and the definition of momentum, $\dot{q} = \dfrac{\partial H}{\partial p} = \dfrac{p}{m}$, and the second Hamiltonian equation corresponds to the actual equation of motion (Equation (3.1))

$$\dot{p} = m\ddot{q} = -\frac{\partial H}{\partial q} = -\frac{\partial E_{pot}}{\partial q}$$

Any function of q and p (but not explicitly of time t) $A(q, p)$ evolves in time according to

$$\frac{dA}{dt} = \frac{\partial A}{\partial q}\dot{q} + \frac{\partial A}{\partial p}\dot{p} = \frac{\partial A}{\partial q}\frac{\partial H}{\partial p} - \frac{\partial A}{\partial p}\frac{\partial H}{\partial q} \tag{3.4}$$

As next the so-called Poisson bracket for any two functions $f(q, p)$ and $g(q, p)$ will be introduced

$$\{f, g\} \equiv \frac{\partial f}{\partial q}\frac{\partial g}{\partial p} - \frac{\partial f}{\partial p}\frac{\partial g}{\partial q} \tag{3.5}$$

In particular it follows that, $\{q, q\} = 0 = \{p, p\}$ and $\{q, p\} = 1$,since q and p are independent variables. By means of the Poisson bracket the equation of motion (Equation (3.4)) reads

$$\dot{A} = \frac{\partial A}{\partial q}\frac{\partial H}{\partial p} - \frac{\partial A}{\partial p}\frac{\partial H}{\partial q} = \{A, H\} \tag{3.6}$$

The transition to the quantum formulation of the equation of motion proceeds through two steps:

1. Any measureable variable $A(q, p)$ (and the position and momentum coordinate themselves) becomes a (Hermitian) operator $\underline{A}$ (the underline symbol will denote from now on operators). Such an operator acts on so-called state functions $\psi(x, t)$ which are in general space and time dependent complex valued functions. The result of any macroscopic (=classical) measurement on the state ψ of the variable $A(q, p)$ corresponds to the following expectation value

$$\langle\psi|A|\psi\rangle = \int_{-\infty}^{\infty} \psi^*(x, t)\,\underline{A}(q, p)\,\psi(x, t)\,dx \tag{3.7}$$

   whereas the action of the position operator $\underline{q}$ on the state $\psi(x, t)$ just "reads" the space coordinate for that space: $\underline{q}\,\psi = x\,\psi$. States will be often denoted by $|\psi\rangle$ and the above expectation value will be compactly written as $\langle A \rangle$, when there is no possibility of confusion regarding on which state

the expectation value is being calculated. The states will be assumed to be properly normalized such that the following relation always hold

$$\langle \psi | \psi \rangle = \int_{-\infty}^{\infty} \psi^*(x,t)\,\psi(x,t)\,dx = 1 \tag{3.8}$$

2. The Poisson bracket $\{A,\,B\}$ of the Classical Mechanics, which describes the dynamics within framework of the Hamilton formulation, becomes the commutator between the corresponding operators $[\underline{A},\,\underline{B}] = \underline{A}\,\underline{B} - \underline{B}\,\underline{A} = -[\underline{B},\,\underline{A}]$ but multiplied by the imaginary factor $\dfrac{1}{i\hbar}$ ($\hbar$ denotes the (reduced) Planck constant)

$$\{A,\,B\} \;\longrightarrow\; [\underline{A},\,\underline{B}] \tag{3.9}$$

In particular the corresponding commutator for the position and momentum operators

$$[\underline{q},\,\underline{p}] = i\hbar \tag{3.10}$$

actually incorporates the Uncertainty Principle (Appendix A.3.4) $\Delta q\,\Delta p \geq \dfrac{\hbar}{2}$. It also is consistent with the classical equation of motion for an explicitly time independent Hamilton operator $\underline{H} = \dfrac{\underline{p}}{2m} + E_{pot}(\underline{q})$

$$\dot{\underline{q}} = \frac{1}{i\hbar}\,[\underline{q},\,\underline{H}] = \frac{1}{i\hbar}\left[\underline{q},\,\frac{\underline{p}}{2m}\right] + 0 = \frac{1}{i\hbar}\frac{2}{2m}\overbrace{[\underline{q},\,\underline{p}]}^{i\hbar}\underline{p} = \frac{\underline{p}}{m}$$

$$\dot{\underline{p}} = \frac{1}{i\hbar}\,[\underline{p},\,\underline{H}] = 0 + \frac{1}{i\hbar}\,[\underline{p},\,E_{pot}(\underline{q})] = \frac{1}{i\hbar}\underbrace{[\underline{p},\,\underline{q}]}_{-i\hbar}\frac{\partial E_{pot}}{\partial \underline{q}} = -\frac{\partial E_{pot}}{\partial \underline{q}}$$

whereas the following relation has been used

$$\begin{aligned}
[\underline{A}\,\underline{B},\,\underline{C}] &= \underline{A}\,\underline{B}\,\underline{C} - \underline{C}\,\underline{A}\,\underline{B} = \underline{A}\,\underline{B}\,\underline{C} - \underline{C}\,\underline{A}\,\underline{B} \mp \underline{B}\,\underline{A}\,\underline{C} \\
&= \underline{A}\,[\underline{B},\,\underline{C}] + [\underline{A},\,\underline{C}]\,\underline{B}
\end{aligned} \tag{3.11}$$

For any operator $\underline{A} = A(\underline{q},\underline{p})$ its time evolution is determined by the commutator with the Hamiltonian through

$$\dot{\underline{A}} = \frac{1}{i\hbar}\,[\underline{A},\,\underline{H}] \tag{3.12}$$

The time evolution of the state function $\psi(x,t)$ is determined by the Schrödinger equation

$$i\hbar\dot{\psi} = \underline{H}\,\psi \tag{3.13}$$

in order to be consistent on the one hand with $\dot{\underline{A}} = \dfrac{1}{i\hbar}\,[\underline{A},\,\underline{H}]$ and on the other hand with the first quantization step where the macroscopic result of a measurement of $\underline{A}$ on ψ is given by the expectation values $\langle A \rangle$

$$\begin{aligned}
\langle \dot{A} \rangle &= \int_{-\infty}^{\infty} \psi^*(x,t)\,\dot{\underline{A}}\,\psi(x,t)\,dx = \frac{1}{i\hbar}\int_{-\infty}^{\infty}\left(\psi^*\,\underline{A}\,\overbrace{\underline{H}\,\psi}^{i\hbar\dot{\psi}} - \overbrace{\psi^*\,\underline{H}}^{-i\hbar\dot{\psi}^*}\,\underline{A}\,\psi\right)dx \\
&= \int_{-\infty}^{\infty}\left(\psi^*\,\underline{A}\,\dot{\psi} + \dot{\psi}^*\,\underline{A}\,\psi\right)dx = \frac{d}{dt}\langle A \rangle
\end{aligned}$$

3.1.1 Fermi's Golden Rule

From now on any wave function with the whole time-space dependence will be written in capital letter, $\Psi(t, \vec{x})$, whereas lowercase, $\psi(\vec{x})$, is reserved for the case where the time dependence has been already separated ([82], § 35). Consider a bound electron within an atom, the interaction with its corresponding nucleus is described by the Hamiltonian $\underline{H}_0$ which has $\Psi_n^{(0)}(t, \vec{x}) = e^{-iE_n^{(0)}t/\hbar} \psi_n^{(0)}(\vec{x})$ as time dependent eigenfunctions, with $E_n^{(0)}$ the corresponding energy eigenvalue

$$
\begin{aligned}
i\hbar \frac{\partial}{\partial t} \Psi_n^{(0)} = \underline{H}_0 \Psi_n^{(0)} \quad &\Longrightarrow \quad e^{-iE_n^{(0)}t/\hbar} E_n^{(0)} \psi_n^{(0)} = e^{-iE_n^{(0)}t/\hbar} \underline{H}_0 \psi_n^{(0)} , \\
\underline{H}_0 \psi_n^{(0)}(\vec{x}) = E_n^{(0)} \psi_n^{(0)}(\vec{x}) \quad &\overset{\text{in short}}{\Longleftrightarrow} \quad \underline{H}_0 \ket{n} = E_n^{(0)} \ket{n}
\end{aligned}
\tag{3.14}
$$

The Hamilton operator $\underline{H}_0$ will be called the unperturbed Hamiltonian. For simplicity no energy degeneration is assumed such that the eigenfunctions of different energy eigenvalues are orthogonal to each other

$$
\langle n|m \rangle = \int \left(\psi_n^{(0)}(\vec{x}) \right)^* \psi_m^{(0)}(\vec{x}) \, d^3\vec{x} = \delta_{nm} = \begin{cases} 1 & n = m \\ 0 & n \neq m \end{cases}
\tag{3.15}
$$

This is a direct consequence of the calculation of $\langle n|\underline{H}_0| \rangle$, once calculated with the (unperturbed) Hamiltonian acting on the state to its right, once calculated with $\underline{H}_0$ acting on the state to its left:

$$
\langle n| \underbrace{\underline{H}_0 \ket{m}}_{E_m^{(0)} \ket{m}} = \underbrace{\langle n| \underline{H}_0}_{E_n^{(0)} \bra{n}} \ket{m} \quad \Rightarrow \quad \left(E_m^{(0)} - E_n^{(0)} \right) \langle n|m \rangle = 0
$$

with the only possible solution $E_n^{(0)} \neq E_m^{(0)}$ for the case $\langle n|m \rangle = 0$. Now an additional interaction is switched on, described by the so-called perturbation Hamiltonian $\underline{H}_{int}$. The task is now to determine the eigenfunctions $\Psi_n(t, \vec{x})$ of the total Hamiltonian $\underline{H} = \underline{H}_0 + \underline{H}_{int}$

$$
\underline{H} \, \Psi_n(t, \vec{x}) = i\hbar \frac{\partial}{\partial t} \Psi_n(t, \vec{x})
\tag{3.16}
$$

assuming that the energy scale of the additional interaction is much lower than that responsible for the electron to be bound to its own nucleus. The solution ansatz is to expand $\Psi_n(t, \vec{x})$ as a linear superposition of the eigenfunctions of the unperturbed Hamiltonian with time dependent weights $c_{nm}(t)$

$$
\Psi_n(t, \vec{x}) = \sum_m c_{nm}(t) \, \Psi_m^{(0)}(t, \vec{x}) = \sum_m c_{nm}(t) \, e^{-iE_m^{(0)}t/\hbar} \ket{m}
\tag{3.17}
$$

The squared $|c_{nm}|^2$ describes the probability at time t to find the m-th unperturbed energy state within the state $\Psi_n(t, \vec{x})$. From Equation (3.17) follows

$$
\left(\underline{H}_0 + \underline{H}_{int} \right) \psi_n = i\hbar \frac{\partial}{\partial t} \psi_n = i\hbar \sum_m \dot{c}_{nm} e^{-iE_m^{(0)}t/\hbar} \ket{m} + \sum_m c_{nm} e^{-iE_m^{(0)}t/\hbar} E_m^{(0)} \ket{m} ,
$$

$$
\sum_m \dot{c}_{nm} e^{-iE_m^{(0)}t/\hbar} \ket{m} = -\frac{i}{\hbar} \sum_m c_{nm} e^{-iE_m^{(0)}t/\hbar} \underline{H}_{int} \ket{m} \quad \text{(scalar product with } \bra{k})
$$

$$
\dot{c}_{nk} = -\frac{i}{\hbar} \sum_m c_{nm}(t) \, e^{i\left(E_k^{(0)} - E_m^{(0)} \right)t/\hbar} \bra{k} \underline{H}_{int} \ket{m}
\tag{3.18}
$$

The scalar product with $\bra{k}$ has extracted the probability amplitude for undergoing a transition to a final state $\ket{k}$. Since this is a first order differential equation one initial condition is required, for instance

$$
c_{nk}(t = 0) = \delta_{nk}
\tag{3.19}
$$

which corresponds to the situation where the system is initially in the unperturbed n-th energy state. The time integration of Equation (3.18) between $t = 0$ and an arbitrary t allows the calculation of the

probability amplitude for a later transition from $|n\rangle$ to $|k\rangle \neq |n\rangle$

$$\overbrace{c_{nk}(t)}^{c_{n\rightarrow k}} - \delta_{nk} = -\frac{i}{\hbar} \sum_m \int_0^t c_{nm}(t')\, e^{i\left(E_k^{(0)}-E_m^{(0)}\right)t'/\hbar} \langle k|\, \underline{H}_{int}\, |m\rangle\; dt'$$

$$\approx -\frac{i}{\hbar} \sum_m \langle k|\, \underline{H}_{int}\, |m\rangle \int_0^t c_{nm}(t')\, e^{i\left(E_k^{(0)}-E_m^{(0)}\right)t'/\hbar}\; dt'$$

(3.20)

whereas in the last step it has been assumed that the interaction Hamiltonian $\underline{H}_{int}$ displays a far slower time evolution as that in the exponential $e^{i\left(E_k^{(0)}-E_m^{(0)}\right)t'/\hbar}$, the latter arising from the interaction of the electron with its nucleus. This is again consistent with the assumption that the perturbation has an energy scale much lower than that of the interaction between bound electron and nucleus.

Since the Equation (3.20) contains the unknown $c_{nm}(t)$ on the left and on the right side of the integral equation, only approximative solutions of increasing accuracy can be obtained:

1. Solution of Equation (3.20) up to first order in $\underline{H}_{int}$ by using the initial condition as $c_{nk}(t)$ inside the integral

$$c_{nk}(t) \approx \delta_{nk} - \frac{i}{\hbar} \sum_m \langle k|\, \underline{H}_{int}\, |m\rangle \int_0^t \delta_{nm}\, e^{i\left(E_k^{(0)}-E_m^{(0)}\right)t'/\hbar}\; dt'$$

$$c_{nk}(t) \approx \delta_{nk} + \frac{\langle k|\, \underline{H}_{int}\, |n\rangle}{E_k^{(0)} - E_n^{(0)}} \left(1 - e^{i\left(E_k^{(0)}-E_n^{(0)}\right)t/\hbar}\right), \quad k \neq n$$

(3.21)

2. Solution of Equation (3.20) up to second order in $\underline{H}_{int}$ by using the solution up to first order (Equation (3.21)) inside the integral

$$c_{nk}(t) \approx \delta_{nk} - \frac{i}{\hbar} \sum_m \langle k|\, \underline{H}_{int}\, |m\rangle \int_0^t \left[\delta_{nm} + \frac{\langle m|\, \underline{H}_{int}\, |n\rangle}{E_m^{(0)} - E_n^{(0)}} \left(1 - e^{i\left(E_m^{(0)}-E_n^{(0)}\right)t/\hbar}\right)\right] \times$$

$$\times\, e^{i\left(E_k^{(0)}-E_m^{(0)}\right)t'/\hbar}\, dt'$$

$$c_{nk}(t) \approx \delta_{nk} + \frac{\langle k|\, \underline{H}_{int}\, |n\rangle}{E_k^{(0)} - E_n^{(0)}} \left(1 - e^{i\left(E_k^{(0)}-E_n^{(0)}\right)t/\hbar}\right)$$

$$+ \sum_m \frac{\langle k|\, \underline{H}_{int}\, |m\rangle \langle m|\, \underline{H}_{int}\, |n\rangle}{\left(E_k^{(0)} - E_m^{(0)}\right)\left(E_m^{(0)} - E_n^{(0)}\right)} \left(1 - e^{i\left(E_k^{(0)}-E_m^{(0)}\right)t/\hbar}\right)$$

$$- \sum_m \frac{\langle k|\, \underline{H}_{int}\, |m\rangle \langle m|\, \underline{H}_{int}\, |n\rangle}{\left(E_k^{(0)} - E_n^{(0)}\right)\left(E_m^{(0)} - E_n^{(0)}\right)} \left(1 - e^{i\left(E_k^{(0)}-E_n^{(0)}\right)t/\hbar}\right), \quad k \neq n.$$

(3.22)

3. From these solutions for the coefficients $c_{nk}(t)$ also the energy eigenvalues of the complete Hamiltonian can be obtained (again in increasing order in powers of $\underline{H}_{int}$) up to second order the following holds

$$\underline{H}\, \Psi_n = E_n\, \Psi_n$$

$$\left(\underline{H}_0 + \underline{H}_{int}\right) \left[e^{-iE_n^{(0)}t/\hbar}\, |n\rangle + \sum_{m\neq n} \frac{\langle m|\, \underline{H}_{int}\, |n\rangle}{E_m^{(0)} - E_n^{(0)}} \left(1 - e^{i\left(E_m^{(0)}-E_n^{(0)}\right)t/\hbar}\right) e^{-iE_m^{(0)}t/\hbar}\, |m\rangle\right]$$

$$= E_n \left[e^{-iE_n^{(0)}t/\hbar}\, |n\rangle + \sum_{m\neq n} \frac{\langle m|\, \underline{H}_{int}\, |n\rangle}{E_m^{(0)} - E_n^{(0)}} \left(e^{-iE_m^{(0)}t/\hbar} - e^{-iE_n^{(0)}t/\hbar}\right) |m\rangle\right]$$

and by multiplying with $e^{iE_n^{(0)}t/\hbar}\langle n|$ one obtains

$$\underbrace{\langle n|\,\underline{H}_0\,|n\rangle}_{E_n^{(0)}} + \langle n|\,\underline{H}_{int}\,|n\rangle + 0 + \sum_{m\neq n}\frac{\langle m|\,\underline{H}_{int}\,|n\rangle}{E_m^{(0)}-E_n^{(0)}}\left(e^{-i\left(E_m^{(0)}-E_n^{(0)}\right)t/\hbar}-1\right)\underbrace{\langle n|\,\underline{H}_{int}\,|m\rangle}_{\langle m|\,\underline{H}_{int}\,|n^*\rangle}$$

$$= E_n$$

or equivalently

$$E_n = E_n^{(0)} + \langle n|\,\underline{H}_{int}\,|n\rangle + \sum_{m\neq n}\frac{|\langle m|\,\underline{H}_{int}\,|n\rangle|^2}{E_n^{(0)}-E_m^{(0)}}\left(1-e^{-i\left(E_m^{(0)}-E_n^{(0)}\right)t/\hbar}\right) \tag{3.23}$$

The final step is to derive the Fermi's Golden Rule, therefore the probability per unit time t shall be considered (with t large enough) for transitions from the initial state $|n\rangle$ to a continuum of close packed final states around (and starting at) state $|k\rangle \neq |n\rangle$

$$\frac{|c_{n\to k}|^2}{t} = \sum_{\substack{k'\text{ close}\\\text{to }k}}\frac{|c_{nk'}|^2}{t} \tag{3.24}$$

In first order in $\underline{H}_{int}$ this transition rate reads

$$\frac{|c_{n\to k}|^2}{t} = \sum_{\substack{k'\text{ close}\\\text{to }k}}\frac{|\langle kk|\,\underline{H}_{int}\,|n\rangle|^2}{\left(E_{k'}^{(0)}-E_n^{(0)}\right)^2 t}\left[2-2\cos\left(\frac{\left(E_{k'}^{(0)}-E_n^{(0)}\right)t}{\hbar}\right)\right]$$

$$\approx 2\int_{-\infty}^{\infty}\frac{|\langle kk|\,\underline{H}_{int}\,|n\rangle|^2}{\left(E_{k'}^{(0)}-E_n^{(0)}\right)^2 t}\left[1-\cos\left(\frac{\left(E_{k'}^{(0)}-E_n^{(0)}\right)t}{\hbar}\right)\right]D\left(E_{k'}^{(0)}\right)dE_{k'}^{(0)} \tag{3.25}$$

$$= 4\int_{-\infty}^{\infty}\frac{|\langle kk|\,\underline{H}_{int}\,|n\rangle|^2}{\left(E_{k'}^{(0)}-E_n^{(0)}\right)^2 t}\sin^2\left(\frac{\left(E_{k'}^{(0)}-E_n^{(0)}\right)t}{2\hbar}\right)D\left(E_{k'}^{(0)}\right)dE_{k'}^{(0)}$$

with $D\left(E_{k'}^{(0)}\right)$ the density of states, i.e. $D\left(E_{k'}^{(0)}\right)dE_{k'}^{(0)}$ denotes how many states are available with energies within the infinitesimal window between $E_{k'}^{(0)}$ and $E_{k'}^{(0)}+dE_{k'}^{(0)}$.

The probability rate being considered applies in the case where the time t is much higher than the typical time scales $\dfrac{\hbar}{E_n^{(0)}}$, $\dfrac{\hbar}{E_{k'}^{(0)}}$ corresponding to the energy levels of the bound electron. Hence the

(positive) function $\dfrac{\sin^2\left(\dfrac{\left(E_{k'}^{(0)}-E_n^{(0)}\right)t}{2\hbar}\right)}{\left(E_{k'}^{(0)}-E_n^{(0)}\right)^2 t}$ is quite small such that the main contribution arises from

the energy level $E_{k'}^{(0)} = E_k^{(0)}$ which is closest to $E_n^{(0)}$; all the other levels $E_{k'}^{(0)}$ having a higher energy yield a nearly vanishing contribution

$$\frac{|c_{n\to k}|^2}{t} \approx 2\frac{|\langle k|\,\underline{H}_{int}\,|n\rangle|^2}{t}D\left(E_k^{(0)}\right)\int_{-\infty}^{\infty}\frac{1-\cos\left(\frac{\left(E_{k'}^{(0)}-E_n^{(0)}\right)t}{\hbar}\right)}{\left(E_{k'}^{(0)}-E_n^{(0)}\right)^2 t}dE_{k'}^{(0)}$$

$$\stackrel{\omega=\left(E_{k'}^{(0)}-E_n^{(0)}\right)/\hbar}{=} 2\frac{|\langle k|\,\underline{H}_{int}\,|n\rangle|^2}{\hbar t}D\left(E_k^{(0)}\right)\left[\mathrm{Re}\int_{-\infty}^{\infty}\frac{1-e^{i\omega t}}{\omega^2}d\omega\right] \tag{3.26}$$

The last integral can be performed on the complex plane along a closed path consisting of

36

- A straight path form $-\infty$ to $+\infty$ along the real axis (the actual integral to be carried out) but with a small arc around the pole at $\omega = 0$ (Figure 3.1). This arc has an infinitesimal small radius ϵ and goes from $\theta = \pi$ to $\theta = 0$ across values $\omega = \epsilon\, e^{i\theta}$.
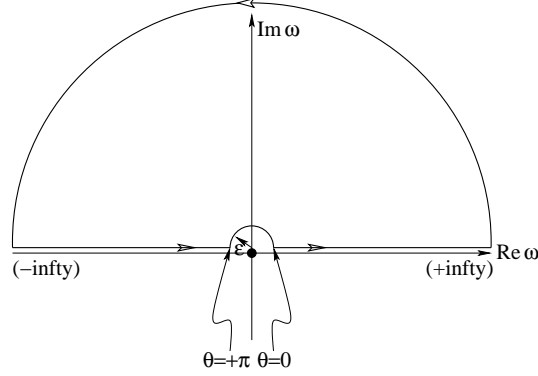

Figure 3.1: Schematic of the closed integration path for the frequency integral in Equation (3.26)

- A large curved arc from $+\infty$ back again to $-\infty$, but across values with a very high positive imaginary component. This arc produces no contribution to $e^{i\omega t} = e^{i(\mathrm{Re}\,\omega)t}\, e^{-(\mathrm{Im}\,\omega)t}$ due to the positive imaginary part. Since this part crosses a region of very large values in ω the complete contribution of this arc to the integral $\displaystyle\int_{\text{large arc}} \frac{1 - e^{i\omega t}}{\omega^2}\, d\omega$ is vanishing.

Since the integrand has no pole inside the region enclosed by the closed integration path the sum

$$\int_{\text{real axis}} \frac{1 - e^{i\omega t}}{\omega^2}\, d\omega + \int_{\text{infinitesimal arc}} \frac{1 - e^{i\omega t}}{\omega^2}\, d\omega + \int_{\text{large arc}} \frac{1 - e^{i\omega t}}{\omega^2}\, d\omega$$

identically vanishes. Hence

$$\int_{-\infty}^{\infty} \frac{1 - e^{i\omega t}}{\omega^2}\, d\omega = -\lim_{\epsilon \to 0} \int_{\theta=\pi}^{\theta=0} \frac{1 - \overbrace{\exp\left(i\,t\epsilon e^{i\theta}\right)}^{-i\,t\epsilon e^{i\theta}}}{\epsilon^2 e^{i2\theta}}\, i\epsilon e^{i\theta}\, d\theta = -t\,(0 - \pi) \tag{3.27}$$

Substituting into Equation (3.26) produces the Fermi's Golden Rule

$$\frac{\left|c_{n\to k}\right|^2}{t} \approx \frac{2\pi}{\hbar} \left|\langle k|\, \underline{H}_{int}\, |n\rangle\right|^2\, D\left(E_k^{(0)}\right) \tag{3.28}$$

Or equivalently

$$\frac{\left|c_{i\to f}\right|^2}{t} = \frac{2\pi}{\hbar} \left|\langle f|\, \underline{H}_{int}\, |i\rangle\right|^2\, D\left(E_f^{(0)}\right) \tag{3.29}$$

with i for the initial state and f for the final state, both eigenvectors of the unpertuberd Hamiltonian.

3.1.2 State transition rate for the interaction between a bound electron and the electromagnetic radiation

Now the general formulation of Fermi's Golden Rule (Equation (3.29)) shall be modified to derive the probability per unit time for the case of interest in this work. This case is the transition of a bound electron starting in a high energy state (initial state) and ending with the bound electron in a lower state (final state) and one photon emitted therefore. Similarly to the previous section, first of all the classical Hamiltonian for such system has to be derived in order to quantize it in a second step. Initially one electron (of charge $-e$ and mass m_e) is bound to its respective atom through the potential energy $E_{pot}(\vec{q})$ which is a function of the electron position $\vec{q}$ and therefore the Hamiltonian for the bound electron is $\frac{1}{2m_e}(\vec{p})^2 + E_{pot}(\vec{q})$. The description for the classical Hamiltonian for a bound electron between two states is formulated in Appendix A.3.1, based on the quantum mechanical treatment of the harmonic oscillator. Additionally the free electromagnetic field is described by the Hamiltonian $\iiint \left(\frac{\varepsilon_0}{2} \vec{E}^2 + \frac{1}{2\mu_0} \vec{B}^2 \right) d^3\vec{x}$, discussed in Appendix A.3.2. Hence the Hamiltonian H_0 without interaction between the bound electron and the free photons is given by the superposition of these two isolated subsystems

$$H_0 = \frac{1}{2m_e}(\vec{p})^2 + E_{pot}(\vec{q}) + \iiint \left(\frac{\varepsilon_0}{2} \vec{E}^2(\vec{x},t) + \frac{1}{2\mu_0} \vec{B}^2(\vec{x},t) \right) d^3\vec{x}$$

It is worth noting that the particle's position $\vec{q}$, later to become an operator after quantizing the system, is different from the local space coordinate $\vec{x}$ (which is never an operator), but only the location where the vector potential, the electric and the magnetic fields (these three are also operators) are evaluated. Now the interaction between these two isolated systems (bound electron and free electromagnetic field) has to be incorporated, this is achieved by means of the so-called "minimal coupling" ansatz ([82], §57). The particle momentum is substituted by the momentum minus the vector potential $\vec{A}$ of the electromagnetic field (multiplied by the particle's charge) and the electrostatic potential energy arising from the scalar potential ϕ is added to the potential energy

$$\vec{p} \longrightarrow \vec{p} - (-e)\vec{A}(\vec{q},t) \qquad \text{and} \qquad E_{pot} \longrightarrow E_{pot} + (-e)\phi \tag{3.30}$$

with the vector potential in general being a function of time and the position where the particle is located. The resulting full Hamiltonian is thus equal to

$$H_0 = \frac{1}{2m_e}\vec{p}^2 + E_{pot}(\vec{q}) + \iiint \left(\frac{\varepsilon_0}{2} \vec{E}^2(\vec{x},t) + \frac{1}{2\mu_0} \vec{B}^2(\vec{x},t) \right) d^3\vec{x},$$

$$\longrightarrow H = \frac{1}{2m_e} \left(\vec{p} - (-e)\vec{A}(\vec{q},t) \right)^2 + E_{pot}(\vec{q}) + (-e)\phi(\vec{q},t) \tag{3.31}$$

$$+ \iiint \left(\frac{\varepsilon_0}{2} \vec{E}^2(\vec{x},t) + \frac{1}{2\mu_0} \vec{B}^2(\vec{x},t) \right) d^3\vec{x}$$

Such a Hamiltonian reproduces the expected equation of motion for the electron; the proof will be carried out without any previous choice of gauge for the potentials $\vec{A}$ and ϕ. For the bound electron the Hamiltonian equations for the time evolution of its position component q_k ($k = 1, 2, 3$) and its corresponding momentum component p_k are

$$\dot{q}_k = \frac{\partial H}{\partial p_k} = \frac{1}{m_e} \left(p_k + eA_k \right)$$

$$\dot{p}_k = -\frac{\partial H}{\partial q_k} = -\frac{1}{m_e} \sum_j \left(p_j + eA_j \right) e \frac{\partial A_j}{\partial q_k} - \frac{\partial E_{pot}}{\partial q_k} + e \frac{\partial \phi}{\partial q_k} \tag{3.32}$$

38

and therefore the following equation of motion results for the bound electron

$$
\begin{aligned}
m_e \frac{d}{dt} \dot{q}_k &= \frac{d}{dt} \left(p_k + e A_k(\vec{q}, t) \right) = \dot{p}_k + e \sum_j \frac{\partial A_k}{\partial q_j} \dot{q}_j + e \frac{\partial A_k}{\partial t} \\
&= -e \sum_j \underbrace{\frac{p_j + e A_j}{m_e}}_{=\dot{q}_j} \frac{\partial A_j}{\partial q_k} - \frac{\partial E_{pot}}{\partial q_k} + e \frac{\partial \phi}{\partial q_k} + e \sum_j \frac{\partial A_k}{\partial q_j} \dot{q}_j + e \frac{\partial A_k}{\partial t} \\
&= -\frac{\partial E_{pot}}{\partial q_k} - e \left[\underbrace{\left(-\frac{\partial \phi}{\partial q_k} - \frac{\partial A_k}{\partial t} \right)}_{= E_k} + \underbrace{\sum_j \left(\dot{q}_j \frac{\partial A_j}{\partial q_k} - \dot{q}_j \frac{\partial A_k}{\partial q_j} \right)}_{= \left(\dot{\vec{q}} \times \operatorname{curl} \vec{A} \right)_k = \left(\dot{\vec{q}} \times \vec{B} \right)_k} \right]
\end{aligned}
\tag{3.33}
$$

beside the force $-\dfrac{\partial E_{pot}}{\partial \vec{q}}$ responsible for the electron staying confined within the atom, another contribution appears which is nothing else than the electromagnetic Lorentz force $-e \left[\vec{E} + \dot{\vec{q}} \times \vec{B} \right]$ created by an electric and magnetic field on an electron. This proves that the approach (Equation (3.30)) correctly incorporates the electromagnetic interaction to the dynamic of a bound electron. Note that for a vanishing electric charge $e = 0$ the interaction also vanishes.

The quantization can now be performed in order to identify the interaction Hamilton operator required for the Fermi's Golden Rule. The derivation will be carried in the gauge choice $\phi = 0$. First of all the electron's position and momentum are operators with the following (3-dimensional) commutation relations

$$
\left[\underline{q}_j, \underline{p}_k \right] = i\hbar \delta_{jk}, \qquad \left[\underline{q}_j, \underline{q}_k \right] = 0 = \left[\underline{p}_j, \underline{p}_k \right]
\tag{3.34}
$$

A possible implementation of the first commutator is a multiplicative (3-dimensional) $\underline{\vec{q}}$ operator, which only "reads" the electron's 3-dimensional position when applied to a state, and a differential momentum operator given by $\underline{\vec{p}} = -i\hbar \dfrac{\partial}{\partial \vec{q}}$. Subsequently the vector potential of the electromagnetic field also becomes an operator according to (Equation (A.18))

$$
\underline{\vec{A}}(\vec{x}) = \frac{\underline{A}_\omega \, e^{ikz} + \underline{A}_\omega^+ \, e^{-ikz}}{\sqrt{2}} \begin{pmatrix} 1 \\ 0 \\ 0 \end{pmatrix}
\tag{3.35}
$$

with the following commutation relations (Equation (A.24))

$$
\left[\underline{A}_\omega, \underline{A}_\omega^+ \right] = \frac{\hbar}{L^3 \varepsilon_0 \omega} \qquad \left[\underline{A}_\omega, \underline{A}_\omega \right] = 0 = \left[\underline{A}_\omega^+, \underline{A}_\omega^+ \right]
\tag{3.36}
$$

and therefore

$$
\left[\underline{A}_j(\vec{q}), \underline{p}_k \right] = \hbar k \, \frac{\underline{A}_\omega \, e^{ikq_z} - \underline{A}_\omega^+ \, e^{-ikq_z}}{\sqrt{2}} \, \delta_{j1} \delta_{k3}
\tag{3.37}
$$

since the only dependence on the electron's position arises in the first component of the vector potential and this is only for the third component of $\vec{q}$. The resulting Hamilton operator can be directly read from (Equation (3.31)) together with (Equation (3.34))

$$
\underline{H} = \overbrace{\frac{1}{2m_e} (\underline{\vec{p}})^2 + E_{pot}(\underline{\vec{q}}) + L^3 \varepsilon_0 \omega^2 \left(\underline{A}_\omega^+ \underline{A}_\omega + \frac{1}{2} \right)}^{\underline{H}_0} + \frac{e}{2m_e} \underbrace{\left(\underline{\vec{p}} \cdot \underline{\vec{A}} + \underline{\vec{A}} \cdot \underline{\vec{p}} \right)}_{\overset{(3.37)}{=} \underline{\vec{A}} \cdot \underline{\vec{p}} + 0} + \frac{e^2}{2e} \underline{\vec{A}} \cdot \underline{\vec{A}}
\tag{3.38}
$$

The interaction Hamilton operator for the Fermi's Golden Rule can be directly read out, since within the framework of the Golden Rule that interaction $\underline{H}_{int}$ has to be considered as a slight perturbation

(when compared to the energy scales involved in $\underline{H}_0$) and since for $e = 0$ the interaction disappears, the Golden Rule applies only for low order terms of the charge e to be consistent. Thus the term proportional to e^2 (or higher powers in e) is to be neglected when compared to terms proportional to e

$$\underline{H}_{int} = e\vec{\underline{A}} \cdot \frac{\vec{\underline{p}}}{m_e} + O(e^2) \stackrel{(3.32)}{=} e\vec{\underline{A}} \cdot \dot{\vec{q}} + O(e^2) \stackrel{(3.12)}{=} \frac{e}{i\hbar} \vec{\underline{A}} \cdot [\vec{\underline{q}}, \underline{H}] + O(e^2)$$

$$= \frac{e}{i\hbar} \vec{\underline{A}} \cdot [\vec{\underline{q}}, \underline{H}_0] + O(e^2) \tag{3.39}$$

after implementing the equation of motion for $\dot{\underline{q}}_k$ and neglecting those new terms which arise and are proportional to e^2.

In Fermi's Golden Rule (Equation (3.29)) $\frac{|c_{i \to f}|^2}{t} = \frac{2\pi}{\hbar} |\langle f| \underline{H}_{int} |i\rangle|^2 \, D\left(E_f^{(0)}\right)$ the initial and final states $|i\rangle$ and $|f\rangle$ are eigenstates of the unperturbed Hamiltonian $\underline{H}_0$ corresponding in this case to the sum of the uncoupled subsystems "bound electron" and "free electromagnetic field":

$$\underline{H}_0 = \frac{1}{2m_e} \vec{\underline{p}}^2 + E_{pot}(\vec{\underline{q}}) + L^3 \varepsilon_0 \omega^2 \left(\underline{A}_\omega^+ \underline{A}_\omega + \frac{1}{2} \right) \tag{3.40}$$

Hence the eigenstates are just the product of the eigenstates for the subsystem "bound electron" (denoted by $^{(e)}$) and of the eigenstates for the subsystem "free electromagnetic field" (denoted by $^{(\gamma)}$) without any kind of mixing between both subsystems. In the case under consideration where an electron at an excited level $i^{(e)}$ within an atom undergoes a transition to a lower energy level $f^{(e)}$ by means of the electromagnetic interaction (by emitting a photon) the initial state is given by $\left|0^{(\gamma)}\right\rangle \left|i^{(e)}\right\rangle$ (without any photon) and the final state by $\left|1^{(\gamma)}\right\rangle \left|f^{(e)}\right\rangle$. By energy conservation, if $\left(E_i^{(0)} - E_f^{(0)}\right)$ is the energy difference between the levels of the bound electron, the frequency ω_{if} of the emitted electromagnetic energy (=photon) is given by $\omega_{if} = \dfrac{\left(E_i^{(0)} - E_f^{(0)}\right)}{\hbar}$. Thus by neglecting higher orders of terms of e and using the already derived results (Equation (A.28)) one obtains

$$\langle f| \underline{H}_{int} |i\rangle = \frac{e}{i\hbar} \left\langle 1^{(\gamma)} \left| \vec{\underline{A}} \right| 0^{(\gamma)} \right\rangle \cdot \left\langle f^{(e)} \left| [\vec{\underline{q}}, \underline{H}_0] \right| i^{(e)} \right\rangle + O(e^2)$$

$$= \frac{e}{i\hbar} \sin\theta \overbrace{\left\langle 1^{(\gamma)} \left| \underline{A}_x \right| 0^{(\gamma)} \right\rangle}^{\frac{e^{ikx}}{\sqrt{2}} \cdot 0 + \frac{e^{-ikx}}{\sqrt{2}} \sqrt{\frac{\hbar}{L^3 \varepsilon_0 \omega_{if}}}} \left[\left\langle f^{(e)} \left| \vec{\underline{q}} \right| \underbrace{\underline{H}_0 \left| i^{(e)} \right\rangle}_{E_i^{(0)} \left| i^{(e)} \right\rangle} - \underbrace{\left\langle f^{(e)} \left| \underline{H}_0 \right.}_{E_f^{(0)} \left\langle f^{(e)} \right|} \left| \vec{\underline{q}} \right| i^{(e)} \right\rangle \right] + O(e^2)$$

$$= \frac{e}{i\hbar} \sin\theta \frac{e^{-ikx}}{\sqrt{2}} \sqrt{\frac{\hbar}{L^3 \varepsilon_0 \omega_{if}}} \left(E_i^{(0)} - E_f^{(0)} \right) \left\langle f^{(e)} \left| \vec{\underline{q}} \right| i^{(e)} \right\rangle + O(e^2)$$

$$|\langle f| \underline{H}_{int} |i\rangle| = e \sin\theta \sqrt{\frac{\hbar \omega_{if}}{2 L^3 \varepsilon_0}} \left| \left\langle f^{(e)} \left| \vec{\underline{q}} \right| i^{(e)} \right\rangle \right| + O(e^2) \tag{3.41}$$

with θ the angle between the electron's position vector $\vec{q}$ and the propagation direction of the emitted photon, the latter perpendicular to the direction of the vector potential $\vec{A}$.

The final result for the transition rate between the initial and final states according to the Fermi's Golden Rule requires the calculation of the density of states for the final energy $D\left(E_f^{(0)}\right)$, being $D\left(E_f^{(0)}\right) dE_f^{(0)}$ the number of different possible photons emitted with frequency ω_{if} within the interval of final electron energy between $E_f^{(0)} = E_i^{(0} + \hbar\omega_{if}$ and $E_f^{(0)} + dE_f^{(0)}$. This is achieved as follows, classically for each particle (photon as well as electron) moving in 3 dimensions the exact values of the position $\vec{x}$ and momentum $\vec{p}$ coordinates defines completely its state within the phase space; in other words, a 0-dimensional point in phase space characterizes the state of a particle. Quantum mechanically, nevertheless, the uncertainty relation between position and momentum makes that different states are

described by small volume of the size h^3 (instead of extremely fine points without size) such that phase points within this small volume cannot correspond to different states, in other words within the phase volume $d^3\vec{x}\, d^3\vec{p}$ there exist actually only $\dfrac{d^3\vec{x}\, d^3\vec{p}}{h^3}$ different states. Hence for the density of states of the emitted photons inside the whole system volume L^3 one obtains the following expression

$$D\left(E_f^{(0)}\right)\, dE_f^{(0)} = \frac{L^3\, p^2\, dp\, d\Omega}{h^3} \times g_f = g_f\, \frac{L^3}{8\pi^3\hbar^3} p^2 \frac{dp}{dE_f^{(0)}}\, d\Omega\, dE_f^{(0)}$$

with $d\Omega = 2\pi \sin\theta\, d\theta$ the infinitesimal solid angle for the direction of the emitted photons and g_f the number of polarizations of those photons. For a photon the relation between momentum p and energy E_γ is given by $p = \dfrac{E_\gamma}{c} = \dfrac{\hbar\omega_{if}}{c}$ and thus $\dfrac{dp}{dE_f^{(0)}} = \dfrac{1}{c}$ holds (because of $E_f^{(0)} = E_i^{(0} + \hbar\omega_{if}$)

$$D\left(E_f^{(0)}\right) = g_f\, \frac{L^3}{4\pi^2\hbar}\, \frac{\omega_{if}^2}{c^3}\, \sin\theta\, d\theta \tag{3.42}$$

By collecting the last result together with (Equation (3.41)) the probability per unit time for the electron's transition between an initial excited state and a lower energy level with the emission of a photon is equal to (again neglecting the higher order terms in e) [1]

$$\begin{aligned}
\frac{|c_{i\to f}|^2}{t} &= \frac{2\pi}{\hbar}\, |\langle f|\, \underline{H}_{int}\, |i\rangle|^2\, D\left(E_f^{(0)}\right)\\
&= \frac{2\pi}{\hbar} e^2 \frac{\hbar\omega_{if}}{2L^3\varepsilon_0} \left|\left\langle f^{(e)}\right|\, |\vec{\underline{q}}|\, \left|i^{(e)}\right\rangle\right|^2 g_f\, \frac{L^3}{4\pi^2\hbar}\, \frac{\omega_{if}^2}{c^3} \int_0^\pi \sin^3\theta\, d\theta \\
&= g_f \frac{\omega_{if}^3}{3\pi\varepsilon_0\hbar c^3} \left|\left\langle f^{(e)}\right|\, (e\, |\vec{\underline{q}}|)\, \left|i^{(e)}\right\rangle\right|^2
\end{aligned} \tag{3.43}$$

Since $e\vec{q}$ represents the dipole moment $\vec{d}_{dip}$ the just derived probability per unit time is also called the dipole induced transition rate.

This equation can again be reformulated using the relation

$$f_{if} = \frac{2m_e\,\omega_{if}}{3\hbar} \left|\left\langle f^{(e)}\right|\, (e\, |\vec{\underline{q}}|)\, \left|i^{(e)}\right\rangle\right|^2, \tag{3.44}$$

with the new quantity f_{if} being the oscillator strength of the transition $i \to f$. This leads to

$$\frac{|c_{i\to f}|^2}{t} = g_f\, \frac{\omega_{if}^2}{2\, m_e\, \pi\varepsilon_0\, c^3}\, f_{if}, \tag{3.45}$$

since all quantities here are natural constants for the regarded transition (except for the oscillator strength, but its data is also available for the considered gas species) this state transistion rate can be easily calculated using the data from [68].

---

[1] Using the result $\displaystyle\int_{\theta=0}^{\theta=\pi} \sin^3\theta\, d\theta = \int_0^\pi \sin\theta\, d\theta - \int_0^\pi \cos^2\theta\, d\theta = \left[-\cos\theta\right]_0^\pi + \left[\frac{\cos\theta}{3}\right]_0^\pi = \frac{4}{3}.$

3.2 Spectral line intensity of plasma radiation

In the previous section it has been shown how often an excited bound electron is connected through the dipole operator to a lower energy level of the same electron. Thus leading to the state transition rate for an electron between two levels within an atom. Based on this formulation a basic description for the spectral intensity emitted by such a process can be found, in general following the explanations given in [29]. At some point instead of following this more exact but overloaded notation in ([29], §4 and [81], §4) the discussion will follow the description in ([83], §5).

The energy difference between both levels is also the energy of the photon emitted whose frequency is thus $\omega_{if} = \dfrac{\left(E_i^{(0)} - E_f^{(0)}\right)}{\hbar}$ and the corresponding emitted power is obtained by multiplying the transition rate (Equation (3.43)) with the photon's energy

$$\dot{W}_{if} = \frac{|c_{i \to f,\,\text{atom } a}|^2}{t} \hbar \omega_{if} = g_f \frac{\omega_{if}^4}{3\pi\varepsilon_0 c^3} \left| \left\langle f^{(e)} \right| \left(e \left| \underline{\vec{q}}^{(a)} \right| \right) \left| i^{(e)} \right\rangle \right|^2 \tag{3.46}$$

The spectral distribution of this power (i.e. how much power is emitted within an infinitesimal frequency window ω) is given by

$$\frac{d\dot{W}}{d\omega} d\omega = g_f \frac{\omega_{if}^4}{3\pi\varepsilon_0 c^3} \left| \left\langle f^{(e)} \right| \left(e \left| \underline{\vec{q}}^{(a)} \right| \right) \left| i^{(e)} \right\rangle \right|^2 \delta(\omega - \omega_{if})\, d\omega \,, \tag{3.47}$$

such that $\displaystyle\int_{-\infty}^{\infty} \frac{d\dot{W}}{d\omega} d\omega = \dot{W}_{if}$ holds. The spectral distribution is therefore extremely sharp located at $\omega = \omega_{if}$ (which is therefore denoted spectral line). If the emitting bound electrons are nevertheless placed inside a gas the many collisions of the corresponding atoms between themselves or with free electrons if the gas is partially ionized (= plasma) let the sharp spectral lines of the isolated atom become broadened. The spectral distribution is no longer a sharp Dirac delta but a smoother profile $\mathcal{L}(\omega)$

$$\frac{d\dot{W}}{d\omega} d\omega = g_f \frac{\omega_{if}^4}{3\pi\varepsilon_0 c^3} \left| \left\langle f^{(e)} \right| \left(e \left| \underline{\vec{q}} \right| \right) \left| i^{(e)} \right\rangle_{1\,\text{atom}} \right|^2 \mathcal{L}(\omega)\, d\omega \tag{3.48}$$

with the normalization condition

$$\int_{-\infty}^{\infty} \mathcal{L}(\omega)\, d\omega = 1 \tag{3.49}$$

3.2.1 Spectral broadening and the line profile

To derive an equation for the still missing line profile $\mathcal{L}(\omega)$ the following concept shall be considered. If many atoms (each one with its own bound and emitting electron) with their respective electron's position operator is acting at different times, which results in the introduction of the full time dependence in the initial and final state of the bound electrons

$$\left\langle f^{(e)} \right| \left(e \left| \underline{\vec{q}} \right| \right) \left| i^{(e)} \right\rangle_{\text{one atom}} \longrightarrow \left\langle \Psi_f^{(e)} \right| \left(e \sum_{\text{atoms } a} \left| \underline{\vec{q}}^{(a)} \right| \right) \left| \Psi_i^{(e)} \right\rangle_{\text{many atoms}} \tag{3.50}$$

The profile $\mathcal{L}(\omega)$ is defined subsequently as

$$\mathcal{L}(\omega) \overset{\text{def}}{=} \lim_{T \to \infty} \frac{\left| \displaystyle\int_{-T/2}^{T/2} e^{i\omega t} \left\langle \Psi_f^{(e)} \right| \left(e \sum_{\text{atoms } a} \left| \underline{\vec{q}}^{(a)} \right| \right) \left| \Psi_i^{(e)} \right\rangle_{\text{many atoms}} dt \right|^2}{2\pi T \left| \left\langle f^{(e)} \right| \left(e \left| \underline{\vec{q}} \right| \right) \left| i^{(e)} \right\rangle_{\text{one atom}} \right|^2} \tag{3.51}$$

This definition transforms into a Dirac delta in the case of a single atom. In such a case the only time dependence in $\left\langle \Psi_f^{(e)} \right| \left(e \displaystyle\sum_{a=1} \left| \underline{\vec{q}}^{(a)} \right| \right) \left| \Psi_i^{(e)} \right\rangle_{\text{many atoms}=1\,\text{atom}}$ exclusively arises from the initial and final

states of the single bound electron

$$\Psi_{i/f}^{(e)}(t) = e^{-iE_{i/f}^{(0)}t/\hbar}\, |i/f\rangle\,,$$

$$\left\langle \Psi_f^{(e)}\middle|\left(e\sum_{a=1}|\vec{q}|\right)\middle|\Psi_i^{(e)}\right\rangle_{1\ \text{atom}} = e^{-i\omega_{if}t}\,\overbrace{\left\langle f^{(e)}\middle|\left(e\,|\vec{q}|\right)\middle|i^{(e)}\right\rangle}^{\text{time independent}}{}_{1\ \text{atom}}$$

$$\mathcal{L}(\omega) = \frac{1}{2\pi}\underbrace{\int_{-\infty}^{\infty} e^{i\omega t}\,e^{-i\omega_{if}t}\,dt}_{\delta(\omega-\omega_{if})}\lim_{T\to\infty}\frac{\displaystyle\int_{-T/2}^{T/2} e^{-i\omega t'}\,e^{+i\omega_{if}t'}\,dt'}{T}$$

$$= \delta(\omega-\omega_{if})\underbrace{\lim_{T\to\infty}\frac{\displaystyle\int_{-T/2}^{T/2} e^{-i\omega t'}\,e^{+i\omega_{if}t'}\,dt'\Big|_{\omega=\omega_{if}}}{T}}_{=\,1}$$

In the general case of many atoms the time dependence is more complicated and will be collected into the function $\varphi(t)$

$$\left\langle \Psi_f^{(e)}\middle|\left(e\sum_{\text{atoms }a}\left|\underline{q}^{(a)}\right|\right)\middle|\Psi_i^{(e)}\right\rangle_{\text{many atoms}} \overset{\text{def}}{=} \varphi(t)\left\langle f^{(e)}\middle|\left(e\,|\underline{q}|\right)\middle|i^{(e)}\right\rangle_{1\ \text{atom}} \tag{3.52}$$

such that the profile $\mathcal{L}(\omega)$ can be rewritten as the Fourier transform of the correlation function of $\varphi(t)$ with itself shifted in time

$$\mathcal{L}(\omega) = \frac{1}{2\pi}\lim_{T\to\infty}\frac{1}{T}\int_{-T/2}^{T/2} e^{-i\omega t'}\,\varphi^*(t')\,dt'\int_{-\infty}^{\infty} e^{i\omega t}\,\varphi(t)\,dt$$

$$\overset{\substack{\tau=t-t'\\ dt\,\overset{.}{=}\,d\tau}}{} \frac{1}{2\pi}\int_{-\infty}^{\infty} e^{i\omega\tau}\underbrace{\left[\lim_{T\to\infty}\frac{1}{T}\int_{-T/2}^{T/2}\varphi^*(t')\,\varphi(t+\tau)\,dt'\right]}_{\text{correlation function }\mathcal{C}(\tau)}d\tau \tag{3.53}$$

Due to the normalization condition (Equation (3.49)) the value of the correlation function at $\tau=0$ is already fixed

$$1 = \int_{-\infty}^{\infty}\mathcal{L}(\omega)\,d\omega = \int_{-\infty}^{\infty}\underbrace{\frac{1}{2\pi}\int_{-\infty}^{\infty} e^{i\omega\tau}\,d\omega}_{\delta(\tau)}\,\mathcal{C}(\tau)\,d\tau = \mathcal{C}(\tau=0) \tag{3.54}$$

Since $\mathcal{L}(\omega)$ is a real function the correlation function $\mathcal{C}(\tau)$ must fulfill $\mathcal{C}(-\tau)=\mathcal{C}^*(\tau)$ and thus

$$\mathcal{L}(\omega) = \frac{1}{2\pi}\int_{0}^{\infty}\left(e^{i\omega\tau}\,\mathcal{C}(\tau) + e^{-i\omega\tau}\,\mathcal{C}^*(\tau)\right)d\tau \tag{3.55}$$

It remains to discuss how the interaction to the different atoms determines the form of the profile $\mathcal{L}(\omega)$ or equivalently how the correlation function $\mathcal{C}$ evolves with the time shift τ. Therefore a small time interval $\Delta\tau$ and the value of $\varphi(t'+\tau+\Delta)$ in (Equation (3.52)) shall be considered.

$$\varphi(t'+\tau+\Delta\tau) = e^{-i\overbrace{\left(E_i^{(0)}-E_f^{(0)}\right)/\hbar}^{\omega_{if}}\Delta\tau}\,e^{-i\chi}\,\varphi(t'+\tau)$$

Here the first exponential arises from the time dependence of the initial and final bound electron's state $\Psi_{i/f}^{(e)}(t)$ and the second exponential from the interactions of the bound electrons with the surroundings,

which modifies the phase of φ with a contribution $\chi \sim \Delta\tau$ depending on the interaction energy scale. In order to be more precise, those interactions are collisions with charged particles (=free electrons and free ions) within a gas in plasma state, which corresponds to the so-called line broadening due to the Stark effect. Moreover the time interval $\Delta\tau$ is considered small enough such that only one collision to one atom (and its respective bound electron) takes place. This is the impact approximation which allows to add the contribution of each separate bound electron by considering each collision as uncorrelated from each other

$$\mathcal{C}(\tau + \Delta\tau)\Big|_{\substack{\text{1 col. with 1 atom}}} = e^{-i\omega_{if}\Delta\tau}\, e^{-i\chi} \mathcal{C}(\tau)$$

$$\frac{d\mathcal{C}}{d\tau} = \overline{\frac{\mathcal{C}(\tau+\Delta\tau) - \mathcal{C}(\tau)}{\Delta\tau}} = \mathcal{C}(\tau)\frac{1}{\Delta\tau}\overline{\left(-1 + e^{-i\omega_{if}\Delta\tau}\, e^{-i\chi}\right)} \quad (3.56)$$

$$\overset{\Delta t \text{ small}}{=} \mathcal{C}(\tau)\left[-i\omega_{if} - \frac{\overline{(1 - e^{-i\chi})}}{\Delta\tau} + O(\Delta\tau)\right]$$

In the last equation the overline $\overline{}$ represents the sum or average over all uncorrelated collisions with maximal one collision with each single atom in the system. Such an average is obtained by using the probability for collisions with the free electrons in the plasma, which is proportional to the volume density of free electrons $\tilde{n}_e$, to the free electron's velocity v_e, to the time interval $\Delta\tau$ and to the collision cross-section $d\sigma_{col}(\chi, v_e)$

collision probability for phase between χ and $\chi + d\chi$ at v_e: $\tilde{n}_e\, v_e\, \Delta\tau\, d\sigma_{col}(\chi, v_e)$

Hence the average involves not only an integration over the different values of χ but also over the different electron's velocities, with $f_e(v_e)\, dv_e$ the corresponding distribution probability becomes

$$\overline{(1 - e^{-i\chi})} = \overline{1 - \cos\chi} + i\overline{\sin\chi}$$

$$\overline{1 - \cos\chi} = \tilde{n}_e\, \Delta\tau \iint f_e(v_e)\, (1 - \cos\chi)\, d\sigma_{col}(\chi, v_e)\, dv_e \equiv \tilde{n}_e\, \Delta\tau\, \overline{\sigma_{(1-\cos\chi)v_e}} \quad (3.57)$$

$$\overline{\sin\chi} = \tilde{n}_e\, \Delta\tau \iint f_e(v_e)\, \sin\chi\, d\sigma_{col}(\chi, v_e)\, dv_e \overset{\Downarrow}{\equiv} - \tilde{n}_e\, \Delta\tau\, \overline{\sigma_{\sin\chi v_e}}$$

In the last relation the minus sign marked by $\Downarrow$ arises from the fact that a higher value of the phase shift χ occurs when the interacting particles are closer to each other and thus correponds to a lower value of the collision cross-section. Substituting this into Equation (3.56) leads to

$$\frac{d\mathcal{C}}{d\tau} = \mathcal{C}(\tau)\left[-i\omega_{if} - \tilde{n}_e\, \overline{\sigma_{(1-\cos\chi)v_e}} + i\tilde{n}_e\, \overline{\sigma_{\sin\chi v_e}}\right]$$

$$\mathcal{C}(\tau) = \mathcal{C}(\tau=0)\exp\left[-i\left(\omega_{if} - \tilde{n}_e\, \overline{\sigma_{\sin\chi v_e}}\right)\tau\right]\exp\left[-\tilde{n}_e\, \overline{\sigma_{(1-\cos\chi)v_e}}\tau\right] \quad (3.58)$$

with $\mathcal{C}(\tau=0) = 1$ according to (Equation (3.54)). Profile $\mathcal{L}(\omega)$ follows from integral (Equation (3.55))

$$\mathcal{L}(\omega) = \frac{1}{2\pi}\left[\frac{1}{\tilde{n}_e\, \overline{\sigma_{(1-\cos\chi)v_e}} - i\left(\omega - \omega_{if} + \tilde{n}_e\, \overline{\sigma_{\sin\chi v_e}}\right)}\right.$$

$$\left. + \frac{1}{\tilde{n}_e\, \overline{\sigma_{(1-\cos\chi)v_e}} + i\left(\omega - \omega_{if} + \tilde{n}_e\, \overline{\sigma_{\sin\chi v_e}}\right)}\right] \quad (3.59)$$

$$= \frac{\tilde{n}_e\, \overline{\sigma_{(1-\cos\chi)v_e}}}{\pi}\frac{1}{\left(\omega - \left(\omega_{if} - \tilde{n}_e\, \overline{\sigma_{\sin\chi v_e}}\right)\right)^2 + \left(\tilde{n}_e\, \overline{\sigma_{(1-\cos\chi)v_e}}\right)^2}$$

which is a Lorentz profile with a maximum at the frequency $\omega_{if} - \tilde{n}_e\, \overline{\sigma_{\sin\chi v_e}}$ (the maximum is shifted from ω_{if} by $\tilde{n}_e\, \overline{\sigma_{\sin\chi v_e}}$) and a half width at half maximum equal to $\tilde{n}_e\, \overline{\sigma_{(1-\cos\chi)v_e}}$. This latter width characterizes the spectral line broadening $\Delta\omega_{broad}$ of the initially sharp line at ω_{if} due to the superposition of uncorrelated collisions with the plasma's free electrons

$$\Delta\omega_{broad}\Big|_{\text{impact approx.}} = \tilde{n}_e\, \overline{\sigma_{(1-\cos\chi)v_e}} \quad (3.60)$$

3.2.2 Pressure dominated broadening - the Stark effect

Similar to the more detailed discussion in the last section, leading to Equation (3.60). This result for the spectral line width within the framework of the impact approximation can be qualitatively derived directly from the time-energy uncertainty relation in Appendix A.3.4. This relates the lifetime Δt and the corresponding uncertainty in energy ΔE, leading to

$$\Delta t \, \Delta E \sim \hbar \tag{3.61}$$

The uncertainty in energy is given by the uncertainty in frequency $\Delta\omega_{broad}$ characterizing the broadening of the transition frequency at ω_{if} ($\Delta E = \hbar\Delta\omega_{broad}$) and the lifetime Δt is given by the averaged time between consecutive collisions, i.e. the time interval Δt required for having a collision probability equal to 1: $\tilde{n}_e \, v_e \, \Delta t \, \sigma_{col} \sim 1$ or equivalently $\dfrac{1}{\Delta t} \sim \tilde{n}_e \, \sigma_{col} \, v_e$. Hence it follows

$$\Delta\omega_{broad} \sim \frac{1}{\Delta t} \sim \tilde{n}_e \, \sigma_{col} \, v_e \tag{3.62}$$

To determine the value of $\Delta\omega_{broad}\big|_{\text{impact approx.}}$ the following description shall outline the basic mechanism of the phenomenon of pressure broadening, thus leading to the Stark effect. The dipole induced emission of a photon of a very sharp frequency ω_{if} by an excited bound electron becomes fuzzy or broadened in its emitted frequency, through the interaction with surrounding free electrons and ions within a plasma. The main source here is the interaction of the free charges with the atomic electric dipole formed by the emitting bound electron, assuming that the electron distribution inside the atom is asymmetric enough for the atom to display a dipole. The Hamiltonian for such an interaction is given by (Appendix A.3.3)

$$\underline{H}_{int} = \frac{e}{4\pi\varepsilon_0} \left| \vec{\underline{d}}_{dip} \right| \frac{\cos\theta}{r^2} \,, \tag{3.63}$$

with θ the relative orientation of the dipole with respect to the position where the interaction is being evaluated and r the distance to such position. It is worth noting that the dipole interaction being considered now is added to the already discussed dipole interaction with a free electromagnetic field responsible for the emission of a photon by the excited bound electron. The additional interaction creates the broadening of the already existing spectral line originated by the latter interaction. The just described effect is called the quadratic Stark effect, due to it being a second order pertubation. It accounts for elements where no permanent electric dipole is present, like rare gas atoms, with the second order effect being the dominant broadening mechanism. In contrast for elements, which have a permanent electric dipole (that is the case for ionized rare gas species Ar^+, Ar^{++} or metal vapour plasmas) the dominant broadening mechanism is another one, called the linear Stark effect. To not pertube the explanations presented here, the latter mechanism is briefly described in Appendix A.3.5. However it has been incooperated into the presented software, which will be described later on in this work. The general contribution to the electron energy of such an additional interaction has already been described in the section devoted to the Fermi's Golden Rule (see Equation (3.23))

$$E_i = \overbrace{E_i^{(0)}}^{\text{0th order}} + \underbrace{\langle i | \underline{H}_{int} | i \rangle}_{\text{1st order}} + \overbrace{\sum_{f\neq i} \frac{|\langle f | \underline{H}_{int} | i \rangle|^2}{E_i^{(0)} - E_f^{(0)}} \left(1 - e^{-\mathbf{i}\left(E_f^{(0)} - E_i^{(0)}\right)t/\hbar} \right)}^{\text{2nd order}} + \ldots$$

where $|i\rangle$ represents the energy eigenstates of the undisturbed Hamiltonian. Argon atoms, due to their inert gas structure and their corresponding highly symmetric distribution of electrons, show no atomic dipole and thus there is no possibility of connecting $|i\rangle$ with the same eigenstate through the action once of $\underline{H}_{int}$: $\langle i | \underline{H}_{int} | i \rangle = 0$. Hence for argon atoms the first non vanishing correction to the electron's energy arises from the second order contribution proportional to $|\langle f | \underline{H}_{int} | i \rangle|^2$. The physical process occurs in the following way: a free electron flies by and slightly deforms the symmetric bound electron distribution of the argon atom, inducing an electric dipole for a short time interval; a second free electron can thus interact with the short lived dipole. Such an interaction, involving the concerted

action of two free electrons, is much weaker and improbable than it would have been if the atom itself had an own electric dipole: the resulting spectral line broadening is correspondingly weaker.

The contribution to the electron's potential energy by this weak effect is described by the following equation

$$\Delta U(r) = \left(\frac{e}{4\pi\varepsilon_0}\right)^2 \frac{1}{2}\frac{1}{r^4} \sum_{f\neq i} \frac{\left|\left\langle f\right|\left|\vec{d}_{dip}\right|\left|i\right\rangle\right|^2}{E_i^{(0)} - E_f^{(0)}} \left(1-0\right) \equiv \frac{A_4}{r^4}, \tag{3.64}$$

which in a first approximation has been already averaged in time and over all different dipole's orientations θ. The resulting dependence with the distance to the dipole $\sim \frac{1}{r^4}$, which for increasing r decreases much more rapidly than $\sim \frac{1}{r}$ of a single point charge, is the hallmark of being considered a second order correction.

In the remaining discussion in this section the scale of the spectral line broadening in argon will be calculated. In order to estimate the strength A_4 a rough evaluation of the expectation value of the dipole moment is required. This will be carried out in the following in a semi-classical way. The dipole can be depicted as the result of the oscillation of the bound electron between the energy levels $|i\rangle$ and $|f\rangle$, oscillation produced by the action of an external electric field $\vec{E}_0$, the latter created by the plasma's free electron. If $\frac{a_{dip}}{2}$ denotes the oscillation amplitude of the bound electron, such that the resulting dipole moment is equal to $d_{dip} = e\,a_{dip}$, the Newton Law yields

$$m_e \underbrace{\omega_{if}^2 \frac{a_{dip}}{2}}_{\text{acceleration}} = e\left|\vec{E}_0\right|$$

The energy gained by the dipole through its interaction with the electric field is given by $\vec{d}_{dip}\vec{E}_0$ and this corresponds to the energy difference between the two energy levels, between which the bound electron is oscillating

$$d_{dip}^2 \overset{d_{dip}=ea_{dip}}{=} \frac{2e^2}{m_e\omega_{if}^2} \underbrace{\left|\vec{E}_0\right| d_{dip}}_{E_i^{(0)} - E_f^{(0)}} = \frac{2e^2\hbar^2}{m_e\left(E_i^{(0)} - E_f^{(0)}\right)}$$

and thus

$$\left|\left\langle f\right|\left|\vec{d}_{dip}\right|\left|i\right\rangle\right|^2 \sim \frac{2e^2\hbar^2}{m_e\left(E_i^{(0)} - E_f^{(0)}\right)} \implies A_4 \sim \frac{1}{8\pi^2}\left(\frac{e^2}{4\pi\varepsilon_0}\right)^2 \frac{1}{m_ec^2}\sum_{f\neq i}\lambda_{if}^2 \tag{3.65}$$

where the wavelength λ_{if} for the transition between the states $|i\rangle$ and $|f\rangle$ is obtained from $\left(E_i^{(0)} - E_f^{(0)}\right) = \hbar\omega_{if} = 2\pi\hbar\frac{c}{\lambda_{if}}$. Finally the line broadening due to the collisions with the free electrons inside the plasma can be evaluated. At first the collision cross-section σ_{col} has to be estimated, which requires the length scale a_{col} for the effective extension of such cross-section $\sigma_{col} = \pi a_{col}^2$. During the short time interval Δt for which the separation between the bound and the free electron is shorter than $2a_{col}$ the interaction takes place and an interchange in energy in the order of magnitude $\Delta U(r = a_{col})$ occurs. That time interval can be estimated as $\Delta t \sim \frac{2a_{col}}{v_{e,th}}$, where $v_{e,th} \sim \sqrt{\frac{2k_BT_e}{m_e}}$ describes the scale of the thermal velocity of the plasma electrons (T_e is the electron temperature, assuming the free electrons to have already reached the thermal equilibrium). Since during this time interval Δt the bound electron's energy is altered in an amount of $\Delta U(r = a_{col})$, the time-energy uncertainty relation $\Delta t\,\Delta U \sim \hbar$ leads to the following estimation for the collision cross-section

$$\hbar \sim \frac{2a_{col}}{v_{e,th}}\frac{A_4}{a_{col}^4} \;\Rightarrow\; a_{col} \sim \left(\frac{2A_4}{\hbar v_{e,th}}\right)^{1/3} \;\Rightarrow\; \sigma_{col} = \pi a_{col}^2 \sim \pi\left(\frac{2A_4}{\hbar v_{e,th}}\right)^{2/3} \tag{3.66}$$

According to Equation (3.60) (or to the more simple Equation (3.62)) the full width at half maximum expressed both in frequency and in wavelength is approximately

$$2\Delta\omega_{broad} \sim 2\tilde{n}_e \sigma_{col} v_{e,th}$$

$$\sim \tilde{n}_e \left(\frac{1}{2\pi}\right)^{1/3} \frac{1}{(\hbar m_e c^2)^{2/3}} \left(\frac{e^2}{4\pi\varepsilon_0}\right)^{4/3} v_{e,th}^{1/3} \left(\sum_{m\neq n} \lambda_{if}^2\right)^{2/3}$$

$$2\Delta\lambda_{broad} \sim \frac{\lambda_{if}^2}{2\pi c} 2\Delta\omega_{broad}$$

$$\sim \tilde{n}_e \frac{1}{(4\pi^2)^{2/3}} \frac{\lambda_{if}^2}{(\hbar c\, m_e c^2)^{2/3}} \left(\frac{e^2}{4\pi\varepsilon_0}\right)^{4/3} \left(\frac{v_{e,th}}{c}\right)^{1/3} \left(\sum_{f\neq i} \lambda_{if}^2\right)^{2/3}$$

(3.67)

For argon's spectral line at $\lambda_{if} = 696.54$ nm and at an electron plasma temperature $k_B T_e = 1$ eV the resulting full width in wavelength is given by

$$2\Delta\lambda_{broad} \sim \tilde{n}_e \frac{1}{(4\pi^2)^{2/3}} \frac{\lambda_{if}^{10/3}}{(\hbar c\, m_e c^2)^{2/3}} \left(\frac{e^2}{4\pi\varepsilon_0}\right)^{4/3} \left(\frac{2k_B T_e}{m_e c^2}\right)^{1/6}$$

$$2\Delta\lambda_{broad}[\text{nm}]\Big|_{T_e=1\ \text{eV}} \sim 3.9 \times 10^{-25}\, \tilde{n}_e[\text{m}^{-3}]$$

(3.68)

whose order of magnitude agrees with the more detailed calculation for the same electron temperature $2\Delta\lambda_{broad}[\text{nm}]\Big|_{T_e=1\ \text{eV}} = 8.5 \times 10^{-25}\, \tilde{n}_e[\text{m}^{-3}]$ ([84], §9).

A more general consideration for the radiation transition leads to a modification of Equation (3.65), taking into account the oscillator strength f_{if} of the transition $i \implies f$, which leads to:

$$\left|\left\langle f \right| \left|\vec{d}_{dip}\right| \left| i \right\rangle\right|^2 \sim \frac{2 f_{if} e^2 \hbar^2}{m_e \left(E_i^{(0)} - E_f^{(0)}\right)} \implies A_4 \sim \frac{1}{8\pi^2} \left(\frac{e^2}{4\pi\varepsilon_0}\right)^2 \frac{1}{m_e c^2} \sum_{f\neq i} f_{if} \lambda_{if}^2$$

(3.69)

as relation for the collision amplitude and for the full broadening width at half maximum it leads to:

$$2\Delta\omega_{broad} \sim 2\tilde{n}_e \sigma_{col} v_{e,th}$$

$$\sim \tilde{n}_e \left(\frac{1}{2\pi}\right)^{1/3} \frac{1}{(\hbar m_e c^2)^{2/3}} \left(\frac{e^2}{4\pi\varepsilon_0}\right)^{4/3} v_{e,th}^{1/3} \left(\sum_{f\neq i} f_{if} \lambda_{if}^2\right)^{2/3}$$

$$2\Delta\lambda_{broad} \sim \frac{\lambda_{if}^2}{2\pi c} 2\Delta\omega_{broad}$$

$$\sim \tilde{n}_e \frac{1}{(4\pi^2)^{2/3}} \frac{\lambda_{if}^2}{(\hbar c\, m_e c^2)^{2/3}} \left(\frac{e^2}{4\pi\varepsilon_0}\right)^{4/3} \left(\frac{v_{e,th}}{c}\right)^{1/3} \left(\sum_{f\neq i} f_{if} \lambda_{if}^2\right)^{2/3}$$

(3.70)

This set of equations is valid as long as the collision times of a cloud of electrons colliding with a cloud of atoms τ_e is large compared to the time scale where these quantum mechanical interactions take place τ_{inter}. Further it should be noted that the main contributions to the spectral line broadening emerges from the excited levels that are close to the emitting transition:

$$f_{up-f} \lambda_{up-f}^2 \sim \frac{h^2 c^2 f_{up-f}}{\left(E_{up}^{(0)} - E_f^{(0)}\right)^2}$$

(3.71)

The closer the level $E_f^{(0)}$ is to the emitting upper level $E_{up}^{(0)}$ the stronger is the contribution to the broadening. Strong lines with high oscillator strengths $f_{up-down}$ (for example argon lines) often have weak lines in their energetic proximity corresponding to small values of f_{up-f}. Therefore the spectral line broadening of these strong lines is often quite small and absorption becomes increasingly important for such lines.

3.3 Integrated radiation intensity for plasma diagnostics and the cost function minimalisation

To derive the radiation intensity coming from the plasma the approach is to solve the equation for the radiative tranfer in radial coordinates. With the assumption of a cylinder symmetrical plasma model (Figure 2.1) and neglecting dispersion and scattering processes, the two dominating processes are [80]:

- absorption of the incoming intensity along dr, $-\kappa_\lambda' I_\lambda dr$

- emission of radiation from the centre of the system within dr, $\epsilon_\lambda dr$

thus leading to the equation for radiative energy transfer (with only the radial coordinate here).[2]

$$\frac{1}{r}\frac{d(rI_\lambda)}{dr} = -\kappa_\lambda' I_\lambda + \epsilon_\lambda \tag{3.72}$$

With ϵ_λ being the spectral emissivity, with dr being the differential step in radial direction of the cylinder and κ_λ' the corrected absorption coefficient. The general solution to this equation under the given assumptions is:

$$I_\lambda = \int_0^{r_{cool}} \epsilon_\lambda \exp\left(-\kappa_\lambda' I_\lambda\right) dr \tag{3.73}$$

with r_{cool} being the distance to the cold surrounding (actually there is a position the plasma temperature falls below a limit $\approx 6000K$, corrsponding to a position where the contribution of ϵ_λ and κ_λ will be reduced significantly). Now due to the underlying plasma temperature profile (resulting from Equation (2.5)) this integral can be approximated as a sum [3]:

$$I_\lambda = \sum_i \epsilon_\lambda(T_p(i)) \exp\left(-\kappa_\lambda'(T_p(i))I_\lambda\right) \Delta r \tag{3.74}$$

The spectral emissivity ϵ_λ depends on different physical processes, the most dominant one for intensities in the visible spectrum is the bound-bound transition. The contribution of the free-bound transitions of electrons in the plasma was neglected in a first approximation, since its effect is comparably small to the bound-bound transition contribution and will not be further discussed. If a bound electron inside of an atom jumps between discrete energy levels E_f and E_i, a photon of well-defined energy $\lambda_{if} = \frac{hc}{E_f - E_i}$ is emitted. If the emitting bound electrons are nevertheless placed inside a partially ionized gas (= plasma) the many collisions of the corresponding atoms between themselves or with free electrons make the sharp spectral lines of the isolated atom become broadened.

The spectral distribution is no longer a sharp Dirac delta, but takes the form a smoother function, the Lorentz profile $\mathcal{L}(\omega)$ according to Equation (3.59). The expression for $\mathcal{L}(\lambda)$ can then be derived with the equation

$$\hbar\omega_{if} = 2\pi\hbar\frac{c}{\lambda_{if}} \tag{3.75}$$

---

[2]The scattering mean free path of a photon in a partially ionized gas is generally much greater than of the corresponding absorption contribution. The scattering leads to significant contributions if the level of ionization comes close to one (being fully ionized) or the gas density is significantly lowered. In these cases the free-free (or bremsstrahlung) contribution to the absorption is small, since it is proportional to the square of the electron density. [80]

[3]The contribution of the radiative transfer to the radial temperature profile of the arc is at least an order of magnitude lower than the contribution of the diffusive heat transfer (at least for noble gases) and will therefore be neglected.

The transition probability A_{if} is defined by Equation (3.45) and combined with eq. (3.46), the connetion to the emitted power of the radiation is given. Thus leading to the following equation [80]:

$$\epsilon_\lambda^{(bb)} = \sum_{if} \frac{1}{4\pi} n_f \frac{hc}{\lambda_{if}} A_{if} \mathcal{L}(\lambda_{if}) = \frac{1}{4\pi} n_f \dot{W}_{if} \tag{3.76}$$

Here $\sum_{if}$ is the sum over all contributing states of an atom or ion. The density of atoms n_f that corresponds to the upper energy level E_f (running from the ground state), can be derived with the Boltzmann factor (as initially stated this assumptions holds for thermal arc plasmas)

$$n_f = \frac{g_f}{g_{ground}} n_{ground} \exp\left(\frac{-E_f}{k_B T_p}\right) = g_f \frac{n_{atom}}{Z_{atom}} \exp\left(\frac{-E_f}{k_B T_p}\right) \tag{3.77}$$

with g_f and g_{ground} being the degenerancy factors of the respective states and n_{atom} being the particle density of the plasma atoms. This leads to:

$$\epsilon_\lambda = \sum_{if} \epsilon_\lambda^{(bb)} = \frac{1}{4\pi} \frac{hc}{\lambda_{if}} A_{if} \frac{g_\uparrow}{Z_A} n_A e^{\frac{-E_f}{k_B T}} \mathcal{L}(\lambda) \tag{3.78}$$

This procedure can be adapted for ions as well and as such has been included in the calculations, but regarding the small density of ions in the considered temperature range $n_{A+} \ll n_A$ the expected emissivities will be quite low.

For the above mentioned process of discrete emission of radiation after a stimulated transition of an electron between two electronic states, there is also an inverse process where a photon is absorbed. This process is characterized by the spectral absorption coefficient κ_λ. In thermal equilibrium the spectral absorption coefficient is correlated with the spectral emission coefficient through Plank's law:

$$\frac{\epsilon_\lambda}{\kappa_\lambda} = \frac{\lambda^5}{2hc^2} e^{-\frac{hc}{\lambda k_B T}} \tag{3.79}$$

Absorption requires the presents of photons, which in turn can also induce another emission of a photon. Therefore the absorption coefficient needs to be corrected through the occurence of the stimulated emission [80]:

$$\kappa_\lambda' = \kappa_\lambda \left(1 - e^{-\frac{hc}{\lambda k_B T}}\right) \tag{3.80}$$

Combining these equations leads to the corrected spectral absorption coefficient:

$$\frac{\epsilon_\lambda}{\kappa_\lambda'} = \frac{\lambda^5}{2hc^2} \left(e^{\frac{hc}{\lambda k_B T}} - 1\right) \tag{3.81}$$

Last but not least a scheme shall be introduced to compare the calculated spectral intensities, with measured spectral intensities from OES measurement. Therefore a cost function is introduced to compare both quantities:

$$Q = \left(\int_\lambda \left(I_\lambda|_{meas.} - I_\lambda|_{calc.}\right)^2 d\lambda\right)$$

with I_λ being the radiative intensity along the line of sight of the measurement, normalized to the maximum value of a certain line of the regarded spectrum (in this case it will preferably be the 696.5 nm Ar I line, either experimentally measured or theoretically calculated). Furthermore $\int_\lambda d\lambda$ is the integral over all wavelengths taken into account by the external observer. To reduce the computation time additional limitations have to be supplemented. The integral over the wavelength is limited by the upper and lower bound of the spectrometer spectral window, in this case 320 - 950 nm. The cost function then takes the form:

$$Q = \sum_{\Delta\lambda} \left(I_\lambda|_{meas.} - I_\lambda|_{calc.}\right)^2 \Delta\lambda \tag{3.82}$$

This does not pose a problem so far, since the influence of the line intensities and broadening widths have way more impact on the cost function than the selected spectral range, with respect to the used gases. Furthermore the wavelength resolution for the calculations is limited to 0.05 nm. This ensures that no mismatches of the intensity values occur, due to coarse data values and still keeps the required computation power low. Still a trade-off between spectral width of the cost function and the computation time need to be taken into account. The spectral window and the resolution within that window shall be regarded as input parameters for a matching algorithm, so the detailed choice of these values is still open for the particular problem this method is applied too.

An example for such a matching algorithm can be build in the following way:

1. first the cost function is derived for a desired spectral window according to the equations prior in this section, with $I_\lambda\big|_{\text{calc.}}$ being calculated for a given value of r_{cool}

2. then r_{cool} is slightly varied by some small deviation $\pm\Delta r$ and the corresponding values of the cost function Q_+, Q_- are derived

3. both values are comparedto the original Q to create a local gradient, repeat all steps until the minimum of Q is found

This is only a general procedure and the convergence can take quiet long depending on the starting solution for r_{cool}, it is good to derive the order of r_{cool} with some other method (e.g. the method presented latter on in this work).

Some additional remarks:

The spectral radiance derived with eq. (3.74) can be integrated over the wavelength, to derive the total irradiance coming from the plasma:

$$I_{rad} = \int_0^\infty I_\lambda d\lambda \tag{3.83}$$

For the regarded problem with a finite spectral range available for analysis this equation can further be approximated as summation over the wavelength, with $\lambda \to \lambda(i)$ being discretized between the minimum λ_{min} and maximum value λ_{max} of the spectral window with the resolution $\Delta\lambda$. This leads to the following formulation, together with Equation (3.45), for the total irradiance

$$I_{rad} = \sum_{\lambda(i)=\lambda_{min}}^{\lambda_{max}} I_{\lambda(i)} = \sum_{\lambda(i)=\lambda_{min}}^{\lambda_{max}} \sum_{i=r_{min}}^{r_{max}} \epsilon_\lambda(T_p(i)) \exp\left(-\kappa_\lambda'(T_p(i))I_\lambda\right) \Delta r \, \Delta\lambda \tag{3.84}$$

3.4 Simulation tool for the radiation model

In this section the own developed MATLAB/Simulink code for simulating the radiation spectrum, the cost function minimalization method and the corresponding subroutines, shall be briefly explained. The detailed description remains within the code itself and can be obtained from the reference in Appendix A.4. The simulation results will be presented and discussed later on in this work Section 5.1, at first the plasma composition for the different working gases will be displayed, than the corresponding calculated and measured spectra from [9] will be compared. Furthermore the electron densities and plasma temperature profiles will be displayed and compared to the results from the same experiment. The simulation is initiated with a Matlab script, which:

- calculates the particle densities of all species depending on the plasma temperature T_p

- provides all necessary plasma transport parameters (σ_{el}, $\lambda_{th,p}$, $c_{p,p}$, ρ_p) [59, 60, 85] and cathode material parameters ($\lambda_{th,c}$, $c_{p,c}$, ρ_c) [86, 87]

- sets the geometrical boundary conditions and operational parameters (z_c, r_{cool}, ℓ_{arc}, I_{arc})

- starts the radiation calculation script and cost function minimalization parametric sweep script

The radiation model (matlab scripts), consists of the following parts:

- Linear Stark Broadening

- Quadratic Stark Broadening

- Combined Transition Radiation

- Radiation QM Calculation

- Calc Angular Radiation Distribution

- Display Angular Radiation Distribution

The cost function minimalization model (matlab scripts), consists of the following parts:

- Determine cost function value and minimize

Radiation QM Calculation   This matlab script calls all underlying radiation calculations to determine the Stark broadening widths, the line profile and the radiated spectral power Equation (3.46). Conclusively the spectral emission coefficient and the absorption coefficient are calculated. This function precalculates all these quantities depending on a plasma temperature vector $T_e =$ 5000 - 30 000 K, with a resolution of $\Delta T_e = 100$ K and the corresponding value of the particle densities and stores them in a lookup table.

Linear Stark Broadening   This function calcualtes the Linear Stark broadening width for the regarded working gas and species, according to Appendix A.3.5.

Quadratic Stark Broadening   This function calcualtes the Quadratic Stark broadening width for the regarded working gas and species, according to Equation (3.70).

Combined Transition Radiation   This function gathers all the calculated infromation on the Stark broadening widths, the radiated power and combines them with the data on the state transition rate and the oscillator strength taken from [68]. To determine the emission and absorption coefficients.

Calc Angular Radiation Distribution   This function performs the numerical integration to determine the total (and spectrally resolved) radiation intensity emitted from the plasma, according to Equations (3.74) and (3.84). It depends on the results for the plasma temperature profile, the electron density and the emission and absorption coefficients.

Display Angular Radiation Distribution   This function gathers all previous results and displays them according a desired display style defined within it. The laser heating simulation has its own display windows for the temporal evolution. Only the convergence solutioon at the end of the laser pulse is transfered and display with this function.

Determine cost function value and minimize   The cost function minimalization is a parametric sweep technique to call the radiation model with a specific set of parameters, calculate the results and determine the corresponding cost function value for the evaluation. The values are stored and compared over the whole parameter set.

Chapter 4

Plasma dynamics and control system

In general the dynamics of a real system to be controlled is determined by the behavior of a certain number of degrees of freedom which are called state variables and are gathered as a collective state vector x; in order to keep the notation simple the symbol $\vec{}$ for a vector will not be explicitly written at this stage. The number of degrees of freedom is the *order of the dynamics* and will be denoted by n; thus x contains n components x_i, with $i = 1, \ldots, n$: $x = \begin{pmatrix} x_1 \\ \vdots \\ x_n \end{pmatrix}$. And the time evolution (or dynamics) of all these degress of freedom is described by a set of n differential equations of 1st order (one equation for each state variable).

If this system is to be driven along some desired behavior (and only such systems are of interest here) at least one variable (called input) must exist which can be externally controlled or designed. Nevertheless in most of the systems the number of state variables to be driven/controlled (the n degrees of freedom) is much higher than the number of input variables which can be designed, and such dynamics are called *underactuated*: the dynamics to be considered in this work belongs to this class, in particular to the worst situation where only one input variable must be designed for controlling all n state variables. From now on this single input variable will be denoted by u. The general basic
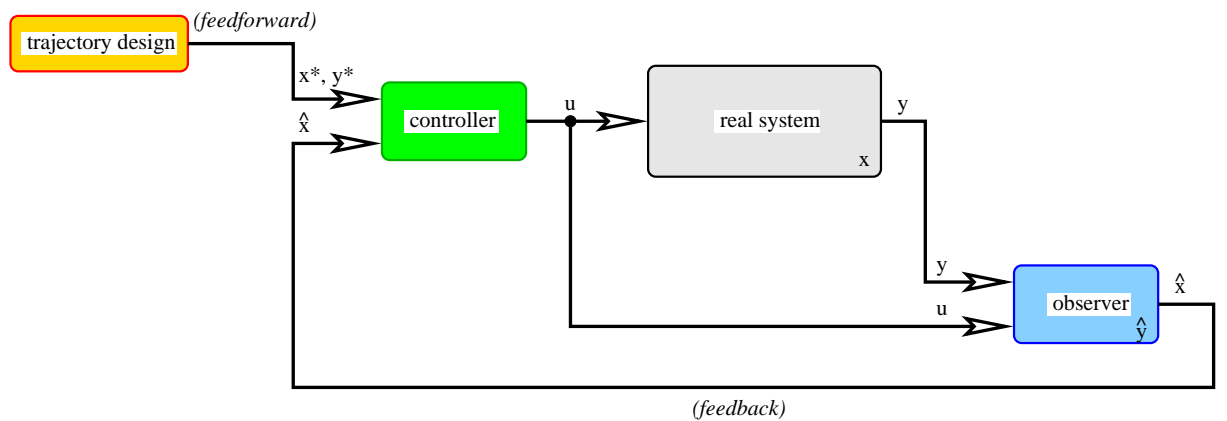
Figure 4.1: Schematic structure a controller of a dynamic system, designed to track a desired trajectory

structure of the task to be solved is represented in Figure 4.1. Instead of performing the deduction of the model based control with the more specific depiction from the introduction Figure 1.2, a more general description will be applied now, since only the system structure is required not the precise physical implementation behind it. The real dynamics corresponds to a block operating as a "black box" by taking some input (vector) and yielding some output (vector) but whose internal details remain hidden to all the other blocks. The calculation of the correct input u is carried out in the *controller* block according to some method, which will be explained later on in this work and this usually requires a complete knowledge of the current values of all degrees of freedom, i.e. of the full state vector x. In most situations nevertheless this is not practicable since for the full system only few sensors are avalaible yielding a reduced number of measurement outputs, collectively denoted as the output vector y. Again in this work the situation is considered where only one single component can be measured for the output, analogous to the single input variable to control the whole system. Hence the control design needs (assuming enough information of the full system dynamics is contained in the output y) a reconstruction of the full state vector from the output: this state estimation is denoted by $\hat{x}$, which is fed back into the controller for achieving the desired behaviour. The block responsible for the state reconstruction is called *observer*.

The already mentioned desired behaviour (denoted from now on with the symbol $*$) corresponds to some *trajectory design* for all degrees of freedom of the system (and equivalently for its output variable), calculated in a separated block and whose results are directly passed onto the controller; this latter process is called feedforward. If the dynamics of the real system to be controlled is fast, as it is the case in this work, the controller as well as the observer must operate very quickly. Considering the current limitations in computing power the control/observer design may well require a simplified dynamics model, with whom a lower number of degrees of freedom than the actual system dynamics is still capable of describing the main effects to be controlled.

Summarizing this part of the present thesis, the general structure for the task to be discussed consists of 4 elements:

- The real system (**gray block**) actually planned to be controlled, which exists either as a physical machine or as a numerical model in a computer, in both cases driven by the input u, being output y the only information one gets from the system.

- The trajectory design (**orange block**) determining the desired behavior to be followed by the real system, this has been precalculated on a computer.

- The observer (**blue block**) to estimate the full state vector from the only information, the output available from the real system. The observer is usually implemented in a fast microprocessor which yields at a high rate the state reconstruction.

- And finally the central block, the controller (**green block**), implemented again in a fast microprocessor and which determines the input u for implementing the desired trajectory by compensating any deviation between the desired behavior x^* and the reconstructed system state $\hat{x}$. Controller and observer can be combined into one single block (within the same microprocessor), if desired.

This part of the work is constituted as follows, since there was no possibility of implementing this structure in a physical facility the real system has been numerically modelled according to the equations discussed in the Section 2.1. At first a simplified model for the system dynamics will be derived from these equations in the consecutive sections, both of whom the observer and controller will be based on. It is important to emphasize that the "real" system dynamics are more complicated than the model used for designing the control. Thereby the "black box" character of the real system dynamics, whose details are hidden from the controller, is thus ensured. Additionally a noise component is added to the full system dynamics to better validate the performance of the control being designed. This accounts for the non-modeled physical effects in the thermal arc model Equation (2.5). Subsequently it is considered how to numerically integrate the nonlinear equations of motion in such a way as to avoid generating uncontrolled growing behaviours, which indicate a poor numerical solution. In order to develop a fast algorithm for realtime applications a makeshift numerical integration scheme will be implemented, instead of using a common integration technique. Following on the main original contribution of this

part of the thesis is displayed, the development of a flatness-based control suited to the simplified model of the combined "plasma arc - cathode spot" dynamical system. This flatness-based technique [88] is an advanced method of nonlinear control able to track a desired trajectory in a precise way by using a particular property of the equations of motion for the simplified model. Also the design of a efficient observer for the state estimation required by the control is considered in that section. The simulation results based on the just developed algorithms of the thesis will be presented in the succeeding chapter for different trajectories of interest, together with their corresponding discussion.

4.1 Simplified model for control design

Since the plasma dynamics is a fast process, a control model able to react to any deviation from some desired behavior must be calculated at a high rate. For such a task the previous model (Equation (2.5)) for the temperature distribution within the plasma arc, although more detailed, is not well suited since its state vector contains too many components to be tracked. A much simpler model, with a reduced number of state variables but still containing the essential effects of the plasma arc as well as cathode spot dynamics, is required for an eventual control design. The dynamics for the cathode spot
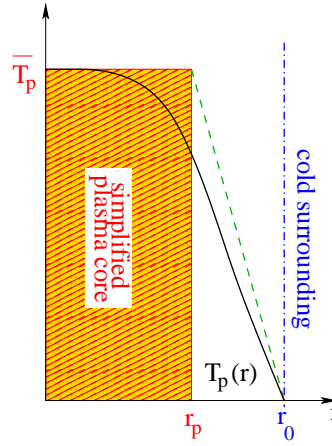
Figure 4.2: Schematic of the simplified plasma core with effective core radius r_p

temperature, already described by a single variable T_c, cannot be further reduced. Taking the latter as a model, a description for the plasma arc by using only one variable is now intended. This is achieved by approximating the radial distribution of the plasma arc temperature by a homogeneous cylindrical core of uniform temperature $\overline{T}_p$ and radius r_p, see Figure 4.2. The temperature $\overline{T}_p$ corresponds to the inner most temperature in the more detailed model and radius r_p has no direct physical meaning, being only an effective variable condensing the form of the actual, no longer resolved, radial profile of the arc temperature (black line in Figure 4.2). Such an effective radius is a function of the core temperature $\overline{T}_p$, whose form will be discussed at the end of this section, for now it will be assumed as already derived and thus known. The enthalpy content of the plasma is only located inside the plasma core of radius r_p and therefore its evolution is described in a similar way as Equation (2.1)

$$\frac{\partial}{\partial t}\left(\pi r_p^2 \ell_{arc} \int_{T_0}^{\overline{T}_p} \rho_p(T)\, c_{p,\,p}(T)\, dT\right) \approx \underbrace{+2\pi r_p \ell_{arc}\left(\lambda_{th,\,p}\frac{\partial T_p}{\partial r}\right)\Big|_{\text{core edge}}}_{\substack{\text{power loss due to diffusion}\\\text{crossing core's lateral surface}}}$$
$$+ \underbrace{\pi r_p^2 \ell_{arc}\, \sigma_{el}(\overline{T}_p)\,(E_{arc})^2}_{\substack{\text{power gain due to Joule heating}\\\text{inside core}}} \qquad (4.1)$$

with the main focus on two effects: the radial heat diffusion and the Joule heating within the core.

- The heat diffusion at the core's lateral edge can be approximated by the average of the power flow $\lambda_{th,p}\dfrac{\partial T_p}{\partial r}$ over the narrow space from the core's external surface until the cold surrounding is reached

$$\text{averaged } \lambda_{th,p}\frac{\partial T_p}{\partial r} = \frac{1}{r_0 - r_p}\int_{r_p}^{r_0}\lambda_{th,p}\frac{\partial T_p}{\partial r}\,dr = -\frac{1}{r_0 - r_p}\int_{T_0}^{\overline{T}_p}\lambda_{th,p}(T)\,dT$$
$$\approx -\frac{\lambda_{th,\,film}\left(\overline{T}_p - T_0\right)}{r_0 - r_p}$$

(4.2)

This corresponds to assuming a nearly linear decrease of gas temperature between $r = r_p$ and $r = r_0$ (green line in Figure 4.2). In the previous equation $\lambda_{th,\,film}$ represents the gas thermal conductivity evaluated at the average temperature between the core temperature $\overline{T}_p$ and the temperature T_0 of the cold surrounding wall

$$\lambda_{th,\,film} \equiv \lambda_{th,p}\left((\overline{T}_p + T_0)/2\right)$$

(4.3)

and thus $\lambda_{th,\,film}\left(\overline{T}_p - T_0\right)$ is a first approximation for the integral $\int_{T_0}^{\overline{T}_p}\lambda_{th,p}(T)\,dT$.

- Being consistent with the uniformly conducting plasma core of the simplified model, the full electric current and thus the Joule heating is exclusively concentrated inside the plasma core, leading to the following relation

$$I_{arc} = E_{arc}\int_0^{r_0}\sigma_{el}(T(r))\,2\pi r\,dr = \pi r_p^2\,\sigma_{el}(\overline{T}_p)\,E_{arc}$$
$$\sigma_{el}(\overline{T}_p)E_{arc}^2 = \frac{1}{\pi^2\sigma_{el}(\overline{T}_p)\,r_p^4}I_{arc}^2$$

(4.4)

Hence the simplified model for the system "plasma arc - cathode spot" can now be formulated. It is described by a 2-dimensional state vector $\vec{x} = \begin{pmatrix} T_c \\ \overline{T}_p \end{pmatrix}$, whose equations of motion are taken Equations (4.1) to (4.4) and Equation (2.50) to formulate the following set of equations:

$$\frac{dT_c}{dt} = -\frac{\lambda_{th,c}}{\rho_c c_{p,c} z_c^2}(T_c - T_0) - \frac{\varepsilon_c \sigma_{SB}}{\rho_c c_{p,c} z_c}T_c^4 + \frac{1}{\rho_c c_{p,c} z_c}\left(A_R T_c^2 \exp\left(-\frac{e\Phi_c}{k_B T_c}\right) + en_{e,\infty}\sqrt{\frac{k_B \overline{T}_p}{m_i}}\right) \times$$
$$\times \left(\frac{E_{ion}}{e}\frac{en_{e,\infty}\sqrt{\frac{k_B \overline{T}_p}{m_i}}}{A_R T_c^2 \exp\left(-\frac{e\Phi_c}{k_B T_c}\right)} - \Phi_c\right)$$
$$\equiv f_1(T_c, \overline{T}_p)$$

$$\frac{d\overline{T}_p}{dt} = -\frac{2\lambda_{th,p}((\overline{T}_p + T_0)/2)\left(\overline{T}_p - T_0\right)}{\rho_p(\overline{T}_p)c_{p,p}(\overline{T}_p)\left(r_p(\overline{T}_p)\right)^2\left(\frac{r_0}{r_p(\overline{T}_p)} - 1\right)} + \frac{1}{\pi^2\sigma_{el}(\overline{T}_p)\rho_p(\overline{T}_p)c_{p,p}(\overline{T}_p)\left(r_p(\overline{T}_p)\right)^4}I_{arc}^2$$
$$\equiv f_2(\overline{T}_p) + g_2(\overline{T}_p)\,\underbrace{I_{arc}^2}_{u}$$

(4.5)

Again the square of the electric current acts as the input u for the dynamics. For the simplified model the Saha-Eggert equation for solving the electron density $n_{e,\infty}$ is calculated according to Equation (2.25).

4.1.1   Estimation of an effective plasma core radius r_p

The only remaining part to be discussed for the simplified model is how the effective core radius r_p depends on the single variable describing the plasma arc: core temperature $\overline{T}_p$. This still unknown dependence is determined by the radial heat diffusion, which is described by the differential term $\frac{1}{r}\frac{\partial}{\partial r}\left(\lambda_{th,\,p}(T_p)\,r\,\frac{\partial T_p}{\partial r}\right)$. As a first step, let this last term be reformulated by using the so-called thermal potential

$$\psi_{th,\,p}(T_p) = \int_{T_0}^{T_p} \lambda_{th,\,p}(T)\,dT \tag{4.6}$$

as well as a dimensionless radial coordinate $x = \left(\dfrac{r}{r_0}\right)^2$

$$\frac{1}{r}\frac{\partial}{\partial r}\left(\lambda_{th,\,p}(T_p)\,r\,\frac{\partial T_p}{\partial r}\right) = \frac{4}{r_0^2}\frac{\partial}{\partial x}\left(x\,\frac{\partial \psi_{th,\,p}}{\partial x}\right) \tag{4.7}$$

The plasma arc's radial temperature profile displays a negative curvature and thus the previous differential term is in general a negative function. Since there is no much space between the plasma arc core and the cold surroundings, such negative function cannot display a strong x-dependence, otherwise the heat flow would become too inhogeneous over the considered narrow fringe separating the arc from $r = r_0$. Thus the simplest form for $\frac{\partial}{\partial x}\left(x\,\frac{\partial \psi_{th,\,p}}{\partial x}\right)$ is just a negative constant

$$\frac{4}{r_0^2}\frac{\partial}{\partial x}\left(x\,\frac{\partial \psi_{th,\,p}}{\partial x}\right) \approx -\frac{4}{r_0^2}\kappa_1 \quad \text{with constant} \quad \kappa_1 > 0\,. \tag{4.8}$$

This simplified approximation must be validated *a posteriori* after having solved the detailed model (this will be discussion in the next chapter), but it can be expected to hold at least for small r_0. The integration of the previous equations yields

$$\frac{\partial \psi_{th,\,p}}{\partial x} = \lambda_{th,\,p}\frac{\partial T_p}{\partial x} \approx -\kappa_1 + \overbrace{\frac{C_0}{x}}^{=\,0}\,,$$
$$\psi_{th,\,p}(x) = \int_{T_0}^{T_p(x)} \lambda_{th,\,p}(T)\,dT \approx \kappa_1\,(1-x) \tag{4.9}$$

where in the first equation C_0 must be set equal to zero since otherwise $\frac{\partial T_p}{\partial x}$ would unphysically diverge at $x = 0$, the core center; in the last integration the boundary condition $T_p(x = 1) = T_0$, or equivalently $\psi_{th,\,p}(x = 1) = 0$, has been used. Evaluating the last equation in Equation (4.9) at the core center $x = 0$ allows to obtain a good estimation of constant κ_1

$$\kappa_1 = \int_{T_0}^{\overline{T}_p} \lambda_{th,\,p}(T_p)\,dT_p \tag{4.10}$$

Now let us connect the previous general discussion to the homogeneous cylindrical core of the simplified model: in both cases the same electric current and electric field along the arc must apply and thus the following relation must be satisfied

$$\frac{I_{arc}}{E_{arc}} = \underbrace{\int_0^{r_0} 2\pi r\sigma_{el}(T_p(r))\,dr}_{\text{detailed model}} \overset{!}{=} \underbrace{\pi r_p^2\sigma_{el}(\overline{T}_p)}_{\text{simplified model}}$$

$$\left(\frac{r_p}{r_0}\right)^2 \overset{x=r^2/r_0^2}{=} \frac{1}{\sigma_{el}(\overline{T}_p)}\int_{x=0}^{x=1}\sigma_{el}(T_p(x))\,dx = \frac{1}{\sigma_{el}(\overline{T}_p)}\int_{x=0\to\overline{T}_p}^{x=1\to T_0}\sigma_{el}(T_p(x))\frac{dx}{dT_p}\,dT_p \tag{4.11}$$

According to the approximation in the detailed model Equation (4.9), where the radial gradient of the
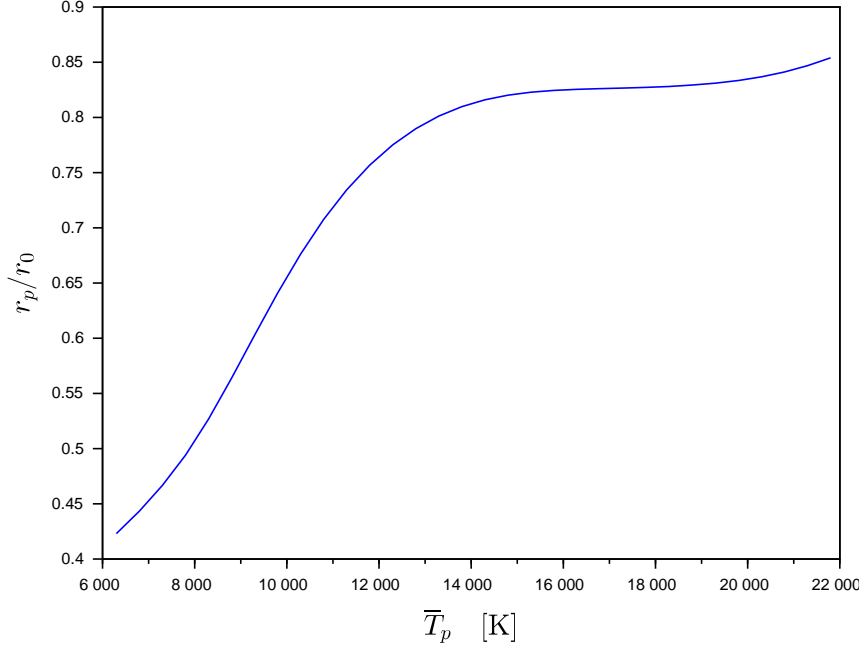
Figure 4.3: Evolution of estimated r_p/r_0 with plasma core temperature $\overline{T}_p$ for an Argon plasma at atmospheric pressure

thermal potential is nearly constant, the previous equation can be written in a way fully determined by the transport parameters of the plasma gas, without any dependence on the plasma arc geometry.

$$\left(\frac{r_p}{r_0}\right)^2 \approx -\frac{1}{\sigma_{el}(\overline{T}_p)}\frac{1}{\kappa_1}\int_{\overline{T}_p}^{T_0}\sigma_{el}(T_p)\lambda_{th,\,p}(T_p)\,dT_p \stackrel{\text{eq. (4.10)}}{=} \frac{1}{\sigma_{el}(\overline{T}_p)}\frac{\displaystyle\int_{T_0}^{\overline{T}_p}\sigma_{el}(T_p)\lambda_{th,\,p}(T_p)\,dT_p}{\displaystyle\int_{T_0}^{\overline{T}_p}\lambda_{th,\,p}(T_p)\,dT_p} \tag{4.12}$$

For an Argon plasma at atmospheric pressure, using the thermodynamical data in the appendix tables of [59], the resulting dependence of r_p/r_0 on the core temperature $\overline{T}_p$ is shown in Figure 4.3. This curve $r_p(\overline{T}_p)$ can be simply saved into a look-up table when performing any numerical simulation using the simplified dynamics. Or alternatively it can be fitted to some smooth function: the curve data in Figure 4.3 are well fitted by the following polynomial

$$\frac{r}{r_0} \approx c_0 + c_1\left(1 - \frac{\overline{T}_p}{10000}\right) + c_2\left(1 - \frac{\overline{T}_p}{10000}\right)^2 + c_3\left(1 - \frac{\overline{T}_p}{10000}\right)^3,$$
$$c_0 = +0.66247,\quad c_1 = -0.53413,\quad c_2 = -0.53958,\, c_3 = -0.18185$$

4.2 Numerical integration of the simplified dynamics

The simplified dynamics eq. (4.5) are discretized in an analogous way to the full system dynamics (see Appendix A.2.1). The system is described by a 2-dimensional state vector $\vec{x}(t) = \begin{pmatrix} T_c(t) \\ \overline{T}_p(t) \end{pmatrix}$, which is again driven by the input $u(t) = \left(I_{arc}(t)\right)^2$. The discretization of the equation of motion for the

cathode spot temperature is just eq. (2.61) again and for the plasma core temperature the discretization leads to the following expression.

$$
T_c(t + \Delta t) \left[1 + \frac{\Delta t\, \lambda_{th,\,c}}{z_c^2 \rho_c c_{p,\,c}} + \frac{\Delta t\, \varepsilon_c \sigma_{SB}}{\rho_c c_{p,\,c}\, z_c} \left(T_c^{(prov)} \right)^3 \right.
$$

$$
\left. + \frac{\Delta t}{z_c \rho_c c_{p,\,c}} \left(A_R \left(T_c^{(prov)} \right)^2 \exp\left(-\frac{e\Phi_c}{k_B T_c^{(prov)}} \right) + en_{e,\,\infty}^{(prov)} \sqrt{\frac{k_B \overline{T}_p^{(prov)}}{m_i}} \right) \frac{\Phi_c}{T_c^{(prov)}} \right]
$$

$$
= T_c(\overset{\Downarrow}{t}) + \frac{\Delta t\, \lambda_{th,\,c}}{z_c^2 \rho_c c_{p,\,c}} T_0 + \frac{\Delta t\, E_{ion} n_{e,\,\infty}^{(prov)} \sqrt{\frac{k_B \overline{T}_p^{(prov)}}{m_i}}}{z_c \rho_c c_{p,\,c}} \left(1 + \frac{en_{e,\,\infty}^{(prov)} \sqrt{\frac{k_B \overline{T}_p^{(prov)}}{m_i}}}{A_R \left(T_c^{(prov)} \right)^2 \exp\left(-\frac{e\Phi_c}{k_B T_c^{(prov)}} \right)} \right)
$$

$$
\overline{T}_p(t + \Delta t) \left[1 + \frac{2\Delta t\, \lambda_{th,\,p}((\overline{T}_p + T_0)/2)}{\left(\rho_p c_{p,\,p} r_p^2 \left(\frac{r_0}{r_p} - 1 \right) \right) \Big|_{\overline{T}_p^{(prov)}}} + \xi\, \frac{\frac{\Delta t}{\left(\pi^2 \sigma_{el} \rho_p c_{p,\,p} r_p^4 \right) \big|_{\overline{T}_p^{(prov)}}} \frac{\left(I_{arc}(t + \Delta t) \right)^2}{\overline{T}_p^{(prov)}}}{} \right]
$$

$$
= \overline{T}_p(\overset{\Downarrow}{t}) + \frac{2\Delta t\, \lambda_{th,\,p}((\overline{T}_p + T_0)/2)}{\left(\rho_p c_{p,\,p} r_p^2 \left(\frac{r_0}{r_p} - 1 \right) \right) \Big|_{\overline{T}_p^{(prov)}}} T_0 + \left(1 + \underline{\xi} \right) \frac{\Delta t}{\pi^2 \left(\sigma_{el} \rho_p c_{p,\,p} r_p^4 \right) \big|_{\overline{T}_p^{(prov)}}} \left(I_{arc}(t + \Delta t) \right)^2 \quad (4.13)
$$

With a factor ξ (comparable to Equation (2.56)) to ensure the convergence of the numerical solution, as stated in Appendix A.2.1 and using the same abbreviations for the provisional solution at $t + \Delta t$; $T_c^{(prov)} \equiv T_c^{(prov)}(t + \Delta t)$ and $\overline{T}_p^{(prov)} \equiv \overline{T}_p^{(prov)}(t + \Delta t)$. Otherwise the iterative method remains the same as for the full dynamics. The set of equations for the cathode sheath layer (Section 2.3.2) are recalculated in every time step of the integration, before calculating the new value for the cathode temperature. This integration is now processed until the residual error of two consecutive values of the cathode temperature has droped below some given error limit. This is typically achieved after less than 60 iterations.

4.3 Flatness-based control and observer design

The main property to be managed in a plasma process for its technological use is the gas temperature, which also determines the amount of free electrons inside the plasma. Nevertheless to have direct access to the value of the gas temperature requires a very precise control, since the time scales involved in the temporal evolution of the gas temperature are very short. The relevant time scales can be read from the equations of motion Equation (4.5) at the terms $\frac{dx}{dt} \sim -\frac{1}{\tau} x + \ldots$:

$$
\tau_c = \frac{\rho_c c_{p,\,c} z_c^2}{\lambda_{th,\,c}}
$$

$$
\tau_p = \frac{\rho_p c_{p,\,p} r_p^2}{\lambda_{th,\,p}}
$$

(4.14)

with r_p, z_c being the respective characteristic length scales of the effective plasma core temperature and the cathode temperature. The first parameter is derived through Equation (4.12) and the second one is a given input parameter. For typical values of an argon plasma at atmospheric pressure and a plasma temperature about $\hat{T}_p = 12\,000\,\text{K}$ ($\lambda_{th,\,p} \sim 1.5\,\text{W/m K}$, $\rho_p \sim 3.6 \times 10^{-2}\,\text{kg/m}^3$, $c_{p,\,p} \sim 4400\,\text{J/kg K}$ and $r_p = 4.1\,\text{mm}, r_0 = 5.5\,\text{mm}$) combined with a tungsten cathode

$(\lambda_{th,\,c} \sim 170\ \mathrm{W/m\,K}$, $\rho_c \sim 19.3 \times 10^3\ \mathrm{kg/m^3}$, $c_{p,\,c} \sim 138\ \mathrm{J/kg\,K}$ and $z_c = 4\ \mathrm{mm})$, these two characteristic time scales are in the order of magnitude of

$$\tau_c = \frac{19.3 \times 10^3 \times 138 \times (0.004)^2}{170} = 250.6\,\mathrm{ms}$$

$$\tau_p = \frac{3.6 \times 10^{-2} \times 4400 \times (0.0041)^2}{1.5} = 1.8\,\mathrm{ms}$$

$$\frac{\tau_c}{\tau_p} \approx 139$$

With the plasma temperature evolution being over 139 times faster than the evolution of the cathode spot temperature, the first one will be the driving factor for the control. In the current applications, when it comes down trying to imprint a pulsed pattern in the plasma temperature, one hopes that the system will be following some periodic trajectory, without any particularly detailed control of the trajectory form and even less trying to compensate any deviation from some desired behaviour. The main reasons for this rather poor performance are on the one hand the impossibility of measuring the plasma core temperature at a rate close to kHz and on the other hand not having a simple enough control design which can be calculated fast enough. These two issues will be addressed in this chapter.

At first the central method, the flatness-based control, is introduced. Its application to the considered plasma system requires the finding of a so-called flat output, which fortunately is a simple task to perform ,for this simplified arc model. Additionally this flat output is easily measured and therefore it offers a viable path for designing the required observers, which are needed to reconstruct the plasma core temperature, without directly measuring it. The chapter concludes with the discussion of two different observers, both of them based on the existence of a flat output for the simplified dynamics, which are able to estimate the plasma core temperature.

Remark:
In the present work the characteristic length scale for the cathode temperature evolution was chosen to be z_c. However this only remains true for this one dimensional consideration, with a single cathode spot in the middle of the cathode, as initially stated in Section 2.3. A 2 dimensional formulation of that problem would lead to another important length scale, the radial extension of the cathode spot. The smallest extend of this length scale would be the cathode spot radius r_c (this would assume an instant cold boundary condition beyond this radial extend), which poses as a lower boundary condition.
The cathode spot radius r_c can be estimated in the following way section 4.3:

$$I_{arc} = \pi r_c^2 \left(j_{e,\,th} + j_{i,\,sp} \right)$$

$$r_c = \sqrt{\frac{I_{arc}}{\pi \left(A_R T_c^2 \exp\left(-\frac{e\Phi_c}{k_B T_c} \right) + e\, n_{e,\,\infty}(\overline{T}_p)\sqrt{\frac{k_B \overline{T}_p}{m_i}} \right)}}$$

The current I_{arc} along the plasma arc is also the electric current flowing across the cathode sheath and arriving at the cathode spot, which is given by the total current density $(j_{e,\,th} + j_{i,\,sp})$ times the spot area. The equilibrium solution for the cathode spot radius is initially derived from the input current of the steady state solution. The relation between the two characteristic length scales, the plasma bulk radius r_p and the cathode spot radius r_c is displayed in Figure 4.4.
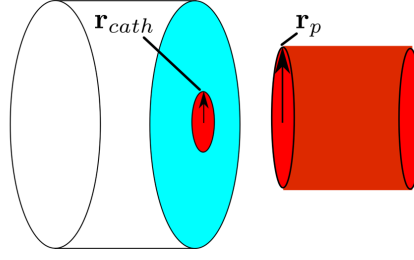
Figure 4.4: Schematic for the relation between the length scales of the cathode spot and the effective plasma core radius

Typically r_c lies in the order of less than $< 1\,\mathrm{mm}$. Recalculating the characteristic time scales (Equation (4.14)) with that value would lead to a relation $\frac{\tau_c}{\tau_p} \approx 8$. The initial remark that the plasma temperature evolution is the fastest driving mechanism off that coupled dynamics is still valid in this context. However the spot formation would have significantly more impact and would need to be included in the model based control. Still this is beyond the scope of this work, based on the initially stated operational conditions of the regarded thermal arcs, but should be memorized for future extension of the model.

4.3.1 Basic idea of flatness-based control

The main task addressed in this chapter is how to ensure the tracking of a desired trajectory by applying the technique of flatness-based control ([89], [88], § 2 and § 6). Even if the mathematical definition of flatness is quite abstract, the main idea behind it is simple. In general the system dynamics are described by n degrees of freedom (or state variables), collected together into a state vector with n components $\vec{x} = \begin{pmatrix} x_1 \\ \vdots \\ x_n \end{pmatrix}$ [1], and driven by a single input variable u. The system dynamics are described by the following system of n differential equations of 1st order (in general nonlinear)

$$\frac{d\vec{x}}{dt} \equiv \frac{d}{dt} \begin{pmatrix} x_1 \\ \vdots \\ x_n \end{pmatrix} = \begin{pmatrix} f_1(x_1, \ldots, x_n) \\ \vdots \\ f_n(x_1, \ldots, x_n) \end{pmatrix} + \begin{pmatrix} g_1(x_1, \ldots, x_n) \\ \vdots \\ g_n(x_1, \ldots, x_n) \end{pmatrix} u \equiv \vec{f}(\vec{x}) + \vec{g}(\vec{x})\, u \qquad (4.15)$$

The order of the system dynamics is therefore n. The restriction to a dynamic formulation which is linear in the input variable, i.e. equations of motion containing a term independent of u and a term directly proportional to u, is no oversimplification since the dynamics being considered for the plasma arc (either in the simplified form or in the more detailed one) displays this feature, where I_{arc}^2 is taken as the actual input.

An important definition for the following discussion is the *relative degree r* of an arbitrary dynamical variable y: it is the lowest time derivative applied on y, according to the dynamics eq. (4.15), for the input variable u to appear explicitly. Hence a relative degree of y equal to $r = 2$ means that both y as well as its first time derivative $\dot{y}$ do not explicitly contain u, this holds until the u occurs in the differential equation for $\ddot{y}$ as input variable. This also implies that through u one has access to the dynamics of y, which are of 2nd order. Clearly, if the system dynamics of order n (Equation (4.15))

---

[1] In the initial sections of this chapter the vector notation with the symbol ⃗ will be explicitly written in order to clearly separate which variables have several components and which variables are only a single scalar. Later in this chapter, when discussing the observers and there is no longer any possible confusion, such symbol will be dropped for keeping the notation simple.

describes the complete dynamics without leaving any degree of freedom "unattended", there is no variable with a relative degree strictly higher than n, since this would lead to the contradiction that an equation of motion of order higher than n is hidden inside the dynamics, which only has n degrees of freedom. Now if a single variable y can be found for this system (as many as input components in the dynamics), such that its relative degree equals the dynamics order n: $r = n$. This variable with full (=maximum) relative degree is called a **flat output** for the dynamics (Equation (4.15)) and will be denoted y_f from now on.

From its very definition, controlling the dynamics of the flat output means controlling the full system, without any degree of freedom being unmanaged. This holds even if it is a single output component and the dynamics displays a higher number of state variables. In other words, by forcing the flat output to follow some desired trajectory, each state component can no longer freely evolve but is also constrained to follow the flat output. Moreover, since the both flat output and the input have the same number of components (in this case only 1 component) the relation between both can be inverted by writing the input as some algebraic combination of the flat output and its derivatives until its relative degree is $r = n$. Also the full state vector can be analogously expressed as some algebraic combination of the flat output and its derivatives, this time only until the relative degree *minus* one is reached (since a further derivation would make the input appear). Therefore, if the desired trajectory for the flat output is given as some smooth function, the required input as well as the full state vector are completely determined by such trajectory, without the need to solve any system of differential equations, only algebraic operations. Additionally a state feedback can be easily designed for the input which converts the (originally nonlinear) output dynamics into an exact linear differential equation, without any kind of approximation, for which the usual methods of the Linear Control Theory can be applied to produce a stable trajectory tracking. This will be discussed in the following.

4.3.2 A more exact formulation of flatness

The just discussed shall be put into a more mathematical description. The time derivative of some arbitrary function $y(\vec{x})$ of the state variables $\vec{x}$ is according to the equations of motion (4.15)

$$\frac{dy}{dt} \equiv \dot{y} = \begin{pmatrix} \frac{\partial y}{\partial x_1} & \cdots & \frac{\partial y}{\partial x_n} \end{pmatrix} \begin{pmatrix} f_1 \\ \vdots \\ f_n \end{pmatrix} + \begin{pmatrix} \frac{\partial y}{\partial x_1} & \cdots & \frac{\partial y}{\partial x_n} \end{pmatrix} \begin{pmatrix} g_1 \\ \vdots \\ g_n \end{pmatrix} u = \frac{\partial y}{\partial \vec{x}} \cdot \vec{f} + \frac{\partial y}{\partial \vec{x}} \cdot \vec{g}\, u \qquad (4.16)$$

, which can be written in a more compact way by introducing the Lie (or directional) derivative of any scalar function y along the direction of a vector function $\vec{v}(\vec{x})$ as the projection (or scalar product) of the gradient $\frac{\partial y}{\partial \vec{x}}$ along such direction $\vec{v}$

$$L_{\vec{v}}\, y \stackrel{\text{def}}{=} \begin{pmatrix} \frac{\partial y}{\partial x_1} & \cdots & \frac{\partial y}{\partial x_n} \end{pmatrix} \begin{pmatrix} v_1 \\ \vdots \\ v_n \end{pmatrix} = \frac{\partial y}{\partial \vec{x}} \cdot \vec{v} \qquad (4.17)$$

In an analogous way the second Lie derivative of a scalar function y first along $\vec{v}$ and subsequently along $\vec{w}$ is

$$L_{\vec{w}} L_{\vec{v}}\, y = \left(\frac{\partial}{\partial \vec{x}} L_{\vec{v}} h \right) \cdot \vec{w} \qquad (4.18)$$

and in compact notation $L_{\vec{v}} L_{\vec{v}}\, y = L_{\vec{v}}^2 y$. Hence the task of finding a single variable $y_f(t) = h(\vec{x})$ which does not contain explicitly the input u and simultaneously have full relative degree $r = n$ corresponds to satisfying the following n conditions

$$\frac{dy_f}{dt} = \frac{\partial h}{\partial \vec{x}} \cdot \vec{f} + \frac{\partial h}{\partial \vec{x}} \cdot \vec{g}\, u = L_{\vec{f}}h + \overbrace{L_{\vec{g}}h}^{=0}\, u = L_{\vec{f}}h \qquad \text{(no } u \text{ contained explicitly)}$$

$$\frac{d^2 y_f}{dt^2} = \left(\frac{\partial}{\partial \vec{x}} L_{\vec{f}}h\right) \cdot \vec{f} + \left(\frac{\partial}{\partial \vec{x}} L_{\vec{f}}h\right) \cdot \vec{g} = L_{\vec{f}}L_{\vec{f}}h + \overbrace{L_{\vec{g}}L_{\vec{f}}h}^{=0}\, u = L_{\vec{f}}^2 h \qquad \text{(no } u \text{ contained explicitly)}$$

$$\vdots \qquad \vdots \qquad\qquad \vdots \qquad\qquad\qquad \text{(no } u \text{ contained explicitly)}$$

$$\frac{d^{n-1} y_f}{dt^{n-1}} = \overbrace{L_{\vec{f}} \cdots L_{\vec{f}}}^{(n-1)\text{-times}} h + \underbrace{L_{\vec{g}} \overbrace{L_{\vec{f}} \cdots L_{\vec{f}}}^{(n-2)\text{-times}} h}_{=0}\, u = L_{\vec{f}}^{n-1}h \qquad \text{(no } u \text{ contained explicitly)}$$

$$\frac{d^n y_f}{dt^n} = \overbrace{L_{\vec{f}} \cdots L_{\vec{f}}}^{n\text{-times}} h + \underbrace{L_{\vec{g}} \overbrace{L_{\vec{f}} \cdots L_{\vec{f}}}^{(n-1)\text{-times}} h}_{\neq 0}\, u = L_{\vec{f}}^n h + \underbrace{\left(L_{\vec{g}}L_{\vec{f}}^{n-1}h\right)}_{\neq 0} u \qquad (\underline{\text{does}} \text{ explicitly contain } u) \quad (4.19)$$

or equivalently to solving the following n differential equations

$$L_{\vec{g}}h = 0$$
$$L_{\vec{g}}L_{\vec{f}}h = 0$$
$$\vdots \qquad \vdots$$
$$L_{\vec{g}}L_{\vec{f}}^{n-2}h = 0$$
$$L_{\vec{g}}L_{\vec{f}}^{n-1}h \neq 0 \qquad\qquad (4.20)$$

Before even trying to solve the previous system of equations, where each subsequent equation contains an increasing number of Lie derivatives, the first 2 equations shall be combined in the following way. From $L_{\vec{g}}h = 0$ it trivially follows that $L_{\vec{f}}L_{\vec{g}}h = 0$, which together with the second equation $L_{\vec{g}}L_{\vec{f}}h = 0$ leads to the following combination of 2 consecutive Lie derivatives

$$\left[L_{\vec{f}}L_{\vec{g}} - L_{\vec{g}}L_{\vec{f}}\right] y = \sum_{i=1}^{n} f_i \frac{\partial}{\partial x_i}\left(\sum_{j=1}^{n} g_j \frac{\partial y}{\partial x_j}\right) - \sum_{i=1}^{n} g_i \frac{\partial}{\partial x_i}\left(\sum_{j=1}^{n} f_j \frac{\partial y}{\partial x_j}\right)$$

$$= \sum_{j=1}^{n} \underbrace{\left[\sum_{i=1}^{n} \frac{\partial g_j}{\partial x_i} f_i - \sum_{i=1}^{n} \frac{\partial f_j}{\partial x_i} g_i\right]}_{\text{vector with components } w_j} \frac{\partial y}{\partial x_j} \equiv L_{\vec{w}}y \qquad (4.21)$$

This can be written as a single Lie derivative along the new direction defined by $\vec{w}$. Such a direction is called the Lie bracket (of 1st order, see [88], § 2) of the direction $\vec{f}$ with the direction $\vec{g}$ [2]

$$\mathrm{ad}_{\vec{f}}\vec{g} \equiv \mathrm{ad}_{\vec{f}}^1 \vec{g} \equiv \left[\vec{f}, \vec{g}\right] = \begin{pmatrix} \frac{\partial g_1}{\partial x_1} & \vdots & \frac{\partial g_1}{\partial x_n} \\ \vdots & \ddots & \vdots \\ \frac{\partial g_n}{\partial x_1} & \vdots & \frac{\partial g_n}{\partial x_n} \end{pmatrix} \begin{pmatrix} f_1 \\ \vdots \\ f_n \end{pmatrix} - \begin{pmatrix} \frac{\partial f_1}{\partial x_1} & \vdots & \frac{\partial f_1}{\partial x_n} \\ \vdots & \ddots & \vdots \\ \frac{\partial f_n}{\partial x_1} & \vdots & \frac{\partial f_n}{\partial x_n} \end{pmatrix} \begin{pmatrix} g_1 \\ \vdots \\ g_n \end{pmatrix} \qquad (4.22)$$

---

[2] A Lie bracket is a vector, in contrast to the Lie derivative which yiels a scalar.

This can be generalized to combinations of a higher number of Lie derivatives

$$\mathrm{ad}_{\vec{f}}^2 \vec{g} = \mathrm{ad}_{\vec{f}} \mathrm{ad}_{\vec{f}} \vec{g} = \left[\vec{f}, \mathrm{ad}_{\vec{f}} \vec{g}\right] = \left[\vec{f}, \left[\vec{f}, \vec{g}\right]\right]$$

$$= \begin{pmatrix} \frac{\partial\left(\mathrm{ad}_{\vec{f}} \vec{g}\right)_1}{\partial x_1} & \vdots & \frac{\partial\left(\mathrm{ad}_{\vec{f}} \vec{g}\right)_1}{\partial x_n} \\ \vdots & \ddots & \vdots \\ \frac{\partial\left(\mathrm{ad}_{\vec{f}} \vec{g}\right)_n}{\partial x_1} & \vdots & \frac{\partial\left(\mathrm{ad}_{\vec{f}} \vec{g}\right)_n}{\partial x_n} \end{pmatrix} \begin{pmatrix} f_1 \\ \vdots \\ f_n \end{pmatrix} - \begin{pmatrix} \frac{\partial f_1}{\partial x_1} & \vdots & \frac{\partial f_1}{\partial x_n} \\ \vdots & \ddots & \vdots \\ \frac{\partial f_n}{\partial x_1} & \vdots & \frac{\partial f_n}{\partial x_n} \end{pmatrix} \begin{pmatrix} \left(\mathrm{ad}_{\vec{f}} \vec{g}\right)_1 \\ \vdots \\ \left(\mathrm{ad}_{\vec{f}} \vec{g}\right)_n \end{pmatrix} \tag{4.23}$$

$$\mathrm{ad}_{\vec{f}}^3 \vec{g} = \left[\vec{f}, \mathrm{ad}_{\vec{f}}^2 \vec{g}\right]$$

and so on. Together with the notation $\mathrm{ad}_{\vec{f}}^0 \vec{g} \equiv \vec{g}$. Finally the system of n differential equations Equation (4.20) to be solved for obtaining a flat output is equivalent to a new system of n equations, this time formulated by means of only single Lie derivatives

$$L_{\vec{g}} h = 0 \qquad\qquad \implies \qquad L_{\mathrm{ad}_{\vec{f}}^0 \vec{g}} h = 0$$

$$L_{\vec{g}} L_{\vec{f}} h = 0 \qquad\qquad \overset{\text{combined with}}{\underset{\text{previous equation}}{\implies}} \qquad L_{\mathrm{ad}_{\vec{f}}^1 \vec{g}} h = 0$$

$$\vdots \qquad \vdots$$

$$L_{\vec{g}} \overbrace{L_{\vec{f}} \cdots L_{\vec{f}}}^{(n-2)\text{-times}} h = 0 \qquad \overset{\text{combined with}}{\underset{\text{previous equations}}{\implies}} \qquad L_{\mathrm{ad}_{\vec{f}}^{n-2} \vec{g}} h = 0$$

$$L_{\vec{g}} \overbrace{L_{\vec{f}} \cdots L_{\vec{f}}}^{(n-1)\text{-times}} h \neq 0 \qquad \overset{\text{combined with}}{\underset{\text{previous equations}}{\implies}} \qquad L_{\mathrm{ad}_{\vec{f}}^{n-1} \vec{g}} h \neq 0 \tag{4.24}$$

According to the Frobenius theorem (see [90], §1 and [88], §2) the existence of a solution for the previous equation system is determined by two necessary conditions to be satisfied:

- The system dynamics takes place in a n-dimensional space and per definition the flat output dynamics must cover the full dimensionality of the system dynamics, so the n directions of the Lie brackets $\left\{\mathrm{ad}_{\vec{f}}^0 \vec{g}, \mathrm{ad}_{\vec{f}}^1 \vec{g}, \ldots, \mathrm{ad}_{\vec{f}}^{n-1} \vec{g}\right\}$, defining the solution for the flat output, must cover n different dimensions and thus be linearly independent. Otherwise, if two of these Lie bracket directions were parallel to each other, one of the conditions in Equation (4.24) would be superfluous and the flat output will be not determined by all the n dimensions of the original system dynamics.

  This condition can be equivalently reformulated as follows: the quadratic matrix constructed column-wise with the n directions defined by the Lie brackets

$$\mathcal{C} = \left(\begin{array}{c|c|c|c} \mathrm{ad}_{\vec{f}}^0 \vec{g} & \mathrm{ad}_{\vec{f}}^1 \vec{g} & \ldots & \mathrm{ad}_{\vec{f}}^{n-1} \vec{g} \end{array} \right) \tag{4.25}$$

  must be invertible (or regular). This matrix $\mathcal{C}$ is called the *controllability matrix* of the system dynamics Equation (4.15).

- The previous condition is in general not sufficient, and an additional constraint must still be satisfied for a flat output to exist: according to Equation (4.24) the last direction $\mathrm{ad}_{\vec{f}}^{n-1} \vec{g}$ has been singled out for the coupling with the input u to occur, and thus the additional condition applies only on the remaining $(n-1)$ directions $\left\{\mathrm{ad}_{\vec{f}}^0 \vec{g}, \mathrm{ad}_{\vec{f}}^1 \vec{g}, \ldots, \mathrm{ad}_{\vec{f}}^{n-2} \vec{g}\right\}$, which have to be involutive [3]. In other words, any Lie bracket calculated from these $(n-1)$ directions can be expressed as a linear combination of just $(n-1)$ directions, without any contribution of the singled out direction $\mathrm{ad}_{\vec{f}}^{n-1} \vec{g}$. The meaning of this second condition will not be discussed here

---

[3] In general terms for a function to be involutive, it must be its own inverse $f(f(x)) = x$, for all values of x [91]

since for the simplified plasma dynamics used for the control design such involutivity condition is trivially satisfied. The simplified dynamics is of order $n = 2$ and thus the involutivity condition must be satisfied by only one direction, $\left\{ \text{ad}_{\vec{f}}^0 \vec{g} \equiv \vec{g} \right\}$, which is immediately involutive since the Lie bracket of $\vec{g}$ with itself identically vanishes (due to its very definition, see Equation (4.22)) and zero is always a linear combination of any direction. A more detailed discussion in this context can be found in [92] and for the general discussion in [88], § 2.

Once it has been proven that a flat output exists for a given system dynamics, the n equations (4.24) have to be solved, which only can be performed analytically for a low order n. If such a solution could be found, that would create some advantages:

- first of all the flat output dynamics, in general nonlinear, can be exactly transformed into a linear differential equation by means of the following simple state feedback (see [88], § 9 and [93], § 13)

$$u = u(\vec{x}) = \frac{1}{L_{\vec{g}} L_{\vec{f}}^{n-1} h} \left[-L_{\vec{f}}^n h + v(t) \right] \quad \Longrightarrow \quad \frac{d^n y_f}{dt^n} = v(t) \tag{4.26}$$

where the denominator $L_{\vec{g}} L_{\vec{f}}^{n-1} y_f$ never vanishes due to the very definition of the flat output as a variable with full ($r = n$) relative degree (see Equation (4.19)). $v(t)$ in the previous equation is a free part in the input, still to be determined.

- in a second step the free $v(t)$ can be designed in order to ensure that the system tracks a given desired trajectory for the output variable $y_f^*(t)$, this time using the common techniques of the Linear Control Theory

$$v(t) = \frac{d^n y_f^*}{dt^n} - c_{n-1} \left(\overbrace{\frac{d^{n-1} y_f}{dt^{n-1}}}^{L_{\vec{f}}^{n-1} y_f} - \frac{d^{n-1} y_f^*}{dt^{n-1}} \right) - \ldots - c_1 \left(\overbrace{\frac{dy_f}{dt}}^{L_{\vec{f}} y_f} - \frac{dy_f^*}{dt} \right) - c_0 \left(y_f - y_f^* \right) \tag{4.27}$$

Both points leading to the following formulation for the control output (Equation (4.28)):

$$u = \frac{1}{L_{\vec{g}} L_{\vec{f}}^{n-1} y_f} \left[-L_{\vec{f}}^n y_f + \frac{d^n y_f^*}{dt^n} \right.$$

$$\left. - c_{n-1} \left(L_{\vec{f}}^{n-1} y_f - \frac{d^{n-1} y_f^*}{dt^{n-1}} \right) - \ldots - c_1 \left(L_{\vec{f}} y_f - \frac{dy_f^*}{dt} \right) - c_0 \left(y_f - y_f^* \right) \right] \tag{4.28}$$

where $y_f^*(t)$ is given, fully known, for instance as a smooth function or polynomial, and therefore all its time derivatives appearing in u are completely determined. In the previous equation constant coefficients c_0, c_1, ..., c_{n-1} are to be chosen in such a way that the error between the actual output and the desired output y_f^* ($e_y = y_f - y_f^*$) decays asymptotically with time, since after applying eq. (4.27) the error dynamics of the respective system is described by the following linear differential equation

$$\frac{d^n y_f}{dt^n} = v(t) \quad \Longrightarrow \quad \frac{d^n e_y}{dt^n} + c_{n-1} \frac{d^{n-1} e_y}{dt^{n-1}} + \ldots + c_1 \frac{de_y}{dt} + c_0 e_y = 0$$

characterisitic polynomial: $\quad p(s) = s^n + c_{n-1} s^{n-1} + \ldots + c_1 s + c_0$ (4.29)

The constants c_0, c_1, ..., c_{n-1} must be selected such that all the eigenvalues $\tilde{\lambda}_i$ of the previous characteristic polynomial have a strictly negative real part, such that the error e_y evolves as $e_y(t) \sim e^{\tilde{\lambda}_i t}$ [94]. It is worth mentioning that all the required Lie derivatives $\left\{ L_{\vec{f}} y_f(\vec{x}), \ldots, L_{\vec{f}}^n y_f(\vec{x}), L_{\vec{g}} L_{\vec{f}}^{n-1} y_f(\vec{x}) \right\}$ (as

well as $y_f = h(\vec{x})$) for determining the input u , to implement the stable trajectory tracking are functions of the state variables (but not of the input u itself). Thus the control law (Equation (4.28)) is actually a state feedback, which of course precises full knowledge of all the state variables, this is an issue still to be addressed in the following.

Until now it has been discussed how having a flat output leads easily to the design of a stable tracking of a desired trajectory, written as a purely algebraic expression. This is not the only advantage of a flat output: also the full state can be "extracted" from the information "contained" into the flat output (and its derivatives), without integrating any differential equation. Returning back to the system of equations (Equation (4.19)) the n-th time derivative of the flat output contains the input u; but the other n scalar functions $\left\{ y_f = h(\vec{x}), \dfrac{dy_f}{dt} = L_{\vec{f}} h(\vec{x}), \ldots, \dfrac{d^{n-1} y_f}{dt^{n-1}} = L_{\vec{f}}^{n-1} h(\vec{x}) \right\}$ are not coupled explicitly to the input. Since n is also the number of components in the state vector $\vec{x}$, it must be possible to transform and reverse the transform (at least locally) of the n coordinates between both representations

$$\text{original coordinates: } \vec{x} = \begin{pmatrix} x_1 \\ x_2 \\ \vdots \\ x_n \end{pmatrix} \longleftrightarrow \text{ new coord.: } \vec{z} = \begin{pmatrix} z_1 = y_f = h(\vec{x}) \\ z_2 = \frac{dy_f}{dt} = L_{\vec{f}} h(\vec{x}) \\ \vdots \\ z_n = \frac{d^{n-1} y_f}{dt^{n-1}} = L_{\vec{f}}^{n-1} h(\vec{x}) \end{pmatrix}, \qquad (4.30)$$

because all components in $\vec{z}$ are independent of each other (since the differential equation for the flat output is of order n). Hence if at some location $\vec{z}$ (and its correponding $\vec{x}$) is known (for instance at the initial state) and now $\vec{z}$ changes by some known infinitesimal $d\vec{z}$, the corresponding change $d\vec{x}$ displayed in the original coordinates for getting the new $\vec{x}$ is given by

$$\vec{z} + d\vec{z} = \vec{z}(\vec{x} + d\vec{x}) = \vec{z} + \left(\frac{\partial \vec{z}}{\partial \vec{x}} \right)_{\big| \vec{x}} d\vec{x} \quad \Longrightarrow \quad d\vec{x} = \left[\left(\frac{\partial \vec{z}}{\partial \vec{x}} \right)_{\big| \vec{x}} \right]^{-1} d\vec{z}.$$

The inversion between both coordinates (mathematically such invertible coordinate transformation is called a local diffeomorphism) is guaranteed since the quadratic matrix constructed row-wise with the gradients of the n scalar functions $\left\{ y_f = h(\vec{x}), \dfrac{dy_f}{dt} = L_{\vec{f}} h(\vec{x}), \ldots, \dfrac{d^{n-1} y_f}{dt^{n-1}} = L_{\vec{f}}^{n-1} h(\vec{x}) \right\}$

$$\mathcal{O} = \begin{pmatrix} \frac{\partial}{\partial \vec{x}} h \\ \hline \frac{\partial}{\partial \vec{x}} L_{\vec{f}} h \\ \hline \vdots \\ \hline \frac{\partial}{\partial \vec{x}} L_{\vec{f}}^{n-1} h \end{pmatrix}, \qquad (4.31)$$

must be a regular matrix when y_f is a flat output: in such a case the original $\vec{x}$ can be reconstructed from $\vec{z}$, i.e., can be extracted from the flat output and its time derivatives to the order $(n-1)$. This matrix $\mathcal{O}$ is called the *observability matrix* of the system dynamics (Equation (4.15)) for the output $y_f = h(\vec{x})$.

4.3.3 Derive a flat output for the simplified dynamics of the combined plasma arc and cathode spot dynamics

The tracking of a desired trajectory in the case of the simplified dynamics developed in the previous chapter, described by a 2-dimensional state vector $\vec{x} = \begin{pmatrix} x_1 = T_c \\ x_2 = T_p \end{pmatrix}$ is considered. The dynamics evolve in time according to the following 2 highly nonlinear equations of motion (Equation (4.13))

$$\frac{dx_1}{dt} = -\frac{\lambda_{th,\,c}}{\rho_c c_{p,\,c}\, z_c^2}\,(x_1 - T_0) - \frac{\varepsilon_c \sigma_{SB}}{\rho_c c_{p,\,c}\, z_c}\, x_1^4$$

$$+ \frac{1}{\rho_c c_{p,\,c}\, z_c}\left(A_R x_1^2 \exp\left(-\frac{e\Phi_c}{k_B x_1}\right) + e n_{e,\,\infty}(x_2)\sqrt{\frac{k_B x_2}{m_i}}\right) \times$$

$$\times \left(\frac{E_{ion}}{e}\, \frac{e n_{e,\,\infty}(x_2)\sqrt{\frac{k_B x_2}{m_i}}}{A_R x_1^2 \exp\left(-\frac{e\Phi_c}{k_B x_1}\right)} - \Phi_c \right)$$

$$\equiv f_1(x_1, x_2)\,,$$

$$n_{e,\,\infty}(x_2) = -K_{saha}(x_2) + \sqrt{(K_{saha}(x_2))^2 + \frac{P}{k_B x_2} K_{saha}(x_2)}\,,$$

$$K_{saha}(x_2) = \frac{2 Z_{A^+}(x_2)}{Z_A(x_2)}\left(\frac{2\pi m_e k_B x_2}{h^2}\right)^{3/2} \exp\left(-\frac{E_{ion}}{k_B x_2}\right)\,,$$

$$\frac{dx_2}{dt} = -\frac{2\lambda_{th,\,p}((x_2 + T_0)/2)}{\rho_p(x_2) c_{p,\,p}(x_2)\, (r_p(x_2))^2 \left(\frac{r_0}{r_p} - 1\right)}\,(x_2 - T_0) + \frac{1}{\pi^2 \sigma_{el}(x_2)\rho_p(x_2) c_{p,\,p}(x_2)\, (r_p(x_2))^4}\,\overbrace{I_{arc}^2}^{u}$$

$$\equiv f_2(x_2)) + g_2(x_2)\, u\,,$$

$$\frac{d\vec{x}}{dt} = \frac{d}{dt}\begin{pmatrix} x_1 \\ x_2 \end{pmatrix} = \underbrace{\begin{pmatrix} f_1(x_1, x_2) \\ f_2(x_2) \end{pmatrix}}_{\vec{f}(\vec{x})} + \underbrace{\begin{pmatrix} 0 \\ g_2(x_2) \end{pmatrix}}_{\vec{g}(\vec{x})} u\,. \tag{4.32}$$

This nonlinear dynamics of 2nd order driven by input $u = I_{arc}^2$ has a flat output since the controllability condition is satisfied

$$\mathrm{ad}_f^0 \vec{g} \equiv \vec{g} = \begin{pmatrix} 0 \\ g_2(x_2) \end{pmatrix}, \quad \mathrm{ad}_f^1 \vec{g} = \begin{pmatrix} 0 & 0 \\ 0 & \frac{\partial g_2}{\partial x_2} \end{pmatrix}\begin{pmatrix} f_1(x_1, x_2) \\ f_2(x_2) \end{pmatrix} - \begin{pmatrix} \frac{\partial f_1}{\partial x_1} & \frac{\partial f_1}{\partial x_2} \\ 0 & \frac{\partial f_2}{\partial x_2} \end{pmatrix}\begin{pmatrix} 0 \\ g_2(x_2) \end{pmatrix} = \begin{pmatrix} \frac{\partial f_1}{\partial x_2} g_2 \\ \frac{\partial g_2}{\partial x_2} f_2 - \frac{\partial f_2}{\partial x_2} g_2 \end{pmatrix}$$

$$\mathcal{C} = \begin{pmatrix} 0 & \frac{\partial f_1}{\partial x_2} g_2 \\ g_2 & \frac{\partial g_2}{\partial x_2} f_2 - \frac{\partial f_2}{\partial x_2} g_2 \end{pmatrix} \tag{4.33}$$

because matrix $\mathcal{C}$ is invertible (its determinant doesn't vanish) as soon as following condition holds

$$\frac{\partial f_1}{\partial x_2} g_2 \neq 0 \quad \overset{g_2 \neq 0}{\Longleftrightarrow} \quad \frac{\partial f_1}{\partial x_2} \neq 0\,. \tag{4.34}$$

According to the discussion in Equation (4.24) a flat output candidate for the considered simplified dynamics results from the 2 differential equations

$$L_{\mathrm{ad}_f^0 \vec{g}} h = g_2 \frac{\partial h}{\partial x_2} = 0 \quad \Longrightarrow \quad \frac{\partial h}{\partial x_2} = 0\,,\; h \text{ is independent of } x_2\,,$$

$$L_{\mathrm{ad}_f^1 \vec{g}} h = \frac{\partial f_1}{\partial x_2} g_2 \frac{\partial h}{\partial x_1} + \left(\frac{\partial g_2}{\partial x_2} f_2 - \frac{\partial f_2}{\partial x_2} g_2 \right) \underbrace{\frac{\partial h}{\partial x_2}}_{=0 \text{ (previous eq.)}} \neq 0\,, \tag{4.35}$$

which can immediately be solved: $y_f = h(x_1, x_2) = x_1$ (or any smooth function of x_1).

$$\frac{dy_f}{dt} = f_1(x_1, x_2),$$

$$\frac{d^2 y_f}{dt^2} = \underbrace{\frac{\partial f_1}{\partial x_1} f_1(x_1, x_2) + \frac{\partial f_1}{\partial x_2} f_2(x_2)}_{L_{\tilde{f}}^2 y_h} + \underbrace{\frac{\partial f_1}{\partial x_2} g_2(x_2)}_{L_{\tilde{g}} L_{\tilde{f}} y_h} \overset{\Downarrow}{u}. \tag{4.36}$$

The same result can be directly obtained by noticing that $y_f = T_c = x_1$ does not explicitly display the input variable (marked by an arrow) to its 2nd time derivative Equation (4.36), since the coupling to the input is mediated by the factor $\dfrac{\partial f_1}{\partial x_2} g_2$, y_f is a flat output when this factor does not vanish, as already obtained from the controllability condition, see Equation (4.34). Three tasks remain to be performed before the discussion of the flatness-based control for the simplified dynamics is fully concluded:

1. What are the constraints for the controllability condition $\dfrac{\partial f_1}{\partial x_2} \neq 0$ to hold and thus $T_c(t)$ to be a flat output for the simplified dynamics.

2. The control law for achieving the tracking of some desired trajectory of the flat output.

3. How to derive the flat output trajectory for the corresponding desired behavior of the plasma core temperature, the latter being ultimately which has to be implemented for the plasma process.

The controllability condition For the simplified dynamics the condition (Equation (4.34)) is unfortunately not always satisfied. The reason is the density of free electrons in plasma core not being a monotonic increasing function of the plasma temperature x_2, since $n_{e,\infty}$ initially increases during the ionization process but once the gas is nearly fully ionized, the electron density (being equal to the ion density) is given by $\dfrac{P}{2k_B x_2}$ and thus decreases with x_2. This effect makes $\dfrac{\partial f_1}{\partial x_2}$ change its sign and thus go through a zero.

$$\frac{\partial f_1}{\partial x_2} = \frac{1}{\rho_c c_{p,c} z_c} \left((U_s - \Phi_c) \frac{dj_{ion}}{dT_p} + (j_{ee} + j_{ion}) \frac{dU_s}{dT_p} \right)$$

$$\frac{dj_{ion}}{dT_p} = j_{ion} \left(\frac{1}{n_e} \frac{dn_{e,\infty}}{dT_p} + \frac{1}{2T_p} \right) \tag{4.37}$$

$$\frac{dU_s}{dT_p} = \frac{E_{ion}}{e j_{ee}} \frac{dj_{ion}}{dT_p}$$

The derivative of the electron density over the plasma temperature $\frac{dn_{e,\infty}}{dT_p}$ is numerically calculated through the relation given in Equation (2.27). For an argon plasma at atmospheric pressure, where the ionization energy and the energy levels required for solving the Saha-Eggert eq. (2.24) and $n_{e,\infty}$ Equation (2.25) are taken from [68]. The temperature dependence of $\dfrac{\partial f_1}{\partial x_2}$ is displayed in Figure 4.5. The controllability is ensured as long as

$$\overline{T}_p < \overline{T}_{p\,crit} = 18800 \text{ K} \quad (\text{Ar at } P = 1 \text{ bar}) \tag{4.38}$$

Only trajectories satisfying such condition can be implemented with the flatness-based control developed in the following discussion. Below this "critical" temperature the sign of $\dfrac{\partial f_1}{\partial x_2}$ is well-defined and positive.

Trajectory tracking control The tracking control can be easily calculated. For a desired trajectory for the cathode spot temperature $T_c^*(t)$ (* denotes the desired behavior, not the complex conjugate) and by combining Equation (4.36) with the general discussion in Equation (4.28) the following state feedback is obtained

$$I_{arc}^2 = u(x_1, x_2) = \frac{1}{\dfrac{\partial f_1}{\partial x_2} g_2} \left[-\left(\frac{\partial f_1}{\partial x_1} f_1 + \frac{\partial f_1}{\partial x_2} f_2 \right) + \frac{d^2 T_c^*}{dt^2} - c_1 \left(f_1 - \frac{dT_c^*}{dt} \right) - c_0 \left(x_1 - T_c^* \right) \right], \tag{4.39}$$

$$\frac{\partial f_1}{\partial x_1} = -\frac{\lambda_{th,c}}{\rho_c c_{p,c} z_c^2} - 4 \frac{\varepsilon_c \sigma_{SB}}{\rho_c c_{p,c} z_c} x_1^3$$

$$\quad - \frac{1}{\rho_c c_{p,c} z_c} \frac{A_R x_1^2 \exp\left(-\frac{e\Phi_c}{k_B x_1}\right)}{x_1} \left(2 + \frac{e\Phi_c}{k_B x_1} \right) \left(\frac{E_{ion}}{e} \left(\frac{e n_{e,\infty} \sqrt{\frac{k_B x_2}{m_i}}}{A_R x_1^2 \exp\left(-\frac{e\Phi_c}{k_B x_1}\right)} \right)^2 + \Phi_c \right)$$

$$\frac{\partial f_1}{\partial x_1} < 0 \,,$$

$$\frac{\partial f_1}{\partial x_2} = \frac{1}{\rho_c c_{p,c} z_c} \frac{e n_{e,\infty} \sqrt{\frac{k_B x_2}{m_i}}}{x_2} \left(\frac{-n_{e,\infty} \left(2 + \frac{E_{ion}}{k_B x_2} \right) + \frac{P}{2 k_B x_2} \left(\frac{3}{2} + \frac{E_{ion}}{k_B x_2} \right)}{\frac{P}{k_B x_2} - n_{e,\infty}} \right) \times$$

$$\quad \times \left(\frac{E_{ion}}{e} \left(2 \frac{e n_{e,\infty} \sqrt{\frac{k_B x_2}{m_i}}}{A_R x_1^2 \exp\left(-\frac{e\Phi_c}{k_B x_1}\right)} + 1 \right) - \Phi_c \right)$$

$$\frac{\partial f_1}{\partial x_2} > 0 \quad \text{for } \overline{T}_p < \overline{T}_{p,crit}, \text{ see eq. (4.38)} \tag{4.40}$$
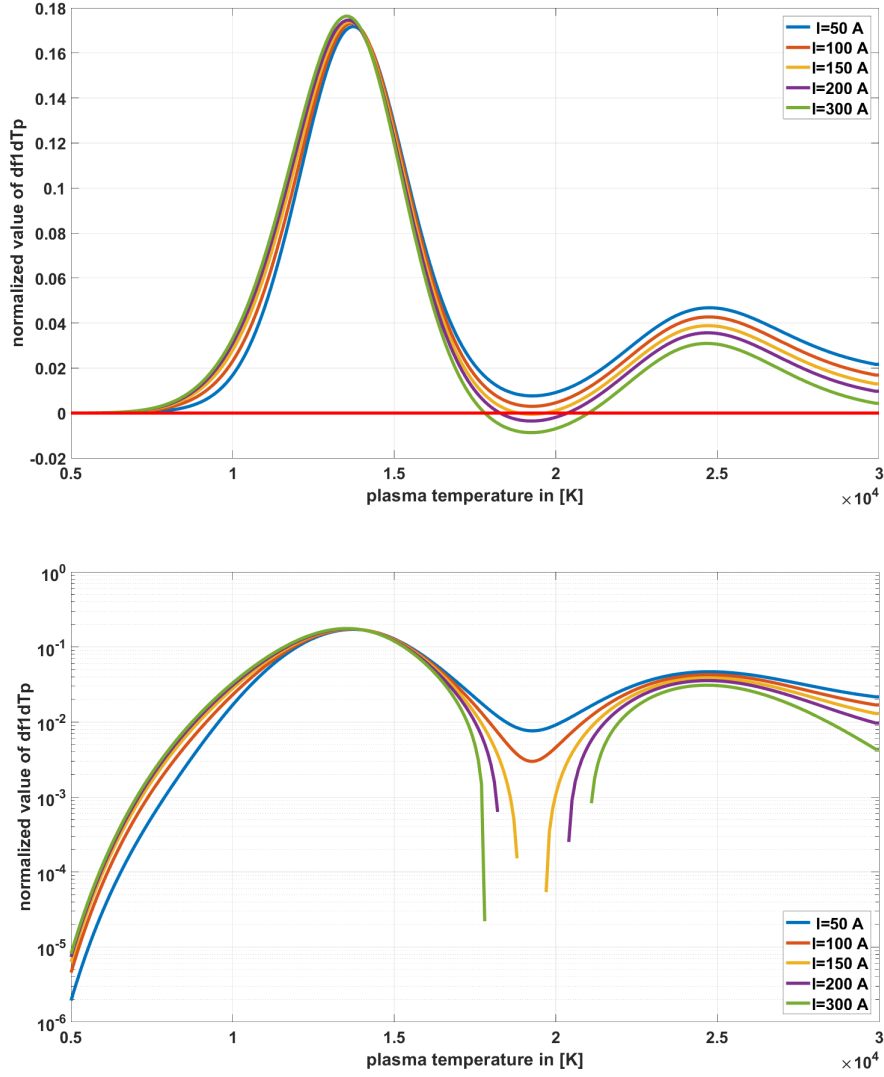
Figure 4.5: Evolution of $\dfrac{\partial f_1}{\partial x_2}$ with plasma core temperature $\hat{T}_p$ for an argon plasma at atmospheric pressure. The upper graphic showing the linear scaling to display the overall behaviour of the parameter and the lower graphic displaying the discontinuity where the parameter goes through zero and becomes negative.

After applying this control law the resulting dynamics for the error in the cathode spot temperature, $e_{control} = T_c - T_c^*$, is linear and of 2nd order

$$\ddot{e}_{control} + c_1\,\dot{e}_{control} + c_0\,e_{control} = 0\,. \tag{4.41}$$

The two eigenvalues $\tilde{\lambda}_{1/2}$ of the characteristic polynomial to the previous linear differential equation

$$\tilde{\lambda}_{1/2} = -\frac{c_1}{2} \pm \sqrt{\left(\frac{c_1}{2}\right)^2 - c_0}$$

determine the error time evolution as $e_{control}(t) \sim e^{\tilde{\lambda}_{1/2}t}$. For $c_1,\,c_0 > 0$ these two eigenvalues are either both real and negative, if $\left(\dfrac{c_1}{2}\right)^2 - c_0 \geq 0$, or complex conjugated to each other with a negative real part,

if $\left(\frac{c_1}{2}\right)^2 - c_0 < 0$. In both cases the asymptotic stability of the trajectory tracking is guaranteed [94]; $e_{control}(t) \xrightarrow{t \to \infty} 0$. For the choice of a complex conjugated pair, the eigenvalues can be rewritten as $\tilde{\lambda}_{1/2} = -\frac{\tilde{d}}{\tilde{\tau}_{control}} \pm i \frac{\sqrt{1 - \tilde{d}^2}}{\tilde{\tau}_{control}}$, with $0 < \tilde{d} \leq 1$ (the so-called damping factor) and $\tilde{\tau}_{control} > 0$ the characteristic time scale for the error decay; $i = \sqrt{-1}$. This corresponds to $c_0 = \frac{1}{\tilde{\tau}_{control}^2}$ and $c_1 = \frac{\tilde{d}}{\tilde{\tau}_{control}}$, both of them strictly positive, and the resulting state feedback Equation (4.39) becomes

$$I_{arc}^2 = u(x_1, x_2) = \frac{1}{\frac{\partial f_1}{\partial x_2} g_2} \left[-\left(\frac{\partial f_1}{\partial x_1} f_1 + \frac{\partial f_1}{\partial x_2} f_2 \right) + \frac{d^2 T_c^*}{dt^2} - \frac{\tilde{d}}{\tilde{\tau}_{control}} \left(f_1 - \frac{dT_c^*}{dt} \right) - \frac{1}{\tilde{\tau}_{control}^2} (x_1 - T_c^*) \right]$$

(4.42)

Calculation of desired trajectory $T_c^*(t)$ In practical applications not the cathode spot temperature, but rather the internal plasma temperature is the actual variable of interest. Let us assume the system should follow a desired time-dependent pattern in the plasma core temperature $\overline{T}_p^*(t)$. This pattern shall always kept below the "critical" plasma core temperature Equation (4.38) to guarantee the controllability of the simplified dynamics. The corresponding trajectory in the cathode spot temperature is obtained by an iterative, numerical integration of the equation of motion for T_c:

- The time interval of the trajectory is discretized in time steps of equal duration Δt, with $T_c(t)$ denoting the actual (and known) value of the cathode spot temperature and $T_c(t + \Delta t)$ the value at the next time step which has to be calculated.

- From a provisional estimation for the next time step $T_c^{(prov)}(t + \Delta t)$ an improved solution $T_c(t + \Delta t)$ is calculated by using Equation (2.61), now with the desired (known) $\overline{T}_p^*$ in place of $\overline{T}_p^{(prov)}$

$$T_c(t + \Delta t) \left[1 + \frac{\Delta t \lambda_{th,c}}{z_c^2 \rho_c c_{p,c}} + \frac{\Delta t \varepsilon_c \sigma_{SB}}{\rho_c c_{p,c} z_c} \left(T_c^{(prov)}(t + \Delta t) \right)^3 \right.$$

$$+ \frac{\Delta t}{z_c \rho_c c_{p,c}} \left(A_R \left(T_c^{(prov)}(t + \Delta t) \right)^2 \exp\left(-\frac{e\Phi_c}{k_B T_c^{(prov)}(t + \Delta t)} \right) + e n_{e,\infty}^{(prov)} \sqrt{\frac{k_B \overline{T}_p^*}{m_i}} \right) \frac{\Phi_c}{T_c^{(prov)}(t + \Delta t)} \right]$$

$$= T_c(t) + \frac{\Delta t \lambda_{th,c}}{z_c^2 \rho_c c_{p,c}} T_0 + \frac{\Delta t E_{ion} n_{e,\infty}^{(prov)} \sqrt{\frac{k_B \overline{T}_p^*}{m_i}}}{z_c \rho_c c_{p,c}} \left(1 + \frac{e n_{e,\infty}^{(prov)} \sqrt{\frac{k_B \overline{T}_p^*}{m_i}}}{A_R \left(T_c^{(prov)} \right)^2 \exp\left(-\frac{e\Phi_c}{k_B T_c^{(prov)}} \right)} \right)$$

- As usual, the just obtained solution is now used as the provisional estimation and an even better improved solution is re-calculated. This process is iterated for each time step until the change between two consecutively calculated improved solutions falls below some limit; for the first iteration the provisional estimation is set equal to the value $T_c(t)$ of the previous time step.

The resulting array of single values for T_c at each time step can now be fitted to a smooth polynomial, to define the desired trajectory $T_c^*(t)$. From this the required 1st and 2nd time derivative $\frac{dT_c^*}{dt}, \frac{d^2 T_c^*}{dt^2}$ are determined for the control law (Equation (4.42)).

4.3.4 Flatness-based state estimation

Nevertheless the control law designed in the previous section needs a full state feedback, where both the cathode spot temperature (the flat output and 1st component of the state vector) as well as the plasma core temperature (the 2nd state component) are required. The possibility of reconstructing the state of the simplified model from the flat output and its first time derivative (only the first time derivative since the dynamics order is $n = r = 2$) is however guaranteed. The observability matrix (Equation (4.31)) for the considered simplified dynamics is invertible

$$y_f = x_1, \quad L_{\vec{f}} y_f = f_1(x_1, x_2) \quad \Rightarrow \quad \mathcal{O} = \begin{pmatrix} 1 & 0 \\ \frac{\partial f_1}{\partial x_1} & \frac{\partial f_1}{\partial x_2} \end{pmatrix}, \quad \det \mathcal{O} = \frac{\partial f_1}{\partial x_2} \neq 0 \qquad (4.43)$$

It is noteworthy that the observability condition in this case is actually equivalent to the controllability condition, see Equation (4.34), $\frac{\partial f_1}{\partial x_2} \neq 0$ (since $g_2 \neq 0$ is trivially satisfied, otherwise there would be no coupling of the external current source to the plasma dynamics). Hence it is feasible to extract the plasma core temperature from the information in the cathode spot temperature and its derivative. Two methods for this estimation will be discussed now.

4.3.4.1 Flatness-based simple state reconstruction

Reconstructing the current value of the plasma core temperature $\overline{T}_p$ from the flat output content requires the evaluation of the time derivative $\dot{T}_c$. The real system only provides y_f as an output, but not its time derivative, the latter has to be estimated. In most systems the output variables of the sensor measurments are nevertheless not ideal (because of an overlapped noise signal), which makes any estimation of the derivative more difficult. A simple solution is a least square estimator, which in the case where the sensor noise is distibuted normally (according to a Gaussian probability distribution) yields also the optimum derivative estimation as a result of the Cramér-Rao bound [95]. If the noise is not normally distributed this is still a good estimator.

The first time derivative has to be estimated at the current time step t_0 and the series of output y values is known at t_0 and at $(N-1)$ previous equally separated time steps, where Δt_c is the time duration of each time step. For this array of values $\{(t_0 - i\Delta_c, y_{-i}) : i = 0, \ldots, (N-1)\}$ a polynomial of 2nd order should be found for a good estimation $\hat{y}$ of the output value during the considered time interval between $t_0 - (N-1)\Delta t_c$ and t_0

$$\hat{y}(t) = \kappa_0 + \kappa_1 \left(\frac{t - t_0}{\Delta t_c} \right) + \kappa_2 \left(\frac{t - t_0}{\Delta t_c} \right)^2 \qquad (4.44)$$

with the time coordinate given by $t = t_0 - i\Delta t_c$ and the yet unknown coefficients. For white sensor noise the best fit, i.e. the optimum choice of constant parameters $\{\kappa_0, \kappa_1, \kappa_2\}$ is achieved after defining a (positive) cost function

$$J = \frac{1}{N} \sum_{i=0}^{N-1} (\hat{y}_{-i} - y_{-i})^2 = \frac{1}{N} \sum_{i=0}^{N-1} \left(\kappa_0 - \kappa_1 i + \kappa_2 i^2 - y_{-i} \right)^2 \qquad (4.45)$$

, which shall be minimized by the appropriate selection of κ values, resulting in the 3 conditions $\frac{\partial J}{\partial \kappa_0} = 0 = \frac{\partial J}{\partial \kappa_1} = \frac{\partial J}{\partial \kappa_2}$. Such conditions can be written as the following linear algebraic equation system

$$\begin{pmatrix} 1 & -\frac{1}{N}\sum_{i=0}^{N-1} i & \frac{1}{N}\sum_{i=0}^{N-1} i^2 \\ -\frac{1}{N}\sum_{i=0}^{N-1} i & \frac{1}{N}\sum_{i=0}^{N-1} i^2 & -\frac{1}{N}\sum_{i=0}^{N-1} i^3 \\ \frac{1}{N}\sum_{i=0}^{N-1} i^2 & -\frac{1}{N}\sum_{i=0}^{N-1} i^3 & \frac{1}{N}\sum_{i=0}^{N-1} i^4 \end{pmatrix} \begin{pmatrix} \kappa_0 \\ \kappa_1 \\ \kappa_2 \end{pmatrix} = \begin{pmatrix} +\frac{1}{N}\sum_{i=0}^{N-1} y_{-i} \\ -\frac{1}{N}\sum_{i=0}^{N-1} i\, y_{-i} \\ +\frac{1}{N}\sum_{i=0}^{N-1} i^2\, y_{-i} \end{pmatrix} \qquad (4.46)$$

Using the Faulhaber's formula [96] the elements in the quadratic matrix can be calculated directly

$$\frac{1}{N}\sum_{i=0}^{N-1} i = \frac{N-1}{2} \qquad \frac{1}{N}\sum_{i=0}^{N-1} i^2 = \frac{2N^2 - 3N + 1}{6}$$

$$\frac{1}{N}\sum_{i=0}^{N-1} i^3 = \frac{N(N-1)^2}{4} \qquad \frac{1}{N}\sum_{i=0}^{N-1} i^4 = \frac{6N^4 - 15N^3 + 10N^2 - 1}{30}$$

(4.47)

and thus from the inversion of the matrix on the left hand side of eq. (4.46) the following estimation for the 1st derivative of the output is obtained [4]

$$\frac{dT_c}{dt}\bigg|_{t=t_0} = \frac{\kappa_1}{\Delta t_c} = \frac{(bc - ad)\sum_{i=0}^{N-1} y_{-i} - (d - b^2)\sum_{i=0}^{N-1} i\, y_{-i} + (ab - c)\sum_{i=0}^{N-1} i^2\, y_{-i}}{N\Delta t_c\, (bd + 2abc - b^3 - c^2 - a^2 d)}$$

(4.48)

with

$$a = -\frac{N-1}{2}, \quad b = +\frac{2N^2 - 3N + 1}{6}, \quad c = -\frac{N(N-1)^2}{4}, \quad d = +\frac{6N^4 - 15N^3 + 10N^2 - 1}{30}$$

$$(bc - ad) = -\frac{(N-1)^2}{120}\left(-2N^3 + 3N^2 + 3N - 2\right) \qquad -(d - b^2) = -\frac{16N^4 - 30N^3 - 5N^2 + 30N - 11}{180}$$

$$(ab - c) = +\frac{(N-1)^2(N+1)}{12} \qquad \left(bd + 2abc - b^3 - c^2 - a^2 d\right) = \frac{(N^2 - 1)^2(N^2 - 4)}{2160}$$

Once derivative $\dot{T}_c$ is evaluated, the plasma core temperature can be extracted from the vector

$$\vec{z} = \begin{pmatrix} z_1 = y_f = T_c \\ z_2 = \dot{y}_f = \dot{T}_c \end{pmatrix}$$

(4.49)

in an iterative way by means of the Newton-Raphson algorithm (Appendix A.2.2). $\vec{z}$ is a (nonlinear) function of the actual state vector $\vec{x} = \begin{pmatrix} x_1 = T_c \\ x_2 = \overline{T}_p \end{pmatrix}$, starting at a provisional solution $\vec{x}^{(prov)} = \begin{pmatrix} T_c \\ \overline{T}_p^{(prov)} \end{pmatrix}$ and by calculating the first two terms in a Taylor expansion of $\vec{z}(\vec{x})$ the following solution for an improved $\vec{x}$ is obtained

$$\vec{z}(\vec{x}) \approx \vec{z}(\vec{x}^{(prov)}) + \left(\frac{\partial \vec{z}}{\partial \vec{x}}\right)\bigg|_{\vec{x}^{(prov)}} \left(\vec{x} - \vec{x}^{(prov)}\right)$$

$$\overline{T}_p \approx \overline{T}_p^{(prov)} + \begin{pmatrix} 0 & 1 \end{pmatrix} \left[\underbrace{\begin{pmatrix} 1 & 0 \\ \frac{\partial f_1}{\partial x_1} & \frac{\partial f_1}{\partial x_2} \end{pmatrix}\bigg|_{\vec{x}^{(prov)}}}_{\mathcal{O}} \right]^{-1} \begin{pmatrix} 0 \\ \dot{T}_c - f_1(T_c, \overline{T}_p^{(prov)}) \end{pmatrix}$$

$$= \overline{T}_p^{(prov)} + \frac{\left(\dot{T}_c - f_1(T_c, \overline{T}_p^{(prov)})\right)}{\frac{\partial f_1}{\partial x_2}(T_c, \overline{T}_p^{(prov)})}$$

(4.50)

The denominator of the previous relation does not vanish since it just corresponds to the observability condition Equation (4.31). The solution for the actual $\overline{T}_p$ is carried out in two iterations. The first iteration $\overline{T}_p^{(prov)}$ takes the value of $\overline{T}_p$ from the previous time step and an improved $\overline{T}_p$ is calculated, the latter being used in the second iteration as $\overline{T}_p^{(prov)}$ for an even better $\overline{T}_p$ and so on. If the time step Δt_c at which the output sensor yields values is short enough (typically $1/4$ of the time scale for the plasma dynamics, i.e., about 0.2 ms) the iterative solution can be reduced to a single iteration.

---

[4]Together with $\begin{pmatrix} 0 & 1 & 0 \end{pmatrix} \begin{pmatrix} 1 & a & b \\ a & b & c \\ b & c & d \end{pmatrix}^{-1} = \frac{1}{bd + 2abc - b^3 - c^2 - a^2 d} \begin{pmatrix} (bc - ad) & (d - b^2) & (ab - c) \end{pmatrix}$.

4.3.4.2 Flatness-based high-gain observer

In the previous reconstruction of the plasma core temperature it was assumed that the output sensor in the real system was not ideal, but the simplified dynamics on the other hand are still accurate enough to describe the full system. Thus the flat output of this simplified model could be safely applied for extracting any information from the real system. In many situations, however, the model being used to design the control is only an approximation to the real underlying dynamics which contains some additional non-modelled effects. This occurs because these effects are either not relevant for the time scales being resolved during the control or because such effects are too complicated to describe . In this case the corresponding mathematical model would considerably slow down the controller and make it useless. This is also the situation in the considered system. The simplifed model is a 2nd order dynamics, able only of reproducing some of the relevant effects, but without any detail about the radial plasma temperature distribution. Hence the reconstruction of the plasma core temperature from such simplified model might be quite poor (again, a direct measurement of such a plasma temperature is not viable at the frequency rate required for controlling).

There is nevertheless an efficient solution proposed by Luenberger half a century ago [97], initially for linear systems: the observer. Implemented on a microprocessor the observer takes the input u into the real system as well as the output y measured from it and follows the system dynamics according to the simplified model (including output $\hat{y}$), <u>but</u> with an additional correction proportional to the error $e_y = y - \hat{y}$ between the real and the modelled output. The idea behind it is:

- This error e_y is negligible, the simplified model is currently yielding an accurate description of the actual system dynamics and therefore the modelled state vector of the observer is also a fine estimation for the non-accessible state in the real system.

- If, on the contrary, e_y is not small the simplified model within the observer has to be adjusted along the appropriate direction to correct this error and bring it back to a situation with a negligible e_y.

The question is, how strong should the correction e_y be coupled to each state component when formulating the observer's equations of motion and how this is expressed mathematically.

From now on any estimation/reconstruction calculated within the observer will be marked by the symbol ˆ and therefore to avoid an overloaded notation the vector symbol will be dropped in the following discussion (always keeping in mind that x has n components, as well as f and g, but u and y have only one). The equations of motion for the real system and the observer are, respectively, given by

$$
\begin{aligned}
\text{real system:} & \left\{
\begin{array}{ll}
\dfrac{dx}{dt} & = f(x) + g(x)\,u + (\ldots)_1 \\
y & = h(x) + (\ldots)_2
\end{array}
\right. \\[2ex]
\text{observer:} & \left\{
\begin{array}{ll}
\dfrac{d\hat{x}}{dt} & = f(\hat{x}) + g(\hat{x})\,u + \underline{L(\hat{x})\,(y - \hat{y})} \\
\hat{y} & = h(\hat{x})
\end{array}
\right.
\end{aligned}
\tag{4.51}
$$

where the $(\ldots)_1$ in the equations of motion for the real state vector x represents the non-modelled effects discussed earlier; in the output equation for y, the $(\ldots)_2$ indicates the sensor noise. Now to design the n components of the column vector $L(\hat{x})$ multiplied by $e_y = y - \hat{y}$ (term marked by a single underline), in such a way that the state estimation $\hat{x}$ remains close to the real x. Without measuring the full state (which is not viable), but only by having the information contained in the output. Assuming that the observer manages to keep the state reconstruction error $e_x = x - \hat{x}$ small (a column vector with n components), the equation of motion for such error vector can be approximated by keeping only the linear term in e_x for its Taylor expansion

$$\frac{de_x}{dt} = \Big(f(x) - f(\hat{x}) \Big) + \Big(g(x) - g(\hat{x}) \Big) u - L(\hat{x}) \Big(h(x) - h(\hat{x}) \Big) + \dots$$

$$\approx \overbrace{\left[\underbrace{\left(\frac{\partial f}{\partial x}\right)\Big|_{\hat{x}}}_{\substack{\text{quadratic} \\ n \times n \text{ matrix}}} + \underbrace{\left(\frac{\partial g}{\partial x}\right)\Big|_{\hat{x}}}_{\substack{\text{quadratic} \\ n \times n \text{ matrix}}} u - \underbrace{L(\hat{x})}_{\substack{\text{column} \\ n \times 1 \text{ vector}}} \underbrace{\frac{\partial h}{\partial x}\Big|_{\hat{x}}}_{\substack{\text{row} \\ 1 \times n \text{ vector}}} \right]}^{\text{observer matrix } \mathbf{A}_{\mathcal{O}}} \overbrace{(x - \hat{x})}^{e_x} + \dots \tag{4.52}$$

The main intention of an observer is to maintain the vector e_x small, observer matrix $\mathbf{A}_{\mathcal{O}}$ in the previous equation must be a Hurwitz matrix, i.e. all its eigenvalues must have a strictly negative real part so that e_x cannot grow in an uncontrolled way. For the simplified dynamics (4.32), which are of order $n = 2$, this observer matrix reads

$$\begin{aligned}
\mathbf{A}_{\mathcal{O}} &= \begin{pmatrix} \frac{\partial f_1}{\partial x_1} & \frac{\partial f_1}{\partial x_2} \\ 0 & \frac{\partial f_2}{\partial x_2} \end{pmatrix}\Big|_{\hat{x}} + \begin{pmatrix} 0 & 0 \\ 0 & \frac{\partial g_2}{\partial x_2} \end{pmatrix}\Big|_{\hat{x}} u - \begin{pmatrix} \ell_1(\hat{x}) \\ \ell_2(\hat{x}) \end{pmatrix} \begin{pmatrix} 1 & 0 \end{pmatrix} \\
&= \begin{pmatrix} \frac{\partial f_1}{\partial x_1}(\hat{x}) - \ell_1(\hat{x}) & \frac{\partial f_1}{\partial x_2}(\hat{x}) \\ -\ell_2(\hat{x}) & \frac{\partial f_2}{\partial x_2}(\hat{x}) + u \frac{\partial g_2}{\partial x_2}(\hat{x}) \end{pmatrix}
\end{aligned} \tag{4.53}$$

and for both eigenvalues to have a strictly negative real part, the following two conditions must be satisfied. The trace of the matrix must be negative and its determinant must be positive.

$$\ell_1(\hat{x}) > \left(\frac{\partial f_1}{\partial x_1} + \frac{\partial f_2}{\partial x_2} + u \frac{\partial g_2}{\partial x_2} \right)\Big|_{\hat{x}},$$

$$\ell_2(\hat{x}) \frac{\partial f_1}{\partial x_2}(\hat{x}) > - \left(\frac{\partial f_1}{\partial x_1} - \ell_1 \right)\Big|_{\hat{x}} \left(\frac{\partial f_2}{\partial x_2} + u \frac{\partial g_2}{\partial x_2} \right)\Big|_{\hat{x}} > \left(\frac{\partial f_2}{\partial x_2} + u \frac{\partial g_2}{\partial x_2} \right)^2\Big|_{\hat{x}} \tag{4.54}$$

Yet determining two constant values for ℓ_1 and ℓ_2, in such a way that the above inequalities are satisfied for nearly the whole value range of the state components (and the input) is quite a demanding task to solve. Particularly if those bounds include the input u itself, a value that can strongly vary. Fortunately there exists a particular observer formulation, the so-called high-gain observer ([93], § 14), which applied to a dynamics with a flat output yields a robust state estimation ([98], § 7). This observer is characterized by a simple structure and by constant values for ℓ_1 and ℓ_2. Instead of discussing the high-gain observer in general only its application to the simplified model for the "plasma arc and cathode spot" dynamics will be presented here. As a first step, the simplified dynamics is described in the follwoing new state coordinates $z = \begin{pmatrix} z_1 = y_f \\ y_2 = \dot{y}_f \end{pmatrix}$, which contains the same information as the original state vector x since y_f is a flat output. The equations of motion for these transformed state variables are

$$\begin{aligned}
\dot{z}_1 &= \dot{y}_f \equiv z_2 \\
\dot{z}_2 &= \ddot{y}_f = L_{\vec{f}}^2 y_f + \underbrace{L_{\vec{g}} L_{\vec{f}} y_f}_{\neq 0} u
\end{aligned} \tag{4.55}$$

and thus the real system as well as the observer are described as follows

$$\text{real system:} \begin{cases} \dfrac{dz}{dt} = \begin{pmatrix} 0 & 1 \\ 0 & 0 \end{pmatrix} z + \begin{pmatrix} 0 \\ 1 \end{pmatrix} \left[\overbrace{L_{\vec{f}}^2 y_f(x) + L_{\vec{g}} L_{\vec{f}} y_f(x) \, u + \underbrace{\dotsb}_{\substack{\text{additional effects} \\ \text{additional degree of freedom}}}}^{\text{scalar function } \varphi(z, u)} \right] \end{cases}$$

$$\text{observer:} \begin{cases} \dfrac{d\hat{z}}{dt} = \begin{pmatrix} 0 & 1 \\ 0 & 0 \end{pmatrix} \hat{z} + \begin{pmatrix} 0 \\ 1 \end{pmatrix} \left[\overbrace{L_{\vec{f}}^2 y_f(\hat{x}) + L_{\vec{g}} L_{\vec{f}} y_f(\hat{x}) \, u}^{\text{scalar function } \hat{\varphi}(\hat{z}, u)} \right] + \begin{pmatrix} \ell_1 \\ \ell_2 \end{pmatrix} \begin{pmatrix} 1 & 0 \end{pmatrix} \big(z - \hat{z} \big) \end{cases} \tag{4.56}$$

again with the correcting term in the observer marked by a straight underline. The state reconstructiong error in the transformed coordinates, $e_z = z - \hat{z} = \begin{pmatrix} e_{y_f} = y_f - \hat{y}_f \\ \frac{de_{y_f}}{dt} \end{pmatrix}$, has the equation of motion

$$\frac{de_z}{dt} = \begin{pmatrix} -\ell_1 & 1 \\ -\ell_2 & 0 \end{pmatrix} e_z + \begin{pmatrix} 0 \\ 1 \end{pmatrix} \left(\varphi(z, u) - \hat{\varphi}(\hat{z}, u) \right) \tag{4.57}$$

This time without any approximative linearization (as it was the case in Equation (4.52)). Let us now assume the following choice for constant ℓ_1 and ℓ_2

$$\ell_1 = -\frac{1}{\tilde{\varepsilon}} \left(\tilde{\lambda}_1 + \tilde{\lambda}_2 \right), \quad \ell_2 = \frac{1}{\tilde{\varepsilon}^2} \tilde{\lambda}_1 \tilde{\lambda}_2, \tag{4.58}$$

, where $\tilde{\lambda}_1$ and $\tilde{\lambda}_2$ represent constant eigenvalues with negative real part (either both real or complex conjugated to each other) and $\tilde{\varepsilon}$ is a positive (small) number still to be determined. The next step is to re-scale the time coordinate in such a way to follow the evolution of the transformed state reconstruction error e_z in more detail

$$t' = \tilde{\varepsilon}^{-1} t \quad \Longrightarrow \quad \frac{d}{dt} = \tilde{\varepsilon}^{-1} \frac{d}{dt} \tag{4.59}$$

Correspondingly a modified error vector ζ is introduced whose 2nd component is the derivative of the 1st component, but now according to the new time coordinate t'

$$\zeta = \begin{pmatrix} \zeta_1 = e_{y_f} = y_f - \hat{y}_f \\ \zeta_2 = \frac{de_{y_f}}{dt'} \end{pmatrix}. \tag{4.60}$$

This new vector is related to the original vector z by means of $\zeta = \begin{pmatrix} 1 & 0 \\ 0 & \tilde{\varepsilon} \end{pmatrix} z$ and its dynamics is given by

$$\frac{de_z}{dt} = \tilde{\varepsilon}^{-1} \begin{pmatrix} 1 & 0 \\ 0 & \tilde{\varepsilon}^{-1} \end{pmatrix} \frac{d\zeta}{dt'} \quad \Longrightarrow \quad \frac{d\zeta}{dt'} = \tilde{\varepsilon} \begin{pmatrix} 1 & 0 \\ 0 & \tilde{\varepsilon} \end{pmatrix} \frac{de_z}{dt}$$

$$\frac{d\zeta}{dt'} = \tilde{\varepsilon} \begin{pmatrix} 1 & 0 \\ 0 & \tilde{\varepsilon} \end{pmatrix} \begin{pmatrix} -\ell_1 & 1 \\ -\ell_2 & 0 \end{pmatrix} \begin{pmatrix} 1 & 0 \\ 0 & \tilde{\varepsilon}^{-1} \end{pmatrix} \zeta + \tilde{\varepsilon} \begin{pmatrix} 1 & 0 \\ 0 & \tilde{\varepsilon} \end{pmatrix} \begin{pmatrix} 0 \\ 1 \end{pmatrix} \left(\varphi(z, u) - \hat{\varphi}(\hat{z}, u) \right)$$

$$= \underbrace{\begin{pmatrix} \tilde{\lambda}_1 + \tilde{\lambda}_2 & 1 \\ -\tilde{\lambda}_1 \tilde{\lambda}_2 & 0 \end{pmatrix}}_{\mathbf{A}'_{\mathcal{O}}} \zeta + \tilde{\varepsilon}^2 \begin{pmatrix} 0 \\ 1 \end{pmatrix} \left(\varphi(z, u) - \hat{\varphi}(\hat{z}, u) \right) \tag{4.61}$$

The re-scaling of the time coordinate makes the advantage of this observer formulation clear. By choosing $\tilde{\varepsilon} \to 0$ (which leads to high $\ell_{1/2}$ values, thus the name of "high gain") the contribution $\varphi(z, u) - \hat{\varphi}(\hat{z}, u)$ becomes negligible, with all the involved nonlinearities in the state variable as well as the explicit dependence on the input. Moreover for $\tilde{\varepsilon} \to 0$ (typically $\tilde{\varepsilon} = 0.1$ is enough) the remaining observer dynamics reduces to $\frac{d\zeta}{dt'} = \mathbf{A}'_{\mathcal{O}} \zeta$, where the eigenvalues of the matrix $\mathbf{A}'_{\mathcal{O}}$ are $\tilde{\lambda}_1$ and $\tilde{\lambda}_2$. As soon as both eigenvalues have a strictly negative real part the behaviour $\zeta \xrightarrow{t' \to \infty} 0$ follows, independent of the form in $\varphi(x)$ and $\hat{\varphi}(\hat{x})$. This last property is referred to as *robustness*. Since $\zeta \xrightarrow{t' \to \infty} 0$ implies also $\hat{z} \xrightarrow{t \to \infty} z$ the stable operation of the observer is guaranteed. If eigenvalues $\tilde{\lambda}_{1/2}$ are chosen large enough in magnitude the time it takes to achieve the convergence goes to infinity "$t \to \infty$", but this already occurs for a shorter time intervalas well, since the components in ζ evolve as $e^{\tilde{\lambda}_{1/2} t'}$. A convenient choice for these eigenvalues is

$$\frac{\tilde{\lambda}_{1/2}}{\tilde{\varepsilon}} \sim \frac{10}{\tilde{\tau}_c} \tag{4.62}$$

for the observer to reconstruct the state in a time scale faster than $\tilde{\tau}_c$, with the latter defining the stabilizing state feedback (4.42) which requires an already fine enough estimation of the state.

76

And as a final step, it remains only to write the observer equations back into the original $\hat{x}$ state coordinates. This is easily carried out since the transformation matrix connecting $\dfrac{d\hat{z}}{dt}$ to $\dfrac{d\hat{x}}{dt}$ is just the observability matrix (evaluated at the current state estimation)

$$\frac{d\hat{x}}{dt} = \Big[\underbrace{\left(\frac{\partial \hat{z}}{\partial \hat{x}} \right)\Big|_{\hat{x}}}_{\substack{\text{observability} \\ \text{matrix } \mathcal{O}}} \Big]^{-1} \frac{d\hat{z}}{dt} \tag{4.63}$$

Hence the equations of motion for the high-gain observer, formulated in the original state variables $\hat{x} = \begin{pmatrix} \hat{x}_1 = \hat{T}_c \\ \hat{x}_2 = \hat{T}_p \end{pmatrix}$, are

$$\frac{d}{dt} \begin{pmatrix} \hat{x}_1 \\ \hat{x}_2 \end{pmatrix} = \overbrace{\frac{1}{\frac{\partial f_1}{\partial x_2}\Big|_{\hat{x}}} \begin{pmatrix} \frac{\partial f_1}{\partial x_2} & 0 \\ -\frac{\partial f_1}{\partial x_1} & 1 \end{pmatrix}\Big|_{\hat{x}}}^{\mathcal{O}^{-1}} \Big[\begin{pmatrix} 0 & 1 \\ 0 & 0 \end{pmatrix} \begin{pmatrix} \hat{x}_1 \\ f_1(\hat{x}_1, \hat{x}_2) \end{pmatrix}$$

$$+ \begin{pmatrix} 0 \\ 1 \end{pmatrix} \left(\frac{\partial f_1}{\partial x_1} f_1 + \frac{\partial f_1}{\partial x_2} (f_2 + g_2\, u) \right)\Big|_{\hat{x}} + \begin{pmatrix} \ell_1 \\ \ell_2 \end{pmatrix} \left(T_c^{(meas)} - \hat{x}_1 \right) \Big] \tag{4.64}$$

where the output emanating from the real system has been written as $T_c^{(meas)}$ to stress its measurement character. Now the separated components for the observer's equations of motion are given by

$$\frac{d\hat{x}_1}{dt} = f_1(\hat{x}_1, \hat{x}_2) + \ell_1 \left(T_c^{(meas)} - \hat{x}_1 \right)$$

$$\frac{d\hat{x}_2}{dt} = f_2(\hat{x}_2) + g_2(\hat{x}_2)\, u + \frac{-\ell_1 \frac{\partial f_1}{\partial x_1}\Big|_{\hat{x}} + \ell_2}{\frac{\partial f_1}{\partial x_2}\Big|_{\hat{x}}} \left(T_c^{(meas)} - \hat{x}_1 \right) \tag{4.65}$$

The numerical integration is carried out in an interative way, similarly to equations (4.13) and using again the 2 methods (A.3) as well as the sign conditions derived in (4.40)

$$\hat{x}_1(t + \Delta t)\left[1 + \Delta t\frac{f_1^{(-)}(\hat{x}_1^{(prov)}, \hat{x}_2^{(prov)})}{\hat{x}_1^{(prov)}} + \Delta t\,\ell_1\right] = \hat{x}_1(\overset{\Downarrow}{t}) + \Delta t\,f_1^{(+)}(\hat{x}_1^{(prov)}, \hat{x}_2^{(prov)}) + \Delta t\,\ell_1 T_c^{(meas)}$$

$$\hat{x}_2(t + \Delta t)\left[1 + \Delta t\frac{\left(f_2(\hat{x}_2^{(prov)}) + g_2(\hat{x}_2^{(prov)})\,u\right)^{(-)}}{\hat{x}_2^{(prov)}} + \Delta t\frac{-\ell_1\left.\dfrac{\partial f_1}{\partial x_1}\right|_{\left(\hat{x}_1^{(prov)}, \hat{x}_2^{(prov)}\right)} + \ell_2}{\left.\dfrac{\partial f_1}{\partial x_2}\right|_{\left(\hat{x}_1^{(prov)}, \hat{x}_2^{(prov)}\right)}}\frac{\hat{x}_1^{(prov)}}{\hat{x}_2^{(prov)}}\right] \tag{4.66}$$

$$= \hat{x}_2(\overset{\Downarrow}{t}) + \Delta t\left(f_2(\hat{x}_2^{(prov)}) + g_2(\hat{x}_2^{(prov)})\,u\right)^{(+)} + \Delta t\frac{-\ell_1\left.\dfrac{\partial f_1}{\partial x_1}\right|_{\left(\hat{x}_1^{(prov)}, \hat{x}_2^{(prov)}\right)} + \ell_2}{\left.\dfrac{\partial f_1}{\partial x_2}\right|_{\left(\hat{x}_1^{(prov)}, \hat{x}_2^{(prov)}\right)}}T_c^{(meas)}$$

$$f_1^{(+)} = \frac{\lambda_{th,c}}{\rho_c c_{p,c} z_c^2}T_0 + \frac{E_{ion}n_{e,\infty}^{(prov)}\sqrt{\frac{k_B\hat{x}_2^{(prov)}}{m_i}}}{\rho_c c_{p,c} z_c}\left(1 + \frac{en_{e,\infty}^{(prov)}\sqrt{\frac{k_B\hat{x}_2^{(prov)}}{m_i}}}{A_R\left(\hat{x}_1^{(prov)}\right)^2\exp\left(-\frac{e\Phi_c}{k_B\hat{x}_1^{(prov)}}\right)}\right)$$

$$\frac{f_1^{(-)}}{\hat{x}_1^{(prov)}} = \frac{\lambda_{th,c}}{\rho_c c_{p,c} z_c^2} + \frac{\varepsilon_c\sigma_{SB}}{\rho_c c_{p,c} z_c}\left(\hat{x}_1^{(prov)}\right)^3$$

$$+ \frac{1}{\rho_c c_{p,c} z_c}\left(A_R\left(\hat{x}_1^{(prov)}\right)^2\exp\left(-\frac{e\Phi_c}{k_B\hat{x}_1^{(prov)}}\right) + en_{e,\infty}^{(prov)}\sqrt{\frac{k_B\hat{x}_2^{(prov)}}{m_i}}\right)\frac{\Phi_c}{\hat{x}_1^{(prov)}}$$

$$(f_2 + g_2\,u)^{(+)} = \frac{2\lambda_{th,p}((\hat{x}_2^{(prov)} + T_0)/2)}{\left(\rho_p c_{p,p} r_p^2\left(\frac{r_0}{r_p} - 1\right)\right)\Big|_{\hat{x}_2^{(prov)}}}T_0 + \left(1 + \underline{\xi}\right)\frac{1}{\pi^2\left(\sigma_{el}\rho_p c_{p,p} r_p^4\right)\Big|_{\hat{x}_2^{(prov)}}}\,u$$

$$\frac{(f_2 + g_2\,u)^{(-)}}{\hat{x}_2^{(prov)}} = \frac{2\lambda_{th,p}((\hat{x}_2^{(prov)} + T_0)/2)}{\left(\rho_p c_{p,p} r_p^2\left(\frac{r_0}{r_p} - 1\right)\right)\Big|_{\hat{x}_2^{(prov)}}} + \xi\frac{1}{\pi^2\left(\sigma_{el}\rho_p c_{p,p} r_p^4\right)\Big|_{\hat{x}_2^{(prov)}}}\frac{u}{\hat{x}_2^{(prov)}}$$

$$\frac{\partial f_1}{\partial x_1} = -\frac{\lambda_{th,c}}{\rho_c c_{p,c} z_c^2} - 4\frac{\varepsilon_c\sigma_{SB}}{\rho_c c_{p,c} z_c}\left(\hat{x}_1^{(prov)}\right)^3$$

$$- \frac{1}{\rho_c c_{p,c} z_c}\frac{A_R\left(\hat{x}_1^{(prov)}\right)^2\exp\left(-\frac{e\Phi_c}{k_B\hat{x}_1^{(prov)}}\right)}{\hat{x}_1^{(prov)}}\left(2 + \frac{e\Phi_c}{k_B\hat{x}_1^{(prov)}}\right)\times$$

$$\times\left(\frac{E_{ion}}{e}\left(\frac{en_{e,\infty}^{(prov)}\sqrt{\frac{k_B\hat{x}_2^{(prov)}}{m_i}}}{A_R\left(\hat{x}_1^{(prov)}\right)^2\exp\left(-\frac{e\Phi_c}{k_B\hat{x}_1^{(prov)}}\right)}\right)^2 + \Phi_c\right) < 0$$

$$\frac{\partial f_1}{\partial x_2} = \frac{1}{\rho_c c_{p,c} z_c}\frac{en_{e,\infty}^{(prov)}\sqrt{\frac{k_B\hat{x}_2^{(prov)}}{m_i}}}{\hat{x}_2^{(prov)}}\left(\frac{-n_{e,\infty}^{(prov)}\left(2 + \frac{E_{ion}}{k_B\hat{x}_2^{(prov)}}\right) + \frac{P}{2k_B\hat{x}_2^{(prov)}}\left(\frac{3}{2} + \frac{E_{ion}}{k_B\hat{x}_2^{(prov)}}\right)}{\frac{P}{k_B\hat{x}_2^{(prov)}} - n_{e,\infty}^{(prov)}}\right)\times$$

$$\times\left(\frac{E_{ion}}{e}\left(2\frac{en_{e,\infty}^{(prov)}\sqrt{\frac{k_B\hat{x}_2^{(prov)}}{m_i}}}{A_R\left(\hat{x}_1^{(prov)}\right)^2\exp\left(-\frac{e\Phi_c}{k_B\hat{x}_1^{(prov)}}\right)} + 1\right) - \Phi_c\right) > 0 \quad\text{for } \overline{T}_p < \overline{T}_{p,crit}$$

Now the usual abbreviations $\hat{x}_{1/2}^{(prov)} \equiv \hat{x}_{1/2}^{(prov)}(t + \Delta t)$ for the provisional solution at the next time step and analogously $n_{e,\infty}^{(prov)} \equiv n_{e,\infty}(\hat{x}_2^{(prov)}(t + \Delta t))$ are calculated from the Saha-Eggert equation

considering the first and second ionization. Note that both ℓ_1 and ℓ_2 are positive since all eigenvalues $\tilde{\lambda}_{1/2}$ have a negative real part (and $\tilde{\varepsilon}$ is positive). Once the reconstructed state $\hat{x} = \begin{pmatrix} \hat{x}_1 = \hat{T}_c \\ \hat{x}_2 = \hat{\tilde{T}}_p \end{pmatrix}$ has been determined for the next time step after a few iterations, the second component is used as a reliable estimation for the plasma core temperature $\hat{\tilde{T}}_p$, used in the stabilizing state feedback; there is no need to use the first component of the observer state for such state feedback, since the cathode spot temperature is directly measured.

4.4 Simulation tool for the plasma dynamics

As mentioned at the beginning of this work the developed trajectory tracking control could not be implemented in a real facility. Hence the control performance can only be tested in a simulation where nevertheless the numerical model for the real system has a higher complexity (plus an additional stochastic contribution) than the simplified model which the control design is based on. In this section the own developed MATLAB/Simulink code for simulating the system dynamics is presented, together with the trajectory design for the plasma core temperature, the observer and the controller for a stable trajectory tracking discussed in the previous chapter. The simulation results will be presented and discussed later on in this work (Section 5.3), at first for different stationary states and finally showing the performance at achieving a stable trajectory tracking control. The desired trajectory for these latter simulations corresponds to a periodic pulsed pattern in the plasma core temperature of an argon gas at atmospheric pressure ($P = 10^5$ Pa).

The simulation will again be initiated with the Matlab script, mentioned in (Section 3.4), which:

- calculates the particle densities of all species depending on the plasma temperature T_p ($\theta = 1$)

- provides all necessary plasma transport parameters (σ_{el}, $\lambda_{th,p}$, $c_{p,p}$, ρ_p) [59, 60, 85] and cathode material parameters ($\lambda_{th,c}$, $c_{p,c}$, ρ_c) [86, 87]

- sets the geometrical boundary conditions and operational parameters (z_c, r_{cool}, ℓ_{arc}, I_{arc})

- starts the plasma dynamics simulink model

The plasma dynamics simulation itself is a simulink model, which consists of the following parts:

- Trajectory generator

- Feedforward control

- Plasma system (numerical model for the radial plasma temperature evolution of the electrical arc with stochastic contribution for non-modelled effects)

- Derivative estimator

- Feedback control (nonlinear flatness based feedback controller)

- State observer (flatness based high gain observer)

The toplayer structure of the entire controller model is displayed in Figure 4.6. The structure and data flows of each component of that model are broken down in the consecutive subsections.
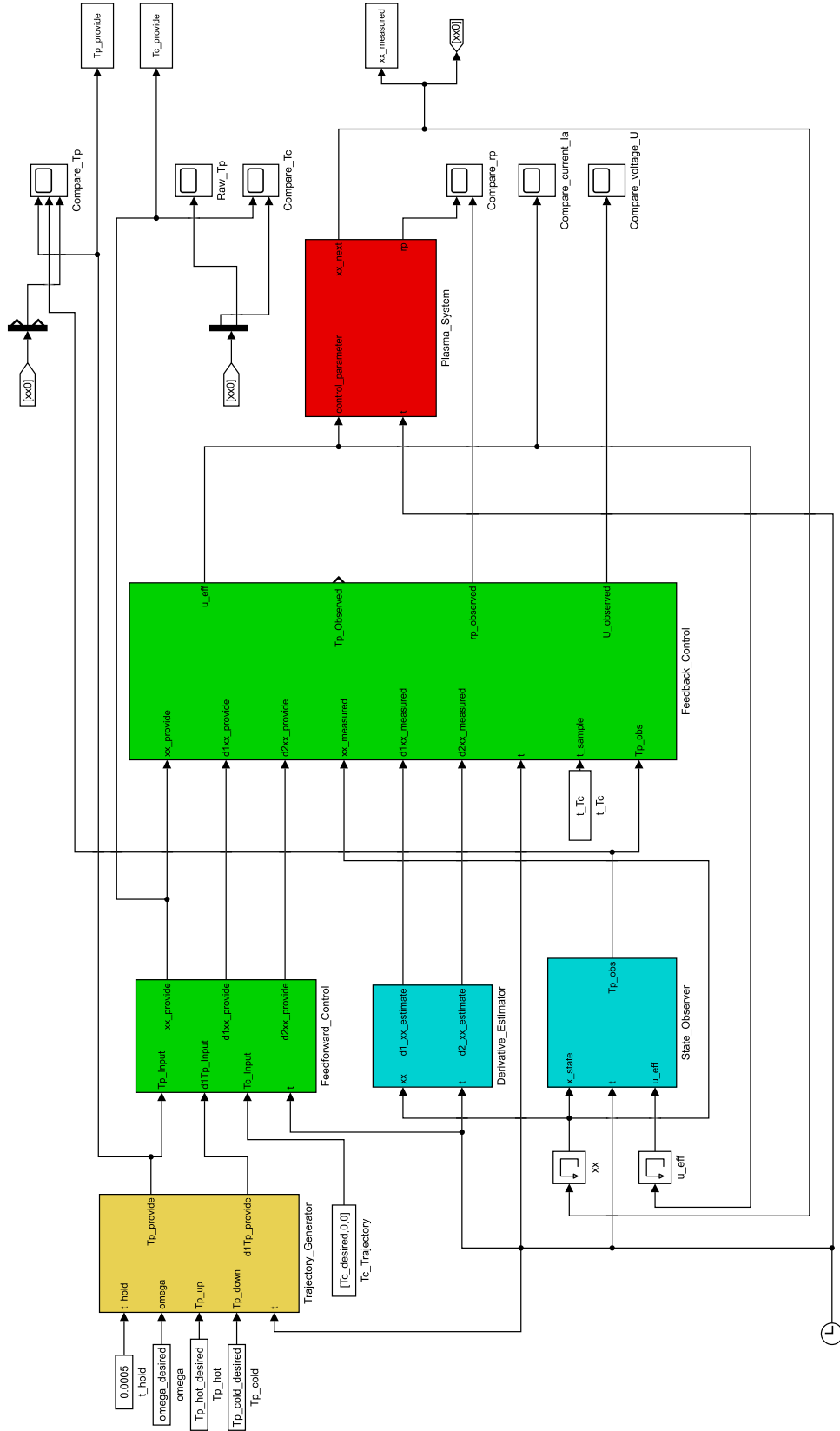
Figure 4.6: Overall structure of the nonlinear flatness based feedback control model
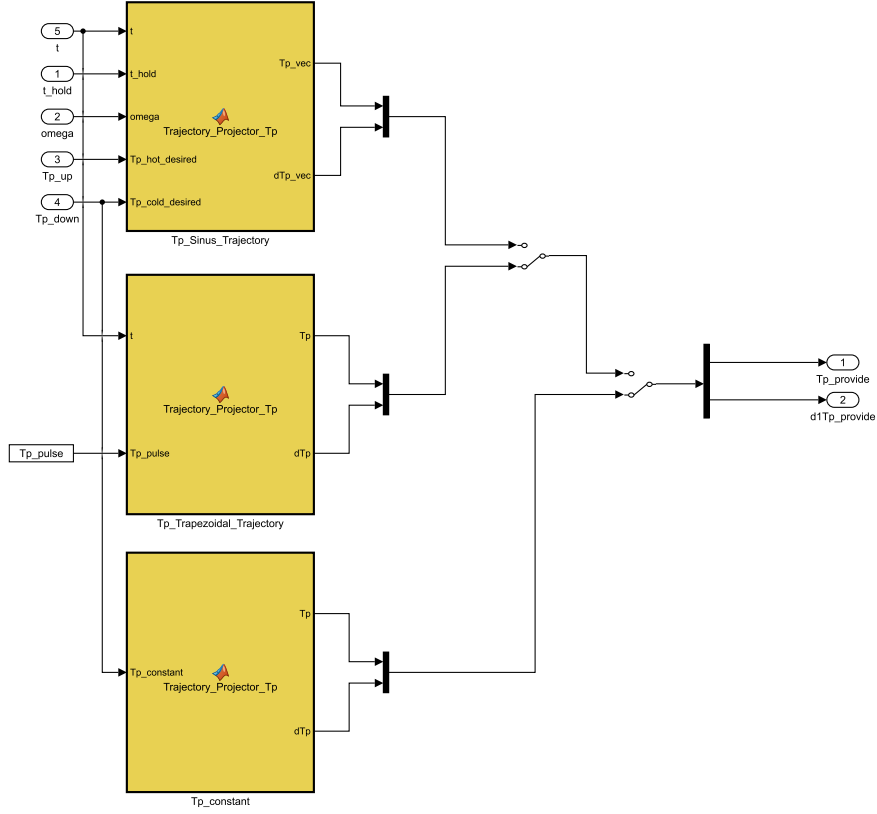
Figure 4.7: Component of the plasma dynamics simulation, for the generation of the desired plasma trajectory

Trajectory generator   The trajectory generator Figure 4.7 creates the pulse train for the desired plasma temperature trajectory. Currently three types of trajectories can be chosen:

- plasma temperature trajectory with sinusoidal pulse shape

- plasma temperature trajectory with trapezoidal pulse shape

- constant cathode temperature trajectory

In the present controller model the form of the pulse train is chosen to be plasma temperature profile with trapezoidal pulse shape, in order to evaluate the performance of the controller model, see (Figure 4.8), has been choosen to:

- create large temperature gradients within the trajectory

- create large pulse repetition rate of pulses within the trajectory

81
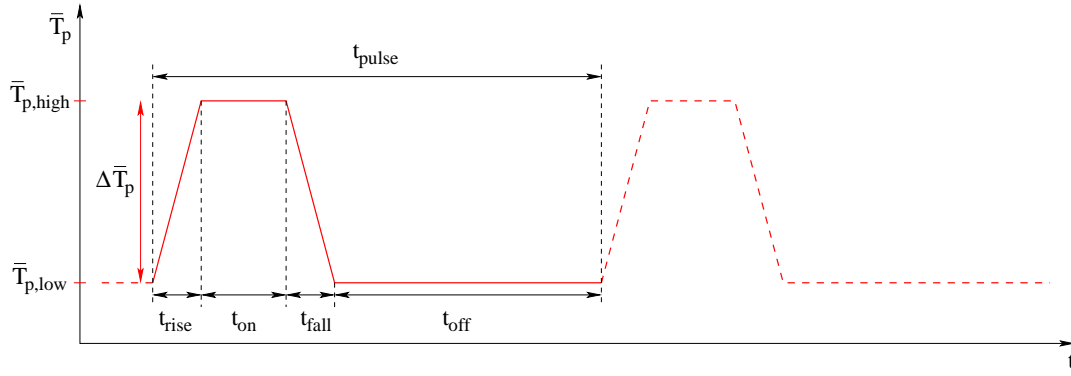
Figure 4.8: Schematic of the pulse shape profile of the desired trajectory. The overall duration is denoted with t_{pulse}, the lower $\overline{T}_{p,low}$ and upper $\overline{T}_{p,high}$ desired values of the plasma temperature increase during the pulse.
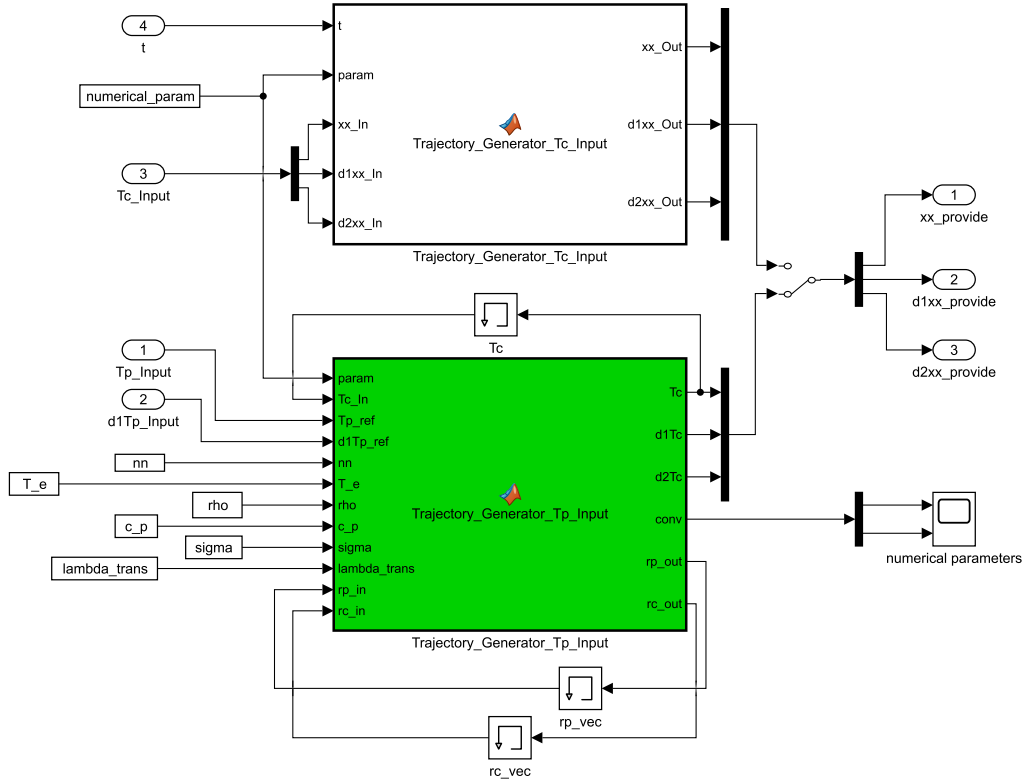
Figure 4.9: Feedforward controller to generate the input T_c trajectory and its first and second time derivative from the trajectory data of T_p, $\dot{T}_p$.

Feedforward control   The Feedforward controller, see Figure 4.9 creates the profile of the cathode temperature T_c^* and its derivatives according to the desired trajectory in T_p. The inputs to that function are the time dependent values of $T_p(t)$ and $\dot{T}_p(t)$, now the initial solution for the cathode temperature is guessed (it is convenient to choose the temperature from the steady state calculation in that case). Now all the information needed to calculate the function $f_1(T_c, \hat{T}_p)$ from (Equation (4.32)) is given. The numerical integration scheme from (Equation (A.4)) can now be taken to find a converged solution for the time step and then evolve the solution for all time steps of the regarded time frame to describe

the full trajectory. The solutions for $T_c^*(t)$ and $\dot{T}_c^*(t)$ are now given and one needs to calculate the second derivative for the full control scheme. This can be achieved with the help of (Equation (4.32)) and the assumption that no control is applied $u_{eff}(t) = 0$, which leads to the relation:

$$
\begin{aligned}
\frac{d\hat{T}_p}{dt} &= f_2(T_c^*, \hat{T}_p, \ldots) \\
\frac{d^2 T_c^*}{dt^2} &= \frac{\partial f_1}{\partial T_c^*} f_1(T_c, \hat{T}_p) + \frac{\partial f_1}{\partial \hat{T}_p} f_2(T_c, \hat{T}_p, \ldots) \\
&= \frac{\partial f_1}{\partial T_c^*} f_1(T_c, \hat{T}_p) + \frac{\partial f_1}{\partial \hat{T}_p} \frac{d\hat{T}_p}{dt}
\end{aligned}
\tag{4.67}
$$
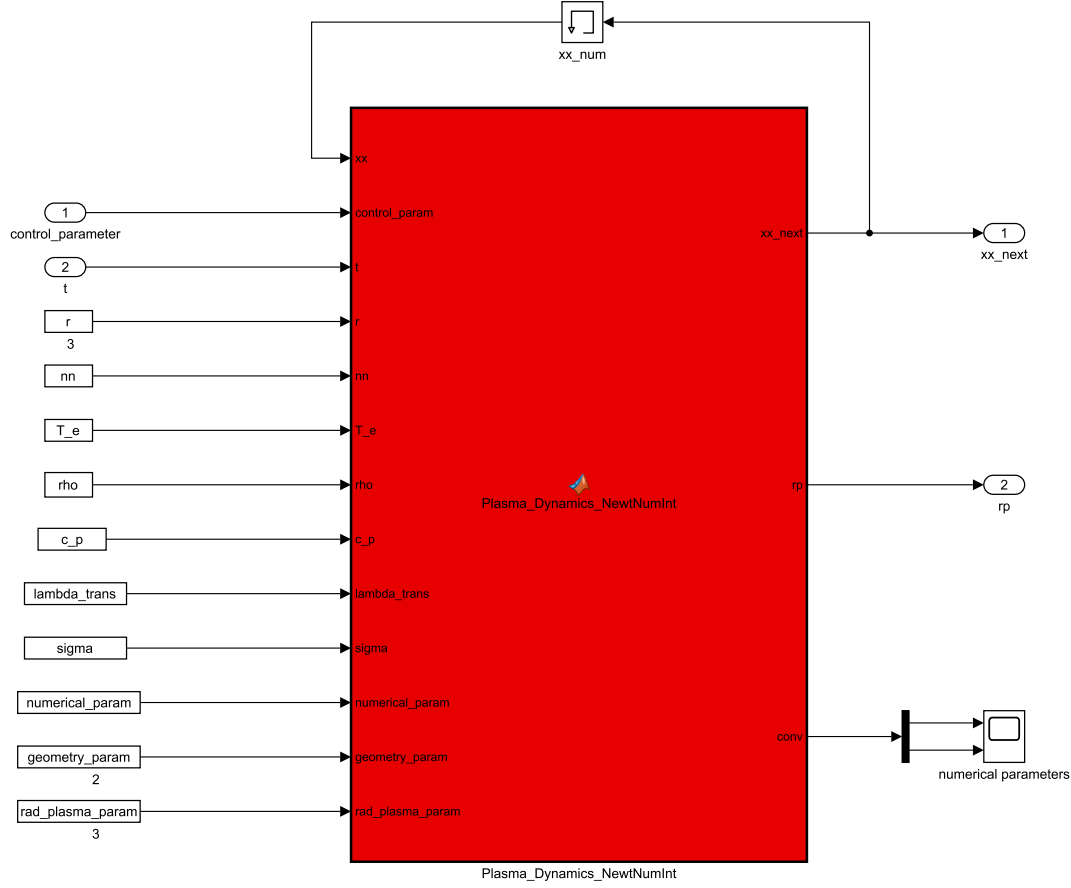
Figure 4.10: Numerical implementation of the radial plasma temperature equation overlapped with a white noise vector defined by the noise amplitute $\tilde{\sigma}_0$ to account for not modelled physical effects in the plasma.

Plasma system: numerical model for the radial plasma temperature evolution of the electrical arc with a stochastic contribution for non-modelled effects The controlled system displayed in Figure 4.10 contains the nonlinear radial plasma temperature eq. (2.60). To account for other nonlinear effects not included in this model, a white noise vector with the noise amplitude $\tilde{\sigma}_0$ is added to the plasma temperature distribution of the system. The noise amplitude is designed to account for deviations around 10% of each element of the plasma temperature distribution. The numerical integration scheme described in Appendix A.2.1 evolves the system of equations with the time step $\Delta t = 1\,\mu\mathrm{s}$. The block returns the new state vector $\vec{x}_{new} = \begin{pmatrix} T_c \\ T_{p,1} \\ \vdots \\ T_{p,N} \end{pmatrix}$ and the value of the effective plasma radius r_p resulting from the current plasma temperature distribution. Since the flatness based control only applies for the central temperature of the arc, the system dynamics of the whole arc are still highly nonlinear and can lead to chaotic behaviour.
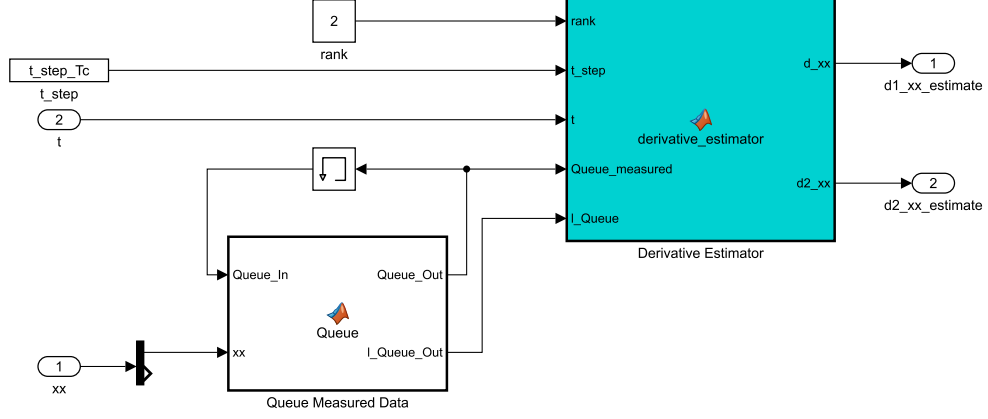
Figure 4.11: Derivative estimator of the first and second time derivative of the cathode temperature $\dot{T}_c, \ddot{T}_c$.

Derivative estimator   The derivative estimator (see Figure 4.11) has the purpose to extract the information of the first time derivative of the cathode temperature $\frac{dT_c}{dt}$ from the measured signal of T_c. Various methods can be choosen here, but regarding the properties of the measured physical quantity T_c (white gaussian noise over the measured signal) it is convinient to choose an estimator that can take care of such fluctuations of the input signal. The estimator scheme was briefly outlined in Section 4.3.4.1 and is taken from [95].

The measured signal shall be seen as the sum of a clear signal $x(t)$ and $\eta(t)$ being the component of white gaussian noise.

$$y(t) = x(t) + \eta(t);$$

The block consists of the derivative estimator algorithm in the eponymous block and a queueing block that stores the data of the number of desired measurements N of the cathode temperature T_c which shall be taken into account for this respective algorithm. It is worth noting that the derivative estimator and the observer are executed at a faster time scale than the nonlinear controller itself, defined by the parameter τ_{obs}.

Figure 4.12: Nonlinear flatness based feedback controller block

Feedback control The nonlinear feedback controller (see Figure 4.12) contains the state controlling law (Equation (4.42)). Its inputs are the values of the planned trajectory $T_c^*, \frac{d\,T_c^*}{d\,t}, \frac{d^2 T_c^*}{d\,t^2}$ and the measured value of T_c, as well as its estimated value of the effective plasma core temperature $\hat{T}_p$. The output of the controller is the current profile $I(t)$, which need to be applied to the controlled system to track the desired behaviour. This output can be directly fed to a real plasma system or a simulation environment to observe the proper behaviour of the controller.

Figure 4.13: Flatness based observer block

State observer The flatness based observer, see Figure 4.13, contains the algorithm to reconstruct the effective plasma core temperature $\overline{T}_p$ from the measured value of the cathode spot temperature T_c, according to the scheme described in Section 4.3.4.2.

Chapter 5

Results and Discussion

"I have not failed. I've just found 10,000 ways that won't work."

Nikola Tesla

5.1 Plasma radiation simulations of the thermal arc and comparison with experimental data of noble gases and mixtures

This section presents the results of the radiation simulation, based on the equations in Chapter 3. At first the particle densities calculated from the Saha eqs. (2.24) and (2.25) are displayed. Subsequently the calculated spectra for the respective gas composition will be compared to measured spectra from [9]. Likewise the electron densities and electron (or better gas) temperatures are compared to measurements from [9]. The calculations can be performed on any composition of noble gases and their mixtures, but due to the wide spread application of argon and helium, most experimental data is available here. Therefore this configuration has been chosen to compare the numerical results with experimental data of Thomson scattering measurements for the electron density and electron temperature, as well as Stark broadening spectroscopy for the electron density. The description of the experimental set up can be seen in [9]. The physical parameters from this experiment, which are important for the simulation are summerized in Table 5.1.

variable	value	meaning
T_{cool}	$300\,\mathrm{K}$	temperature of the cooled surrounding
ℓ_{arc}	$7\,\mathrm{mm}$	length of the plasma arc
I_{arc}	$150\,\mathrm{A}$	input current of the plasma arc
λ_{min}	$300\,\mathrm{nm}$	lower boundary of the spectral window
λ_{max}	$900\,\mathrm{nm}$	upper boundary of the spectral window
$\Delta\lambda$	$0.05\,\mathrm{nm}$	resolution of the spectral window
Q	$14\,\mathrm{slpm}$	gas flow rate of the shielding gas flow
E_p	$25\,\mathrm{mJ}$	energy of the laser pulse
r_{laser}	$250\,\mu\mathrm{m}$	radius of the circular focal area of the laser pulse
t_p	$4\,\mathrm{ns}$	duration of the laser pulse

Table 5.1: Simulation boundary conditions from experimental data of [9]

Based on these boundary conditions Table 5.1, the spectra are calculated for argon and argon-helium as working gases. The cost function for both setups has been calculated and minimized according to the scheme in Section 3.3. For pure argon as a process gas, the cost function reaches its minimum for a value of $r_{cool} = 5.1\,\mathrm{mm}$ as simulation parameter, for argon-helium the respective cost function reaches its minimum with parameter $r_{cool} = 3.65\,\mathrm{mm}$ and for a gas concentration of argon-helium equal to 40 -

60 %. All results will be displayed at first without discussing the deviations and their possible causes. In the following discussion section each result will be references and a combined analysis of the physical causes behind these resuults will be given. This approach is chosen since the interconnection between all results is rather complex and one can easily loose track of each implication.

5.1.1 Gas composition for pure argon and argon-helium mixtures

The gas composition for the different working gases is performed with the equations formulated in (Section 2.2).
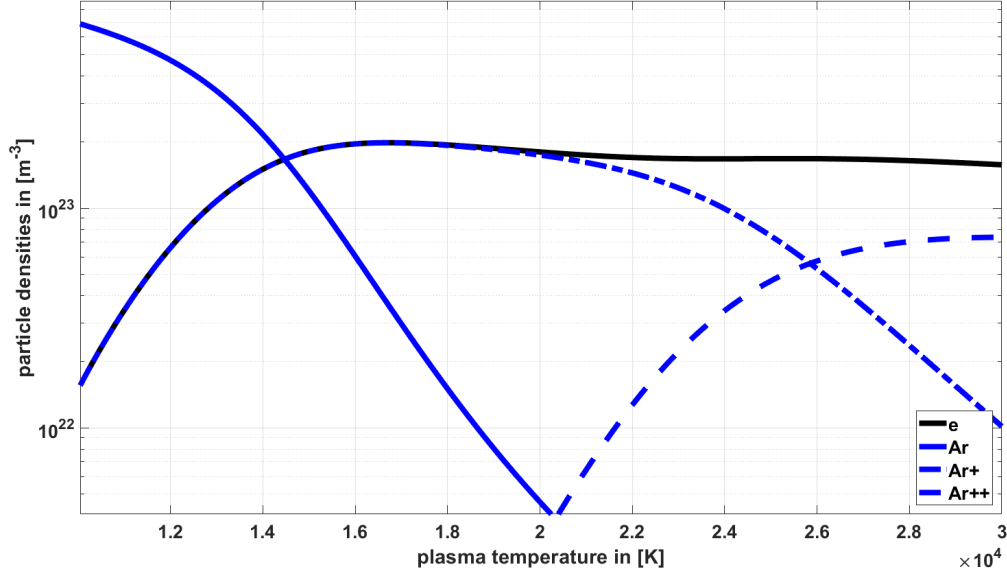
Figure 5.1: Plasma composition for an argon plasma with particle densities of each species plotted over the plasma temperature
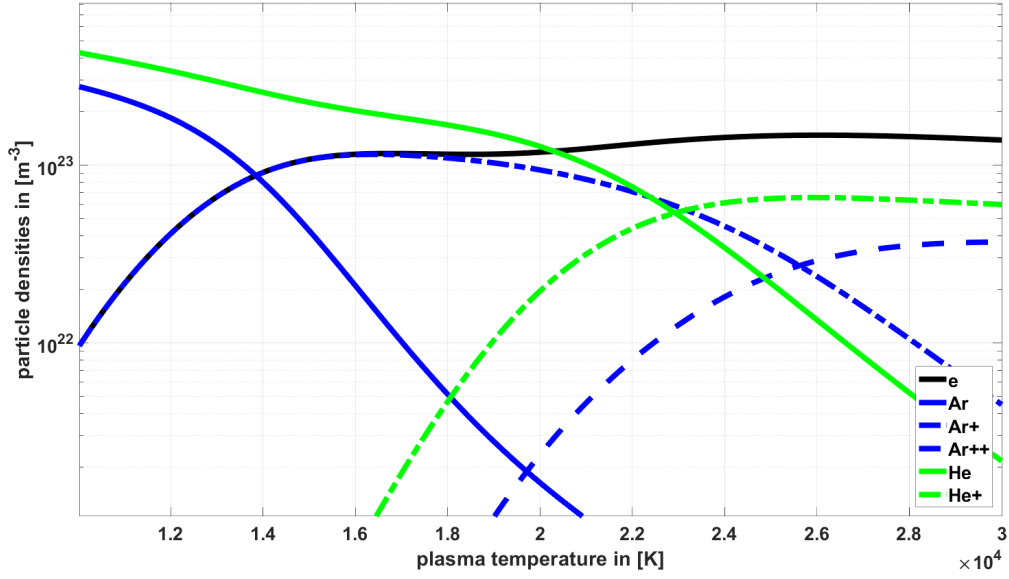
Figure 5.2: Plasma composition for an argon-helium with a ratio of 40 - 60 % plasma with particle densities of each species plotted over the plasma temperature temperature

Figure 5.1 shows the particle distribution over the plasma temperature for pure argon and Figure 5.2 for the case of an argon-helium mixture with a ratio of 40 - 60 %. The displayed curves match very well with other theoretical [99] and experimental results [9], which is reasonable under the assumption of LTE. One can see that the electron density first rises with increasing temperature, reaches a maximum at about $16\,500\,\mathrm{K}$ and than falls slightly below that value afterwards [71].

5.1.2 Sensitivity analysis of the calculated results depending on the boundary condition of the thermal arc model

Now with the data of the particle density evolution (especially the electron density) at hand, it shall be analyzed how sensitive the calculated results of the spectra and the electron densities are on a change of the boundary condition r_{cool} of the thermal arc model. One can see that the sensitivity of the spectral lines is quite different Figure 5.3, some lines (like the $763.5\,\mathrm{nm}$) show greater variation in amplitude and width, while the other selected lines only show differences in width. The changes induced into the electron density profiles is much more prominent Figure 5.4. Both height and width of the profiles chance visibly with only minor changes in r_{cool}.
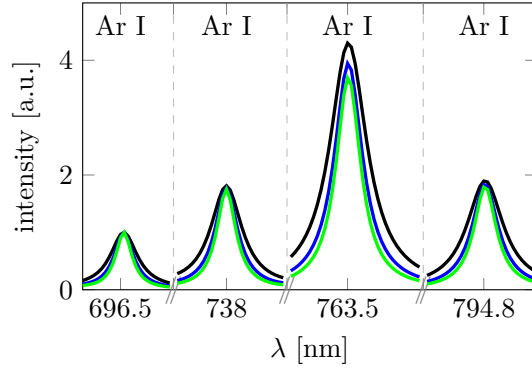
Figure 5.3: Simulated spectral line profiles for different values of the thermal boundary radius $r_{cool} = 5.1\,\text{mm}$ (black), $r_{cool} = 4.1\,\text{mm}$ (green) and $r_{cool} = 6.1\,\text{mm}$ (blue). All the spectra were normalized with the maximal simulated intensity of the Ar I 696.5 nm line and selected lines have been displayed for visibility reason.
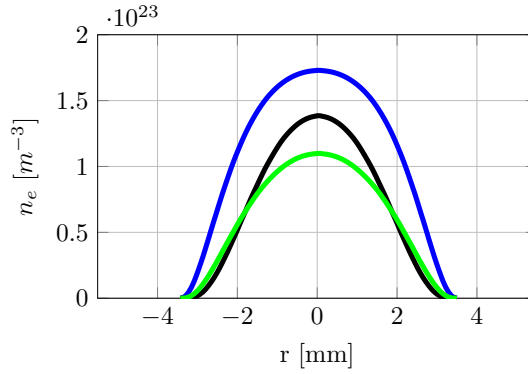
Figure 5.4: Simulated electron density profiles for different values of the thermal boundary radius $r_{cool} = 5.1\,\text{mm}$ (black), $r_{cool} = 4.1\,\text{mm}$ (green) and $r_{cool} = 6.1\,\text{mm}$ (blue).

5.1.3   Spectral emission profile and Stark broadening widths

At first it shall be displayed what dimension the Quadratic Stark broadening widths have, compared with other more detailed theoretical calculations from the literature [30, 100].

Quadratic Stark broadening widths   The Full width at half maximum (FWHM) induced by the Stark effect shall be displayed for some spectral lines. For pure argon the data calculated through this simplified model are compared with results from the literature [30, 100] [1]. The data for λ_{if} and f_{if} are extracted from NIST Atomic Spectra Database [68] for the respective gas. As can be seen in table 5.2 the values are within the order of magnitude of comparable theoretical and experimental work.

---

[1]The results mentioned here (Table 5.2) have been published by the author prior to this thesis [53]

reference	λ_0 [nm]	Ar I 549.6	Ar I 603.2	Ar I 696.54	Ar I 738.4	Ar I 763.5
this work	FWHM [0.1 nm]	1.25	1.35	2.05	1.43	2.18
[100]	FWHM [0.1 nm]	3.75	1.75	1.45	2.5	1.46

Table 5.2: Comparison of estimated Stark width at the electron temperature T_e of $14\,000$ K and electron density n_e of $1.43 \times 10^{23}\,\mathrm{m}^{-3}$

Now it shall be displayed, which spectral resolved profile calculated by the radiation model fits the measured spectral data the best in the optical range, see Table 5.1. This data will be displayed and compared to the results from OES measurements [9].

5.1.3.1 Pure Argon

Figure 5.5 shows four selected Ar I lines. The measured data was not Abel transformed, since simulated spectra were spatially integrated. The presented lines were selected as an example for the fit, as their spectral broadening data are also available in e.g. [29, 30]. As can be seen here, for all cases the measured and simulated spectral lines are in good agreement, only the 763.5 nm line shows a noticeable deviation.
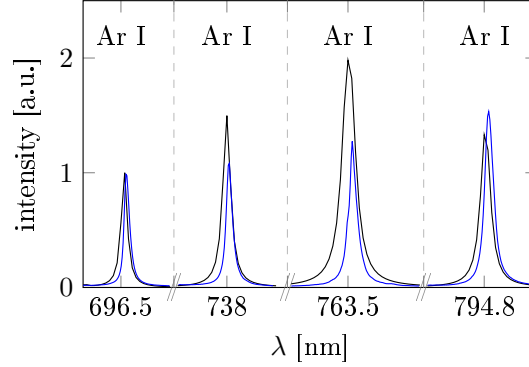
Figure 5.5: Simulated (black) and measured (blue: 2 mm from the tip of the cathode) spectra of selected Ar I lines in the central axis of the arc in pure argon. All the spectra were normalized with the maximal measured/simulated intensity of the Ar I 696.5 nm line.

5.1.3.2 Argon-Helium

For the simulation of emission spectra of the argon-helium arc additionally the gas mixture ratio needs to be estimated. In order to get a first estimate for the further iterations, a gas concentration corresponding to that of the plasma in thermal equilibrium with plasma parameters as measured by Thomson scattering was used [101]. This concentration (argon-helium 40 - 60 %) was assumed to be constant, in a first approximation, over the radius of the arc. This assumption will again be reviewed in the discussion.
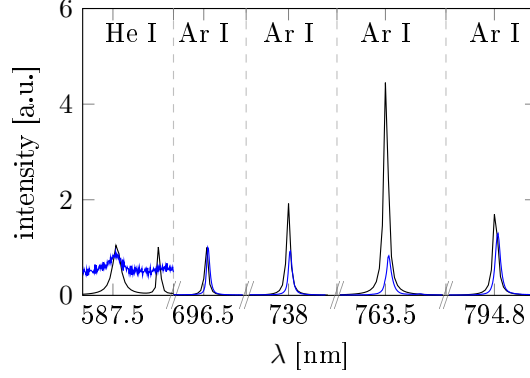
Figure 5.6: Simulated (black) and measured (blue: 2 mm from the tip of the cathode) spectra of selected Ar I lines in the central axis of the arc in argon-helium (40 - 60 %). All the spectra were normalized with the maximal measured/simulated intensity of the Ar 696.5 nm line. For visualisation purposes the He I line intensity is multiplied by factor 50.
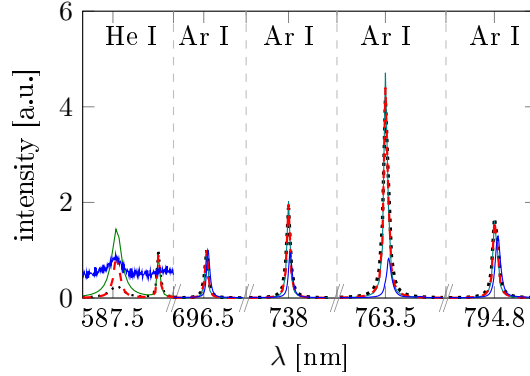
Figure 5.7: Measured (blue: 2 mm from the tip of the cathode) and simulated spectra of a selected Ar I and He I lines in the central axis of the arc for different argon-helium mixtures (red: 40 - 60 %, green: 30 - 70 %, black: 50 - 50 %). All the spectra were normalized with the maximal measured/simulated intensity of the Ar 696.5 nm line. For visualisation purposes the He I line intensity is multiplied by factor 50.

Figure 5.6 shows comparison of calculated and measured spectra for the four previously chosen Ar I lines as well as one He I line, which could be well detected in the spectrum. Here again considerable deviations can be noted for Ar I 763.5 nm line. The same reasons as discussed for the case of pure Argon are assumed here. While the line intensity of the calculated and measured He I line have the same magnitude, their width deviate slightly.

Figure 5.7 additionally shows spectra for variation of the Ar-He ratio. It can be seen that for lower He concentration the He I line becomes broader, while Ar I lines do experience a major reduction of the intensity of the calculated lines. This deviation is caused by the assumption of a constant gas composition throughout the radial coordinate of the arc model. Adding an estimation on the detailed mass fraction distribution would solve this problem and minimize the deviations for both gas components separately.

For the sake of visibility the line intensity segment displayed on the left side of Figures 5.6 and 5.7 was magnified by a factor of 50. Both results display a significant deviation in the line width of the He I line, these deviations shall be discussed in detail in the subsequent section.

5.1.4 Electron density distribution results

Now that the matching of the spectral data could be achieved, the corresponding electron density profile is displayed and compared with the results from Stark line broadening spectroscopy and Thomson scattering diagnostic [9].

5.1.4.1 Pure Argon

Figure 5.8 shows the comparison of the calculated and measured electron density profile. The calculated electron density profile (black solid line) corresponding to these spectral intensities Figure 5.5 and the electron density derived through Thomson scattering (blue dote) show comparable values. Also the evaluation of the Stark broadening of the Ar I 696.5 nm line (red triangles), without the consideration of temperature influence as described in [9] for radially resolved spectra show similar results. The profile width do not match precisely, the deviation is $\sim 10\,\%$.
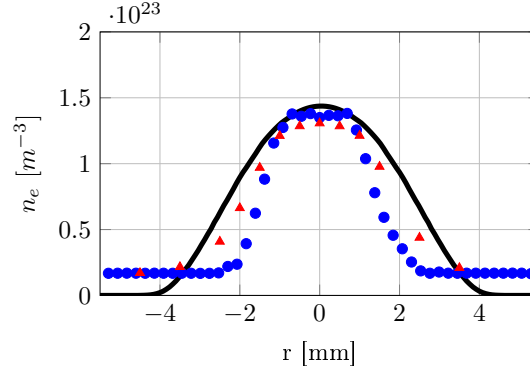
Figure 5.8: Simulated (black solid line) and measured $2\,\mathrm{mm}$ from the tip of the cathode (blue dots: Thomson scattering, red triangles: Stark broadening) electron densities in pure Argon GTAW process

5.1.4.2 Argon-Helium

Figure 5.9 shows the results for the electron density comparison in the case of Argon-Helium for the gas composition of $40 - 60\,\%$ (this ratio has been determined by the cost function minimalization together with the distance to the cold surrounding). Here a very good agreement can be noted for the density profiles determined by Thomson scattering (blue dots) and Stark broadening (red triangles). This can be explained by extending the description given for pure argon to the case of an Argon-Helium gas mixture, the thermal conductivity results from the composition of the shares of both gases. This results in an additional parameter, the mass fraction coefficient, to modify this thermal conductivity. In the case presented here a gas mixture could be found with a thermal conductivity sufficient enough to cause a radial diffusive heat flux to compensate for the Joule heating.
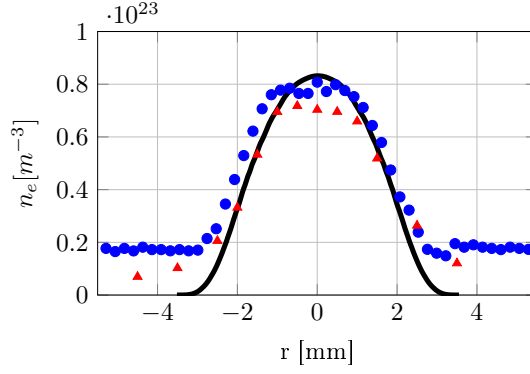
Figure 5.9: Simulated (black: 40 - 60 %) and measured 2 mm from the tip of the cathode (blue dots: Thomson scattering, red triangles: Stark broadening) electron densities in Argon-Helium GTAW process.

5.1.5 Temperature distribution results

Now it shall be discussed how the plasma temperature profile (corresponding to the electron density profile) can be reconstructed. At this point it shall again be emphazised that this data is needed to observe that the plasma temperature follows a desired trajectory, as stated in the introduction. Figure 5.10 (left) shows the comparison of calculated (black line) and measured (blue line) plasma temperature [9]. The profile width and the peak temperature do not match for this case (the devation is $\sim 22\%$ in the height and $\sim 10\%$ in the width of the profile). Comparable results are shown for the Argon-Helium gas mixture Figure 5.11. In advance to the detailed discussion in the next section it shall be explained that various phenomena can cause such deviation. This work focuses on the impact of the laser heating during the Thomson scattering measurement, as possible cause for this effect [102]. The numerical scheme Equation (2.59) has been adapted by an additional term to account for the laser heating, as discussed in Appendix A.1. The data generated with this adaption is displayed on the right side of Figures 5.10 and 5.11. The right subplots in Figures 5.10 and 5.11 show the corrected profiles
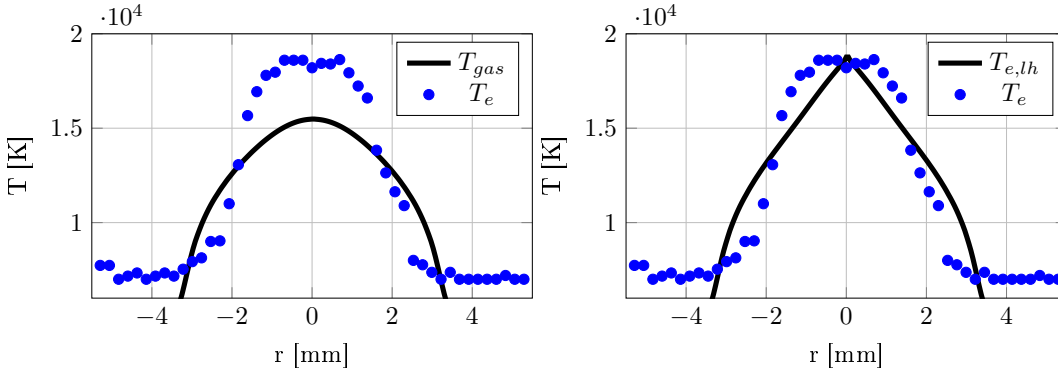
Figure 5.10: (left) Simulated (black solid line) and measured 2 mm from the tip of the cathode (blue dots: Thomson scattering) electron/ plasma temperature profiles in pure Argon GTAW process without (top) and with (right) effect of laser heating

in comparison to the measured value [9]. The peak profile temperature and the profile width are in good agreement with the measurement, if one takes into account the laser light energy of 25 mJ. The profil shape however deviates after the inclusion of the laser heating mechanism. This has been derived accordingly for the Argon-Helium gas mixture with a comparable result, as can be seen in Figure 5.11.
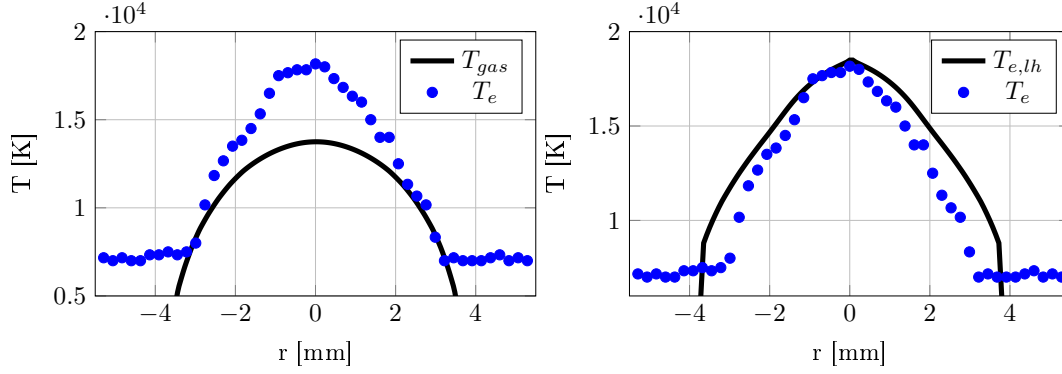
Figure 5.11: Simulated (black solid line) and measured 2 mm from the tip of the cathode (blue dots: Thomson scattering) electron/ plasma temperature profiles for Argon-Helium with gas composition of 40 - 60 % in GTAW process without (left) and with (right) effect of laser heating

The profile shaping taking laser heating into account appears to be much better in the case of Argon-Helium mixtures than the shaping for the case of pure Argon. A discussion will be given in the subsequent section.

5.1.6 Experimental validation of the assumption of a cold boundary for the thermal model

At this point the initial remark from Section 2.1 concerning the underlying plasma temperature distribution, which is defined by the parameter r_{cool}, shall be further strengthened. To clarify that the values of this parameter (which have been displayed so far in this work) are at least in the right order of magnitude, a optical diagnostic technique called Schlieren imaging has been utilized. Schlieren imaging is a visual technique that makes density gradients in the flow field accessible through interferometry of optical light passing through it [103]. It is a favourable technique to study the stream lines of a flow field for processes which work at high enough pressures (in this case atmospheric pressure) [104]. Figure 5.12 shows the Schlieren snapshot of a plasma arc in a GTAW process, with its operation conditions collected in Table 5.3. Evaluation of the pixel width of the optical camera, display the order of magnitude of the

variable	value	meaning
I_{arc}	100 A	current of the plasma arc
ℓ_{arc}	5 mm	length of the plasma arc
Q	30 l/min	gas flow rate of the surrounding cold gas

Table 5.3: Experimental paramters of the Schlieren imaging method applied to a GTAW process

distance between the plasma boundary and the surrounding flow. For the process parameters of Table 5.3 the plasma temperature profile has been calculated and compared to the marked boundaries in the Schlieren snapshot Figure 5.12. In this snapshot on can see the illuminated section in the middle, which corresponds to the discharge region of the arc. The line in green marks the Schlieren edge (only the right side is marked, but the Schlieren edge naturally exists on both sides), which is the density gradient between the flow around the plasma discharge and the surrounding cold gas flow. Two length scales are displayed in Figure 5.12, marking the dimension of the arc discharge region $r_{arc}|_{Schlieren}$ and the distance from the symmetric axis to the Schlieren edge $r_{cool}|_{Schlieren}$. Both values have been evaluated at a distance of 1.5 mm from the cathode tip (to ensure the evaluation is still taken in proximity to the cathode). The value $r_{cool}|_{Schlieren} = 4.1$ mm was deduced and taken as input for the simulation

to calculate the plasma temperature profile and the corresponding radiation intensity profile emitted by the plasma. The calculated distance of the plasma where the radiation intensity drops drastically $r_{arc}|_{calc}$ (this can be regarded as the visible border of the plasma), must be in the order of magnitude as the length $r_{arc}|_{Schlieren}$. With $r_{arc}|_{calc} = 2.0\,\text{mm}$ and $r_{arc}|_{Schlieren} = 1.6\,\text{mm}$ The deviation between both values is $\Delta\, r_{arc} = 0.4\,\text{mm}$.
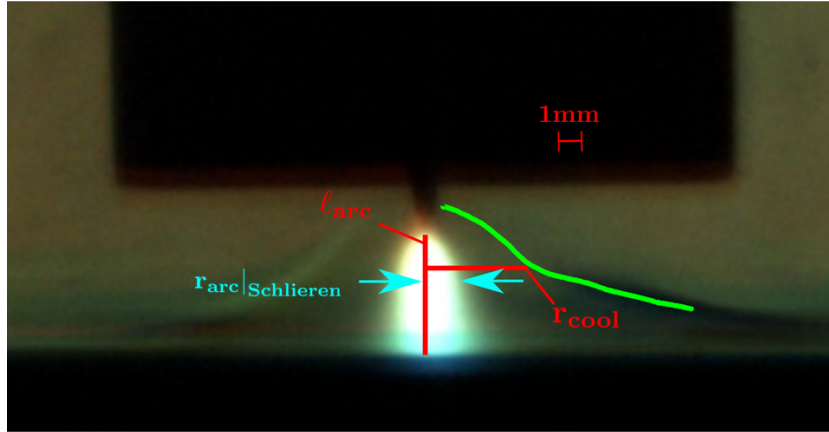
Figure 5.12: Snapshot of optical Schlieren imaging displaying the density gradient between the region of the plasma discharge and the cold gas flow of the shielding - the Schlieren edge (green line).

5.1.7 Estimation of the computational effort for radiation model

The calculations of the radiation model are segregated in three stages

1. Calculation of static radiation properties (emission and absorption coefficient). These quantities can be precalculated for a large number of parameters and stored in a lookup table. Therefore the computational effort for their calculation can be neglected at first.

2. Calculation of the temperature profiles, according to the input current and arc length. These calculation would need to be calculated in an appropriate time scale during process observation. The execution time on the given setup to 2.13 s, using the packaging technique stated at the end of the section, this time can be shortened to $\sim 10\,\text{ms}$

3. The last part is the integration of the radiation intensity, this has been executed for a cylindrically symmetrical arc with 100×100 finite difference elements. The processing time was unoptimized $\sim 37.7\,\text{s}$. Now if only the central region of the arc would be observed (and therefore reconstructed) this would shorten the execution time by a factor of 100 and utilizing packaging technique stated at the end of the section, would yield another factor of 20. This leads to a total processing time of $\sim 18.8\,\text{ms}$.

and were performed with the Matlab/Simulink development enviroment (Version:R2017b) on a desktop computer (Intel Core i5 3450 @ 3100MHz). Since Matlab is an interpreter language (which is naturally slower then source code from compiled languages like c++), the subsequently displayed computation time can be further reduced using Matlab coder to package computationally expansion sections of the code to c++ libraries.
Overall this would lead to an execution in the range of 10 - 100 Hz for intime process observation.

5.2 Discussion of the results for the radiation simulation

First of all it could be shown that the concepts and equations derived in the previous chapters for the radiation model, enabled the development of a novel analysis technique to determine the electron density and electron (gas) temperature within a thermal arc of a GTAW process. This technique is designed to work with data inputs coming from OES measurements and can be applied to processes where alternative measurement techniques like Thomson scattering diagnostics are to elaborate to be of practical use. The results calculated with this technique could successfully be compared to experimental data for argon and argon-helium gas mixtures [9, 53], which will now be discussed in more detail.

The differences in the spectral width and intensity of some lines (see Figures 5.5 to 5.7), especially in the case of the 763.5 nm line, can be caused by the fact that the applied algorithm gives a simplified estimation of the Stark broadening width. Furthermore the Bibermann correction factors for the respective gases are not yet included in the emission coefficients of the radiation.

The deviation in the line width of the He I line is actually a result of an overlap with the contribution of the continuum radiation resulting from the bound-free and free-free (or bremsstrahlung) contributions of the contiuum electrons. As can be seen from the results these effects are important mostly for lines with small intensities (such as He I), but are not the dominant effects in regard of the overall spectrum generation. At least as long as the line intensity lies about the continuum contribution and can therefore be distinguished by the cost function algorithm. Further adaptions of the algorithm shall include continuum emission coefficients (bound-free and free-free transisions). This would improve the presented results for the gas mixtures results (or in general weak line contributions), but need to be validated and examined for their respective computational costs.

The sensitivity analysis of the spectral lines showed only miniscule changes in the height and width of the spectral lines, when a change in r_{cool} is applied. This strengthens the argument stated in the introduction that evaluation of single selected lines is a challenging task. Therefore the proposed adaption, to utilize a wide range of spectral lines and apply a cost function minimalization, poses a novel method to improve the analysis of such spectral data. However since the spectral range is widened for the diagnostic, the minimalization technique is prone to artifacts within the measured spectrum. These could result from impurities of other elements (metal vapour) in the plasma. Therefore it is advisable to either screen the spectrum from such lines beforehand or limit the spectral window again to certain regions of the spectrum.

Likewise the sensitivity analysis showed a significant change induced to the electron density profiles, if r_{cool} is changed. This is a convenient fact, since the electron density is one property of interest and should be generated with this model. Not only the profile height is changed, but also simultanously the width of the profile. This is caused by the following fact. If the electron density value is fixed, so is the maximum achievable electron temperature if the LTE condition is fullfilled (the plasma temperature can be derived from the graphs of the particle densities Figures 5.1 and 5.2. Since the plasma temperature is fixed in the centre of the plasma, the arc widens itself in order to transport the heat towards the cold surrounding and a balance is again maintained.

Also the broader width of the electron density (Figure 5.8) and electron temperature profiles (Figure 5.10) can be explained by the fact that the presented simplified thermal arc model of Section 2.1 takes into account radial diffusive heat transfer as the main and only cooling mechanism for the Joule heating. Although this equation is solved radially and takes the temperature dependence of the thermal conductivity into account, this leads to a slight underestimation of the radial heat flux. Due to this underestimation of the radial cooling effect the plasma temperature distribution is to wide (and a bit to low in the centre), which in turn results in a wider radial electron density distribution.

However the calculated temperature profiles in Figure 5.10 and Figure 5.11 show a 22 % deviation from the measured values in the centre of the arc. Still in this case the initial remark of Section 2.1, that the radial diffusive heat transfer is the main source of energy transfer still remains valid, to some extend. The deviation in the central plasma temperature of $\sim$ 22 % (in the case of argon) can not only be explained by an underestimated energy transport towards the edges. Based on the measurements of the electron density and the Saha equation (in Section 5.1.1), it can be seen that for the measured electron density the corresponding plasma temperature matches the calculated one in Figures 5.10 and 5.11(under the assumption of LTE). Not only the profile height is changed, but

also simultanously the width of the profile. This is caused by the same effect as stated in the case of the electron density profile width, since electron temperature and density are directly coupled. This is further supported by calculations [102] and measurements [35, 37, 38, 101, 105–107], which indicate that other physical causes have considerable impact on this deviation. However the huge deviation in the central temperature contradicts theoretical [29] and experimental [108, 109] evidence, that the regions away from the electrodes and fringes are in (or close to) LTE for electron densities above about $1 \times 10^{23} \, \mathrm{m}^3$. This is caused by the fact that rapid equilibration of states due to the high collision rates take place. Such electron densities occur at temperatures above $12\,800 \, \mathrm{K}$ in atmospheric pressure argon plasmas. However it has been shown in [105](utilizing the Stark Shift measurement, which does not have such a strong plasma temperature dependence as the Stark broadening width in [108, 109]) that for the region in proximity to the cathode (as stated to be closer than $2 \, \mathrm{mm}$ from the tip of the cathode, which is also the case for this work) this condition is non clearly fullfilled. It is stated that in this distance the cathode fringe still has a noticable impact and a slight deviation from LTE ($\theta \sim 1.2$ is possible.

This topic however is still prone to rigorous discussion within the plasma physics community, albeit there are various approaches to explain this deviation [37, 38], this work wants to follow the approach of [102]. According to this concept it means that for the applied measuring method (Thomson scattering diagnostic) additional heating of electrons occurs along the laser line of sight within the plasms arc, due to the influence of the laser pulse. This has significant impact on the reconstruction of the electron temperature value. Since the respective time scale of the interaction of the laser beam with the plasma is too short for the heavy particles to react, due to their inertia, the energy of the beam is primarily transferred to the electrons. This causes a slight deviation in the thermal equilibrium between electrons and heavy species resulting in two separate temperatures during exposure of the plasma to the laser radiation. Comparable discussions about the influence of the laser radiation on the measurement of the plasma temperature have been presented in [106]. The results derived with the additional laser heating term agree well in absolute height and width with the measured profiles for argon and argon-helium mixtures Figures 5.10 and 5.11, the deviation is $\sim 5\,\%$ in height and $\sim 10\,\%$ in width.

However the shape of the profile does not match entirely. The impact of the laser heating contribution based on the presented model is dominated by two effects, the heat transport determined by the thermal conductivity of the plasma mixture and the absorption coefficient of the laser light α in Equation (A.2). This itself is a strongly nonlinear function of the electron density, electron temperature and the refractive index μ. The last quantity μ is again a function of the first two quantities. According to [110] the refractivty μ of the plasma is a sum of the contributions from each respective gas species, while the neutral atom contributions appear to by constant over a wide range of wavelength the dominant contribution of the electron was determined by the classical dispersion formula of Eccles, Larmor, Kramer [110]. This formula is dependent of the square of the wavelength and linear dependent of the electron density. Other contributions were disregarded. From the comparison to the experiment it appears that the deviation of the electron temperature profile leads to a significant change in the absorption coefficient, due to the strong dependence from the electron temperature. However in the case of the given argon helium mixture the mol fraction of helium is higher and thereby the overall thermal conductivity compared to the pure argon case. This higher thermal conductivity benefits the shaping of the temperature profil and in return that of the absorption coefficient. Furthermore the disregard of ion contributions to the refractivity, might not be fitting for the precent case and add up to deviations in the sinlge percent range for the refractivity as well.

Also these deviations are noticable, their impact with regarded to the proposed application of this work is not so strong. The presented radiation model is able to calculate electron density and temperature profiles with comparable size and shape as measured with other experimental methods, but in a much faster time than other data processing techniques. Combined with the results of the estimated computational effort, this enables the possibility to use this technique for data processing on plasma parameters in applications where spectral analysis in the range of 10 - 100 Hz is required.

The discussion above displays the importance of the thermal arc model accuracy for all predictions made by this radiation model. It is therefore important to further validate the assumption on the boundary conditions of that model. As dicussed in Section 2.1 the thermal model is limited to the proximity of the cathode, since it is based on a finite distance to a cool surrounding r_{cool}. This

means that other flow specific mechanisms like turbulence can be disregarded to some extend, since the dominant effect arises from diffusive heat transport. This model therefore accounts quite well for processes where a solid or fluid boundary condition confines the plasma arc. For processes without such a wall one needs to verify if the assumption on the cold surrounding boundary still holds. A diagnostic technique that gives information on the size and shape of the flow field of the respective process is the Schlieren imaging [103]. The results from Section 5.1.6 further strengthens the assumption, that such a distance to a cold surrounding is applicable for the observed process, at least in first order. The comparison of the derived length scales coming from the optical evaluation of the Schlieren snapshot with the calculated ones from the thermal arc model show very good agreement. The deviation in the two length scales is only $\Delta r_{arc} = 0.4\,\mathrm{mm}$, which corresponds to an error $< 20\,\%$. For the Schlieren imaging data presented here, no spectroscopical data was available and the optical filters used do influence the radiation detected coming from the plasma, which poses as a source of error for determining the value of $r_{arc}|_{Schlieren}$. While this is just a coarse quantitative analysis, both presented length scales are of comparable size, so it can be assumed that the initial remark Section 2.1 can be regarded as valid. The flow in proximity to the cathode of the discharge can be regarded as close to being laminar. Disturbances due to cold gas intake can be neglected in a first approximation. Although no detailed spectroscopic analysis has been carried out on this specific process, the data derived with it and the experimental data from [9, 101], show a consistent picture that strengthens the predictions of the displayed radiation model.

For gas mixtures the assumption of a constant gas ratio over the radial profile is only valid in a short time frame of a measurement. This time frame is essentially defined by the diffusion velocity and the radial extension of the plasma arc, since the effect of demixing plays an important role for gas mixtures [111] (especially argon-helium). However the displayed radiation model could successfully demonstrate this possibility to adjust the gas composition ratio by itself in line with the experimental results. A enhancement of the radiation model by including a radial diffusion (demixing) model would therefore be helpful to improve the tracking of gas composition changes.

The presented radiation model incorporates concepts from different existing diagnostic techniques, such as the Fowler-Milne method with all its derivative modifications [44–48] and the net emission coefficient [50, 51] and extends them with a more detailed description for the underlying temperature distribution across the plasma, which is not present in neither of them. First of all, no Abel inversion is needed to evaluate the spectral intensities. Based on the simplified thermal arc model the spectral resolved total radiation intensity is calculated, including the absorption coefficient of each respective line, which is calculated and included to derive the radiation intensity of each element along the integration region. The broadening of spectral lines is included, utilizing a simplified scheme for the Quadratic Stark effect in noble gases. Last but not least, the algorithm incorporates a cost function minimization, which can take either the intensity and spectral width of single lines or a whole spectral range of lines into account.

On the contrary the advantage of the state-of-the-art Fowler-Milne methods lies in the fact that no assumption on the underlying thermal distribution is needed to perform a diagnostic. In contrast the set of lines adaquate for this evaluation must be carefully taken and gases with strongly absorbing lines can only be evaluated under specific circumstances. The presented scheme on the opposite demands a description of the thermal distribution. This could be shown to be reasonable for GTAW processes in the proximity of the cathode, if a shielding or gas flow around the arc is present. Developing this idea further this technique could be fruitful for applications in plasma cutting and plasma spraying [1, 2] as well, if a solid or fluid boundary condition for the distribution of the plasma temperature can be applied.

5.3 Plasma dynamic simulations

This section presents the results of the dynamic plasma simulation. At first the steady state solutions for the radial plasma temperature profile and the thermal potential distribution for a defined input current I_{arc} are displayed. This strengthens the validitiy of the assumption to simplify the dynamics of the plasma for a model based control, by introducing a effective radius r_p to track the motion of the plasma. Further on the steady state solution is the starting solution for the tracking of a desired trajectory later on in this chapter.
Simulation results I: stationary state, containing:

- steady state solutions of the radial plasma temperature profile $T_p(r)$

- corresponding values of the cathode temperature T_c

- radial thermal potential distribution $\Psi_{th,p}$

- current-voltage charactersitic

In the next step it shall be displayed that the model based control is able to maintain the system in a desired state, by tracking a constant state value of the cathode temperature and of the plasma temperature. Afterwards the tracking of a desired trajectory in the plasma temperature $\hat{T}_p$ shall be displayed with a profile according to Figure 4.8, starting from a steady state with the input current $I_{arc} = 150\,\text{A}$. The repetition frequency of the pulse shape is chosen to be $f_{pulse} = 140\,\text{Hz}$, with a sampling frequency of $f_{sample} = 100\,\text{kHz}$, a desired difference in plasma temperature of $\Delta \hat{T}_p = 2000\,\text{K}$ and an observer frequency of $f_{obs} = 500\,\text{kHz}$. This case is further along defined as the reference case and each consecutive case changes one parameter of this set up. The described cases are again summerized in the following:

- tracking constant cathode temperature T_c

- tracking constant plasma temperature $\hat{T}_p$

- tracking reference trajectory in $\hat{T}_p$

- tracking reference trajectory in $\hat{T}_p$ with higher frequency f_{pulse}

- tracking reference trajectory in $\hat{T}_p$ with higher difference temperature $\Delta \hat{T}_p$

The Table 5.4 summerizes these boundary conditions and the following subsections cluster the simulation dataset according to these cases.

case	f_{sample} in [kHz]	f_{pulse} in [Hz]	$\Delta \hat{T}_p$ in [K]	$\tilde{\tau}_{control}$ in [s^{-1}]	$\tilde{d}$	comments
1	40	0	0	0.0002	0.5	constant T_c
2	40	0	0	0.0002	0.5	constant $\hat{T}_p$
3	100	140	2000	0.00005	0.5	
4	100	1400	2000	0.0002	0.5	high pulse repetition rate
5	100	140	4300	0.000125	0.5	high $\Delta \hat{T}_p$

Table 5.4: Summary of cases and boundary conditions for the tracking of a plasma temperature trajectory

All results will be displayed at first, without discusssion of the deviations and their physical causes, this will be carried out in the consecutive section.

5.3.1 Simulation results I: stationary state

This subsection presents the data for the steady state points of the regarded GTAW process. The thermodynamical properties for the Argon gas have been taken from the appendix tables in [59]. The ionization energy and the energy levels for Argon in neutral and the first two ionized states, required for solving the Saha equation and determining the electron density within the plasma arc, are taken from [68]. The other material parameters are listed in Table 5.5.

The stationary state is obtained from the numerical integration of eqs. (2.56) and (2.61) with a very

variable	value	meaning
r_{cool}	$5.5\,\mathrm{mm}$	radial coordinate for cold surrounding with temperature $T_{cool} = 300\,\mathrm{K}$
ℓ_{arc}	$7\,\mathrm{mm}$	arc length
z_c	$4\,\mathrm{mm}$	cathode's with between hot surface and back cooling
ε_c	1	cathode's surface emissivity
ρ_c	$19.25 \times 10^3\,\mathrm{kg\,m^{-3}}$	cathode's mass density (tungsten)
$c_{p,c}$	$138\,\mathrm{J\,kg^{-1}\,K^{-1}}$	cathode's heat capacity (tungsten)
$\lambda_{th,c}$	$170\,\mathrm{W\,m^{-1}\,K^{-1}}$	cathode's thermal conductivity (tungsten)
Φ_c	$4.6\,\mathrm{eV}$	cathode's work function (tungsten)

Table 5.5: Geometrical boundary conditions and material parameters for the plasma arc - cathode spot simulations

large time step $\Delta t \approx 1\,\mu\mathrm{s}$. Five different stationary arc currents are considered Table 5.6. The resulting stationary plasma arc temperature distribution for each stationary case is represented in Figure 5.13, solved for a radial resolution of $N = 50$, i.e. the number of concentric layers from $r = 0$ to $r = r_{cool}$ is $N = 50$.

	Case A	Case B	Case C	Case D	Case E
I_{arc}	$50\,\mathrm{A}$	$100\,\mathrm{A}$	$150\,\mathrm{A}$	$200\,\mathrm{A}$	$300\,\mathrm{A}$

Table 5.6: Cases for the input plasma current to evaluate stationary states for an Argon plasma
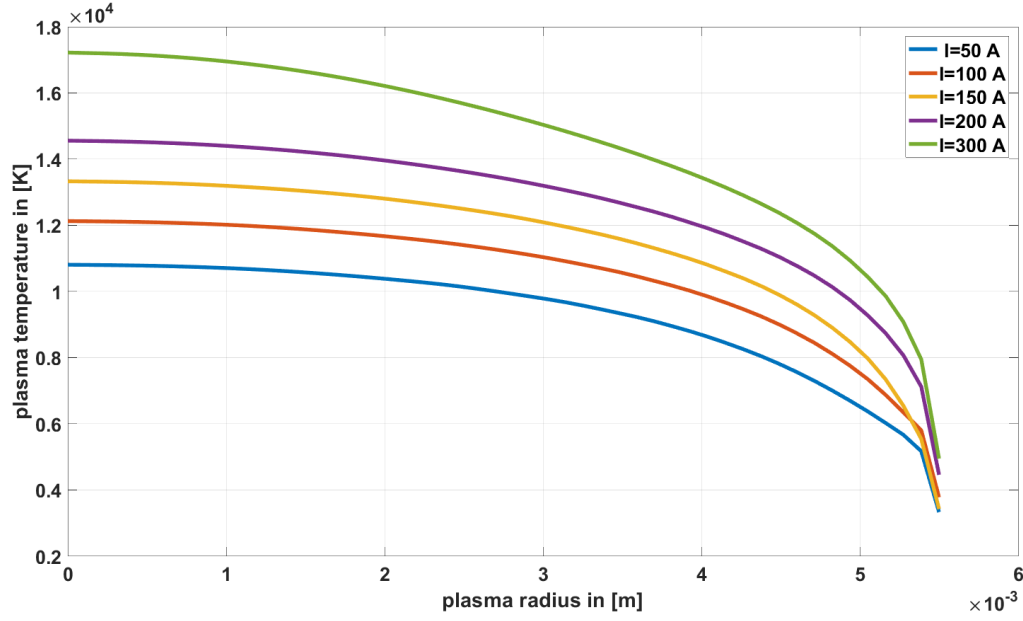
Figure 5.13: Radial profile of plasma arc temperature for the 5 steady states of Table 5.6 and the parameters in Table 5.5; resulting cathode spot temperatures are $T_c = 3474\,\mathrm{K}$ (A), $T_c = 3798\,\mathrm{K}$ (B), $T_c = 3973\,\mathrm{K}$ (C), $T_c = 4074\,\mathrm{K}$ (D), $T_c = 4135\,\mathrm{K}$ (E)

The corresponding radial distribution of $\psi_{th,\,p}(x) = \int_{T_0}^{T_p(x)} \lambda_{th,\,p}(T)\,dT$ as a function $x = \dfrac{r_p^2}{r_0^2}$ for each stationary case is depicted in Figure 5.14, and as it can be seen, it decreases linearly in a first approximation. This result validates the approximation carried out in the simplified dynamics model for determining the effective plasma core radius r_p.
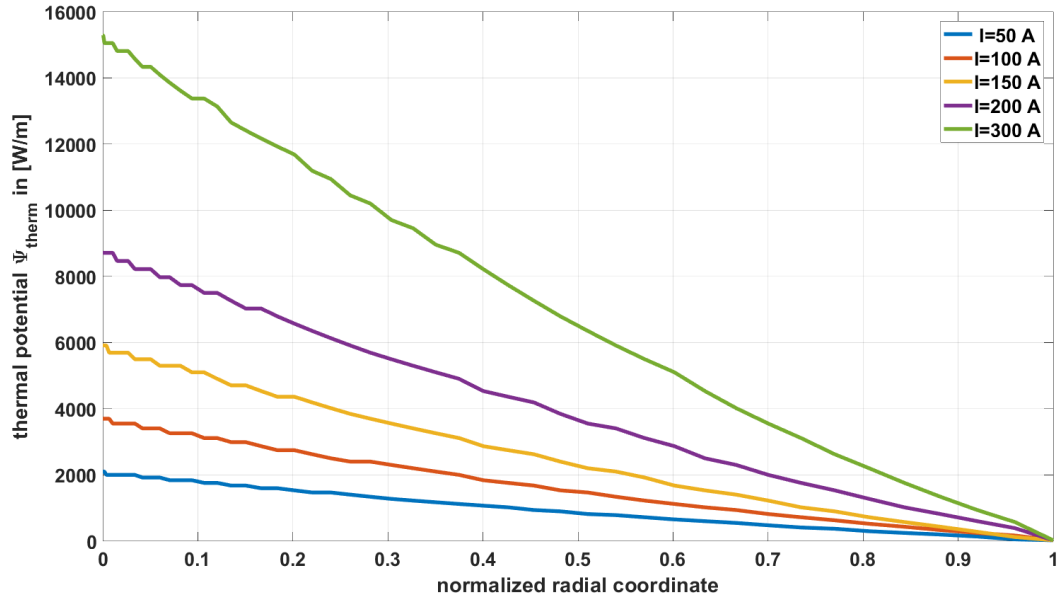
Figure 5.14: Radial profile of $\psi_{th,\,p}(x) = \int_{T_0}^{T_p(x)} \lambda_{th,\,p}(T)\,dT$ as a function of $x = r_p^2/r_0^2$ for the 5 steady states of Table 5.6

To compare the results calculated with Equation (2.53) with experimental data the current-voltage characteristic are again calculated for an arc length $\ell_{arc} = 4\,\mathrm{mm}$
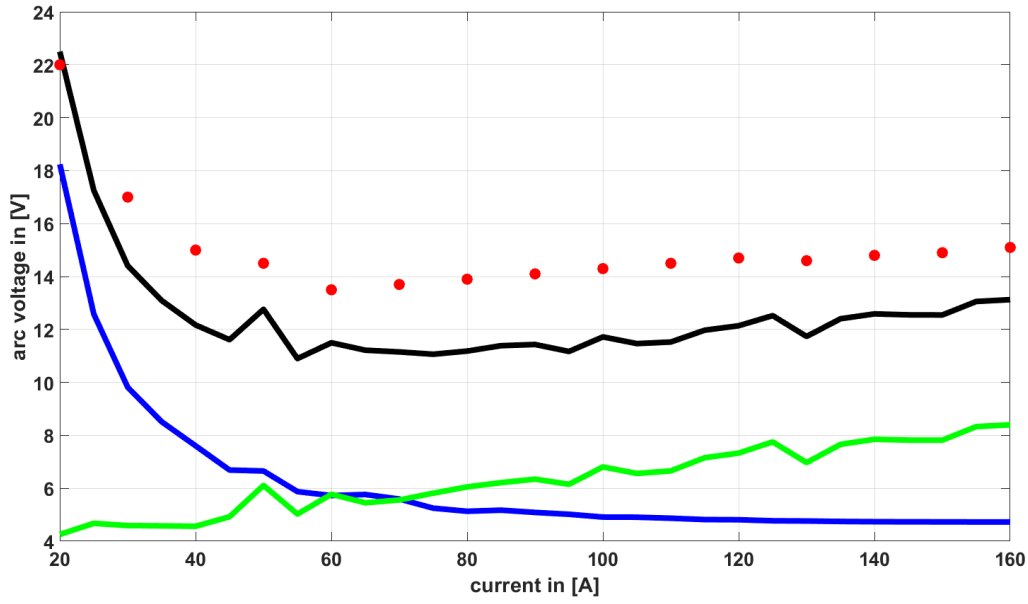
Figure 5.15: Calculated overall current-voltage characteristic of the model (black) and measurements from [112] (red marks). The green line marks the contribution of the plasma bulk and the blue line of the cathode sheath voltage drop.

and a value of $r_{cool} = 2.8$ mm, see Figure 5.15. These operational conditions were taken to compare the calculated data with measurements from [112] for a GTAW process with identical operating parameters $I_{arc} = 100$ A. Although no spectroscopical data is available in that reference, the measurements indicate comparable results for the calcualted and measured steady state solutions. The slight deviation in the voltage of about 2 V results from the missing contribution of the anode voltage drop, which is in that order of magnitude. Nevertheless the characterisitic curve is sorresponding to the measurements, at first a steeply decreasing profile, reaching a minimum and then linearly rising again. This behaviour is well incorporated, since it mostly depends on the cathode voltage drop and the bulk voltage drop contribution.

5.3.2 Simulation results II: trajectory tracking

5.3.2.1 Case 1: Simulation of constant cathode temperature T_c operation

The following graphs display the behaviour of the controller if a trajectory of constant value for the cathode temperature $T_c|_{desired} = 4060\,\text{K}$ is imprinted into the plasma system Figure 5.16. The controller starts from the steady state solution $T_c = 3973\,\text{K}$ for a input current of $I_{arc} = 150\,\text{A}$ and is then raised and maintained at the desired value by the controller. The initial disturbance comes from disturbed data of the observer. The controller recovers this behaviour and reaches a constant value of T_c within the first $0.004\,\text{s}$ and is then able to maintain this state throughout the rest of the regarded time frame. Only a small fraction of that time frame is displayed here in order to make the controlling behaviour visible.

Figure 5.17 shows the corresponding current profile generated by the controller to achieve the above mentioned behaviour in T_c
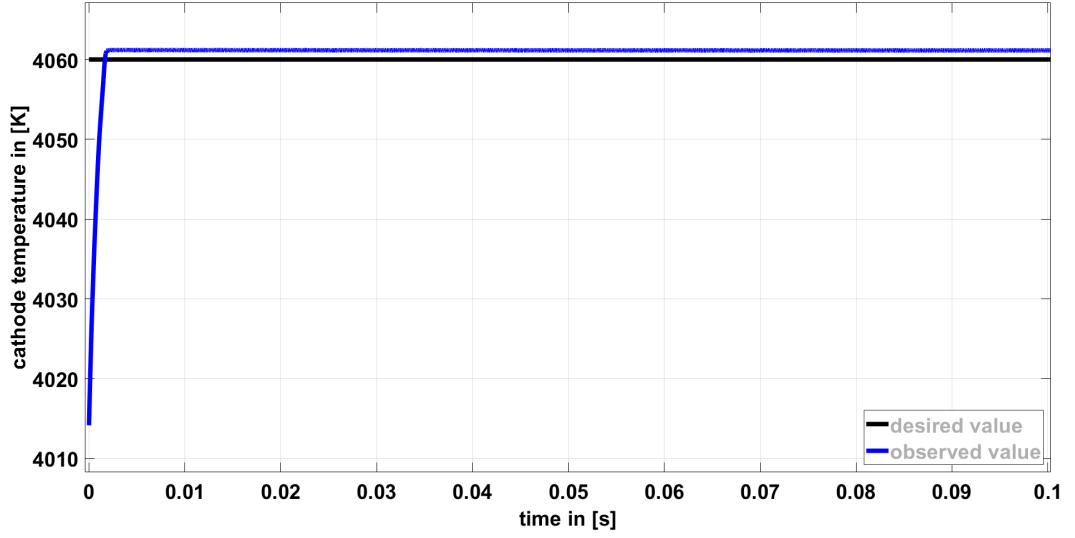
Figure 5.16: Constant T_c trajectory desired value(black) and realized behaviour(blue)
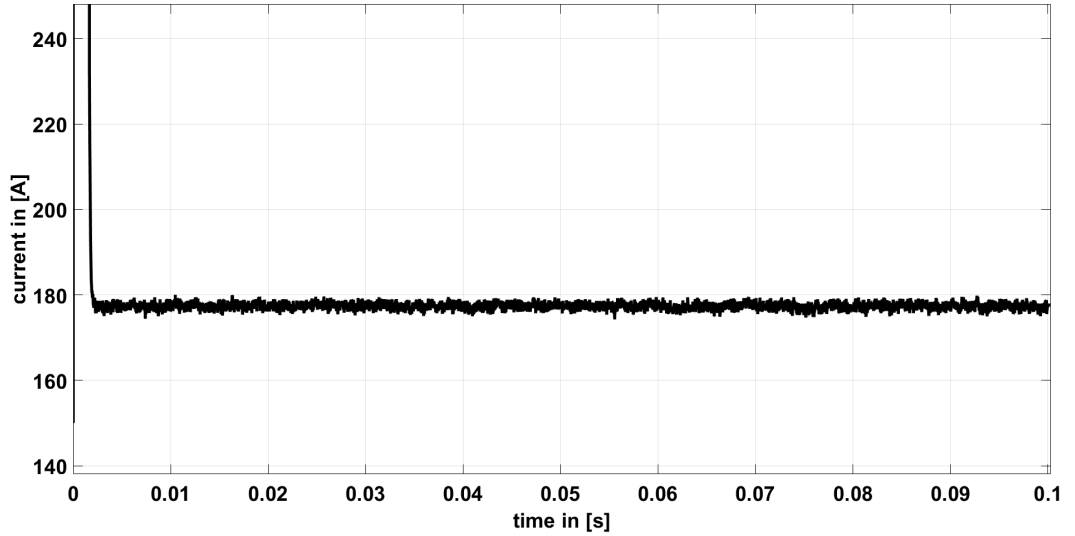
Figure 5.17: Constant T_c trajectory and corresponding current profile I

5.3.2.2 Case 2: Simulation of constant plasma temperature T_p operation

The following graphs display the behaviour of the controller if a trajectory of constant value for the plasma temperature $T_p|_{desired} = 13\,700\,\text{K}$ is imprinted into the plasma system Figure 5.18. The controller starts from the steady state solution $T_p = 13\,855\,\text{K}$ for a input current of $I_{arc} = 150\,\text{A}$ and is then decreased and maintained at the desired value by the controller. The initial disturbance comes from disturbed data of the observer. The controller recovers this behaviour and reaches a constant value of T_p within the first $0.003\,\text{s}$ and is than able to maintain this state throughout the rest of the regarded time frame. Only a small fraction of that time frame is displayed here in order to make the controlling behaviour visible.

Figure 5.19 shows the corresponding current profile generated by the controller to achieve the above mentioned behaviour in T_p
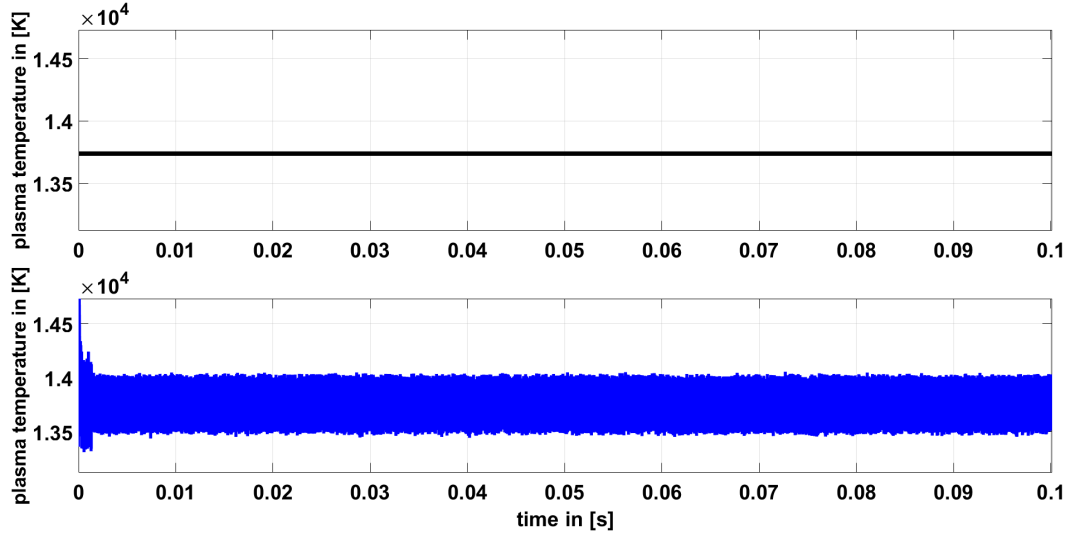
Figure 5.18: Constant T_p trajectory desired value(black) and realized behaviour(blue)
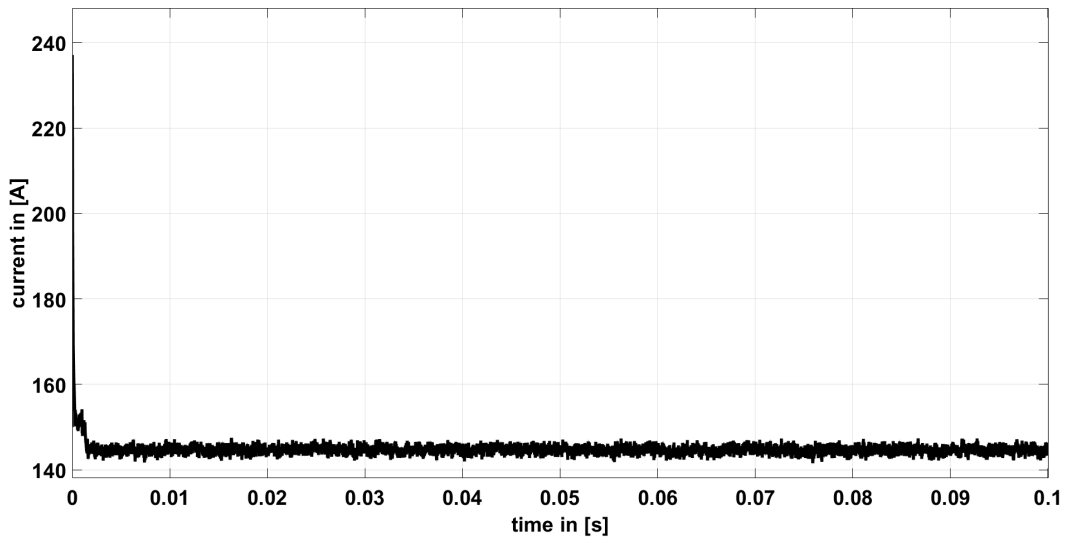
Figure 5.19: Constant T_p trajectory and corresponding current profile I

5.3.2.3   Case 3: tracking of the reference plasma temperature trajectory T_p

The following subsection displays the capabilities of the model based control to track a trajectory in the plasma temperature T_p profile. Various properties are of interest for such a trajectory, the maximum temperature difference ΔT_p achievable between the peak and through points of the curve. The shape of a pulse within the temperature trajectory, which in the presented case is a trapezoid with very steep flanks Table 5.8, as displayed in Figure 5.21. Last but no least the repetition rate of such a pulse shape, which defines the oscillations ontop of the trajectory profile.

Initially the system starts at the stationary state corresponding to a plasma current of $I_{arc} = 150\,\mathrm{A}$, whose plasma temperature radial profile is represented in Figure 5.20; the corresponding cathode spot temperature reads $T_c = 3973\,\mathrm{K}$. Afterwards the periodic pattern of Figure 5.21 is taken as the desired trajectory for the plasma core temperature.
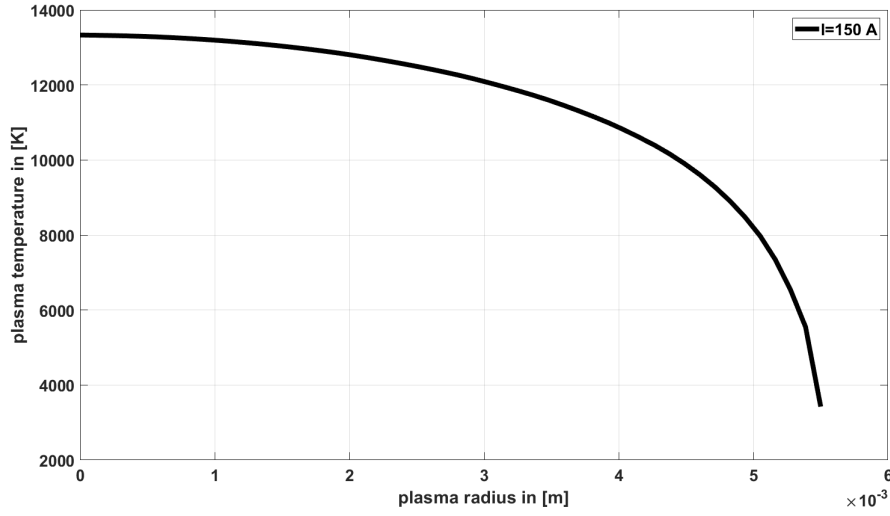
Figure 5.20: Radial profile of plasma arc temperature for a steady state with a arc current $I_{arc} = 150\,\mathrm{A}$ and the parameters in Table 5.5; resulting cathode spot temperature $T_c = 3973\,\mathrm{K}$
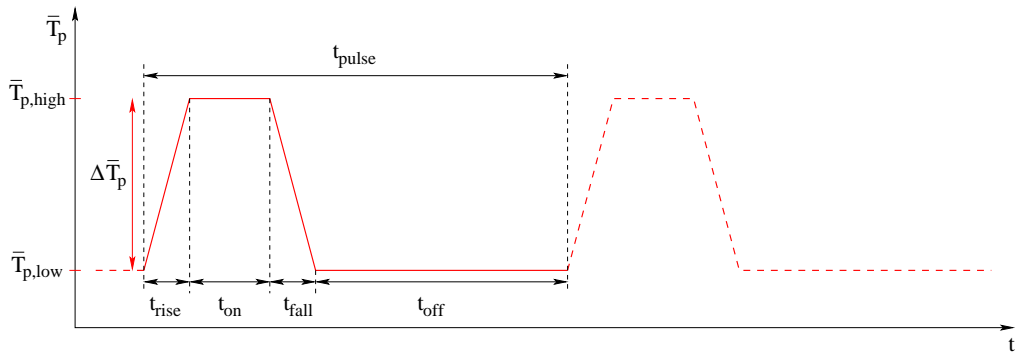
Figure 5.21: Desired periodic trajectory for the plasma core temperature

variable	value	meaning
$\tilde{\tau}_{control}$	$50\,\mu\mathrm{s}$	time scale for flatness-based state feedback
$\tilde{d}$	0.5	damping factor for flatness-based state feedback
$\dot{\lambda}_{1/2}$	$1 \times 10^4\,\mathrm{s}^{-1}$	eigenvalues for high-gain observer
$\tilde{\varepsilon}$	0.5	$\tilde{\varepsilon}$ parameter for high-gain observer

Table 5.7: Case 3 - Derived control and observer parameters for the dynamic simulations

variable	value	meaning
t_{pulse}	$7\,\mathrm{ms}$	pulse period for desired trajectory of plasma core temperature
$t_{rise} = t_{fall}, t_{on}$	$0.5\,\mathrm{ms}, 3\,\mathrm{ms}$	time parameters for desired trajectory
$\Delta \overline{T}_p$	$2000\,\mathrm{K}$	desired amplitude of plasma core pulsation

Table 5.8: Case 3 - Shaping parameters of the desired trajectory

The non-modelled effects in the system dynamics, such as the influence of a high gas flow and turbulence, gradients in pressure and in temperature along the downstream direction, are effectively taken into account by including a white noise contribution as discussed (see Equation (2.60)). The strength of the white noise signal for these simulations is chosen equal to $\tilde{\sigma}_0 = 5 \times 10^8$, corresponding to at least 10% of the total contribution in vector $\vec{b}$. The numerical integration of the equations of motion is performed with a time step $\Delta t = 1\,\mu\mathrm{s}$ and the update of the derivative estimator, as well as of the observer, takes place with a time step $\Delta t_c = 2 \times \Delta t$. The parameters for the control and observer design, as well as for the desired trajectory, are listed in Table 5.7 and Table 5.8. The cathode spot trajectory corresponding to the periodic desired behavior of the plasma arc temperature is represented in Figure 5.23. In Figure 5.23 the desired plasma temperature profile is displayed (black) and the reconstructed value of the effective plasma temperature of the observer, according to Equation (4.5). The resulting behaviour of the real system when applying trajectory $T_c^*(t)$ can be seen in Figure 5.24.
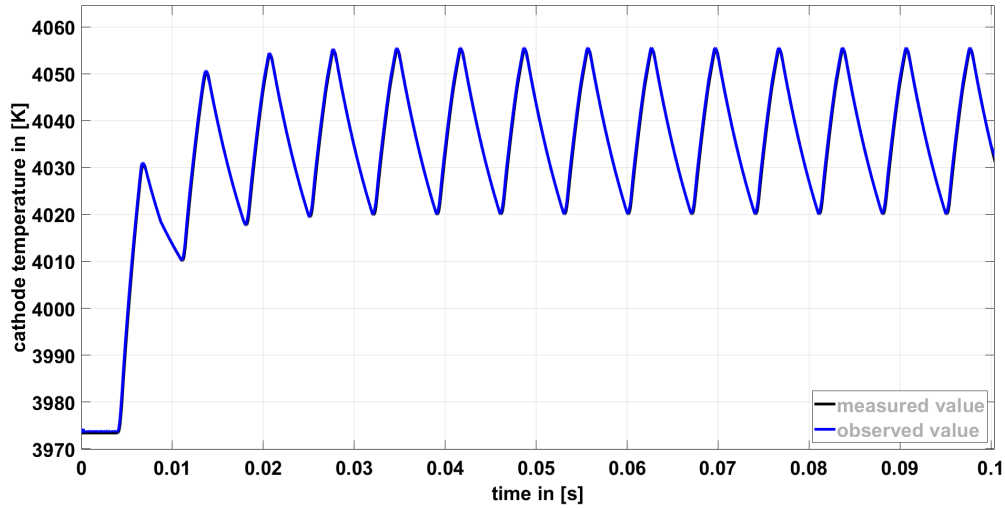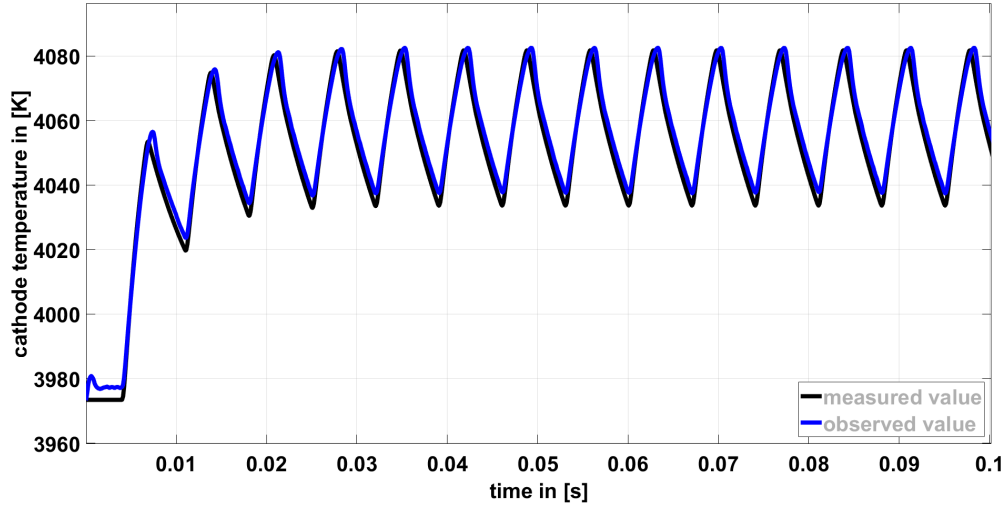

Figure 5.22: Case 3 - Trajectory $T_c^*(t)$ corresponding to the measured (black line) and the observed behavior (blue line) of the plasma arc temperature of Figure 5.21 with parameters of Table 5.8
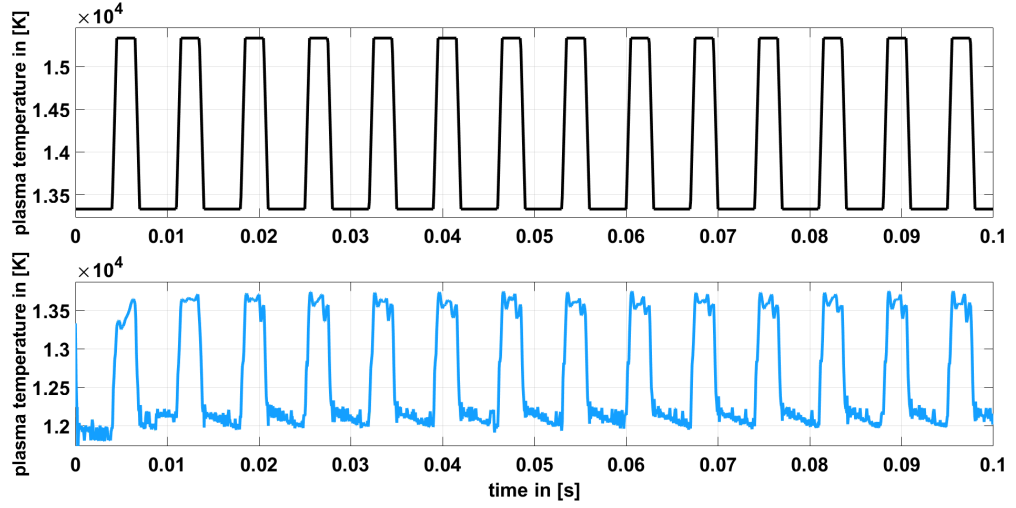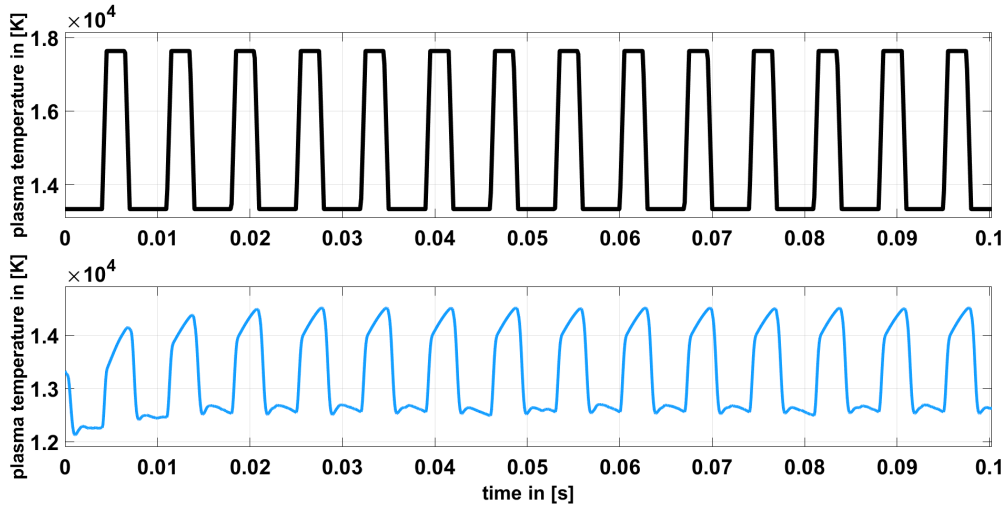
Figure 5.23: Case 3 - Desired plasma arc temperature evolution (black line) and estimated value from the observer (blue line) for the reference case; $\tilde{\tau}_{control} = 50\,\mu\mathrm{s}$, $\Delta t = 1\,\mu\mathrm{s}$, $\Delta t_c = 2\Delta t$, high-gain observer
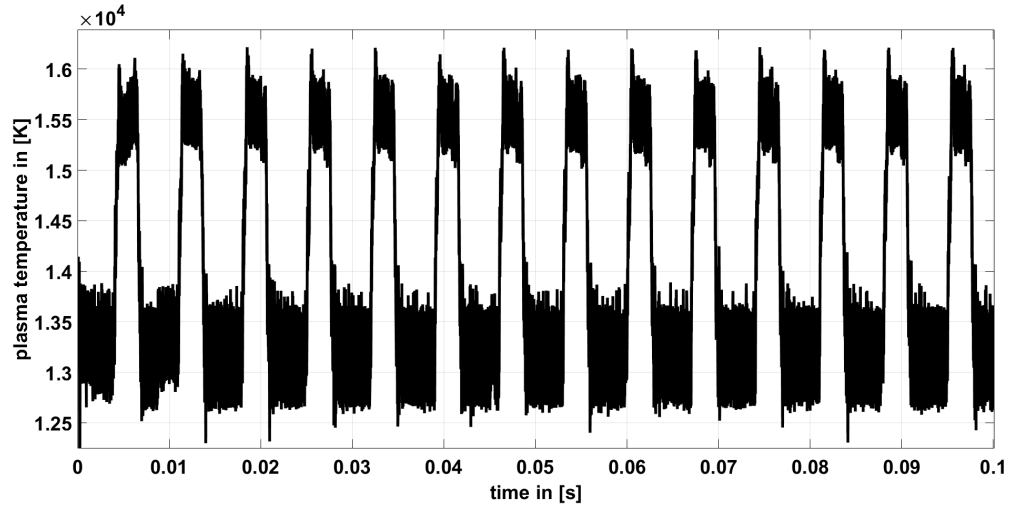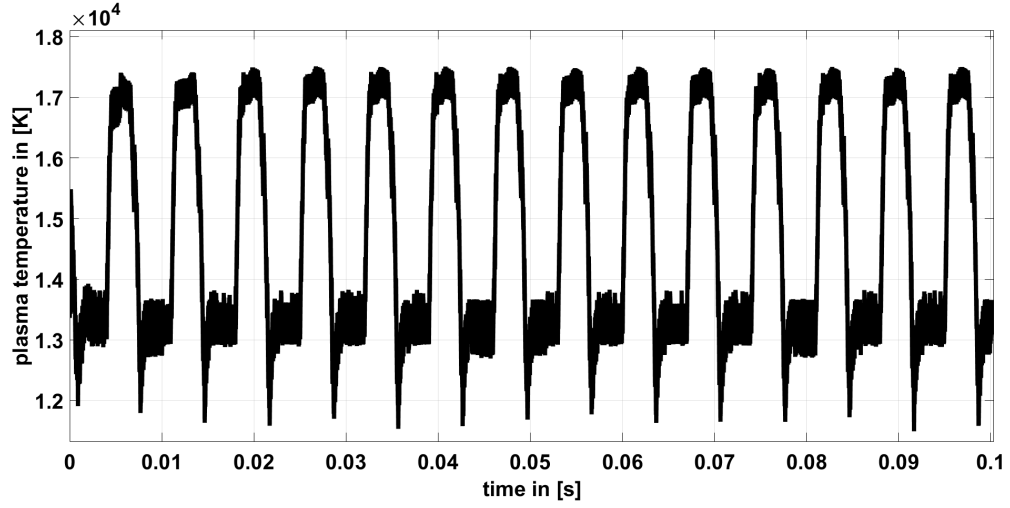

Figure 5.24: Case 3 - Resulting value of the central plasma temperature (the other values of the radial plasma temperature distribution are not displayed for visibility of the profile) corresponding to the current profile generated by the model based control; $\tilde{\tau}_{control} = 50\,\mu\mathrm{s}$, $\Delta t = 1\,\mu\mathrm{s}$, $\Delta t_c = 2\Delta t$, high-gain observer
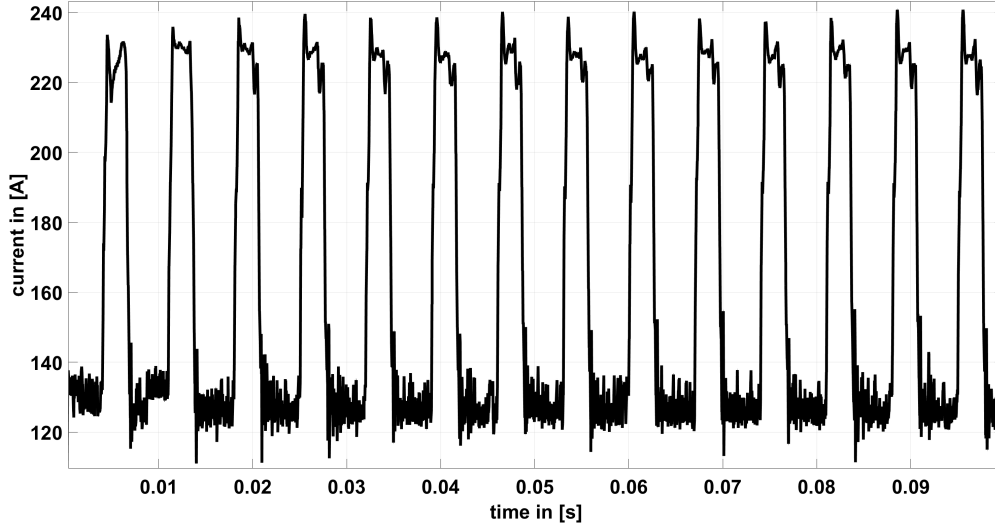
Figure 5.25: Case 3 - Current profile generated by the model based control for the reference case, leading to the behaviour Figures 5.23 and 5.24 in the plasma temperature and Figure 5.22 in the cathode temperature

5.3.2.4 Case 4: tracking of the reference plasma temperature trajectory T_p high repetition rate $f_{pulse} = 1400\,\mathrm{Hz}$

The high repetition rate trajectory case is displayed in the following. In Figure 5.26 the current profile that is generated by the controller is displayed and the resulting T_p trajectory from solving the full radial plasma dynamics is display in Figure 5.24, compared to the desired T_p profile in Figure 5.23. One can see that the pulse shape deviates slightly from the desired signal, but the maximum plasma temperature deviates by 16% from the desired value. However the pulse train could be generated and evolves stable throughout the desired time frame of $1\,\mathrm{s}$, only a snapshot of the full time frame is displayed here, in order to make the controlling behaviour visible.

Initially the system starts at the stationary state corresponding to a external electric current of $I_{arc} = 150\,\mathrm{A}$, whose plasma temperature radial profile is represented in Figure 5.20; the corresponding cathode spot temperature reads $T_c = 3973\,\mathrm{K}$. Afterwards the periodic pattern of Figure 5.21 is taken as the desired trajectory for the plasma core temperature. The non-modelled effects in the system

variable	value	meaning
$\tilde{\tau}_{control}$	$0.0002\,\mu\mathrm{s}$	time scale for flatness-based state feedback
$\tilde{d}$	0.5	damping factor for flatness-based state feedback
$\lambda_{1/2}$	$16.2 \times 10^3\,\mathrm{s}^{-1}$	eigenvalues for high-gain observer
$\tilde{\varepsilon}$	0.5	$\tilde{\varepsilon}$ parameter for high-gain observer

Table 5.9: Case 4 - Derived control and observer parameters for the dynamic simulations

variable	value	meaning
t_{pulse}	$0.7\,\mathrm{ms}$	pulse period for desired trajectory of plasma core temperature
$t_{rise} = t_{fall},\ t_{on}$	$0.05\,\mathrm{ms},\ 0.3\,\mathrm{ms}$	time parameters for desired trajectory
$\Delta \overline{T}_p$	$2000\,\mathrm{K}$	desired amplitude of plasma core pulsation

Table 5.10: Case 4 - Shaping parameters of the desired trajectory

dynamics are again taken into account with a white noise signal, according to Equation (2.60). The strength of the white noise signal for these simulations is chosen equal to $\tilde{\sigma}_0 = 5 \times 10^8$, corresponding to at least 10% of the total contribution in vector $\vec{b}$. The numerical integration of the equations of motion is performed with a time step $\Delta t = 1 \, \mu$s and the update of the control state feedback, as well as of the observer, takes place with a time step $\Delta t_c = 2\Delta t$. The parameters for the control and observer design, as well as for the desired trajectory, are listed in Table 5.9 and Table 5.10. The cathode spot temperature trajectory corresponding to the periodic desired behavior of the plasma arc temperature is represented in Figure 5.26. In Figure 5.23 the desired plasma temperature profile is displayed (black) and the reconstructed value of the effective plasma temperature of the observer, according to Equation (4.5). The resulting behaviour of the real system when applying trajectory $T_c^*(t)$ can be seen in Figure 5.25.
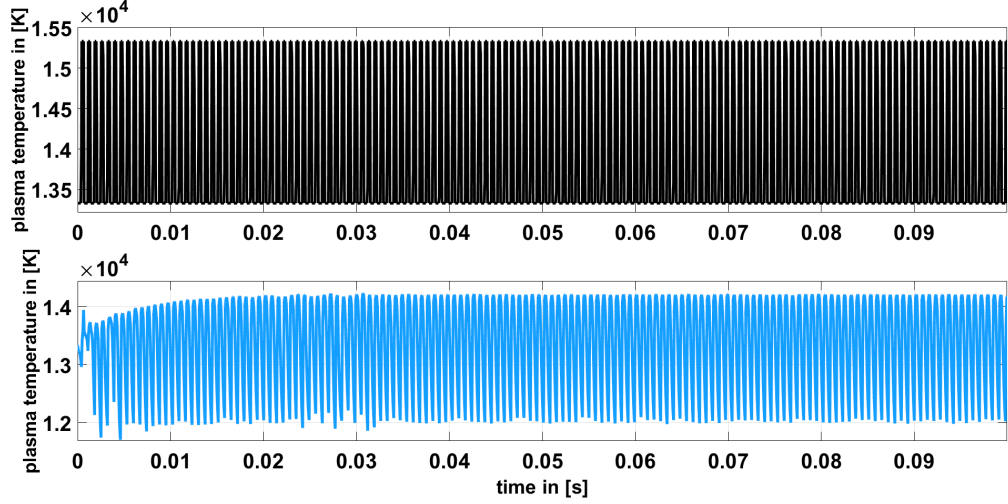
Figure 5.26: Case 4 - Trajectory $T_c^*(t)$ corresponding to the measured (black line) and the observed behavior (blue line) of the plasma arc temperature of Figure 5.21 with parameters of Table 5.10
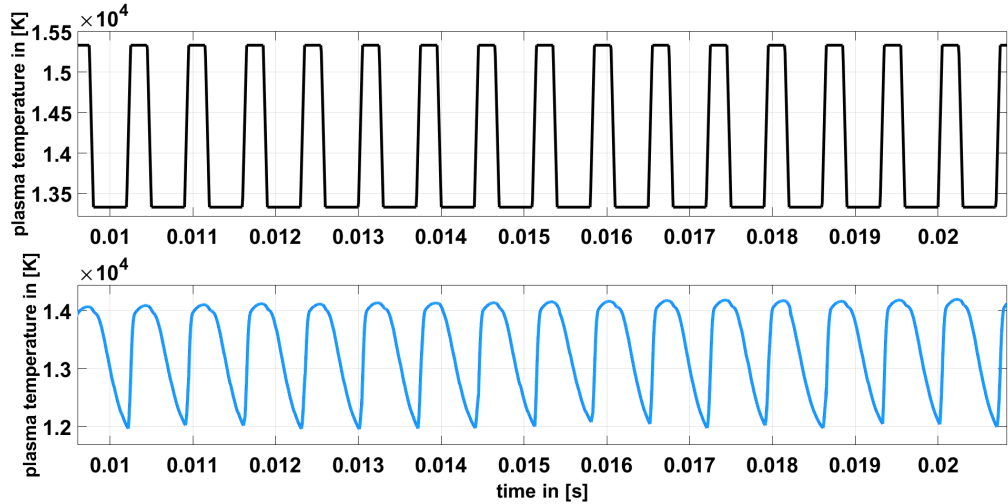
Figure 5.27: Case 4 - Desired plasma arc temperature evolution (black line) and corresponding reconstructed value from the observer (blue line) for the reference case; $\tilde{\tau}_{control} = 0.00005 \, \text{s}^{-1}$, $\Delta t = 1 \, \mu$s, $\Delta t_c = 2\Delta t$, high-gain observer

113
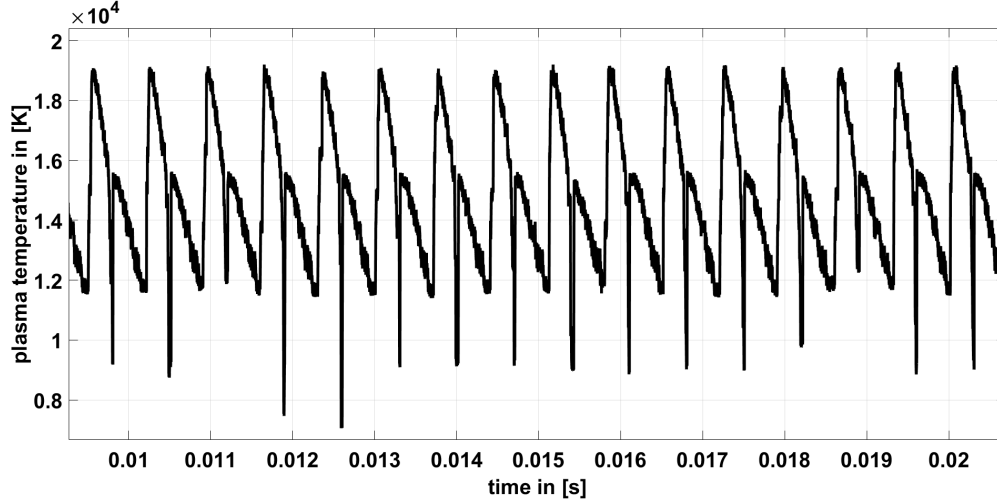
Figure 5.28: Case 4 - Resulting value of the central plasma temperature (the other values of the radial plasma temperature distribution are not displayed for visibility) corresponding to the current profile generated by the model based control; $\tilde{\tau}_{control} = 0.000\,05\,\text{s}^{-1}$, $\Delta t = 1\,\mu\text{s}$, $\Delta t_c = 2\Delta t$, high-gain observer
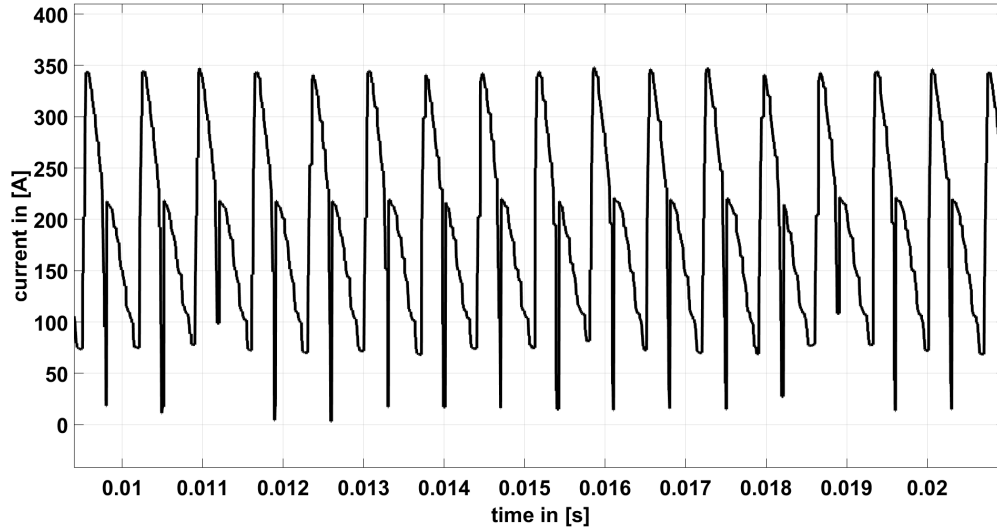
Figure 5.29: Case 4 - Current profile generated by the model based control for the high repetition rate case, leading to the behaviour Figures 5.27 and 5.28 in the plasma temperature and Figure 5.26 in the cathode temperature

As can be seen the pulse shape of the desired trapezoidal plasma temperature trajectory can not be maintained by the controller. The controller rises the current fast enough to generate a plasma temperature 20% higher than desired, but subsequently decreases the current during the hold on time of the pulse τ_{up} to finish with a value of the plasma temperature about 10% lower than desired. The mean value is thus 10% than the desired value of the plasma temperature. The plasma temperature is thereby risen to a value greater than the critical plasma temperature for maintaining the controllability of the plasma system $\overline{T}_p > \overline{T}_{p,\,crit} = 18\,800\,\text{K}$ Equation (4.38).

5.3.2.5 Case 5: tracking of the reference plasma temperature trajectory T_p higher difference temperature $\Delta T_p = 4300\,\mathrm{K}$

Initially the system starts at the stationary state corresponding to a external electric current of $I_{arc} = 150\,\mathrm{A}$, whose plasma temperature radial profile is represented in Figure 5.20; the corresponding cathode spot temperature reads $T_c = 3973\,\mathrm{K}$. Afterwards the periodic pattern of Figure 5.21 is taken as the desired trajectory for the plasma core temperature. The non-modeled effects in the system dynamics

variable	value	meaning
$\tilde{\tau}_{control}$	$0.000\,125\,\mu\,\mathrm{s}$	time scale for flatness-based state feedback
$\tilde{d}$	0.5	damping factor for flatness-based state feedback
$\tilde{\lambda}_{1/2}$	$4.75 \times 10^4\,\mathrm{s}^{-1}$	eigenvalues for high-gain observer
$\tilde{\varepsilon}$	0.1	$\tilde{\varepsilon}$ parameter for high-gain observer

Table 5.11: Case 5 - Derived control and observer parameters for the dynamic simulations

variable	value	meaning
t_{pulse}	7 ms	pulse period for desired trajectory of plasma core temperature
$t_{rise} = t_{fall}$, t_{on}	0.5 ms, 3 ms	time parameters for desired trajectory
$\Delta \overline{T}_p$	4300 K	desired amplitude of plasma core pulsation

Table 5.12: Case 5 - Shaping parameters of the desired trajectory

are again taken into account with a white noise signal, according to Equation (2.60). The strength of the white noise signal for these simulations is chosen equal to $\tilde{\sigma}_0 = 5 \times 10^8$, corresponding to at least 10% of the total contribution in vector $\vec{b}$. The numerical integration of the equations of motion is performed with a time step $\Delta t = 1\,\mu s$ and the update of the control state feedback, as well as of the observer, takes place with a time step $\Delta t_c = 2\Delta t$. The parameters for the control and observer design, as well as for the desired trajectory, are listed in Table 5.11 and Table 5.12. The cathode spot temperature trajectory corresponding to the periodic desired behavior of the plasma temperature is represented in Figure 5.30. In Figure 5.31 the desired plasma temperature profile is displayed (black) and the reconstructed value of the effective plasma temperature of the observer, according to Equation (4.5). The resulting behaviour of the real system when applying trajectory $T_c^*(t)$ can be seen in Figure 5.32.

Figure 5.30: Case 5 - Trajectory $T_c^*(t)$ corresponding to the measured (black line) and the observed behavior of the plasma arc temperature (blue line) of Figure 5.21 with parameters of Table 5.12

Figure 5.31: Case 5 - Desired plasma arc temperature evolution (black line) and corresponding reconstructed value from the observer (blue line) for the reference case; $\tilde{\tau}_{control} = 0.000\,05\,\text{s}^{-1}$, $\Delta t = 1\,\mu\text{s}$, $\Delta t_c = 2\Delta t$, high-gain observer

Figure 5.32: Case 5 - Resulting value of the central plasma temperature (the other values of the radial plasma temperature distribution are blanked out for visibility) corresponding to the current profile generated by the model based control; $\tilde{\tau}_{control} = 0.000\,05\,\mathrm{s}^{-1}$, $\Delta t = 1\,\mu\mathrm{s}$, $\Delta t_c = 2\Delta t$, high-gain observer
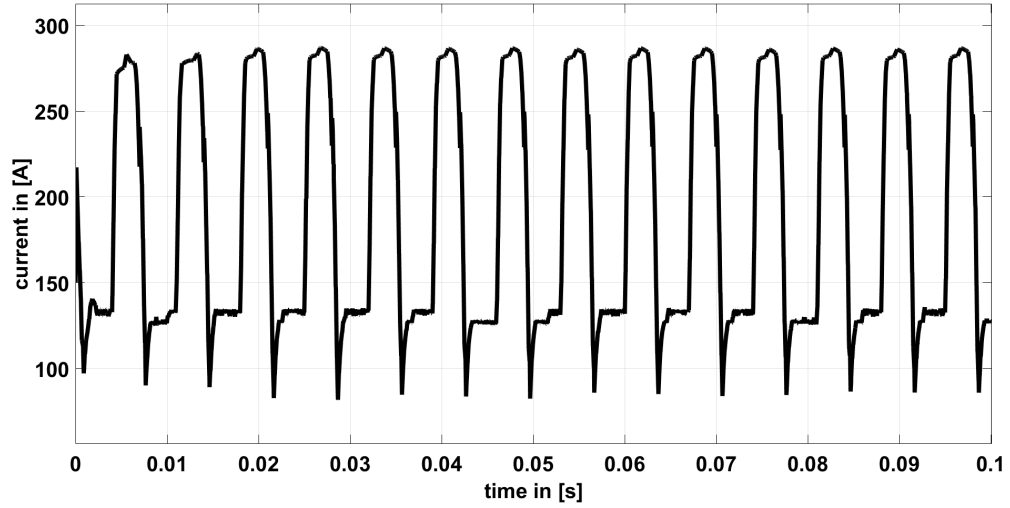
Figure 5.33: Case 5 - Current profile generated by the model based control for the high plasma temperature gain case, leading to the behaviour Figures 5.31 and 5.32 in the plasma temperature and Figure 5.30 in the cathode temperature

5.4 Discussion of the results of the plasma dynamics simulation

The aim of the flatness based control was to enhance present controlling schemes, which are mostly based on phenomenological observations of integral physical quantities (voltage) and geometrical quantities (arc length) [10, 13–18], by an algorithm that includes the behaviour of the plasma dynamics.

The displayed model based control increases the precision of trajectory tracking for the plasma temperature, such that the deviations are less than 10% Figures 5.23 and 5.24 and less than 0.1% Figure 5.22 for the cathode spot temperature. Furthermore it enables the tracking of trajectories with higher repetition rate (more than $1000\,\mathrm{Hz}$) Figure 5.28, the tracking of new pulse shapes (trapezodial with a steep gradient in plasma temperature of more than $8.6 \times 10^8\,\mathrm{K\,s^{-1}}$ and is able to follow trajectories with a gain in plasma temperature as high as $4000\,\mathrm{K}$ during a pulse Figure 5.32. The presented model calculates the steady state points of operation with good accuracy, less than 10% deviation, compared to experimental data [112]. Although the anode voltage drop contribution is still not included in this model, the characteristic evolution of the current-voltage curve is correctly followed.

The case of constant cathode temperature was chosen to display a new method to control the mode switching of an arc. The drift of the cathode temperature measured profile, which can be induced by multiple physical processes like turbulence, material erosion or changes in plasma composition, can be tracked by the controller and compensated up to a certain yet unknown degree.

The case of constant plasma temperature is of interest, since this temperature is directly coupled to the heat flux towards the anode and the chemical composition on the anode side of the discharge. Changes of the plasma composition due to surface reactiosn on the target material or deviations in the heat flux due to melting of a material would induce changes in the current density. This in turn can affect the cathode boundary, if the changes are of a certain quantity. These observations can be linked to the measured cathode temperature and correspondingly be compensated to a certain yet unknown degree. The sensitivity of the cathode temperature measurement is therefore an important criteria.

The cases 3-5 for the tracking of a desired plasma temperature profile are be important if some correlations between heat flux and chemical composition with the cathode temperature have been found and shall therefore be tracked. It has to be mentioned that the deviation between the desired and observed plasma temperature profiles in height of the plasma temperature Figures 5.23, 5.27 and 5.31 results from the fact that two separate temperatures $\hat{T}_p$ (central core) and $\overline{T}_p$ (effective simplified plasma model) are regarded here. With $\overline{T}_p$ corresponding to a greater effective radius of the plasma bulk r_p (of the simplified model). Having this in mind it is clear why both quantities can not be of the same value, this in turn would result in a much higher central plasma temperature induced in the full dynamics simulation of the plasma temperature Figures 5.24, 5.28 and 5.32.

It was shown in Section 5.3.2.4 that the plasma temperature exceeded the critical plasma temperature for maintaining controllability of the plasma system. This explains the sharp decrease in current (and therefore plasma temperature) in the aftermath of a pulse Figures 5.28 and 5.29, since the controllability condition is violated and the system acts chaotically. The controller decreases the current rapidly to recover the system, but this does not lead to smooth profiles. This does not pose a problem, as the controller is able to recover the system and therefore proves to be robust enough against such deviations. It must however be emphazised that desired motions of the plasma temperature must not violate the operational conditions set up for this controller structure Section 4.3.3, in order to function properly.

As discussed in the introduction a successful control of the plasma arc system including the plasma arc temperature requires a high time resolution (with a frequency in the range of 2 kHz) necessary for measuring some output of the system and simultaneously calculating the required control. Hence it is very fortunate that for the simplified dynamics which the control is based on, the flat output variable (which in an oversimplified way of speaking incorporates in one single variable also the information of the plasma core temperature) corresponds to the cathode temperature, a variable relatively easy to be measured by means of a pyrometer with a high time resolution (tyically operating in the kHz range)(examples for such pyrometers applied to a welding process can be seen in [113, 114]). Any other contribution from the internal plasma temperature would have made the previously developed control method no longer viable in practical terms, since any plasma temperature measurement is quite complicated and cannot be performed at the required frequency of kHz. Therefore any flatness-based

state feedback like (Equation (4.28)) is in principle attainable, provided the other state variables as the plasma core temperature (state variable x_2 in the simplified dynamics) can be reconstructed from the flat output. The calculated data for the pulse sequence indicates that profiles with close resemblance to a rectangular pulse shape can be generated and repeated up to a frequency of 1400 Hz. The required current profiles are operated with sampling frequencies from 100 kHz down to 40 kHz, which is well achievable with state-of-the-art power switches.

Although the thermal model of the plasma dynamics has been drastically simplified (in order to be computable in a shorter amount of time than present model based controls), the robustness of the model could be shown by the capacity of tracking the desired trajectory even when a white noise signal is included on the plasma dynamics. This latter contribution accounts for not modeled physical effects like turbulence and heat transfer along the plasma arc.

Chapter 6

Conclusion and Outlook

"Part of the journey is the end."

Robert Downey Junior alias Anthony Stark

There exist a lot of descriptions for the plasma boundaries and the plasma bulk behaviour, for processes where thermal arcs are utilized [78]. Yet few of these fundamental insights seem to be used properly in important aspects for these thermal arc processes, such as plasma spectroscopy, process observation and process control. Conclusively this work can be regarded as a tool set for control and observation of plasma parameters for processes involving thermal arcs, intended to fill the gap by providing simplified physical models that still contain enough of the "true" physical behaviour and can be computed very fast. This was achieved by bridging the gap between different scientific disciplines like plasma physics, quantum mechanics, radiation dynamics and control theory. To derive the formulations needed the process of GTAW has been chosen as paragon, since this process itself is a rather stable and well understood.

Achievements
At first the theoretical framework has been derived, including descriptions of the plasma-electrode interactions, the plasma composition, the radial energy transport within the plasma bulk and a brief outline of the quantum mechnical basis of radiation interaction with matter.

In the second major part of this work a formulation for the radiation emitted from a thermal arc was derived, whose underlying plasma temperature distribution and fluid boundary condition matches those given in this work. This includes descriptions for the line shape of the emitted radiation, the Stark broadening width, the emission and absorption coefficients and a integration scheme for the radiation intensity. All these formulations were condensed into a set of functions for fast evaluation and comparison of calculated spectral resolved data with measured spectral information of an OES measurement of a GTAW process. The underlying assumptions of the plasma temperature profil and the critical topic of deviations from the LTE condition in the measured region of the bulk plasma during a Thomson scattering measurement were briefly discussed. An additional formulation was adopted from the literature, including the impact of laser heating on the electrons in the plasma during the Thomson scattering measurement, to account for the deviations in the radial plasma temperature profile. The originality of this work compared to existing schemes like the various modifications of the Fowler-Milne method [46–48] and the NEC approach [50, 51] was outlined. This lead to the conclusion that this scheme can be regarded as an additional technique to analyze the spectrum of plasma radiation of OES measurements. Due to the underlying assumption of the temperature profile more physical insight on the local emission and absorption characterisitics were generated with this technique. This technique is designated for a fast and easy implementation into processes which do not allow for costly instrumentation and where an assumption on the boundary conditions of the plasma temperature profile (a solid or fluid wall condition) can be made.

In the last part the presented model based control displayed the ability to imprint various desired trajectories into a simulation, that emulates the real behaviour of a GTAW process. Although there are multiple solutions to control of such a system already present in the literature [11–13, 15, 17, 18],

none of these models takes into account the impact of the plasma dynamics. The introduction of a model based control utilizing this feature enables new applications for pulses plasma processes, since their parameter evolution can now precisly being tracked. The presented flatness based control scheme is well established in the literature as well, however finding a flat output to a system of desire is not straight forward and has not been done for a plasma process so far. Therefore this work presents an alternative solution for the control of a plasma system that is unique throughout the current scientific landscape. This work encourages the utilization of the presented algorithms and codes to apply to a GTAW experiment adn comparable thermal arc applications to demonstrate the rigorously discussed control capabilities.

The computational effort was analysed and optimization strategies of the software were proposed. Thereby indicating the applicability of the radiation model for the observation of fast processes in the range of 10 - 100 Hz and for the model based control in the range of 40 - 100 kHz for the tracking and switching of the current.

Applications

The developed model based control and radiation model can be directly applied to processes involving thermal arc's, like Plasma Arc Welding (PAW) [5, 6], Plasma Spraying [1, 2], Plasma Waste Destruction [3] and the discussed thermal arc welding [4]. All mentioned processes involve comparable geometries and polarity of the electrodes and can be regarded, as long as an assumption on the thermal boundary condition of the plasma bulk can be applied. The presented work developed the fundamental theory based on assumptions that are not just applicable to noble gas mixtures as process gases. Looking ahead this work can be adopted for more difficult plasma processes, where the process is inheritly more complex, for example due to the presence of metal vapour in the plasma (e.g. like GMAW) [115, 116].

Future development

With the idea of handling more complex plasma compositions future development of the codes should be undertaken with regard to the plasma transport properties, for example for metal vapour plasmas [117, 118]. This would extend the capabilities of the presented radiation model and the model based control towards these other processes of interest. Therefore the present work layed the foundation, by formulating the pLTE two-temperature Saha equation approach (Section 2.2.2) and the formulation for the Linear Stark broadening width (Appendix A.3.5). Both effects are important for metal vapour species in a plasma, since most of these have a steady electric dipole in their outer atomic shells.

Likewise the contribution of continuum radiation and the Biberman correction coefficients to the spectral emission coefficient should be included, since radiation coming from metal vapour will presumably have greater impact on the plasma temperature distribution than the radiation coming from noble gases.

The importance of the plasma temperature distribution model has been outlined within the discussion sections. To further improve this model, especially in the prospect of gas mixtures as working gases, microscopic formulations for effects like demixing [119] have to be regarded. Including a one dimensional (radial) diffusion model would account for such demixing effects on the spectral radiation intensity profile and pose as a fruitful adaptions. Furthermore corrections to the thermal model, especially the axial heat transfer induced by the gas flow should be taken into account to ensure that the deviations caused this effect do not pose a significant contribution (for some gas mixture or some operational conditions). However increasing the degree of freedom in the spatial dimensions will affect the required computational effort and thereby target the achievable execution time. The need for such an increased effort should be defined by the targeted application alone.

Also there is various work [56, 76] dealing with the topic of diffuse or spot mode arc attachment at the cathode, however present phenomenological models do not inherit enough physical information for stable operation and transition between these modes. The present model unveiled the perspective that the coupling between the plasma temperature and the heat evolution in the cathode can be described by the cathode temperature alone (at a fixed arc length). Thereby measuring the cathode temperature during operation of the arc (in union with the presented controller model) would allow the operation of the arc within fixed limits of the cathode temperature. If one would link this information of the

cathode temperature to a specific mode of operation, this mode could be maintained over large (yet not clearly determined) time scales.

At last to improve the usability of the developed control codes an automated search algorithm for the control and observer parameters (given in Section 5.3) should be written, to accelerate the configuration of a model based control to a specific setup of a desired process.

Bibliography

[1] P Fauchais. "Understanding plasma spraying." In: *Journal of Physics D: Applied Physics* 37.9 (2004), R86–R108. DOI: 10.1088/0022-3727/37/9/r02. URL: https://doi.org/10.1088%2F0022-3727%2F37%2F9%2Fr02.

[2] A. Schütze, J. Y. Jeong, S. E. Babayan, Jaeyoung Park, G. S. Selwyn, and R. F. Hicks. "The atmospheric-pressure plasma jet: a review and comparison to other plasma sources." In: *IEEE Transactions on Plasma Science* 26.6 (1998), pp. 1685–1694. DOI: 10.1109/27.747887.

[3] J. Heberlein and A. Murphy. "Thermal Plasma Waste Treatment." In: *Journal of Physics D Applied Physics* 41 (2008), p. 053001. DOI: 10.1088/0022-3727/41/5/053001.

[4] P. W. Muncaster. *A Practical Guide to TIG (GTA) Welding*. en. Woodhead Publishing, 1991. ISBN: 9781855730205. URL: https://www.elsevier.com/books/a-practical-guide-to-tig-gta-welding/muncaster/978-1-85573-020-5.

[5] C. S. Wu, L. Wang, W. J. Ren, and X. Y. Zhang. "Plasma arc welding: Process, sensing, control and modeling." en. In: *Journal of Manufacturing Processes*. Recent Developments in Welding Processes 16.1 (2014), pp. 74–85. ISSN: 1526-6125. DOI: 10.1016/j.jmapro.2013.06.004. URL: http://www.sciencedirect.com/science/article/pii/S152661251300073X.

[6] K. Nishiguchi. "Plasma Arc Welding and Cutting." en. In: *Advanced Joining Technologies*. Ed. by T. H. North. Dordrecht: Springer Netherlands, 1990, pp. 36–47. ISBN: 9789400904330. DOI: 10.1007/978-94-009-0433-0_3.

[7] J. Norrish. *Advanced Welding Processes*. en. Google-Books-ID: vAakAgAAQBAJ. Elsevier, 2006. ISBN: 9781845691707.

[8] "Front Matter." en. In: ed. by J. F. Lancaster. Pergamon, 1986, p. iii. ISBN: 9780080340760. DOI: 10.1016/B978-0-08-034076-0.50002-5. URL: http://www.sciencedirect.com/science/article/pii/B9780080340760500025.

[9] M. Kühn-Kauffeldt. "Plasma spectroscopy for stationary and transient welding arcs containing metal-gas mixtures." PhD thesis. Bundeswehr University Munich, 2016.

[10] S. Ozcelik and K Moore. *Modeling, sensing and control of gas metal arc welding*. Elsevier, 2003. ISBN: 9780080536620.

[11] J.-B. Song and D. E. Hardt. "Dynamic Modeling and Adaptive Control of the Gas Metal Arc Welding Process." In: *Journal of Dynamic Systems, Measurement, and Control* 116.3 (1994), p. 405. DOI: 10.1115/1.2899235.

[12] Y. K. Liu and Y. M. Zhang. "Model-Based Predictive Control of Weld Penetration in Gas Tungsten Arc Welding." In: *IEEE Transactions on Control Systems Technology* 22.3 (2014), pp. 955–966. DOI: 10.1109/tcst.2013.2266662.

[13] J. Thomsen. "Feedback linearization based arc length control for gas metal arc welding." In: *Proceedings of the 2005, American Control Conference, 2005*. IEEE, 2005. DOI: 10.1109/acc.2005.1470527.

[14] D. Nishar, J. Schiano, W. Perkins, and R. Weber. "Adaptive control of temperature in arc welding." In: *Proceedings of IEEE International Conference on Control and Applications*. IEEE, 1993. DOI: 10.1109/cca.1993.348209.

[15] M. K. Bera, B. Bandyopadhyay, and A. K. Paul. "Robust nonlinear control of GMAW systems-a higher order sliding mode approach." In: *2013 IEEE International Conference on Industrial Technology (ICIT)*. IEEE, 2013. DOI: `10.1109/icit.2013.6505668`.

[16] F. Sikstrom, A.-K. Christiansson, and B. Lennartson. "Model based feedback control of gas tungsten arc welding: An experimental study." In: *2015 IEEE International Conference on Automation Science and Engineering (CASE)*. IEEE, 2015. DOI: `10.1109/coase.2015.7294113`.

[17] R. Crawford, G. Cook, A. Strauss, and D. Hartman. "Adaptive voltage control of gas tungsten arc welding." In: *Int. J. Modelling, Identification and Control Int. J. Modelling, Identification and Control* 1 (Jan. 2006), pp. 133–139. DOI: `10.1504/IJMIC.2006.010106`.

[18] W. Lu, Y.-M. Zhang, C. Zhang, and B. L. Walcott. "ROBUST SENSING AND CONTROL OF WELD POOL SURFACE." In: *IFAC Proceedings Volumes* 38.1 (2005). 16th IFAC World Congress, pp. 301 –306. ISSN: 1474-6670. DOI: `https://doi.org/10.3182/20050703-6-CZ-1902.01472`.

[19] G. Zhang, S. Chen, and L. Wu. "Intelligent control of pulsed GTAW with filler metal." In: *Welding Journal (Miami, Fla)* 84 (Jan. 2005), 9–S.

[20] A. B. Murphy, M Tanaka, K Yamamoto, S Tashiro, T Sato, and J. J. Lowke. "Modelling of thermal plasmas for arc welding: the role of the shielding gas properties and of metal vapour." In: *Journal of Physics D: Applied Physics* 42.19 (2009), p. 194006. URL: `http://stacks.iop.org/0022-3727/42/i=19/a=194006`.

[21] A. E. F. Gick, M. B. C. Quigley, and P. H. Richards. "The use of electrostatic probes to measure the temperature profiles of welding arcs." en. In: *Journal of Physics D: Applied Physics* 6.16 (1973), pp. 1941–1949. ISSN: 0022-3727. DOI: `10.1088/0022-3727/6/16/314`. URL: `https://doi.org/10.1088%2F0022-3727%2F6%2F16%2F314`.

[22] N. A. Sanders and E. Pfender. "Measurement of anode falls and anode heat transfer in atmospheric pressure high intensity arcs." In: *Journal of Applied Physics* 55.3 (1984), pp. 714–722. DOI: `10.1063/1.333129`. URL: `https://doi.org/10.1063/1.333129`.

[23] K. Tomita, S. Yoshitake, K. Uchino, D. Takenaka, H. Toda, M. Hikita, and K. Suzuki. "Measurements of Electron Density and Electron Temperature of Arc Discharge Plasmas Containing Metallic Vapors using Laser Thomson Scattering." In: *IEEJ Transactions on Fundamentals and Materials* 133.9 (2013), pp. 458–464. DOI: `10.1541/ieejfms.133.458`.

[24] S. Akbar and K. Etemadi. "Impact of copper vapor contamination on argon arcs." en. In: *Plasma Chemistry and Plasma Processing* 17.2 (1997), pp. 251–262. ISSN: 1572-8986. DOI: `10.1007/BF02766818`. URL: `https://doi.org/10.1007/BF02766818`.

[25] J. J. Gonzalez, M. Bouaziz, M. Razafinimanana, and A. Gleizes. "The influence of iron vapour on an argon transferred arc." en. In: *Plasma Sources Science and Technology* 6.1 (1997), pp. 20–28. ISSN: 0963-0252. DOI: `10.1088/0963-0252/6/1/004`. URL: `https://doi.org/10.1088%2F0963-0252%2F6%2F1%2F004`.

[26] S Pellerin, K Musiol, B Pokrzywka, and J Chapelle. "Stark width of4s-4p Ar I transition (696.543 nm)." In: *Journal of Physics B: Atomic, Molecular and Optical Physics* 29.17 (1996), p. 3911. URL: `http://stacks.iop.org/0953-4075/29/i=17/a=014`.

[27] S Zielinska, K Musiol, K Dzierzega, S Pellerin, F Valensi, C. de Izarra, and F Briand. "Investigations of GMAW plasma by optical emission spectroscopy." In: *Plasma Sources Science and Technology* 16.4 (Jan. 2007), p. 832. URL: `http://stacks.iop.org/0963-0252/16/i=4/a=019`.

[28] J. Torres, M. van de Sande, J. van der Mullen, A. Gamero, and A. Sola. "Stark broadening for simultaneous diagnostics of the electron density and temperature in atmospheric microwave discharges." In: *Spectrochimica Acta Part B: Atomic Spectroscopy* 61.1 (2006), pp. 58 –68. ISSN: 0584-8547. DOI: `http://dx.doi.org/10.1016/j.sab.2005.11.002`.

[29] H. R. Griem. *Plasma Spectroscopy*. McGraw-Hill, 1964.

[30] M. S. Dimitrijevic, L. Skuljan, and S. Djenie. "Stark Broadening of the Ar I Spectral Lines 763.51, 738.39 and 696.54 nm." In: *Phys. Scr* 66 (2002), pp. 77–81. DOI: 10.1238/Physica.Regular.066a00077.

[31] K. Muraoka and A. Kono. "Laser Thomson scattering for low-temperature plasmas." en. In: *Journal of Physics D: Applied Physics* 44.4 (2011), p. 043001. ISSN: 0022-3727. DOI: 10.1088/0022-3727/44/4/043001. URL: https://doi.org/10.1088%2F0022-3727%2F44%2F4%2F043001.

[32] S. C. Snyder and R. E. Bentley. "A measurement of axial velocity and temperature in a free-burning arc using Thomson scattering." en. In: *Journal of Physics D: Applied Physics* 29.12 (1996), pp. 3045–3049. ISSN: 0022-3727. DOI: 10.1088/0022-3727/29/12/017. URL: https://doi.org/10.1088%2F0022-3727%2F29%2F12%2F017.

[33] H. Terasaki, M. Tanaka, and M. Ushio. "Effects of metal vapor on electron temperature in helium gas tungsten arcs." en. In: *Metallurgical and Materials Transactions A* 33.4 (2002), pp. 1183–1188. ISSN: 1543-1940. DOI: 10.1007/s11661-002-0219-x. URL: https://doi.org/10.1007/s11661-002-0219-x.

[34] M. Tanaka and S. Tashiro. "Electron temperature measurement of tungsten inert gas arcs." en. In: *Thin Solid Films.* 20th Symposium on Plasma Science for Materials (SPSM-20) 516.19 (2008), pp. 6628–6633. ISSN: 0040-6090. DOI: 10.1016/j.tsf.2007.11.036. URL: http://www.sciencedirect.com/science/article/pii/S0040609007018986.

[35] S. C. Snyder, G. D. Lassahn, and L. D. Reynolds. "Direct evidence of departure from local thermodynamic equilibrium in a free-burning arc-discharge plasma." In: *Phys. Rev. E* 48 (5 1993), pp. 4124–4127. DOI: 10.1103/PhysRevE.48.4124. URL: https://link.aps.org/doi/10.1103/PhysRevE.48.4124.

[36] R. E. Bentley. "A departure from local thermodynamic equilibrium within a freely burning arc and asymmetrical Thomson electron features." en. In: *Journal of Physics D: Applied Physics* 30.20 (1997), pp. 2880–2886. ISSN: 0022-3727. DOI: 10.1088/0022-3727/30/20/015. URL: https://doi.org/10.1088%2F0022-3727%2F30%2F20%2F015.

[37] G. Gregori, J. Schein, P. Schwendinger, U. Kortshagen, J. Heberlein, and E. Pfender. "Thomson scattering measurements in atmospheric plasma jets." In: *Phys. Rev. E* 59 (2 1999), pp. 2286–2291. DOI: 10.1103/PhysRevE.59.2286. URL: https://link.aps.org/doi/10.1103/PhysRevE.59.2286.

[38] G. Gregori, U. Kortshagen, J. Heberlein, and E. Pfender. "Analysis of Thomson scattered light from an arc plasma jet." In: *Phys. Rev. E* 65 (4 2002), p. 046411. DOI: 10.1103/PhysRevE.65.046411. URL: https://link.aps.org/doi/10.1103/PhysRevE.65.046411.

[39] A. P. Langheinrich and D. B. Roberts. "Optical Emission Spectroscopy." en. In: ed. by R. E. Wainerdi and E. A. Uken. Monographs in Geoscience. Boston, MA: Springer US, 1971, pp. 169–204. ISBN: 9781468418309. DOI: 10.1007/978-1-4684-1830-9_7. URL: https://doi.org/10.1007/978-1-4684-1830-9_7.

[40] W. L. Wiese. "Spectroscopic diagnostics of low temperature plasmas: techniques and required data." en. In: *Spectrochimica Acta Part B: Atomic Spectroscopy* 46.6 (1991), pp. 831–841. ISSN: 0584-8547. DOI: 10.1016/0584-8547(91)80084-G. URL: http://www.sciencedirect.com/science/article/pii/058485479180084G.

[41] S. S. Glickstein. "Temperature Measurements in a Free Burning Arc." In: *Welding Research Supplement* 54.8 (1976), p. 222. URL: aws.org/w/a/wj/supplement/WJ_1976_08_s222.pdf.

[42] G. S. Mills. "Use of emission spectroscopy for welding arc analysis." In: *Welding Research Supplement* 3 (Jan. 1977), pp. 93–96.

[43] S Pellerin, K Musiol, B Pokrzywka, and J Chapelle. "Investigation of a cathode region of an electric arc." In: *Journal of Physics D: Applied Physics* 27.3 (1994), p. 522. URL: http://stacks.iop.org/0022-3727/27/i=3/a=014.

[44] G. N. Haddad and A. J. D. Farmer. "Temperature determinations in a free-burning arc. I. Experimental techniques and results in argon." In: *Journal of Physics D: Applied Physics* 17.6 (1984), pp. 1189–1196. DOI: 10.1088/0022-3727/17/6/015. URL: https://doi.org/10.1088%2F0022-3727%2F17%2F6%2F015.

[45] M. F. Thornton. "Spectroscopic determination of temperature distributions for a TIG arc." en. In: *Journal of Physics D: Applied Physics* 26.9 (1993), pp. 1432–1438. ISSN: 0022-3727. DOI: 10.1088/0022-3727/26/9/014. URL: https://doi.org/10.1088%2F0022-3727%2F26%2F9%2F014.

[46] S. Ma, H. Gao, and L. Wu. "Modified Fowler–Milne method for the spectroscopic determination of thermal plasma temperature without the measurement of continuum radiation." In: *Review of Scientific Instruments* 82.1 (2011), p. 013104. DOI: 10.1063/1.3529019. eprint: https://doi.org/10.1063/1.3529019. URL: https://doi.org/10.1063/1.3529019.

[47] L. Vilarinho and A. Scotti. "Proposal for a Modified Fowler-Milne Method to Determine the Temperature Profile in TIG Welding at Low Currents." In: *Journal of the Brazilian Society of Mechanical Sciences and Engineering* 26 (2004). DOI: 10.1590/S1678-58782004000100006.

[48] A. B. Murphy. "Modified Fowler–Milne method for the spectroscopic measurement of temperature and composition of multielement thermal plasmas." In: *Review of Scientific Instruments* 65.11 (1994), pp. 3423–3427. DOI: 10.1063/1.1144516. eprint: https://doi.org/10.1063/1.1144516. URL: https://doi.org/10.1063/1.1144516.

[49] A. J. D. Farmer, G. N. Haddad, and L. E. Cram. "Temperature determinations in a free-burning arc. III. Measurements with molten anodes." In: *Journal of Physics D: Applied Physics* 19.9 (1986), pp. 1723–1730. DOI: 10.1088/0022-3727/19/9/016. URL: https://doi.org/10.1088%2F0022-3727%2F19%2F9%2F016.

[50] M Wendt. "Net emission coefficients of argon iron plasmas with electron Stark widths scaled to experiments." In: *Journal of Physics D: Applied Physics* 44.12 (2011), p. 125201. DOI: 10.1088/0022-3727/44/12/125201.

[51] T. Billoux, Y. Cressault, P. Teulet, and A. Gleizes. "Calculation of the net emission coefficient of an air thermal plasma at very high pressure." In: *Journal of Physics Conference Series* 406 (2012), p. 2010. DOI: 10.1088/1742-6596/406/1/012010.

[52] M. Boselli, V. Colombo, E. Ghedini, M. Gherardi, F. Rotundo, and P. Sanibondi. "Comparison between net emission coefficient and P-1 methods in modelling radiation in a plasma arc welding torch." In: *2013 Abstracts IEEE International Conference on Plasma Science (ICOPS)*. 2013, pp. 1–1. DOI: 10.1109/PLASMA.2013.6635162.

[53] M. Mallon, M. Kühn-Kauffeldt, J.-L. Marqués, and J. Schein. "Time efficient radiation model for determination of plasma parameters in atmospheric plasmas." In: *Journal of Physics D: Applied Physics* 52 (June 2019). DOI: 10.1088/1361-6463/ab3117.

[54] F. F. Chen and H. Torreblanca. *Introduction to Plasma Physics and controlled fusion, 3nd edition*. 2016. DOI: 10.1007/978-3-662-55685-6.

[55] O. Mayr. "Beiträge zur Theorie des statischen und des dynamischen Lichtbogens." In: *Archiv für Elektrotechnik* 37.12 (1943), pp. 588–608. ISSN: 1432-0487. DOI: 10.1007/BF02084317. URL: https://doi.org/10.1007/BF02084317.

[56] A. M. M. Benilov. "A Model of the cathode region of atmospheric pressure arcs." In: *J. Phys. D: Appl. Phys.* 28 (1995), pp. 1869–1882.

[57] R Morrow and J. J. Lowke. "A one-dimensional theory for the electrode sheaths of electric arcs." In: *Journal of Physics D: Applied Physics* 26.4 (1993), pp. 634–642. DOI: 10.1088/0022-3727/26/4/016. URL: https://doi.org/10.1088%2F0022-3727%2F26%2F4%2F016.

[58] J. J. Lowke, R Morrow, and J Haidar. "A simplified unified theory of arcs and their electrodes." In: *Journal of Physics D: Applied Physics* 30.14 (1997), pp. 2033–2042. DOI: 10.1088/0022-3727/30/14/011. URL: https://doi.org/10.1088%2F0022-3727%2F30%2F14%2F011.

[59] M. I. Boulos, P Fauchais, and E Pfender. *Thermal Plasmas: Fundamentals and Applications. Volume 1*. Plenum Press, 1994.

[60] A. B. Murphy and C. J. Arundelli. "Transport coefficients of argon, nitrogen, oxygen, argon-nitrogen, and argon-oxygen plasmas." In: *Plasma Chemistry and Plasma Processing* 14.4 (1994), pp. 451–490. ISSN: 1572-8986. DOI: 10.1007/BF01570207. URL: https://doi.org/10.1007/BF01570207.

[61] J Aubreton, M. F. Elchinger, V Rat, and P Fauchais. "Two-temperature transport coefficients in Argon–Helium thermal plasmas." In: *Journal of Physics D: Applied Physics* 37.1 (2003), pp. 34–41. DOI: 10.1088/0022-3727/37/1/007.

[62] A. Murphy. "Transport Coefficients of Helium and Argon/Helium Plasmas." In: *IEEE TRANSACTIONS ON PLASMA SCIENCE* 25.5 (1997), pp. 809–814.

[63] X. Chen and H.-P. Li. "Heat transfer and fluid flow in a high-intensity free-burning arc: An improved modeling approach." In: *International Journal of Heat and Mass Transfer* 44 (2001), pp. 2541–2553. DOI: 10.1016/S0017-9310(00)00290-8.

[64] G. H. Nickel. "Elementary derivation of the Saha equation." In: *American Journal of Physics* 48.6 (1980), pp. 448–450. DOI: 10.1119/1.12002. URL: https://doi.org/10.1119/1.12002.

[65] A. Gleizes, J. J. Gonzalez, and P. Freton. "Thermal plasma modelling." en. In: *Journal of Physics D: Applied Physics* 38.9 (2005), R153–R183. ISSN: 0022-3727. DOI: 10.1088/0022-3727/38/9/R01. URL: https://doi.org/10.1088%2F0022-3727%2F38%2F9%2Fr01.

[66] X. Chen and P. Han. "On the thermodynamic derivation of the Saha equation modified to a two-temperature plasma." In: *Journal of Physics D: Applied Physics* 32.14 (1999), pp. 1711–1718. DOI: 10.1088/0022-3727/32/14/324. URL: https://doi.org/10.1088%2F0022-3727%2F32%2F14%2F324.

[67] J Aubreton, M. F. Elchinger, P Fauchais, V Rat, and P André. "Thermodynamic and transport properties of a ternary Ar–H2–He mixture out of equilibrium up to 30 000 K at atmospheric pressure." In: *Journal of Physics D: Applied Physics* 37.16 (2004), pp. 2232–2246. DOI: 10.1088/0022-3727/37/16/004. URL: https://doi.org/10.1088%2F0022-3727%2F37%2F16%2F004.

[68] A. Kramida, Yu. Ralchenko, J. Reader, and and NIST ASD Team. NIST Atomic Spectra Database (ver. 5.6.1), [Online]. Available: https://physics.nist.gov/asd [2019, April 2]. National Institute of Standards and Technology, Gaithersburg, MD. 2018.

[69] F. C. P. F. J. Gonzalez. "Arc/Cathode Interation Model." In: *IEEE TRANSACTIONS ON PLASMA SCIENCE* 36.4 (2008), pp. 1944–1954.

[70] E. L. Murphy and G. H. Good. "Thermionic Emission, Field Emission, and the Transition Region." In: *Physical Review* 102.6 (1956), pp. 1464—1473. DOI: 10.1103/PhysRev.102.1464.

[71] S. Chowdhury. "The composition of an argon plasma in Saha equilibrium." In: *Journal of Quantitative Spectroscopy and Radiative Transfer* 9.1 (1969), pp. 129 –135. ISSN: 0022-4073. DOI: https://doi.org/10.1016/0022-4073(69)90151-4. URL: http://www.sciencedirect.com/science/article/pii/0022407369901514.

[72] E. L. Murphy and R. H. Good. "Thermionic Emission, Field Emission, and the Transition Region." In: *Phys. Rev.* 102 (6 1956), pp. 1464–1473. DOI: 10.1103/PhysRev.102.1464. URL: https://link.aps.org/doi/10.1103/PhysRev.102.1464.

[73] M. S. Benilov. "Stability of direct current transfer to thermionic cathodes: I. Analytical theory." In: *Journal of Physics D: Applied Physics* 40.5 (2007), pp. 1376–1393. DOI: 10.1088/0022-3727/40/5/011. URL: https://doi.org/10.1088%2F0022-3727%2F40%2F5%2F011.

[74] M Benilov. "Understanding and modelling plasma-electrode interaction in high-pressure arc discharges: A review." In: *Journal of Physics D: Applied Physics* 41 (July 2008), p. 144001. DOI: 10.1088/0022-3727/41/14/144001.

[75] M. S. Benilov and L. G. Benilova. "Field to thermo-field to thermionic electron emission: A practical guide to evaluation and electron emission from arc cathodes." In: *Journal of Applied Physics* 114.6 (2013), p. 063307. DOI: 10.1063/1.4818325. URL: https://doi.org/10.1063/1.4818325.

[76] F. Cayla, P. Freton, and J. Gonzalez. "Arc/Cathode Interaction Model." In: *IEEE Transactions on Plasma Science* 36.4 (2008), pp. 1944–1954. DOI: 10.1109/TPS.2008.927378.

[77] K. U. Riemann. "The Bohm criterion and sheath formation." In: *Journal of Physics D: Applied Physics* 24.4 (1991), pp. 493–518. DOI: 10.1088/0022-3727/24/4/001. URL: https://doi.org/10.1088%2F0022-3727%2F24%2F4%2F001.

[78] J. Wendelstorf, I. Decker, H. Wohlfahrt, and G. Simon. "TIG and Plasma Arc Modelling: A Survey." In: *Mathematical Modelling of Weld Phenomena* 3 (1997), pp. 848–897. DOI: 10.1103/PhysRev.102.1464. URL: https://link.aps.org/doi/10.1103/PhysRev.102.1464.

[79] S. V. Patankar. *Numerial Heat Transfer.* McGraw-Hill, New York, 1980.

[80] Y. P. Zeldovich and Y. Raizer. *Physics of Shock Waves and High-Temperature Hydrodynamic Phenomena.* Dover, 2002.

[81] H. R. Griem. *Principles of Plasma Spectroscopy.* en. Oct. 1997. DOI: 10.1017/CBO9780511524578. URL: /core/books/principles-of-plasma-spectroscopy/90F6DBB512089B7E3AC121744EFE3D93.

[82] L.I.Schiff. *Quantum Mechanics.* 1968.

[83] B. M. Smirnov. *Plasma Processes and Plasma Kinetics.* Wiley-VCH Verlag, 2007.

[84] H. Kunze. *Introduction to Plasma Spectroscopy.* 2009.

[85] A. Murphy. "Transport coefficients of helium and argon-helium plasmas." In: *IEEE Transactions on Plasma Science* 25.5 (1997), pp. 809–814. ISSN: 1939-9375. DOI: 10.1109/27.649574.

[86] *Hütte – Des Ingenieurs Taschenbuch.* de. Page Version ID: 192203370. 2019. URL: https://de.wikipedia.org/w/index.php?title=H%C3%BCtte_%E2%80%93_Des_Ingenieurs_Taschenbuch&oldid=192203370.

[87] *WebElements.* URL: https://www.webelements.com.

[88] J. Lévine. *Analysis and Control of Nonlinear Systems A Flatness-based Approach.* May 2009. DOI: 10.1007/978-3-642-00839-9.

[89] M. Fliess, J. Lévine, P. Martin, and P. Rouchon. "FLATNESS AND DEFECT OF NONLINEAR SYSTEMS: INTRODUCTORY THEORY AND EXAMPLES." In: *International Journal of Control* 61 (June 1995), pp. 13–27. DOI: 10.1080/00207179508921959.

[90] A. Isidori. *Nonlinear Control Systems.* Ed. by M. Thoma, E. D. Sontag, B. W. Dickinson, A. Fettweis, J. L. Massey, and J. W. Modestino. 3rd. Berlin, Heidelberg: Springer-Verlag, 1995. DOI: 10.1007/978-1-84628-615-5.

[91] B. Russell. *The Principles of Mathematics.* en. Google-Books-ID: 63ooitcP2osC. George Allen & Unwin Limited, 1942. ISBN: 9781440054167.

[92] A. T. Lundell. "A Short Proof of the Frobenius Theorem." In: *Proceedings of the American Mathematical Society* 116.4 (1992), pp. 1131–1133. ISSN: 00029939, 10886826. URL: http://www.jstor.org/stable/2159499.

[93] H. K. Khalil. *Nonlinear systems; 3rd ed.* The book can be consulted by contacting: PH-AID: Wallet, Lionel. Upper Saddle River, NJ: Prentice-Hall, 2002. ISBN: 9780130673893. URL: https://cds.cern.ch/record/1173048.

[94] A. Hurwitz. "Ueber die Bedingungen, unter welchen eine Gleichung nur Wurzeln mit negativen reellen Theilen besitzt." de. In: *Mathematische Annalen* 46.2 (June 1895), pp. 273–284. ISSN: 1432-1807. DOI: 10.1007/BF01446812. URL: https://doi.org/10.1007/BF01446812.

[95] P. Mai and C. Hillermeier. "New insights into derivative estimation via least squares approximation - theory and application." In: *2008 American Control Conference.* 2008, pp. 2427–2434. DOI: 10.1109/ACC.2008.4586855.

[96] D. E. Knuth. "Johann Faulhaber and sums of powers." In: 1993. DOI: 10.1090/S0025-5718-1993-1197512-7.

[97] D. G. Luenberger. "Observing the State of a Linear System." In: *IEEE Transactions on Military Electronics* 8.2 (1964), pp. 74–80. DOI: 10.1109/TME.1964.4323124.

[98] J. Adamy. *Nichtlineare Systeme und Regelungen*. Jan. 2018. DOI: 10.1007/978-3-662-55685-6.

[99] V. Rat, A. Murphy, J. Aubreton, M. E. Elchinger, and P. Fauchais. "Treatment of non-equilibrium phenomena in thermal plasma flow." In: *Journal of Physics D: Applied Physics* 41 (2008), p. 183001. DOI: 10.1088/0022-3727/41/18/183001.

[100] M. S. Dimitrijevic, M Christova, and S Sahal-Brechot. "Stark Broadening of visible Ar I spectral lines." In: *Physica Scripta* 75.1 (2007), pp. 809–819.

[101] M Kühn-Kauffeldt, J.-L. Marqués, G Forster, and J Schein. "Electron temperature and density measurement of tungsten inert gas arcs with Ar-He shielding gas mixture." In: *Journal of Instrumentation* 8.C10017 (2013).

[102] A. B. Murphy. "Thomson scattering diagnostics of thermal plasmas: Laser heating of electrons and the existence of local thermodynamic equilibrium." In: *Phys. Rev. E* 69 (1 2004), p. 016408. DOI: 10.1103/PhysRevE.69.016408. URL: http://link.aps.org/doi/10.1103/PhysRevE.69.016408.

[103] G. S. Settles. *Schlieren and Shadowgraph Techniques: Visualizing Phenomena in Transparent Media*. en. Experimental Fluid Mechanics. Berlin Heidelberg: Springer-Verlag, 2001. ISBN: 9783540661559. DOI: 10.1007/978-3-642-56640-0. URL: https://www.springer.com/gp/book/9783540661559.

[104] M. Schnick, M. Dreher, J. Zschetzsche, U. Füssel, and A. Spille-Kohoff. "Visualization and Optimization of Shielding Gas Flows in Arc Welding." en. In: *Welding in the World* 56.1 (2012), pp. 54–61. ISSN: 1878-6669. DOI: 10.1007/BF03321146. URL: https://doi.org/10.1007/BF03321146.

[105] K Dzierzega, B Pokrzywka, and S Pellerin. "Investigations of the cathode region of an argon arc plasma by degenerate four-wave mixing laser spectroscopy and optical emission spectroscopy." In: *Journal of Physics D: Applied Physics* 37.13 (2004), pp. 1742–1749. DOI: 10.1088/0022-3727/37/13/004. URL: https://doi.org/10.1088%2F0022-3727%2F37%2F13%2F004.

[106] S. C. Snyder, L. D. Reynolds, J. R. Fincke, G. D. Lassahn, J. D. Grandy, and T. E. Repetti. "Electron-temperature and electron density profiles in an atmospheric argon plasma jet." In: *Physical Review E* 50.31 (1994), pp. 519–525.

[107] S. C. Snyder, D. M. Crawford, and J. R. Fincke. "Dependence on the scattering angle of the electron temperature and electron density in Thomson-scattering measurements on an atmospheric-pressure plasma jet." In: *Phys. Rev. E* 61 (2 2000), pp. 1920–1924. DOI: 10.1103/PhysRevE.61.1920. URL: https://link.aps.org/doi/10.1103/PhysRevE.61.1920.

[108] A. B. Murphy, A. J. D. Farmer, and J. Haidar. "Laser scattering measurement of temperature profiles of a free burning arc." In: *Applied Physics Letters* 60.11 (1992), pp. 1304–1306. DOI: 10.1063/1.107324. eprint: https://doi.org/10.1063/1.107324. URL: https://doi.org/10.1063/1.107324.

[109] B Bachmann, R Kozakov, G Gött, K Ekkert, J.-P. Bachmann, J.-L. Marqués, H Schöpp, D Uhrlandt, and J Schein. "High-speed three-dimensional plasma temperature determination of axially symmetric free-burning arcs." In: *Journal of Physics D: Applied Physics* 46.12 (2013), p. 125203. DOI: 10.1088/0022-3727/46/12/125203. URL: https://doi.org/10.1088%2F0022-3727%2F46%2F12%2F125203.

[110] E. A. McLean and S. A. Ramsden. "Optical Interferometric and Spectroscopic Measurements of Electron Density in a Plasma." In: *Phys. Rev.* 140 (4A 1965), A1122–A1129. DOI: 10.1103/PhysRev.140.A1122. URL: https://link.aps.org/doi/10.1103/PhysRev.140.A1122.

[111] A. Murphy. "Demixing in free-burning arcs." In: *Physical Review E* 55.6 (1997), pp. 7473–7494.

[112] N. N. da Silva, P. H. Ribeiro, A. M. Moreno, A. R. Arias, and A. Q. Bracarense. "Study on the electric arc of GTAW process." In: *Journal of Physics: Conference Series* 1126 (2018), p. 012013. DOI: 10.1088/1742-6596/1126/1/012013. URL: https://doi.org/10.1088%2F1742-6596%2F1126%2F1%2F012013.

[113] P. M. G. P. Moreira, O. Frazão, S. M. O. Tavares, M. A. V. d. Figueiredo, M. T. Restivo, J. L. Santos, and P. M. S. T. d. Castro. "Temperature field acquisition during gas metal arc welding using thermocouples, thermography and fibre Bragg grating sensors." en. In: *Measurement Science and Technology* 18.3 (2007), pp. 877–883. ISSN: 0957-0233. DOI: 10.1088/0957-0233/18/3/041. URL: https://doi.org/10.1088%2F0957-0233%2F18%2F3%2F041.

[114] K. YAMAZAKI, E. YAMAMOTO, K. SUZUKI, F. KOSHIISHI, S. MIYAZAKO, S. TASHIRO, M. TANAKA, and K. NAKATA. "The Surface Temperature Measurement of Weld Pool by Infrared Two-Color Pyrometry." In: *QUARTERLY JOURNAL OF THE JAPAN WELDING SOCIETY* 27.1 (2009), pp. 34–40. DOI: 10.2207/qjjws.27.34.

[115] A. Murphy. "A self-consistent three-dimensional model of the arc, electrode and weld pool in gas–metal arc welding." In: *Journal of Physics D: Applied Physics* 44 (2011), p. 194009. DOI: 10.1088/0022-3727/44/19/194009.

[116] A. Murphy. "Influence of metal vapour on arc temperatures in gas-metal arc welding: Convection versus radiation." In: *Journal of Physics D: Applied Physics* 46 (2013), p. 224004. DOI: 10.1088/0022-3727/46/22/224004.

[117] Y. Cressault, A. Murphy, P. Teulet, A. Gleizes, and M. Schnick. "Thermal plasma properties for Ar-Cu, Ar-Fe and Ar-Al mixtures used in welding plasmas processes: II. Transport coefficients at atmospheric pressure." In: *Journal of Physics D Applied Physics* 46 (2013), p. 5207. DOI: 10.1088/0022-3727/46/41/415207.

[118] Y. Cressault, A. Gleizes, and G Riquel. "Properties of air–aluminum thermal plasmas." In: *Journal of Physics D-applied Physics - J PHYS-D-APPL PHYS* 45 (July 2012). DOI: 10.1088/0022-3727/45/26/265202.

[119] A. Murphy, M Tanaka, S. Tashiro, T Sato, and J. Lowke. "A computational investigation of the effectiveness of different shielding gas mixtures for arc welding." In: *Journal of Physics D: Applied Physics* 42 (2009), p. 115205. DOI: 10.1088/0022-3727/42/11/115205.

[120] J. Solomon. *Numerical Algorithms: Methods for Computer Vision, Machine Learning, and Graphics.* en. Google-Books-ID: av5XnwEACAAJ. CRC Press, Taylor & Francis Group, 2015. ISBN: 9781482251883.

[121] S. Coleman. *Notes from Sidney Coleman's Physics 253a.* 2011. arXiv: 1110.5013 [physics.ed-ph].

[122] J. Baez. *The Time-Energy Uncertainty Relation.* 2010 (accessed October 14, 2019). URL: http://math.ucr.edu/home/baez/uncertainty.html.

[123] H. R. Griem. *Spectral line broadening by plasmas [by] Hans R. Griem.* English. Academic Press New York, 1974. ISBN: 0123028507.

List of Figures

List of Tables

Appendix A

Appendix

A.1 Effect of nonlinear laser heating on the electron temperature of a thermal arc

The first chapter introduced the concepts and equations for calculating the plasma temperature distribution of a plasma close to a cathode. The results derived with that method are however still prone to deviations when it comes to plasma diagnostics like Thomson scattering. The source of this discrepancy is rigorously discussed in the plasma physics community [35, 37, 38, 101, 105–107]. This section briefly outlines the implications of the effect of laser induced plasma heating onto the radial plasma temperature profile and therefore the emitted radiation from the plasma. The approach has been adopted from [102] and incooperated to be utilized in the presented radiation model. This method describes the impact of the laser light during a Thomson scattering measurements as a significant source of heating of the plasma itself. The electromagnetic wave of a laser pulse passes through the region of the plasma, the ions due to their inertia are not affected by the electric field vector of that wave. The electrons on the other hand, since they are much lighter will be accelerated by the electric field vector. Macroscopically that means the electrons are heated, as the electron gas partially absorbes energy from the electric field an converts it into its own kinetic energy. To account for this effect the one fluid approach is taken, since LTE condition is still assumed to be valid in absence of the laser light. This leads to a modification of Equation (2.5) for the temperature distribution of the plasma, where the . . . term is now replaced by a source term, accounting for the laser heating into the plasma and the radiation loss out of the plasma.

$$\rho_p c_{p,\,p} \frac{\partial T_p}{\partial t} = \frac{1}{r} \frac{\partial}{\partial r} \left(\lambda_{th,\,p}(T_p) \, r \frac{\partial T_p}{\partial r} \right) + \frac{\sigma_{el}}{\left(\int_0^{r_0} \sigma_{el}(T_p(r)) \, 2\pi r \, dr \right)^2} I_{arc}^2 + \frac{\alpha \, E_p}{A_p \, t_p} - I_{rad} \tag{A.1}$$

with E_p, A_p, t_p being the energy, the focal area and time of the laser pulse. The pulse form is assumed to be of gaussian shape and α being the absorption coefficient of the laser light energy of the plasma:

$$\alpha = \frac{n_e \, Z \left(\sum_{i=1}^h n_i \, Z_i \right) e^6 \left[1 - exp \left(\frac{-h\omega}{2\pi \, k_B \, T_e} \right) \right]}{\mu \, 6\pi \, \epsilon_0^3 c \frac{h}{2\pi} \omega^3 m_e^2} \left(\frac{m_e}{2\pi \, k_B \, T_e} \right)^{\frac{1}{2}} \frac{\pi}{3} \overline{g} \, in \left[\frac{W}{m^3} \right] \tag{A.2}$$

with $\overline{g}$ being the gaunt factor, μ being the refractive index of the plasma and I_{rad} being the radiation intensity emitted by the plasma. The last contribution will be calculated using the relation given prior in this work Equation (3.84).

This description is added to the radiation model (matlab scripts + additional simulink model) and consists of the following part:

Laser heating sim (simulink model) The laser heating simulation is a simulink model built on top of the radiation intensity calculated with Section 3.4. It extends the plasma temperature profile with a laser heating term, according to Equation (A.1). It determines the temporal evolution of the plasma (or rather electron) temperature over the duration of the laser pulse.

A.2 Numerical Techniques

A.2.1 Robust numerical integration scheme for control applications

A general nonlinear equation of motion shall be considered $\frac{dx}{dt} = F(x)$ for a variable x, whose values are always positive (as it is the case in the considered dynamics where all the state variables correspond to temperatures, either in the plasma or at the cathode spot, all of them measured in K). Due to the nonlinear dependence in x, these dynamic equations have to be integrated numerically by discretizing the time coordinate in time steps of equal duration Δt, with $x(t)$ being the current value and $x(+\Delta t)$ the still unknown value to be determined at the next time step. The nonlinear character is taken into account in an iterative way. The nonlinear function $F(x)$ is evaluated at a provisional solution $x^{(prov)}(t + \Delta t)$ for the next time step and then used to gain an improved solution $x(t + \Delta t)$ for the

same solution of this next time step. The just obtained solution is again taken as a provisional one and an even better improved solution is calculated. This process is repeated until the desired accuracy is reached. In order to avoid any artifical and uncontrolled oscillating (sign-changing) solution during the iterative process (which is usually generated by a relatively large Δt), the following two useful methods will be implemented:

1. First (see [79], §4) the contributions to the nonlinear function $F(x)$ are separated into a positive and a negative part, $F(x) = F^{(+)}(x) - F^{(-)}(x)$, where both $F^{(+)}(x)$ and $F^{(-)}(x)$ are positive valued functions. As already mentioned, both functions are evaluated at the provisional solution $x^{(prov)}(t + \Delta t)$ for the next time step, but $F^{(-)}(x)$ is additionally multiplied by the factor $\dfrac{x(t + \Delta t)}{x^{(prov)}(t + \Delta t)}$, which is practically equal to one, for an intended stable iterative process. This leads to the following time discretization of the equation of motion

$$\frac{x(t + \Delta t) - x(t)}{\Delta t} \approx F^{(+)}(x^{(prov)}(t + \Delta t)) - F^{(-)}(x^{(prov)}(t + \Delta t)) \overbrace{\frac{x(t + \Delta t)}{x^{(prov)}(t + \Delta t)}}^{\approx 1}$$

$$x(t + \Delta t)\left[1 + \Delta t\, \frac{F^{(-)}(x^{(prov)}(t + \Delta t))}{x^{(prov)}(t + \Delta t)}\right] \approx x(t) + \Delta t\, F^{(+)}(x^{(prov)}(t + \Delta t))$$

where both sides of the resulting equation consist of only positive contributions. The formulation is independent of the time step size, and therefore no sign changes occur between two consecutive iterations.

2. Nevertheless it may still happen that $F^{(+)}(x)$ (or $F^{(-)}(x)$) is a strongly varying function of x such that the previous method is not enough to ensure that $x^{(prov)}(t + \Delta t)$ and the improved solution $x(t + \Delta t)$ are close to each other, thus hindering the convergence of the iterative procedure. Therefore a second step is carried out by sharing the effect of $F^{(+)}(x)$ on both sides of the discretized equation, according to the following algorithm

$$F^{(+)}(x) \rightarrow \left(1 + \underline{\xi}\right) F^{(+)}(x^{(prov)}(t + \Delta t)) \overbrace{-\xi\, F^{(+)}(x^{(prov)}(t + \Delta t))}^{\substack{\text{to be moved to the} \\ \text{left hand side} \\ \text{since negative}}}$$

$$\rightarrow \left(1 + \underline{\xi}\right) F^{(+)}(x^{(prov)}(t + \Delta t)) - \xi\, F^{(+)}(x^{(prov)}(t + \Delta t)) \frac{x(t + \Delta t)}{x^{(prov)}(t + \Delta t)}$$

with $\xi > 0$ (typically $\xi = 10$).

Hence the final resulting discretization of the equation of motion is

$$\frac{x(t + \Delta t) - x(t)}{\Delta t} \approx F^{(+)}(x^{(prov)}(t + \Delta t)) - F^{(-)}(x^{(prov)}(t + \Delta t)) \overbrace{\frac{x(t + \Delta t)}{x^{(prov)}(t + \Delta t)}}^{\approx 1},$$

$$x(t + \Delta t)\left[1 + \Delta t\, \frac{F^{(-)}(x^{(prov)}(t + \Delta t))}{x^{(prov)}(t + \Delta t)} + \xi \Delta t\, \frac{F^{(+)}(x^{(prov)}(t + \Delta t))}{x^{(prov)}(t + \Delta t)}\right]$$

$$\approx x(t) + (1 + \xi)\, \Delta t\, F^{(+)}(x^{(prov)}(t + \Delta t)) \tag{A.3}$$

where all terms on both sides of the equation are positive. Even if $F^{(+)}$ rapidly increases its value, the improved solution $x(t + \Delta t) \approx x(t) \dfrac{1 + \left(1 + \underline{\xi}\right) \Delta t \frac{F^{(+)}}{x(t)}}{1 + \xi \Delta t \frac{F^{(+)}}{x^{(prov)}(t+\Delta t)}}$ still remains close to the value at the previous time step, without divergence. Such a solution procedure can be iteratively repeated using the just obtained improved solution as a provisional value, leading to an even better improved $x(t + \Delta t)$.

A.2.2 Newton-Raphson numerical solver

The Newton-Raphson method or Newton's method uses straight line tangents to quickly find an approximation for the root of a real valued function. This idea holds for continuous, differentiable functions and can be easily implemented. It is therefore a central technique in numerical mathematics [120].

$$\dot{\vec{x}} = f(\vec{x})$$

with $\vec{x}(t)$ given and $\vec{x}(t + \Delta t)$, $\vec{x}^{prov}(t + \Delta t)$ achievable. The Newton-Raphson scheme is as follows:

$$\vec{x}(t + \Delta t) - \vec{x}(t) = \Delta t\, f(\vec{x})(t + \Delta t)$$

$$\approx \Delta t\, f(\vec{x}^{prov}(t + \Delta t)) + \Delta t \frac{\partial f}{\partial \vec{x}}\left(\vec{x}(t + \Delta t) - \vec{x}^{prov}(t + \Delta t)\right)$$

$$\left(\mathbb{K} - \Delta t\, \frac{\partial f}{\partial \vec{x}}\right) \vec{x}(t + \Delta t) = \vec{x}(t) + \Delta t f\left(\vec{x}^{prov}\right) - \Delta t \frac{\partial f}{\partial \vec{x}} \vec{x}^{prov}(t + \Delta t)$$

$$+ \vec{x}^{prov}(t + \Delta t) - \vec{x}^{prov}(t + \Delta t)$$

$$= \left(\mathbb{K} - \Delta t\, \frac{\partial f}{\partial \vec{x}}\right) \vec{x}^{prov}(t + \Delta t) + \vec{x}(t)$$

$$- \vec{x}^{prov}(t + \Delta t) + \Delta t f\left(\vec{x}^{prov}\right)$$

$$\vec{x}(t + \Delta t) = \kappa \left[\vec{x}^{prov}(t + \Delta t) + \left(\mathbb{K} - \Delta t\, \frac{\partial f}{\partial \vec{x}}\right)^{-1} [\vec{x}(t) - \vec{x}^{prov}(t + \Delta t) + \Delta t f\left(\vec{x}^{prov}\right)]\right]$$

$$+ (1 - \kappa)\vec{x}^{prov}(t + \Delta t)$$

$$\vec{x}(t + \Delta t) = \vec{x}^{prov}(t + \Delta t) + \kappa \left(\mathbb{K} - \Delta t\, \frac{\partial f}{\partial \vec{x}}\right)^{-1} [\vec{x}(t) - \vec{x}^{prov}(t + \Delta t) + \Delta t f\left(\vec{x}^{prov}\right)] \qquad \text{(A.4)}$$

with κ being a relaxation factor between 0 and 1.

A.3 Additional remarks on radiation and quantum mechanics

A.3.1 A crash course into the harmonic oscillator

A particle of mass m is subjected to an elastic force such that the resulting one dimensional dynamic is that of the harmonic oscillator [121] with natural frequency ω_0

$$\dot{p} = m\ddot{q} = -m\omega_0^2 \, q \tag{A.5}$$

whereas q denotes the deviation from the equilibrium position and $p = m\dot{q}$ the particle's momentum. This motion is described by the following total energy or Hamiltonian

$$H = \frac{p^2}{2m} + \frac{m}{2}\omega_0^2 \, q^2 \tag{A.6}$$

through the corresponding Hamiltonian equations: $\dot{q} = \dfrac{\partial H}{\partial p} = m\dot{q}$ and $\dot{p} = -\dfrac{\partial H}{\partial q} = -m\omega_0^2 \, q$. For the quantum mechanical description of this system, the position and momentum become operators with the already discussed commutation relations (derived from the respective classical Poisson brackets)

$$\left[\underline{q}, \, \underline{q}\right] = 0 = \left[\underline{p}, \, \underline{p}\right] \quad \text{and} \quad \left[\underline{q}, \, \underline{p}\right] = i\hbar$$

and correspondingly for the Hamiltonian operator $\underline{H} = \dfrac{\underline{p}^2}{2m} + \dfrac{m}{2}\omega_0^2 \, \underline{q}^2$. In order to solve the energy eigenvalues of this Hamiltonian the following dimensionless operators

$$\underline{q}' = \sqrt{\frac{m\omega_0}{\hbar}} \, \underline{q} \quad \text{and} \quad \underline{p}' = \sqrt{\frac{1}{m\omega_0\hbar}} \, \underline{p} \qquad \Rightarrow \qquad \left[\underline{q}', \underline{p}'\right] = i \tag{A.7}$$

will be introduced at first, such that the Hamilton operator becomes.

$$\underline{H} = \frac{\hbar\omega_0}{2} \left(\underline{q}'^2 + \underline{p}'^2\right) \tag{A.8}$$

This can be further transformed by introducing an additional pair of operators, called annihilation and creation operators, $\underline{a}$ and $\underline{a}^+$ which are Hermitian conjugated to each other and thus independent of each other

$$\underline{a} = \frac{\underline{q}' + i\underline{p}'}{\sqrt{2}}, \quad \underline{a}^+ = \frac{\underline{q}' - i\underline{p}'}{\sqrt{2}} \qquad \Rightarrow \qquad \left[\underline{a}, \, \underline{a}^+\right] = \frac{1}{2}\left(0 + (-i)\cdot i + i\cdot(-i) + 0\right) = 1 \tag{A.9}$$

, now the Hamiltonian takes a very simple form.

$$\begin{aligned}
\underline{H} &= \frac{\hbar\omega_0}{4}\left(-\cancel{(\underline{a})^2} + \underline{a}\,\underline{a}^+ + \underline{a}^+\underline{a} - \cancel{(\underline{a}^+)^2} + \cancel{(\underline{a})^2} + \underline{a}\,\underline{a}^+ + \underline{a}^+\underline{a} + \cancel{(\underline{a}^+)^2}\right) \\
&= \frac{\hbar\omega_0}{2}\left(\underline{a}^+\underline{a} + \underbrace{\underline{a}\,\underline{a}^+}_{\underline{a}^+\underline{a}\,+\,1}\right) = \hbar\omega_0\left(\underline{a}^+\underline{a} + \frac{1}{2}\right)
\end{aligned} \tag{A.10}$$

Hence the energy values scale with $\hbar\omega_0$.

Considering the physical meaning of these creation and annihilation operators $\underline{a}^+$ and $\underline{a}$ in more detail leads to the following conclusion. At first the commutators with the Hamiltonian are calculated.

$$\begin{aligned}
\left[\underline{a}, \, \underline{H}\right] &= \hbar\omega_0 \left[\underline{a}, \, \underline{a}^+\underline{a}\right] \overset{(3.11)}{=} \underline{a}^+ \cdot 0 + \left[\underline{a}, \, \underline{a}^+\right]\underline{a} \overset{(A.9)}{=} +\hbar\omega_0 \, \underline{a} \\
\left[\underline{a}^+, \, \underline{H}\right] &= \hbar\omega_0 \left[\underline{a}^+, \, \underline{a}^+\underline{a}\right] \overset{(3.11)}{=} \underline{a}^+\left[\underline{a}^+, \, \underline{a}\right] + 0 \cdot \underline{a} \overset{(A.9)}{=} -\hbar\omega_0 \, \underline{a}^+
\end{aligned} \tag{A.11}$$

Thus if a state $\psi_n(x,t)$ is an eigenvector (properly normalized $\displaystyle\int_{-\infty}^{\infty} \psi_n^* \, \psi_n \, dx = 1$) of the Hamiltonian $\underline{H}$ with the energy eigenvalue E_n (at the moment the index n has no meaning and doesn't have to be an

integer) the states $\underline{a}\,\psi_n$ and $\underline{a}^+\psi_n$ are also eigenvectors of $\underline{H}$ and have the respective energy eigenvalues $E_n - \hbar\omega_0$ and $E_n + \hbar\omega_0$

$$\underline{H}\,(\underline{a}\,\psi_n) = (\underline{a}\,\underline{H} - [\underline{a},\,\underline{H}])\,\psi_n = \underline{a}\,\overbrace{(\underline{H}\,\psi_n)}^{E_n\,\psi_n} - \hbar\omega_0\,\underline{a}\,\psi_n = (E_n - \hbar\omega_0)\,(\underline{a}\,\psi_n)$$
$$\underline{H}\,(\underline{a}^+\psi_n) = (\underline{a}^+\underline{H} - [\underline{a}^+,\,\underline{H}])\,\psi_n = \underline{a}^+\,(\underline{H}\,\psi_n) + \hbar\omega_0\,\underline{a}^+\psi_n = (E_n + \hbar\omega_0)\,(\underline{a}^+\psi_n)$$

The energy cannot become negative (the Hamiltonian is just the sum of squared positive terms), but the repeated action of $\underline{a}$ on any arbitrary eigenvector ψ_n would eventually produce a state of negative energy, therefore an eigenstate ψ_0 must exist, such that $\underline{a}\,\psi_0 = 0$ holds in order to be compatible with the general relation $\underline{H}\,(\underline{a}\,\psi_0) = (E_0 - \hbar\omega_0)\,(\underline{a}\,\psi_0)$ without simultaneously yielding a negative energy value. Such a "annihilated" state, defined by the operator $\underline{a}$, is called the ground state and it will denoted $|0\rangle$. All other eigenstates result from that ground state through the repeated action of the creation operator $\underline{a}^+$ and have energy values, which (up to a constant term) are an integer (n) multiple with $\hbar\omega_0$:

$$\underline{H}\,|0\rangle = \hbar\omega_0\underline{a}^+\overbrace{\underline{a}\,|0\rangle}^{=0} + \frac{\hbar\omega_0}{2}\,|0\rangle = \frac{\hbar\omega_0}{2}\,|0\rangle$$
$$\underline{H}\,(\underline{a}^+\,|0\rangle) = \left(\frac{\hbar\omega_0}{2} + \hbar\omega_0\right)(\underline{a}^+\,|0\rangle) = \left(1 + \frac{1}{2}\right)\hbar\omega_0\,(\underline{a}^+\,|0\rangle)$$
$$\underline{H}\,(\underline{a}^+\underline{a}^+\,|0\rangle) = \left(\frac{3\hbar\omega_0}{2} + \hbar\omega_0\right)(\underline{a}^+\underline{a}^+\,|0\rangle) = \left(2 + \frac{1}{2}\right)\hbar\omega_0\,(\underline{a}^+\underline{a}^+\,|0\rangle)$$
$$\vdots \qquad \vdots$$

The energy eigenstates will be denoted by $|n\rangle$ instead of ψ_n, since $\underline{a}\,|n\rangle$ has an energy eigenvalue $\left((n-1) + \frac{1}{2}\right)\hbar\omega_0$, this state must be proportional to $|n-1\rangle$ and completely analogous for $\underline{a}^+\,|n\rangle$ in relation to $|n+1\rangle$:

$$\underline{a}\,|n\rangle = c_n\,|n-1\rangle$$
$$\underline{a}^+\,|n\rangle = d_n\,|n+1\rangle$$

Here the proportionality factors c_n and d_n are chosen to be real (if the phase of the eigenvectors $|n\rangle$ is properly defined). The value of such proportionality factors can be easily derived

$$\langle n|\,\underline{a}^+\underline{a}\,|n\rangle = \begin{cases} |(\underline{a}\,|n\rangle)|^2 = c_n^2\,\langle n-1|n-1\rangle = c_n^2 \\ c_n\,\langle n|\underline{a}^+|n-1\rangle = c_n d_{n-1}\,\langle n|n\rangle = c_n d_{n-1} \end{cases} \quad \Rightarrow \quad d_{n-1} = c_n$$

$$\langle n|\,\underline{H}\,|n\rangle = \hbar\omega_0\,\langle n|\,\underline{a}^+\underline{a}\,|n\rangle + \frac{\hbar\omega_0}{2}\,\langle n|n\rangle = \hbar\omega_0\left(c_n^2 + \frac{1}{2}\right) \quad \Rightarrow \quad c_n^2 = n$$

and thus

$$\underline{a}\,|n\rangle = \sqrt{n}\,|n-1\rangle \qquad \text{and} \qquad \underline{a}^+\,|n\rangle = \sqrt{n+1}\,|n+1\rangle \tag{A.12}$$

A.3.2 Quantization of the electromagnetic field

At first the electromagnetic field shall be considered, as a step for later regarding its interaction with bound electrons within an atom. The spatial and temporal distribution of the electromagnetic field $\vec{E}(\vec{x}, t)$ and $\vec{B}(\vec{x}, t)$ is described by the Maxwell equations, which in a system like a plasma without

dielectric or diamagnetic properties are

$$\operatorname{div} \vec{B} = \frac{\partial B_x}{\partial x} + \frac{\partial B_y}{\partial y} + \frac{\partial B_z}{\partial z} = 0$$

$$\operatorname{curl} \vec{E} + \frac{\partial}{\partial t} \vec{B} = \begin{pmatrix} \frac{\partial E_z}{\partial y} - \frac{\partial E_y}{\partial z} \\ \frac{\partial E_x}{\partial z} - \frac{\partial E_z}{\partial x} \\ \frac{\partial E_y}{\partial x} - \frac{\partial E_x}{\partial y} \end{pmatrix} + \begin{pmatrix} \frac{\partial B_x}{\partial t} \\ \frac{\partial B_y}{\partial t} \\ \frac{\partial B_z}{\partial t} \end{pmatrix} = \vec{0}$$

(A.13)

$$\operatorname{div} \vec{E} = \frac{\partial E_x}{\partial x} + \frac{\partial E_y}{\partial y} + \frac{\partial E_z}{\partial z} = \frac{1}{\varepsilon_0} \rho_{el}$$

$$\operatorname{curl} \vec{B} - \mu_0 \varepsilon_0 \frac{\partial}{\partial t} \vec{E} = \begin{pmatrix} \frac{\partial B_z}{\partial y} - \frac{\partial B_y}{\partial z} \\ \frac{\partial B_x}{\partial z} - \frac{\partial B_z}{\partial x} \\ \frac{\partial B_y}{\partial x} - \frac{\partial B_x}{\partial y} \end{pmatrix} - \mu_0 \varepsilon_0 \begin{pmatrix} \frac{\partial E_x}{\partial t} \\ \frac{\partial E_y}{\partial t} \\ \frac{\partial E_z}{\partial t} \end{pmatrix} = \mu_0 \vec{j}_{el}$$

The two last equations are inhomogeneous and describe how the sources electrical charge density ρ_{el} and electrical current density $\vec{j}_{el}$ are coupled to the electromagnetic field. The eight Maxwell equations are not all independent of each other , since electromagnetic fields have maximally 3 degrees of freedom in a system with electrical charges and currents or in vacuum an even a lower number of degrees of freedom (2, which are the two polarizations of an electromagnetic wave). Therefore a more compact way of formulating the Maxwell equations is required. The first two homogeneous equations can be automatically fulfilled by introducing the vector and scalar potentials $\vec{A}(\vec{x}, t)$ and $\phi(\vec{x}, t)$ to re-formulating the magnetic and electric field through these potentials

$$\vec{B} = \operatorname{curl} \vec{A} = \begin{pmatrix} \frac{\partial A_z}{\partial y} - \frac{\partial A_y}{\partial z} \\ \frac{\partial A_x}{\partial z} - \frac{\partial A_z}{\partial x} \\ \frac{\partial A_y}{\partial x} - \frac{\partial A_x}{\partial y} \end{pmatrix} \quad \text{and} \quad \vec{E} = -\operatorname{grad} \phi - \frac{\partial}{\partial t} \vec{A} = \begin{pmatrix} -\frac{\partial \phi}{\partial x} - \frac{\partial A_x}{\partial t} \\ -\frac{\partial \phi}{\partial y} - \frac{\partial A_y}{\partial t} \\ -\frac{\partial \phi}{\partial z} - \frac{\partial A_z}{\partial t} \end{pmatrix} . \qquad \text{(A.14)}$$

In this way the number of degrees of freedom has been reduced to 4 (the number of components of the vector and scalar potential together). But even after this reduction there is still one (in the case of a system with free charges) or even two (in the case of vacuum or a system with weak interacting charges) further degrees of freedom which are spurious and can be removed. This later effect is the consequence of the freedom in choice of the potentials to describe the same electromagnetic field configuration. There exists an infinite number of different potentials, as the following pair $\{\phi(\vec{x}, t), \vec{A}(\vec{x}, t)\}$, as well as the pair $\{\phi'(\vec{x}, t), \vec{A}'(\vec{x}, t)\}$, which yield the same electromagnetic field (A.14)

$$\vec{A} \longrightarrow \vec{A}' = \vec{A} + \operatorname{grad} \chi(\vec{x}, t)$$

$$\phi \longrightarrow \phi' = \phi - \frac{\partial}{\partial t} \chi(\vec{x}, t)$$

(A.15)

with $\chi(\vec{x}.t)$ being an arbitrary smooth function of the spatial and temporal coordinates. This property is called gauge invariance (or more improperly "gauge symmetry"). Hence in vacuum a particular $\chi(\vec{x}, t)$ can be chosen, with the potentials fulfilling two further conditions, typically $\phi'(\vec{x}, t) = 0$ and $\operatorname{div} \vec{A}' = 0$, in order to reduce the 4 components contained in the potentials to the 2 actual and physical degrees of freedom. In a system with free charges and currents one condition can still be chosen, typically $\phi'(\vec{x}, t) = 0$. The electromagnetic fields take the following form after such a choice:

$$\vec{B} = \operatorname{curl} \vec{A}' \quad \text{and} \quad \vec{E} = -\frac{\partial}{\partial t} \vec{A}' \qquad \text{(A.16)}$$

together with

$$\operatorname{grad}\left(\operatorname{div} \vec{A}'\right) - \Delta \vec{A}' + \mu_0 \varepsilon_0 \frac{\partial^2}{\partial t^2} \vec{A}' = \mu_0 \vec{j}_{el}$$

$$-\frac{\partial}{\partial t}\left(\operatorname{div} \vec{A}'\right) = \frac{1}{\varepsilon_0} \rho_{el}$$

(A.17)

From now on the prime $'$ will no longer be written explicitly and with the additional condition div $\vec{A}' = 0$ (if we are considering vacuum or a system nearly so diluted as vacuum $\vec{j}_{el} \approx \vec{0}$ and $\rho_{el} \approx 0$).

Considering the most simple electromagnetic configuration in vacuum ($\vec{j}_{el} = \vec{0}$ and $\rho_{el} = 0$): a planar electromagnetic wave propagating along the z direction with a single frequency ω. This configuration is described by the following real vector potential

$$\vec{A}(\vec{x}, t) = \begin{pmatrix} A_x(z,t) \\ 0 \\ 0 \end{pmatrix} \qquad \text{with} \quad A_x(z,t) = \frac{A_\omega(t)\, e^{ikz} + A_\omega^*(t)\, e^{-ikz}}{\sqrt{2}} \tag{A.18}$$

with the time dependence in $A_\omega(t)$ chosen in the way that $\dot{A}_\omega = -i\omega\, A_\omega$ holds and therefore the propagation velocity of the wave is given by $\frac{\omega}{k}$. This vector potential fulfills not only the gauge condition div $\vec{A} = 0$, but also the Maxwell equation (A.17), as long as the following relation holds for the propagation velocity:

$$k^2 - \mu_0 \varepsilon_0\, \omega^2 = 0 \quad \Rightarrow \quad \frac{\omega}{k} = \frac{1}{\sqrt{\mu_0 \varepsilon_0}} \tag{A.19}$$

with the propagation velocity of that electromagnetic wave being the speed of light c in vacuum.

The quantum mechanical formulation of the electromagnetic field's dynamics requires at first the calculation of the corresponding Hamiltonian or total energy for the considered system. This is achieved by the integration over the whole system's volume L^3 of the electromagnetic energy density [1] $\frac{\varepsilon_0}{2}\vec{E}^2 + \frac{1}{2\mu_0}\vec{B}^2$

$$H_{em} = \iiint \left(\frac{\varepsilon_0}{2}\vec{E}^2 + \frac{1}{2\mu_0}\vec{B}^2 \right) d^3\vec{x} = L^2 \int_{-L/2}^{L/2} \left(\frac{\varepsilon_0}{2}\, E_x^2 + \frac{1}{2\mu_0}\, B_y^2 \right) dz \tag{A.20}$$

together with

$$A_x(z,t) = \frac{A_\omega\, e^{ikz} + A_\omega^*\, e^{-ikz}}{\sqrt{2}} \qquad \dot{A}_x(z,t) = -i\omega \frac{A_\omega\, e^{ikz} - A_\omega^*\, e^{-ikz}}{\sqrt{2}}$$

$$E_x(z,t) = -\dot{A}_x(\vec{x},t) = i\omega \frac{A_\omega\, e^{ikz} - A_\omega^*\, e^{-ikz}}{\sqrt{2}} \tag{A.21}$$

$$B_y(z,t) = \frac{\partial A_x}{\partial z} = ik \frac{A_\omega\, e^{ikz} - A_\omega^*\, e^{-ikz}}{\sqrt{2}} \overset{(A.19)}{=} i\sqrt{\mu_0 \varepsilon_0}\, \omega \frac{A_\omega\, e^{ikz} - A_\omega^*\, e^{-ikz}}{\sqrt{2}}$$

Actually the volume extension is infinite but in order to avoid such infinity the system has been put inside a finite box with the additional property that the field variables depend on the propagation coordinate z in a periodic way such that any field variable evaluated at $z = -L/2$ has the same value

---

[1] By scalar multiplying the last Maxwell equation in (A.13) with $-\frac{1}{\mu_0}\vec{E}$ and using the following relation $-\vec{E} \cdot \text{curl}\,\vec{B} = \text{div}\left(\vec{E} \times \vec{B}\right) - \vec{B} \cdot \text{curl}\,\vec{E} = \text{div}\left(\vec{E} \times \vec{B}\right) + \vec{B} \cdot \frac{\partial \vec{B}}{\partial t}$ (the latter equality arises from the 2nd Maxwell equation in (A.13)) one obtains $-\vec{j}_{el} \cdot \vec{E} = -\frac{1}{\mu_0}\vec{E} \cdot \text{curl}\,\vec{B} + \underbrace{\varepsilon_0 \vec{E} \cdot \frac{\partial \vec{E}}{\partial t}}_{\frac{\partial}{\partial t}\left(\frac{\varepsilon_0}{2}\vec{E}^2\right)} = \frac{\partial}{\partial t}\left(\frac{\varepsilon_0}{2}\vec{E}^2 + \frac{1}{2\mu_0}\vec{B}^2\right) + \text{div}\left(\frac{\vec{E} \times \vec{B}}{\mu_0}\right)$. For a local infinitesimal volume the temporal change in $\frac{\varepsilon_0}{2}\vec{E}^2 + \frac{1}{2\mu_0}\vec{B}^2$ contained within such volume results from either a) to the net flux of the current $\frac{\vec{E} \times \vec{B}}{\mu_0}$ through the volume surrounding walls; or b) to the loss at a rate $\vec{j}_{el} \cdot \vec{E}$ within the volume itself. With $\vec{j}_{el} \cdot \vec{E}$ being nothing else than the electrical power dissipated per unit volume (the local formulation of the power loss due to the Joule effect) the quantity $\frac{\varepsilon_0}{2}\vec{E}^2 + \frac{1}{2\mu_0}\vec{B}^2$ is called the density of electromagnetic energy.

like the one at $z = +L/2$ (in other words $kL = 2\pi$). The integral over dz in (A.20) can thus be performed immediately

$$
\begin{aligned}
H_{em} &= \iiint \left(\frac{\varepsilon_0}{2} \vec{E}^2 + \frac{1}{2\mu_0} \vec{B}^2 \right) d^3\vec{x} \\
&= -L^2 \frac{\varepsilon_0 \omega^2}{2} \int_{-L/2}^{L/2} \left((A_\omega)^2 e^{i2kz} + (A_\omega^*)^2 e^{-i2kz} \right) dz \\
&\quad + L^2 \frac{\varepsilon_0 \omega^2}{2} \int_{-L/2}^{L/2} (A_\omega A_\omega^* + A_\omega^* A_\omega)\, dz = 0 + L^3 \frac{\varepsilon_0 \omega^2}{2} (A_\omega A_\omega^* + A_\omega^* A_\omega)
\end{aligned}
$$

$$
H_{em} \equiv \frac{\hbar\omega}{2} \left(\sqrt{\frac{L^3 \varepsilon_0 \omega}{\hbar}} A_\omega \sqrt{\frac{L^3 \varepsilon_0 \omega}{\hbar}} A_\omega^* + \sqrt{\frac{L^3 \varepsilon_0 \omega}{\hbar}} A_\omega^* \sqrt{\frac{L^3 \varepsilon_0 \omega}{\hbar}} A_\omega \right) \tag{A.22}
$$

The quantum mechanical formulation of the system dynamics is now easliy formulated. The variable A_ω becomes an operator and the just obtained Hamiltonian is completely analogous to that of the harmonic oscillator with a natural frequency ω_0 (A.10), $\underline{H} = \frac{\hbar\omega_0}{2} (\underline{a}\,\underline{a}^+ + \underline{a}^+\underline{a})$, with $\sqrt{\frac{L^3 \varepsilon_0 \omega}{\hbar}} \underline{A}_\omega$ instead of the annihilation operator $\underline{a}$. Hence the corresponding annihilation and creation operators for discrete "portions" of electromagnetic energy (called photons) are defined through

$$
\begin{aligned}
\underline{A}_\omega &= \sqrt{\frac{\hbar}{L^3 \varepsilon_0 \omega}}\, \underline{a}_\omega \,, \\
\underline{A}_\omega^+ &= \sqrt{\frac{\hbar}{L^3 \varepsilon_0 \omega}}\, \underline{a}_\omega^+ \,,
\end{aligned}
\tag{A.23}
$$

with commutation relations similar to those of the harmonic oscillator

$$
\begin{aligned}
&[\underline{a}_\omega,\, \underline{a}_\omega^+] = 1, \; [\underline{a}_\omega,\, \underline{a}_\omega] = [\underline{a}_\omega^+,\, \underline{a}_\omega^+] = 0 \\
&[\underline{A}_\omega,\, \underline{A}_\omega^+] = \frac{\hbar}{L^3 \varepsilon_0 \omega}\,, \quad [\underline{A}_\omega,\, \underline{A}_\omega] = [\underline{A}_\omega^+,\, \underline{A}_\omega^+] = 0
\end{aligned}
\tag{A.24}
$$

The Hamilton operator for an electromagnetic waves of frequency ω is accordingly given by

$$
\underline{H}_{em} = \frac{\hbar\omega}{2} (\underline{a}_\omega\,\underline{a}_\omega^+ + \underline{a}_\omega^+\underline{a}_\omega) = \hbar\omega \left(\underline{a}_\omega^+ \underline{a}_\omega + \frac{1}{2} \right) \equiv L^3 \varepsilon_0 \omega^2 \left(\underline{A}_\omega^+ \underline{A}_\omega + \frac{1}{2} \right). \tag{A.25}
$$

Such a (vacuum) Hamilton operator, together with the commutation relations above, reproduces the Maxwell equations for the dynamics of the electric and magnetic field, which now have become operators according to relations (A.21)

$$
\begin{aligned}
\underline{E}_x &= i\omega \frac{\underline{A}_\omega e^{ikz} - \underline{A}_\omega^+ e^{-ikz}}{\sqrt{2}}\,, \\
\underline{B}_y &= i \underbrace{\sqrt{\mu_0 \varepsilon_0}\, \omega}_{k} \frac{\underline{A}_\omega e^{ikz} - \underline{A}_\omega^+ e^{-ikz}}{\sqrt{2}}\,,
\end{aligned}
$$

$$
\begin{aligned}
[\underline{B}_y,\, \underline{H}_{em}] &= \frac{ik}{\sqrt{2}} e^{ikz} L^3 \varepsilon_0 \omega^2 \overbrace{[\underline{A}_\omega,\, \underline{A}_\omega^+ \underline{A}_\omega]}^{\frac{\hbar}{L^3 \varepsilon_0 \omega} \underline{A}_\omega + \underline{A}_\omega^+ \cdot 0} - \frac{ik}{\sqrt{2}} e^{-ikz} L^3 \varepsilon_0 \omega^2 \overbrace{[\underline{A}_\omega^+,\, \underline{A}_\omega^+ \underline{A}_\omega]}^{0 \cdot \underline{A}_\omega - \frac{\hbar}{L^3 \varepsilon_0 \omega} \underline{A}_\omega^+}\,, \\
\frac{1}{i\hbar} [\underline{B}_y,\, \underline{H}_{em}] &= \omega k \frac{\underline{A}_\omega e^{ikz} + \underline{A}_\omega^+ e^{-ikz}}{\sqrt{2}}\,, \\
(\operatorname{curl} \underline{E})_y &= \frac{\partial \underline{E}_x}{\partial z} = -\omega k \frac{A_\omega e^{ikz} + A_\omega^* e^{-ikz}}{\sqrt{2}}\,, \\
\Longrightarrow \quad \frac{d}{dt} \underline{B}_y &= \frac{1}{i\hbar} [\underline{B}_y,\, \underline{H}_{em}] = -(\operatorname{curl} \underline{E})_y\,,
\end{aligned}
\tag{A.26}
$$

as the quantum mechanical dynamic equation (3.12) relates the temporal evolution of the magnetic field to spatial gradients of the electric field (second Maxwell equation in (A.13)). And equivalently

$$[\underline{E}_x, \underline{H}_{em}] = \frac{i\omega}{\sqrt{2}}e^{ikz} L^3\varepsilon_0\omega^2 \overbrace{\left[\underline{A}_\omega, \underline{A}_\omega^+\underline{A}_\omega\right]}^{\frac{\hbar}{L^3\varepsilon_0\omega}\underline{A}_\omega} - \frac{i\omega}{\sqrt{2}}e^{-ikz} L^3\varepsilon_0\omega^2 \overbrace{\left[\underline{A}_\omega^+, \underline{A}_\omega^+\underline{A}_\omega\right]}^{-\frac{\hbar}{L^3\varepsilon_0\omega}\underline{A}_\omega^+},$$

$$\frac{1}{i\hbar}[\underline{E}_x, \underline{H}_{em}] = \omega^2 \frac{\underline{A}_\omega\, e^{ikz} + \underline{A}_\omega^+\, e^{-ikz}}{\sqrt{2}},$$

$$(\text{curl}\,\underline{B})_x = -\frac{\partial \underline{B}_y}{\partial z} = \mu_0\varepsilon_0\,\omega^2 \frac{A_\omega\, e^{ikz} + A_\omega^*\, e^{-ikz}}{\sqrt{2}},$$

$$\implies \quad \frac{d}{dt}\underline{E}_x = \frac{1}{i\hbar}[\underline{E}_x, \underline{H}_{em}] = \frac{1}{\mu_0\varepsilon_0}(\text{curl}\,\underline{B})_x ,$$

(A.27)

as the last Maxwell equation (A.13) in vacuum $(\vec{j}_{el} = \vec{0})$.

The energy eigenstates for the Hamilton operator $\underline{H}_{em}$ (for the frequency ω) will be represented by $\left|0^{(\gamma)}\right\rangle$ for the ground state, $\left|1^{(\gamma)}\right\rangle$ for the state with one photon, and similarly for states with a higher number of photons. Eigenstates with a different number of photons (or belonging to photons of different frequency ω) are orthogonal to each other. Finally the following two transition amplitudes connecting two eigenstates differing in one photon will be useful in the section

$$\left\langle 1^{(\gamma)}|\underline{A}_\omega|0^{(\gamma)}\right\rangle = \sqrt{\frac{\hbar}{L^3\varepsilon_0\omega}} \left\langle 1^{(\gamma)}|\underbrace{\underline{a}_\omega\left|0^{(\gamma)}\right\rangle}_{=\,0} = 0,$$

$$\left\langle 1^{(\gamma)}|\underline{A}_\omega^+|0^{(\gamma)}\right\rangle = \sqrt{\frac{\hbar}{L^3\varepsilon_0\omega}} \left\langle 1^{(\gamma)}|\underbrace{\underline{a}_\omega^+\left|0^{(\gamma)}\right\rangle}_{=\,1\,\cdot\,\left|1^{(\gamma)}\right\rangle} = \sqrt{\frac{\hbar}{L^3\varepsilon_0\omega}}.$$

(A.28)

A.3.3 The pertubed Hamiltonian - electric dipole moment for a bound electron within an atom

A dipole consisting of a positive charge $+e$ located at $\dfrac{a_{dip}}{2}\begin{pmatrix}\cos\theta_0\\\sin\theta_0\end{pmatrix}$ and a negative charge $-e$ at $-\dfrac{a_{dip}}{2}\begin{pmatrix}\cos\theta_0\\\sin\theta_0\end{pmatrix}$ creates an electrostatic potential energy on another charge q at $\begin{pmatrix}x\\y\end{pmatrix}$ with $\sqrt{x^2+y^2} \gg a_{dip}$ equal to

$$E_{pot} = \frac{eq}{4\pi\varepsilon_0}\left[\frac{1}{\sqrt{\left(x-\frac{a_{dip}}{2}\cos\theta_0\right)^2 + \left(y-\frac{a_{dip}}{2}\sin\theta_0\right)^2}} - \frac{1}{\sqrt{\left(x+\frac{a_{dip}}{2}\cos\theta_0\right)^2 + \left(y+\frac{a_{dip}}{2}\sin\theta_0\right)^2}}\right]$$

$$\approx \frac{eq}{4\pi\varepsilon_0}\frac{a_{dip}}{x^2+y^2}\left[\cos\theta_0\frac{x}{\sqrt{x^2+y^2}} + \sin\theta_0\frac{y}{\sqrt{x^2+y^2}}\right] = \frac{q}{4\pi\varepsilon_0}\frac{(ea_{dip})\cos\theta}{x^2+y^2} \equiv \frac{q}{4\pi\varepsilon_0}\frac{\vec{d}_{dip}\cdot\vec{r}}{|\vec{r}|^3}$$

(A.29)

, where the dipole moment of the charge pair is defined as $\vec{d}_{dip} = (ea_{dip})\begin{pmatrix}\cos\theta_0\\\sin\theta_0\end{pmatrix}$ and is oriented from its negative to its positive charge; θ is the angle between the direction of the dipole moment and the position vector $\vec{r} = \begin{pmatrix}x\\y\end{pmatrix}$ where the other charge q is located. If on the other hand a constant electric field $\vec{E}_0$ (at least constant for length scales comparable to the extension of the electric dipole) is applied for instance along the x direction, the potential energy of the previously considered charge pair (with respect to a reference chosen when the dipole and the electric field are parallel to each other) is equal to $E_{pot} = (+e)\displaystyle\int_{ref}^{\theta_0}\vec{E}_0\cdot d\vec{s} + (-e)\displaystyle\int_{ref}^{-\theta_0}\vec{E}_0\cdot d\vec{s} = (ea_{dip})\left|\vec{E}_0\right|\cos\theta_0 \equiv \vec{d}_{dip}\cdot\vec{E}_0.$

x

A.3.4 The time-energy uncertainty relation

For two different operators $\underline{A}$ and $\underline{B}$ and an arbitrary state $|\psi\rangle$ with $\langle\psi|\psi\rangle = \int_{-\infty}^{\infty} \psi^*(x)\,\psi(x)\,dx = 1$, the following expectation values describe the standard deviations for respectively both operators

$$(\Delta A)^2 = \langle\psi|\underline{A}^2|\psi\rangle - (\langle\psi|\underline{A}|\psi\rangle)^2 = \left\langle\psi\right|(\underline{A} - \langle A\rangle)^2\left|\psi\right\rangle \qquad \text{with} \quad \langle A\rangle \equiv \langle\psi|\underline{A}|\psi\rangle$$

$$(\Delta B)^2 = \langle\psi|\underline{B}^2|\psi\rangle - (\langle\psi|\underline{B}|\psi\rangle)^2 = \left\langle\psi\right|(\underline{B} - \langle B\rangle)^2\left|\psi\right\rangle \qquad \text{with} \quad \langle B\rangle \equiv \langle\psi|\underline{B}|\psi\rangle$$

and thus they are called uncertainties. For an arbitrary real number κ following relation

$f(\kappa) = \left\langle\psi\left|\left[\kappa\left(\underline{A} - \langle A\rangle\right) - i\left(\underline{B} - \langle B\rangle\right)\right]^*\left[\kappa\left(\underline{A} - \langle A\rangle\right) - i\left(\underline{B} - \langle B\rangle\right)\right]\right|\psi\right\rangle \geq 0$, is always non-negative as well as real, since it corresponds to the absolute value of a squared expression. This defines a real function of κ [122] which can be rewritten as

$f(\kappa) = \kappa^2(\Delta A)^2 + (\Delta B)^2 - i\kappa\left\langle\psi\right|\underbrace{(\underline{AB} - \underline{BA})}_{[\underline{A},\,\underline{B}]}\left|\psi\right\rangle + 0$. Since $f(\kappa)$ is real and non-negative the commutator $[\underline{A},\,\underline{B}]$ must be pure imaginary (with positive sign in order to keep $f(\kappa)$ non-negative),

$f(\kappa) = \kappa^2(\Delta A)^2 + (\Delta B)^2 + \kappa\left|\langle\psi|[\underline{A},\,\underline{B}]|\psi\rangle\right|$, and additionally, as a function of κ, $f(\kappa)$ is non-negative and corresponds to a parabola oriented upwards. Hence its minimum evaluated at $\kappa = \kappa_0$ is also non-

negative: $\kappa_0 = -\dfrac{\left|\langle\psi|[\underline{A},\,\underline{B}]|\psi\rangle\right|}{2(\Delta A)^2}$ (from condition $\left.\dfrac{df}{d\kappa}\right|_{\kappa=\kappa_0} = 0$) and $(\Delta A)^2(\Delta B)^2 \geq \dfrac{1}{4}\left|\langle\psi|[\underline{A},\,\underline{B}]|\psi\rangle\right|^2$

(from $f(\kappa = \kappa_0) \geq 0$). For the case $\underline{A} = \underline{q}$ (position operator) and $\underline{B} = \underline{p}$ (momentum operator), the commutator $[\underline{q},\,\underline{p}] = i\hbar$ finally leads to the Uncertainty Principle $\Delta q\,\Delta p \geq \dfrac{\hbar}{2}$. With this results now the case with $\underline{B} = \underline{H}$ can be consideres, i.e. the Hamiltonian describing the energy of the system:

$\Delta A\,\Delta H \geq \dfrac{1}{2}\left|\langle\psi|[\underline{A},\,\underline{H}]|\psi\rangle\right|$. Since the Hamiltonian also describes the time evolution of any operator by means of $\dfrac{d}{dt}\underline{A} = \dfrac{1}{i\hbar}[\underline{A},\,\underline{H}]$ it follows

$\Delta A\,\Delta H \geq \dfrac{\hbar}{2}\left|\left\langle\psi\right|\dfrac{d}{dt}\underline{A}|\psi\rangle\right| \equiv \dfrac{\hbar}{2}\left|\dfrac{d\langle A\rangle}{dt}\right|$. If Δt denotes the time scale where a variation in $\langle A\rangle$ takes

place in the order of magnitude of ΔA, then the previous result leads to $\Delta A\,\Delta H \geq \dfrac{\hbar}{2}\dfrac{\Delta A}{\Delta t}$ or equivalently

to $\Delta t\,\Delta E \geq \dfrac{\hbar}{2}$ since the uncertainty in the Hamiltonian describes the uncertainty in energy.

A.3.5 An approximation for spectral broadening due to the Linear Stark effect

A simplified approximation of the line broadening resulting from Linear Stark effect can be derived regarding a system of two colliding electrons. One inside an atom in the outer energy level (which represents a permanent electric dipol) and the other electron moving freely on a colliding path with that atom. The derivation follows in general the descriptions in [123].
The inciding electron moves with the velocity v_e in the reference system and scatering occurs from the center of gravity point of view with the scattering angle χ and the velocities can be described as:

$$\vec{v}_1|_{cm} = \frac{v_e}{2}\begin{pmatrix}1\\0\end{pmatrix},\ \vec{v}_2|_{cm} = \frac{v_e}{2}\begin{pmatrix}-1\\0\end{pmatrix}\ \vec{v}_1'\Big|_{cm} = \frac{v_e}{2}\begin{pmatrix}\cos\chi\\\sin\chi\end{pmatrix}\ \vec{v}_2'\Big|_{cm} = \frac{v_e}{2}\begin{pmatrix}-\cos\chi\\-\sin\chi\end{pmatrix} \tag{A.30}$$

The velocity of the center of gravity moving in the reference system is:

$$\vec{v}_{cm} = \frac{m_e\vec{v}_e + m_e\vec{0}}{2m_e} = \frac{v_e}{2}\begin{pmatrix}1\\0\end{pmatrix} \tag{A.31}$$

the velocity is kept constant, because the interaction force is a inner force between the two electrons:

$$\vec{v}_1' = \vec{v}_1|_{cm} + \vec{v}|_{cm} = \frac{v_e}{2}\begin{pmatrix} 1+\cos\chi \\ \sin\chi \end{pmatrix} \quad \vec{v}_2' = \vec{v}_2|_{cm} + \vec{v}|_{cm} = \frac{v_e}{2}\begin{pmatrix} 1-\cos\chi \\ -\sin\chi \end{pmatrix} \tag{A.32}$$

The transmission of momentum towards the inciding electron perpendicular to the moving directory can be approximated for small scattering angles χ as:

$$m_e \frac{v_e}{2} \approx \frac{e^2}{4\pi\epsilon_0}\frac{1}{b^2}\frac{2b}{v_e} \implies \frac{\chi}{2}\frac{e^2}{4\pi\epsilon_0}\frac{1}{\frac{m_e v_e^2}{2}}\frac{1}{b} \tag{A.33}$$

with the scattering parameter b. The change in kinetic energy of the inciding electron is:

$$\epsilon = -\frac{m_e}{2}\left(\vec{v}_1^2 - \vec{v'}_1^2\right) = -\frac{m_e}{2}\vec{v}_e^2\left[1 - \frac{1}{4}\left((1+\cos\chi)^2 + \sin^2\chi\right)\right] \approx -\frac{m_e}{2}\vec{v}_e^2\frac{\chi^2}{4} \tag{A.34}$$

regarded from the reference system. And the cross section for the energy transfer $|\epsilon|$ between the two interacting electrons can be expressed as:

$$\sigma_{exc} = \pi b^2 \approx \pi\left(\frac{e^2}{4\pi\epsilon_0}\frac{1}{\frac{m_e v_e^2}{2}}\right)^2\frac{4}{\chi^2} = \pi\left(\frac{e^2}{4\pi\epsilon_0}\right)^2\frac{1}{|\epsilon|\frac{m_e v_e^2}{2}} \tag{A.35}$$

with σ_{exc} being the collision cross section and $|\epsilon|$ being the energy that is absorbed if it corresponds to the discrete energy of two neighboring electronic states within the atom $|\epsilon| = E_{if}$. Additionally correcting the Equation (A.35) with the oscillator strength f_{if} of the transition $n \implies m$ and with $E_e = \frac{m_e v_e^2}{2}$ as kinetic energy of the inciding electron leads to:

$$\sigma_{exc,if} \approx \pi\left(\frac{e^2}{4\pi\epsilon_0}\right)^2\frac{f_{if}}{E_{if}E_e} \tag{A.36}$$

The collision time of the two electron system can be expressed as:

$$\frac{1}{\tau_e} = n_e\left\langle\sigma_{exc,if}v_e\right\rangle \tag{A.37}$$

with n_e the free electron density within the plasma and $\langle\sigma_{exc,if}v_e\rangle$ describing the average over all possible velocities of the inciding electrons, that correspond to a kinetic energy equally or larger than the excitation energy E_{if}. Combining the equations (A.36), (A.37) leads to:

$$\begin{aligned}
\langle\sigma_{exc,if}v_e\rangle &\approx \pi\left(\frac{e^2}{4\pi\epsilon_0}\right)^2\frac{f_{if}}{E_{if}}\left\langle\frac{v_e}{\frac{m_e v_e^2}{2}}\right\rangle \\
&= \pi\left(\frac{e^2}{4\pi\epsilon_0}\right)^2\frac{f_{if}}{E_{if}}\frac{2}{m_e}\left(\frac{m_e}{2\pi k_B T_e}\right)^{\frac{3}{2}}\int_{v_{e,min}}^{\infty}\frac{4\pi v_e^2}{v_e}e^{-\frac{m_e v_e^2}{2k_B T_e}}dv_e \\
&= \pi\left(\frac{e^2}{4\pi\epsilon_0}\right)^2\frac{f_{if}}{E_{if}}\frac{4}{m_e}\sqrt{\frac{m_e}{2\pi k_B T_e}}\int_{\sqrt{\frac{E_{if}}{k_B T_e}}}^{\infty}2xe^{-x^2}dx \\
&= 4\pi\left(\frac{e^2}{4\pi\epsilon_0}\right)^2\frac{f_{if}}{E_{if}}\frac{e^{-\frac{E_{if}}{k_B T_e}}}{\sqrt{2\pi m_e k_B T_e}}
\end{aligned} \tag{A.38}$$

Finally the line broadening of the wavelength according to the Linear Stark effect is:

$$\Delta\omega_{if} \sim \frac{1}{\tau_e} \overset{\lambda\omega=c}{\implies} \Delta\lambda_{if} = \frac{\lambda^2}{c}n_e\langle\sigma_{exc,if}v_e\rangle \sim \frac{\lambda^2}{c}4\pi\left(\frac{e^2}{4\pi\epsilon_0}\right)^2\frac{f_{if}}{E_{if}}\frac{e^{-\frac{E_{if}}{k_B T_e}}}{\sqrt{2\pi m_e k_B T_e}}n_e \tag{A.39}$$

This remains valid only for species with a static electric dipol in the outer electronic states, which is interesting for the components of metallic vapours.

A.4   Matlab scripts and functions

The code is structured according to the statements in Section 4.4 for the control model and Section 3.4 for the radiation model.
The corresponding folder, source code, component tests and examples, can be received from the Chair of the laboratory of plasma technology of the Bundeswehr university munich (https://www.unibw.de/plasmatechnik).